# Center-to-limb investigations
# of solar photospheric magnetic features
# at high spatial resolution

Dissertation
zur Erlangung des Doktorgrades
der Mathematisch-Naturwissenschaftlichen Fakultäten
der Georg-August-Universität zu Göttingen

vorgelegt von
**Philippe Kobel**
aus Genf, Schweiz

Göttingen  2009

# Contents

Contents

# Summary

The work presented in this dissertation has been dedicated to the investigation of the center-to-limb (CLV) variation of the appearance and brightness of small-scale magnetic features in the solar photosphere, observed at a very high spatial resolution. The goals of this work were to provide both novel observational constraints for MHD models, and a deeper understanding of the relationhip between the features appearing as Bright Points (BPs) and faculae.

- A photometric method based on Linear Discriminant Analysis was developed to classify BPs and faculae, after their detection via a segmentation algorithm. Applying this method to images of active regions at various heliocentric angles allowed the determination of a CLV of the relative number of BPs and faculae.

- The brightness and morphology of the classified BPs and faculae was statistically investigated. Despite the absence of information about the magnetic field, the results indicate that the frequent faculae near disk center are induced by inclined fields, whereas the apparent BPs near the limb are rather small faculae. The skewness of the facular intensity profiles, quantifying their asymmetry, could represent a valid constraint for models.

- The behaviour of the contrast as a function of the apparent area of BPs and faculae is very reminiscent of similar studies based on magnetogram signal, and thus offers interesting prospects for proxy magnetometry.

- Spectro-polarimetric scans at a constant spatial resolution (Hinode satellite) were used to assess the dependence of the continuum brightness of magnetic features on both the heliocentric distance and on magnetic parameters inferred by inversions: field inclination, strength and filling factor (i.e. the fraction of the resolution element occupied by magnetic fields). The brightness was found to behave differently in two distinct regimes of apparent flux density (net average of flux density in the resolution element), characterizing fields that are tied to granulation and strong magnetic features, respectively. For the latter, the brightness was found to depend essentially on the apparent flux density (with a rather symmetric dependence on the field stength and filling factor), while the fields are quasi-vertical.

# 1   The small-scale magnetic features and their radiative signatures

This Chapter is intended to give a broad overview about the knowledge of small-scale magnetic features, with particular emphasis on their visible signatures and the underlying physics. The observations and known properties of these features will be only briefly presented, as a ground from which the basic theoretical concepts can be developed.

## 1.1   Brief overview of photospheric magnetism

Solar Physics can be thought of as "high-resolution stellar physics". From the astrophysicist's point of view, the Sun occupies a privileged place among the stars, as its proximity allows us to resolve the details of its surface, thus enabling the study of plasmas over a range of scales that can neither be resolved in other stars nor reproduced in the laboratory.
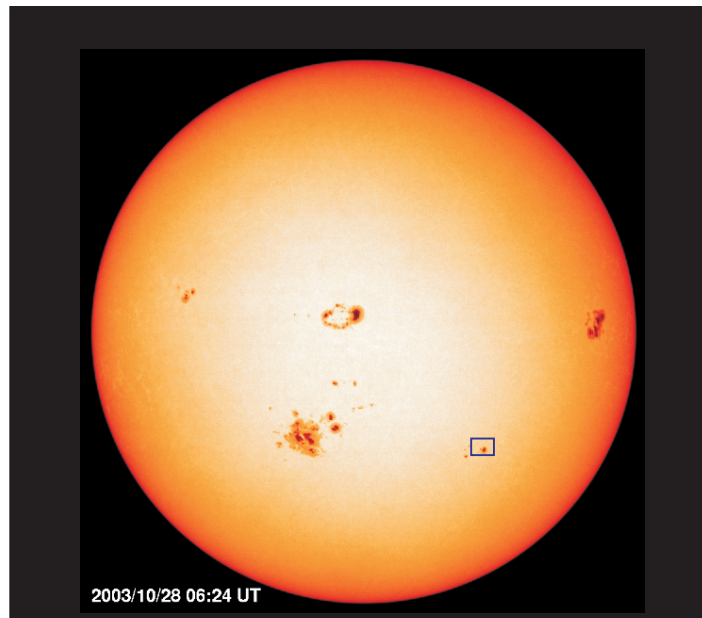


Figure 1.1: Full-disk image of the solar photosphere, recorded at a continuum wavelength near the 676.8 nm Ni I line by the MDI (Michelson Doppler Imager) instrument onboard the SOHO spacecraft. The small blue rectangle outlines the typical size of the field of view covered by high-resolution images like Fig. 1.2.

In that respect, the solar *photosphere* (litterally "sphere of light") is a crucial part of the Solar atmosphere, as it consists of *the range of layers from which the bulk of the solar electromagnetic energy escapes* to outer space (electromagnetic radiation is the most important and often unique carrier of information on astrophysical objects [1]). Because the Sun emits most of its energy in the visible part of the electromagnetic spectrum, the photosphere is also the *source of the visible light*. The Solar spectrum indeed peaks at a wavelength of $\sim 500$ nm in the green, and the integral power of this spectrum (defining the "total solar irradiance") is dominated by the contributions of its visible part. The photosphere is thus the layer of the Sun that we see with our naked eye, or in filter images at visible wavelengths like Fig. 1.1. In such images, the photosphere appears as a sharp edge. There, owing to the sharp decrease of density and opacity (dropping by a factor $1/e$ over a "scale height" of roughly 150 km), the solar plasma that is opaque in deeper layers becomes abruptly transparent [2]. Therefore the photosphere is often thought of as the *effective visible surface* of the Sun. Because the photosphere is so shallow, we often assign to it a nominal level corresponding to an optical depth unity for a wavelength of 500 nm [3], $\tau_{500} = 1$ (although this level rather represents the lower photosphere).

As will be discussed in Sects. 1.2.2 and 1.2.3, the large photon flux emitted by the photosphere allows its observation at high spatial resolution and contains enough information to characterize the magnetic field in these layers. The photosphere is indeed pervaded by intense magnetic fields emerging from the solar interior [4], which makes it a natural starting point to investigate the solar magnetism. Disrupted by the vivid action of convective motions in the outer part of the Solar atmosphere, *the photospheric magnetic field is* not homogeneous but *highly filamented*, distributed in quasi-discrete flux concentrations at different scales and with different visible signatures (separated by ubiquitous weaker fields, see below). That this phenomenon of flux concentration happens in photospheric layers is a fortunate conjunction of events for the solar physicist, as both the emerging intensity and the magnetic field are strong enough to permit measurements.

We will now "zoom" into the photosphere to briefly comment on the different visible features associated with flux concentrations (indicated in Fig. 1.2), in order of decreasing size. Unlike in full-disk images, the phenomenon of granulation (i.e. the visible motion of convection cells overshooting into the photospheric layers) becomes apparent, and the typical size of such granules of $\sim 1000$ km gives a good indication of the typical photospheric length scale. The most famous and strongest flux concentrations are visible as *Sunspots* (discovered among others by Galileo Galilei in 1609), whose sizes can reach $\sim 10000$ km, comparable to the size of the Earth itself, and whose peak field strengths can be as large as 6000 G (see Solanki 2003, Solanki et al. 2006, for reviews). Sunspots are produced by the emergence of magnetic field in a concentrated tube-like form from the interior through the photosphere. As these flux tubes emerge in bipolar

---

[1]A new spectrum of information about the interior of stars is the study of seismic (acoustic and gravity) waves, the so-called asteroseismology and in the case of the Sun, helioseismology.

[2]This is mainly due to the strong temperature dependence of the $H^-$ ions opacity, $\propto T^{10}$.

[3]meaning that the distance separating the photosphere and us is equal to the mean free path of a photon of 500 nm wavelength

[4]The solar magnetic field is believed to be generated by a dynamo operating at the bottom of the "convection zone", i.e. the outer convective envelope of the Sun and other "cool stars". There, shear motions induced by differential rotation generate the field, and the latter rises through the convection zone up to the surface through the buoyancy force (Isik et al. 2008).
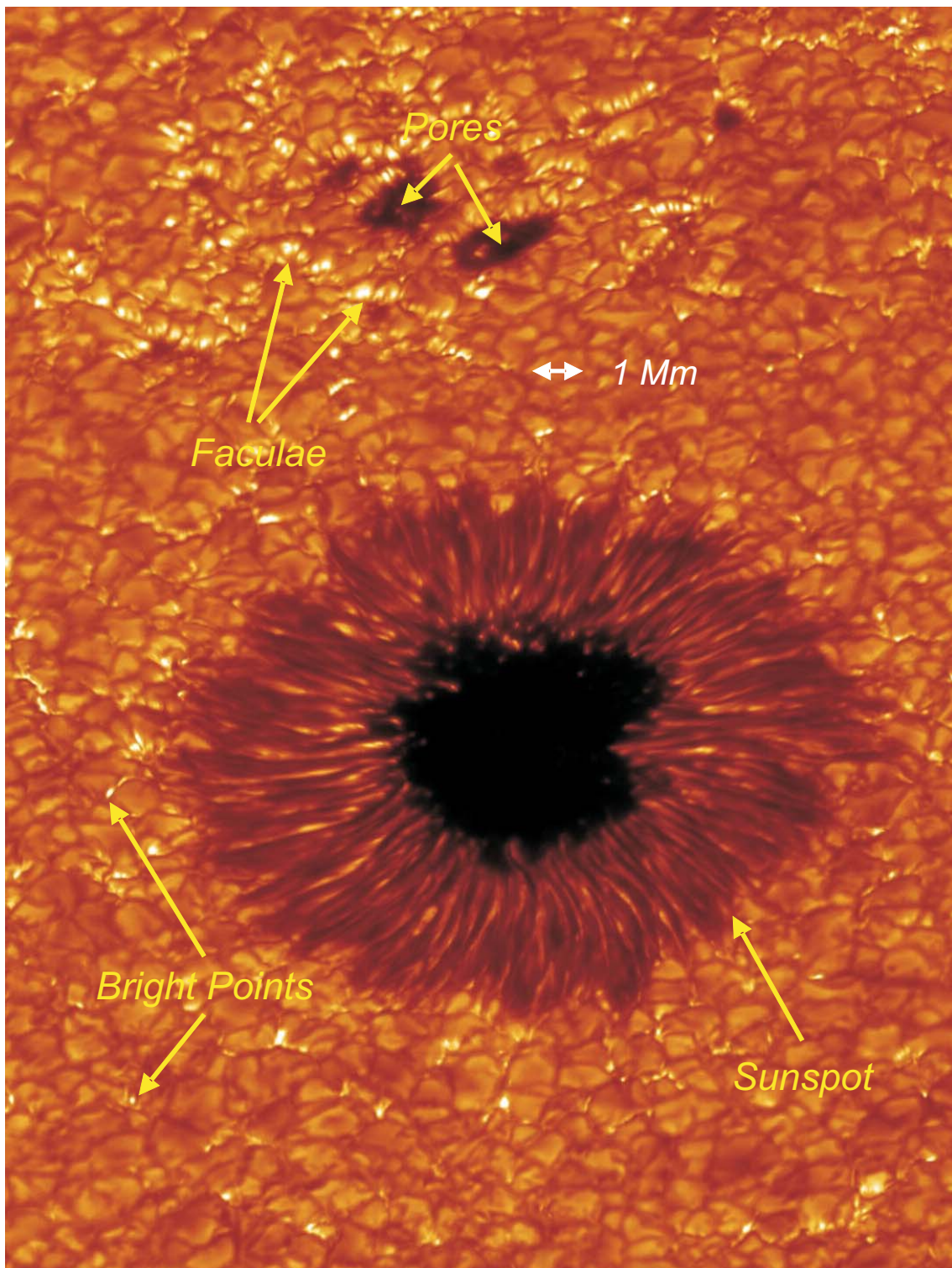
Figure 1.2: High-resolution view of a photospheric active region located at a heliocentric angle (angle between the line of sight and the local normal to the solar surface) of 40.5°, as revealed by the 1-m Swedish Solar Telescope (SST) in La Palma, Spain (courtesy Scharmer and Langhans 2003). This impressive image samples the visible signatures of most photospheric magnetic features (yellow). The typical scale of the photosphere is given by the mean size of a granule (white), of the order of 1000 km, i.e. 700 times smaller than the solar radius.

loops, sunspots usually appear in groups with the "leading" and "following" spots of the group having opposite magnetic polarities. Then come the so-called *pores*, looking like tiny sunspot umbrae, with a diameter of a few thousand km. Whether the magnetic structures subtending pores are deeply rooted in the convection zone, or rather produced by the conglomeration of smaller structures, is still unclear (Puschmann and Wiehr 2006, Hirzberger 2003). At the lower (currently observable) end of this size spectrum, we find the so-called *small-scale magnetic features*. These are tiny flux concentrations located within the intergranular lanes, with sizes of at most a couple of hundred kms (the lower limit of their sizes lies below the currently achievable resolution of the best telescopes). In spite of their small scale, they have in common an intense and roughly constant field strength of about 1-2 kG (cf. Sect. 1.2.2). These features are distinguished from pores and spots not only by their smaller sizes, but by their enhanced brightness relative to the surroundings (if sufficiently resolved, see Sect. 1.2.3). They are often visible as *Bright Points* (BPs) near disk center, and *faculae* near the limb (see Fig. 1.2 and Sect. 1.2.4). These flux concentrations are thought to be essentially local phenomena produced by *magneto-convection*, i.e. the interaction of convective motions in which a magnetic field is embodied (see Sect. 1.3.5).

Although the same name is commonly used to designate a magnetic flux concentration and its visible signature (mainly for historical reasons, cf. Sunspots), oftentimes both referred to as "magnetic features", one should keep in mind a clear distinction between the actual magnetic flux entity in the photosphere and its observed manifestation, i.e. the mere photons that we get from it (resulting from magnetoconvection and radiative processes).

Besides these quasi-discrete magnetic flux concentrations, the solar photosphere seems to harbour weaker magnetic fields almost everywhere, as revealed by recent investigations of the "quiet Sun" (see the reviews of Steiner 2003, de Wijn et al. 2009). Hence, the appropriate picture would rather be a continuous distribution of fields than a discrete one (adequately described by a probability density function, cf. Domínguez Cerdeña et al. 2006), whereby the magnetic features are only separated by some weakly magnetized atmosphere.

## The small-scale magnetic features and the solar activity

The work presented herein essentially focused on the study of small-scale magnetic features via their visible signatures: this paragraph is therefore meant to justify this interest in the context of the global solar magnetism and activity. By *solar activity*, we refer to all the dynamical phenomena associated with and driven by the magnetic field, like the solar cycle, the heating of upper layers, the explosive release of energy (flares, coronal mass ejections) etc., which make the Sun so alive and fascinating for astronomers.

First, more than 90 % of the *net* magnetic flux was found to be located outside sunspots and pores by Frazier and Stenflo (1972) (using magnetograph measurements of active regions with an aperture of $2.''4 \times 2.''4$). Although small kG magnetic flux concentrations occupy only a tiny portion of solar surface, recent estimates revealed that they nonetheless *contain a significant fraction of the photospheric magnetic energy* (combining Zeeman and Hanle measurements, Domínguez Cerdeña et al. 2006, see as well Sect. 1.2.2). Owing to their "flux tube" structures (see Sect. 1.3.1), the small-scale magnetic features are thus

good *candidates of energy transfer to chromospheric layers* (via e.g. the propagation of flux tube waves, as described in Stix 2004). Besides, these features *share similar magnetic and thermal properties* (see Sect. 1.3.2) and their visible brightenings are among the smallest structures resolvable by our telescopes. Therefore they are regarded as some "basic building blocks of the photospheric magnetism" (at least in the magnetic network and active regions), and as such are commonly denominated as *magnetic elements* (see review of Schüssler 1992). In direct connection with the solar activity cycle is the major role that the brightenings associated with the magnetic elements (i.e. the Bright Points and faculae) play in the solar irradiance variability. The integrated brightness of BPs and faculae indeed more than compensate the deficit due to sunspots, such that the solar irradiance is largest at activity maximum (with peak-to-peak variations of about 0.1 %, Fröhlich 2000).

## 1.2 Observations

### 1.2.1 Where do we find them?

As local magneto-convective phenomena, magnetic elements are present at all latitudes on the Sun, but are not uniformly distributed. On the large scale, we find them mostly within the two main global components of the photospheric magnetism: the *active regions* and the *magnetic network*. Active regions are large bipolar regions formed by the emergence of flux loops, characterized by the presence of Sunspots at their footpoints (see Fig. 1.3). There, magnetic elements have the largest number density and form bright clusters dubbed "plages" [5].

Outside active regions, in the quiet Sun, magnetic elements are concentrated into a magnetic network visible as a honeycomb bright pattern outlining the borders of large convection cells (with sizes of $\sim 20-40$ Mm), the "supergranules" (Chapman and Sheeley 1968). The line-of-sight (LOS) component of the supergranulation flow can be seen in a full-disk Dopplergram as in Fig. 1.4. Although the magnetic network is not that obvious in white-light, in becomes very prominent in the chromosphere (not unlike chromospheric plages), where it forms the "chromospheric network". In the last place, magnetic elements can be found in the very quiet regions in between the magnetic network, the so-called *internetwork*, but with the lowest number density (Muller 1983, Lites 2002, Domínguez Cerdeña et al. 2003, de Wijn et al. 2005, 2008).

On a local scale, magnetic elements are located in the downflow regions at the junction of granules, the *integranular lanes*. This is illustrated in Fig. 1.5, where white lines outlining the intergranular lanes are superposed on top of a magnetogram. Hence, the location of magnetic elements reflects the convective flow pattern of the supergranules and granules, which supports the idea that their magnetic field is intensified by convective motions (see Sect. 1.3.5).

---

[5]Historically, the word plage (meaning "beach" in french) originates from chromospheric observations in which these plages appeared as extended bright regions (Zwaan 1987). Since the correspondence between the chromospheric emission and the underlying magnetism has been established, the word plage is now commonly used for its photospheric counterpart as well.

AR 9393 on April 2, 2001, 9:25 UT



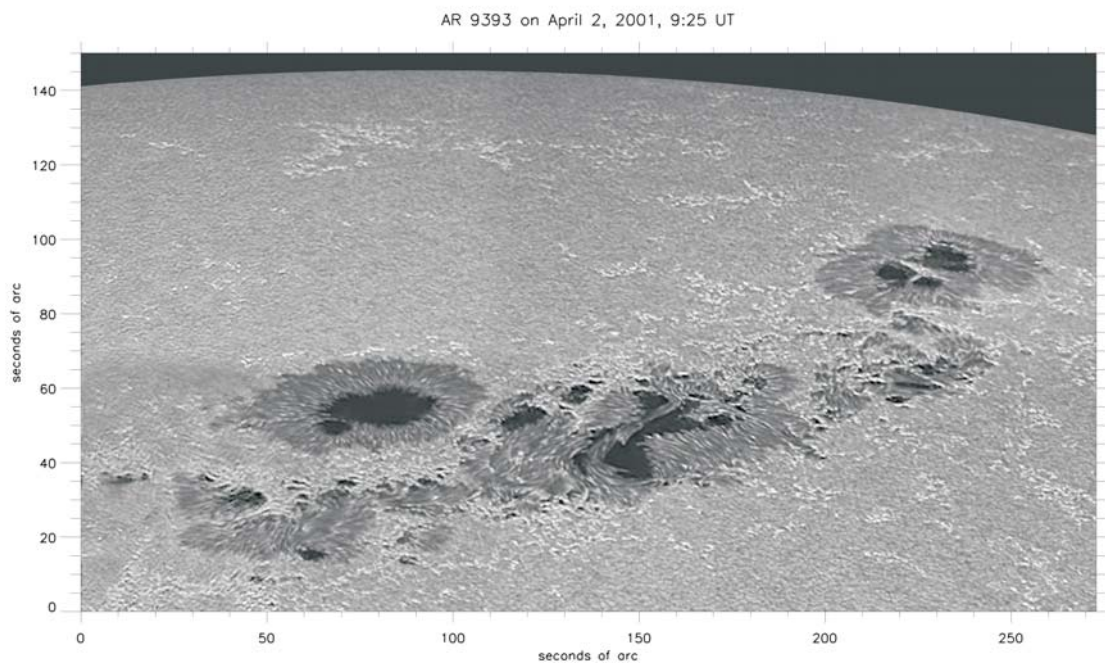Figure 1.3: Image of an active region located near the Solar limb, obtained at the Dutch Open Telescope in La Palma, Spain.
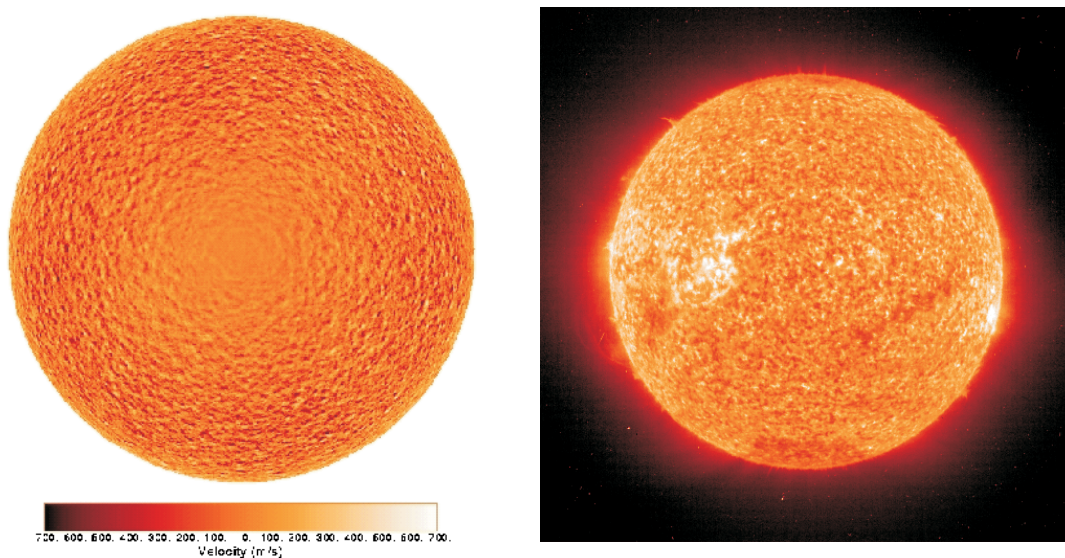


Figure 1.4: Left: Full-disk Dopplergram from SOHO MDI, showing the horizontal supergranular flows, ever more visible toward the limb due to their line-of-sight projection. Right: Corresponding (upper) chromospheric network imaged in the ultra-violet He II line at 304 Å by the EIT instrument onboard SOHO.
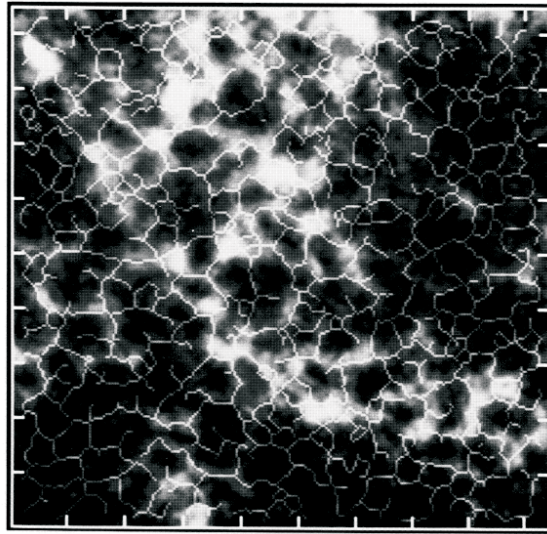
Figure 1.5: Contours of granulation (white) superposed onto a co-temporal magnetogram (Title et al. 1987).

## 1.2.2 Magnetic field measurements

In the solar photosphere and chromosphere, most measurements of the magnetic field strength and orientation rely on the imprint the field leaves on polarized spectra via the Zeeman effect. The introduction of a magnetic field removes the degeneracy of atomic states of different quantum number $M_J$ (projection of the total angular momentum onto the axis of the field), and thereby induces the splitting of spectral line components. Further, the spatial symmetry breaking due to the particular orientation of the magnetic field renders the absorbtion in the line components polarization-selective (Gandorfer 2001). The amount of circular and linear polarization recorded in the Stokes parameters (following Stokes' formalism for the measurement of polarization) thus depends on the orientation of the field vector relative to the observer's line of sight (LOS). However, it should be kept in mind that it is not the field itself which is directly measured, but the polarization. Inferring the magnetic field vector is thus a problem of interpretation, and as such is model-dependent. For a thorough treatment of the Zeeman effect as well as the Stokes formalism, I refer to the book of del Toro Iniesta (2003) and the dissertation of Borrero Santiago (2004).

The first detection of magnetic fields outside sunspots dates back to the magnetographic measurements of Hale in 1922. A magnetograph records the amplitude of the net circular polarization (i.e. Stokes V) in the wing of a Zeeman sensitive line, which scales with the LOS component of the field. The conversion between the signal amplitude and the longitudinal field strength requires a calibration, usually based on the assumption that the line components are not fully split (i.e. the Zeeman splitting does not exceed the Doppler width, Stenflo 2002). But in this so-called "weak-field" regime, the magnetograph signal increases both with the LOS component of the field (due to the progressive splitting of the Zeeman components and because circularly polarized light arises when the magnetic field is parallel to the LOS) and with the fraction of the resolution element occupied by the magnetic field ("filling factor"), as the non-magnetized atmosphere provides

no polarized photons. Hence, in this regime, *magnetograms are only sensitive to the LOS component of the flux*, i.e. the apparent LOS field strength averaged over the resolution element.

Although there were earlier indications that non-spot fields could be intrinsically strong (from the weakening of Fraunhofer lines presumably attributed to the Zeeman splitting), a solid evidence and quantitative estimation of intrinsic field strengths was obtained through the line-ratio technique [6] (Stenflo 1973). These measurements, yielded *photospheric field strength of 1-2 kG* (comparable to sunspot ones, see e.g. Solanki and Schmidt 1993). Moreover, these values are fairly *independent of the location (whether network or active region plages), and of the sizes of magnetic elements* (Zayer et al. 1990). Thus, kG field strengths are an intrinsic property of small-scale magnetic features, suggesting common formation mechanisms and leading to the conjecture of a unique magnetic structure for non-spot fields represented by the magnetic elements (this view has changed recently in favor of a more continuous distribution of field stength, with a large part of it hindered to the Zeeman measurements, see below). Field strengths of $\sim$ 2 kG in deep photospheric layers were further confirmed by the direct observations of strong Zeeman splitting in infrared lines (e.g., Rüedi et al. 1992).

The profiles of such very Zeeman-sensitive lines also implied a *decrease of field strength with height* (Zayer et al. 1989), and the stratification of field strength was confirmed by comparing model calculations with observations using a set of lines with different formation heights (obtaining roughly $\sim$ 2000 G at the deep photospheric level, about 1000 G at the middle photosphere and 200-500 G in the upper photosphere, Bruls and Solanki 1995).

Thanks to the activity minimum, recent interest has been raised for the quiet Sun, where magnetic flux was detected in the internetwork, thus revealed to be "not so quiet" as previously thought (de Wijn et al. 2008). The actual strengths of the internetwork fields remains a controversial issue though, depending on which lines are used for the diagnostics (Bellot Rubio and Collados 2003, visible lines yield kG fields whereas infrared lines reveal a dominance of weaker fields). With its high-resolution seeing-free spectropolarimeter, the Hinode spacecraft (Kosugi et al. 2007) has brought us novel insights on the quiet Sun. Weaker fields with strengths about the equipartition value (magnetic energy similar to the kinetic energy of the flow) seem to be commonplace in the "halo of polarization" surrounding network-like elements, and more horizontal than vertical flux is detected on average (Lites et al. 2008).

However, due to the sensitivity limit of polarimetric measurements, Zeeman measurements are missing an unknown but significant fraction of the magnetic flux: either because their polarization signals have amplitudes lower than the noise, and/or because mixed-polarity fluxes cancel the signal within the resolution element (see Steiner 2003, for a discussion). Yet diagnostics of the Hanle effect are susceptible to fill the gap of weak field measurements. In short, the Hanle effect accounts for the modification of scattering linear polarization in presence of magnetic fields (see Trujillo Bueno 2001). Because it is unaffected by mixed polarities in the resolution element (unlike the Zeeman diagnostics) and responds to the field strength of weak fields (below a few hundred G), it ideally complements Zeeman measurements (see Stenflo 2002, for a review). Hanle diagnostics

---

[6]This technique consists in taking the ratio of the V amplitude in two chosen lines whose properties differ only by their Landé factor, i.e. their magnetic response.

fruitfully revealed a realm of ubiquitous "turbulent" weak fields hidden to the Zeeman measurements (Stenflo 1982, Faurobert-Scholl et al. 1995, Stenflo et al. 1998). Therefore, both diagnostics have been used together to estimate an unbiased probability density function of the quiet-Sun fields strength (Domínguez Cerdeña et al. 2006).

### 1.2.3 Imaging and proxy magnetometry

The problem of polarimetric methods is that they require high spectral resolution, and consequently long integration times to achieve a reasonable signal-to-noise ratio (Schüssler 1992, Solanki et al. 2006). They thus suffer from poor temporal and spatial resolution, inasmuch as turbulences in the Earth's atmosphere cause "seeing" effects (through variations of the refraction index on timescales of $\sim$ 10 ms, much shorter than the typical exposure times, Bonet 1999). Conversely, white light or broad-band filter images collect a large number of photons, allowing to "freeze" the seeing aberrations by reducing the exposure times down to the timescale of the atmospheric turbulence. Therefore, imaging is a powerful tool for the study of (individual) small-scale magnetic features, requiring high spatial and temporal resolution.

As a general rule, the direct imaging of magnetic elements is possible because they often appear brighter than their photospheric surroundings, i.e. they have a *positive contrast*. However, the observed contrast severely depends on the spatial resolution, the wavelength, as well as the heliocentric angle (angle between the LOS and the local normal to the solar surface). For instance, the contrast at continuum wavelengths is rather neutral near disk center, due to the finite spatial resolution of the observations (Title et al. 1992, Topka et al. 1992, Lawrence et al. 1993, Berger et al. 1998). Because the contrast of magnetic elements increases from center to limb (cf. Sect. 1.2.4), however, faculae near the limb are prominent even in white light and could therefore already be observed in early low resolution observations (e.g. Rogerson 1961). Later, increasing the spatial resolution allowed bright structures at disk center to be resolved as well (Dunn and Zirker 1973), notably by near UV observations (at 393.4 nm, Mehltretter 1974) [7].

Disk center observations of bright intergranular features were nevertheless facilitated by realizing that *their contrast is enhanced in spectral line cores and wings* (see Chapman and Sheeley 1968, who at the same time discovered the magnetic network). This brightness excess is particularly pronounced in chromospheric lines such as the widely used Ca II K and Ca II H (around 393.4 nm and 396.8 nm, respectively, see e.g. Lites et al. 1999), or in the bandhead of diatomic molecules such as CN (around 388.7 nm) or CH (around 430.5 nm) which are highly temperature sensitive (see Sect. 1.3.4). As spectral line cores sample higher layers, the internal temperature of magnetic elements relative to their exterior must thus increase with height, implying a shallower temperature gradient inside the magnetic elements than outside.

Based on this consideration, interference filters were developed to probe the bandhead of CN (first used in the work of Sheeley 1969) or CH (pioneered by Muller and Roudier 1984), where the contrast of BPs is particularly pronounced and the broad spectral range

---

[7]In these pioneering works, the brightenings were termed "filigree" or "disk center faculae" or "facular points". Letting aside their historical context, these terms are synonymous, and in the present dissertation will all be refered to as Bright Points for simplicity.

in the blue allows to achieve high spatial resolution [8]. In the 90's, together with the progress of post-facto image reconstruction techniques, adaptive optics systems and the increasing resolution power of solar telescopes (Bonet 1999), filter imaging opened the way for the direct tracking of magnetic elements at high cadence and spatial resolution. This technique is often referred to as *proxy magnetometry*, as it relies on the *identification of magnetic elements with their radiative signatures in filtergrams*, whereby the latter play the role of "proxies". These proxies are generally taken as BPs at disk center, in order to benefit from a top view on magnetic elements (due to the verticality of flux concentrations, cf. Sect. 1.3.1). This identification with proxies has been justified by the comparison of G-band images with magnetograms (Berger and Title 2001), and further confirmed by simulated synthetic images, revealing that the BP structures (if properly distinguised from non-magnetic granular brightenings) precisely outline the magnetic flux concentrations (Schüssler et al. 2003, Shelyag et al. 2004). However, the converse is not true: *magnetic elements are not invariably bright*. Some appear dark because their contrast is smeared within the darker integranular lanes (Title and Berger 1996), or because the brightening fluctuates over the lifetime of the flux concentrations (e.g. due to possible seeing effects, Berger and Title 2001).

As pure imaging provides no quantitative information about the magnetic field itself, proxy magnetometry is best suited for morphological and dynamical studies. The morphology of magnetic elements depends somewhat on the location, appearing rather *point-like in the quiet Sun* network (e.g. Berger et al. 1998, Bovelet and Wiehr 2008) and taking often an *amorphous fluid-like appearance in active regions* (cf. high-resolution images of Berger et al. 2004). This readily indicates that there is no unique structure of the magnetic elements, to be borne in mind when comparing with models of "axisymmetric flux tubes" or "flux sheets" (see Sect. 1.3.1).

High-resolution images have the asset of resolving at least part of the magnetic features, allowing direct size measurements. But statistical analyses reveal that the lower observable sizes of BPs are limited by the currently achievable resolution limit (Wiehr et al. 2004, Puschmann and Wiehr 2006, Berger et al. 1995), such that the *lower limit for the size of magnetic elements is still unknown*.

The dynamics of magnetic flux concentrations can be investigated by tracking BP motions in time series of filtergrams. Magnetic elements are seen to be extremely dynamic, constantly buffeted by the granular motions and dragged along the intergranular lanes (Mehltretter 1974, Berger and Title 1996). The BPs appear to *split, merge and disappear on relatively short timescales of about 6-10 min*, which is comparable to granulation turnover times (Berger and Title 1996, Berger et al. 1998). In addition to the observations of higher BP velocities in the quiet Sun network (Muller et al. 1994) than in active regions, where the convective flows are more disturbed, this provides evidence that *the dynamics of magnetic elements is mostly driven by the granular motions*. Dynamical information from movies of limb faculae is harder to extract, as the latter result from an oblique view on the background granule (see Sect. 1.3.3), whereby the magnetic features and the background granule dynamics are necessarily entangled. Such movies nevertheless lead to the conclusion that much of the faculae changes owes to the background granulation only, but in regions where convective flows are heavily hampered, striated faculae exhibit dynamics

---

[8]According to the Rayleigh criterion, the resolution limit is directly proportional to the wavelength.

very reminiscent of BPs at disk center (De Pontieu et al. 2006).

### 1.2.4   Center-to-Limb Variation

When observing small-scale magnetic features at different disk positions from the center of the disk toward the limb, two effects can be noticed independently of the nature of the location (active regions or quiet Sun): a change of *appearance* associated with a transition from BPs to faculae, and a variation of *contrast* (i.e. brightness relative to quiet surroundings).

As briefly mentioned in Sect. 1.1, magnetic elements appear mainly as BPs at disk center and as faculae near the limb. To have a closer look, Fig. 1.6 shows a comparison of BPs and faculae in high resolution G-band images. BPs are mostly elongated bright features between granules, some of them only looking like isolated roundish points (their morphology is even more complex in active regions, see Sect. 1.2.3). As can be seen in Fig. 1.6 (right), many features lie at the resolution limit with sizes of about 0″.2, indicating that many BPs are smaller than that (and their underlying magnetic elements are as well), as mentioned in Sect. 1.2.3. Closer to the limb, the photosphere takes a 3D corrugated appearance and shows bright faculae, appearing as glowing granular edges, as if this corrugated surface were illuminated by the observer. These facular brightenings are usually larger than BPs, with typical sizes (projected onto the plane of the sky) of ~ 0″.5. Both the granular appearance and the large extent of faculae are attributed to an enhanced radiative escape from the background granular material through the flux concentration (see Sect. 1.3.3). In particular, one can notice the specific elongation of the facular brightenings in the direction of the closest limb, and their typical fan-like and often *striated appearance* visible at high resolution (pattern of bright elongated stripes alternating with relatively darker ones).

Even though BPs and faculae can be observed in the same image at some heliocentric angles (cf. Fig. 1.2 and Chapter 2), they are not distributed evenly on the solar disk. As a matter of fact, *BPs progressively disappear toward the limb and are replaced by faculae*, and both are found to coexist over a range of heliocentric angles (see Chap. 2). Near the limb, faculae form bright patches which are conspicuous features of the white-light solar disk as in Fig. 1.7. For this reason, these facular patches were first observed at low spatial resolution much before BPs, and before these patches could be resolved into small-scale elements and related to the BPs at disk center (see Sect. 1.2.3).

In spite of their relatively different appearance, brightness, and location on the disk, phenomenological arguments were presented for BPs and faculae to be manifestations of small-scale magnetic flux concentrations at different positions on the disk (see Mehltretter 1974). These arguments are based on the increased brightness in line cores at disk center (see Sect. 1.2.3) and the increase of continuum contrast toward the limb (both plausibly indicating a temperature excess in higher layers), as well as on the common Ca K emission of BPs and faculae at chromospheric layers (Wilson 1981). The association of BPs and faculae with magnetic flux concentrations became clear by the obtention of high-resolution magnetograms (Berger et al. 2007). Also, the development of flux tube models allowed to roughly explain their appearance, contrast and distribution on the disk as consequences of the geometry of these flux tubes ("hot-wall" effect, see Sect. 1.3.3). However, the peculiar distribution of BPs and faculae on the disk (in particular their co-
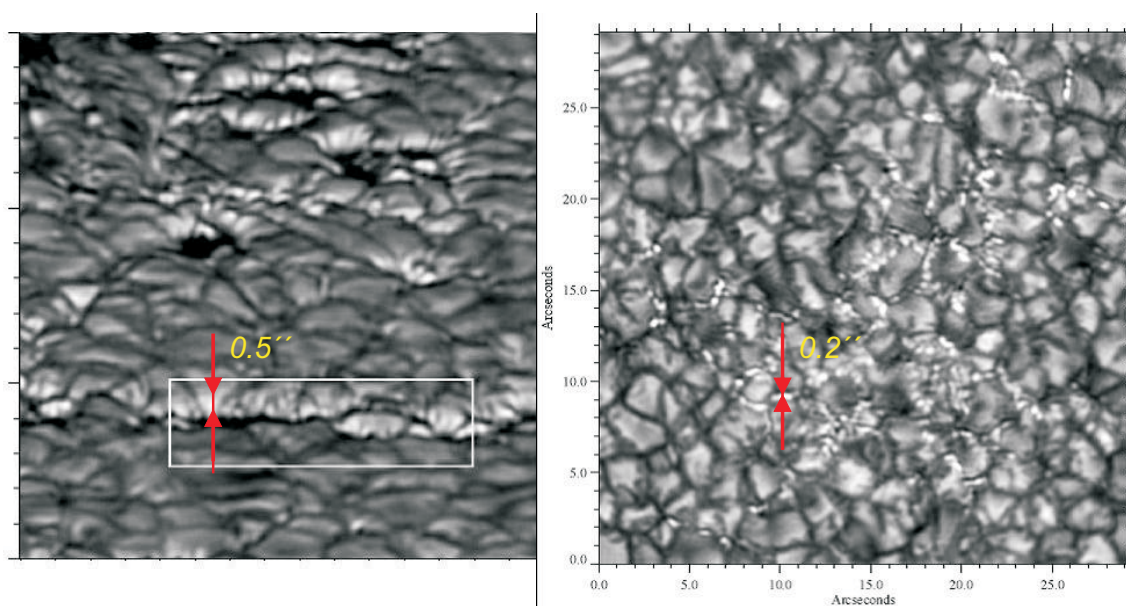
Figure 1.6: Comparison of the appearance of faculae and BPs in high-resolution G-band images. Left: Faculae, observed at the SST with an angular resolution of ~ 0.″12 (Lites et al. 2004). The direction of the closest limb is upwards. Right: Network BPs at disk center observed at the old Swedish Vacuum Tower Telescope, with a twice lower spatial resolution. Tickmarks are spaced by 1″. The red arrows indicate the typical sizes of these features.
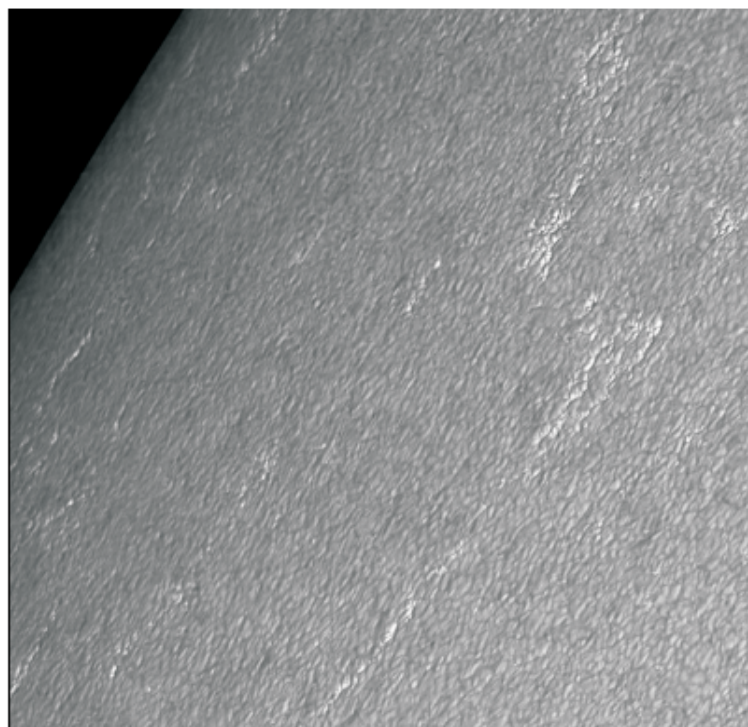


Figure 1.7: Blue continuum image of limb faculae obtained at the SST, showing their bright prominent patches (Hirzberger and Wiehr 2005).

existence over a range of heliocentric angles) still raises questions about their mutual relationship: *Are BPs and faculae associated with similar magnetic elements (size, field strength, inclination), or are they the consequences of selection effects rendering different magnetic features (e.g. with different sizes) best visible at different heliocentric angles?* Providing an answer is subtle, as it requires on one hand the knowledge of the physical conditions yielding BPs and faculae at different heliocentric angles, and on the other hand of the properties of the magnetic elements that do turn bright at these angles (so that they become visible). This second point is related to the center-to-limb variation (CLV) of the brightness of magnetic features.

The continuum brightness contrast of magnetic elements exhibits increasing values as the limb is approached (eventually reaching a maximum). This is the reason why ensembles of faculae near the limb become so prominent in white-light images and their contribution so important for the total solar irradiance. The hope of providing a useful input for irradiance modeling, together with the aim of constraining flux tube models, have stimulated a long list of studies about the center-to-limb variation (CLV) of facular contrast (discussed in Steiner 2007). However, the results are rather controversial regarding whether the contrast values reach a maximum (Lawrence 1988, Sütterlin et al. 1999, Ahern and Chapman 2000, Adjabshirizadeh and Koutchmy 2002) and at which heliocentric angle (Lawrence et al. 1988, Auffret and Muller 1991, Sánchez Cuberes et al. 2002, Berger et al. 2007). The CLV of contrast is thus still a source of debate and of different theoretical modeling.

These questions are at the core of the work presented in this dissertation. While the transition from BPs to faculae is the central point of investigation presented in Chapter 2, Chapter 3 explores the relationship between these features, and Chapter 4 tackles the issue of the contrast CLV and its dependence on physical parameters.

## 1.3   Basic theoretical concepts

For the sake of interpreting the aforementioned observations, we shall now tackle the basic physics behind them, beginning with the paradigm of magnetic elements as *quasi-static flux tubes embedded in a field free surrounding atmosphere*.

### 1.3.1   The MHS "wine-glass" picture

In a general sense, a *flux tube* is a *set of field lines enclosed into a topologically simple "material curve"* (see Cowling 1976, Priest 1982, for rigorous details). A particular property of flux tubes is that this set of field lines is uniquely defined at fixed time, owing to the solenoidality of the magnetic field. This implies that at any fixed time, *the magnetic flux through any section of the flux tube is constant* [9]. Note that this general definition involves the presence of material (photospheric plasma in this case), but without restrictions about the surroundings of the tube. In the context of the solar photosphere though, flux tubes are generally considered *isolated from a field-free atmosphere*. The definition does not specify anything either on the geometry of the tube and its enclosing material curve. While

---

[9]In the limit of "ideal MHD", i.e. neglecting the magnetic diffusivity, the flux is also conserved in time (Alfvén's theorem).

flux tubes are often modeled in an axially (azimuthally) symmetric or "slab" configuration (2D structure with translational symmetry), these models are purely abstractions and the actual topological shape of photospheric flux tubes can be much more complex (as suggested by the bright "fluid-like" ribbons in G-band observations, see Sect. 1.2.3). Last, the definition of a flux tube is purely local, as on larger scales the set of field lines could divide into branches or form loops, which cannot be enclosed by a topologically simple curve anymore.

In order to extract the basic physics from this flux tube concept, we shall make the simplest assumptions, and consider an axially symmetric flux tube (as depicted in Fig. 1.8) in the so-called *Thin Flux tube Approximation* (TFA) (see Schüssler 1992, for a thorough mathematical treatment). The TFA basically means that the internal *radial structure of the tube is neglected*. Strictly speaking, it consists (in its simplest form) of a $0^{th}$-order radial expansion of the MHD equations (i.e. a truncation at $0^{th}$-order, after having Taylor-expanded all quantities in $r$), so that the remaining terms depend only on the axial coordinate $z$. This simplification relies on the assumption that the radius of the tube is significantly smaller than all the relevant spatial scales of the atmosphere, notably the pressure scale height, otherwise the expansion of the tube would cause a radial variation of the field **B** [10]. Second, we consider the flux tube in *magneto-hydrostatic* (MHS) equilibrium, i.e. with vanishing velocities (and time derivatives). This is justified because the magnetic energy density is much larger than the kinetic energy density inside the tube, due to the large Lorentz force opposing to convective motions, and due to the reduced internal density (see below) [11]. Under the above assumptions, it can be shown that the mechanical equilibrium of the tube with the external atmosphere reduces to a *pressure balance* (while the momentum equation reduces to a hydrostatic equation inside the tube and the induction equation for the evolution of the magnetic field vanishes in MHS, see Schüssler 1992), which reads:

$$p_{\mathrm{m}}(z) + p_{\mathrm{i}}(z) = p_{\mathrm{e}}(z), \quad p_{\mathrm{m}}(z) \equiv \frac{B(z)^2}{8\pi} \tag{1.1}$$

where $p_{\mathrm{i}}$ and $p_{\mathrm{e}}$ denote the internal and external thermal gas pressures, respectively, $p_{\mathrm{m}}$ the magnetic pressure [12]. This additional magnetic pressure stems from the decomposition of the Lorentz force into an isotropic pressure force, a curvature force and a tension force, but the two latter do not play any role in TFA. This static pressure balance can be justified on the basis of relevant timescales, as the travel time of a sound wave across the tube (restoring equilibrium after a given perturbation) is of the order of 10 s, very short compared to the typical lifetime of $\sim$ 10 min. Note that without this radial approximation, the pressure balance would only be required locally at the tube's interface with the external atmosphere. But the TFA extends this condition to the whole tube interior, where $p_{\mathrm{i}}$ and $p_{\mathrm{m}}$ are constant at any fixed $z$. In other terms, the exterior of the tube has an influence on the tube interior (pressure, density, opacity). This is the important conclusion from the static TFA and the key to derive the basic properties of magnetic elements.

---

[10]Note that combining the TFA with a field free external atmosphere, Ampère's law implies the formation of a current sheet on the outer boundary of the tube, as the internal field satisfies $\nabla \times \mathbf{B} = 0$ elsewhere.

[11]This does not imply that flux tubes are "strictly static", and they are in fact rather dynamic and in constant interaction with the buffeting motions of the granulation.

[12]Note that in the $0^{th}$ order TFA, $B(z)^2 \sim B_{\mathrm{z}}(z)^2$, so that only the axial component of the field plays a role in the pressure balance.

Figure 1.8: Sketch of an axisymmetric flux tube with axial and radial coordinates $z$ and $r$, respectively. In the thin flux tube approximation, the internal magnetic and external gas pressure are considered solely functions of $z$ and are denoted $p_i(z)$, $p_m(z)$, and $p_e(z)$ respectively.
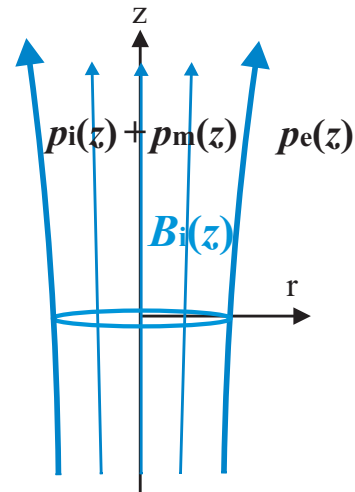
Let us now examine the consequences of the pressure balance statement on the structure of the tube, which will turn out to be of utmost importance to provide explanations for the observational facts:

1. *Internal evacuation*: Since a magnetic pressure adds up inside the tube, the equilibrium can only be sustained if the gas pressure is reduced in proportion, which implies that the internal gas density has to be lower than the external one (assuming similar temperatures and the ideal gas equation of state). Quantitatively, considering a flux tube of 1 kG and the standard value of $2 \; 10^{-4}$ kg m$^{-3}$ for the gas density at the photospheric level, one obtains $p_m \sim 4000$ Pa and $p_e \sim 10000$ Pa (using the ideal gas equation of state). Hence, this implies a *strong evacuation of the tube interior*, whereby the internal gas density must be lower than the external one by a factor $2 - 3$.

2. *Quasi-verticality*: The partial evacuation of the tube engenders a considerable *buoyancy* and therefore leads to the quasi-verticality of photospheric flux tubes.

3. *Opacity depression*: The reduced internal density also causes an opacity depression and thereby a *downward shift of the optical depth unity level*, allowing to see deeper layers inside the tube than in its surroundings (see Fig. 1.10). This is the main cause of the brighter appearance of magnetic elements relative to their surroundings, as discussed below.

4. *Expansion with height*: Because the external pressure $p_e(z)$ drops exponentially with height (assuming hydro-static equilibrium), $p_m$ should decrease for the pressure balance to be maintained, implying an *exponential decrease of $B(z)$*. And owing to the flux conservation inside the tube, the only way to decrease $B(z)$ (equivalent to the flux density in TFA) is an expansion of the tube with height, which is responsible for the typical "wine-glass" shape attributed to photospheric flux tubes [13].

---

[13]This expansion can be hampered at some height as adjacent flux tubes enter into contact, due to the solenoidality of the magnetic field (field lines cannot cross). At this height, the field is believed to reach a quasi horizontal configuration and form a "magnetic canopy" (see e.g. Gabriel 1976, Solanki and Steiner 1990), but its existence is still a matter of debate (Schrijver and Title 2003, Pietarila et al. 2008).
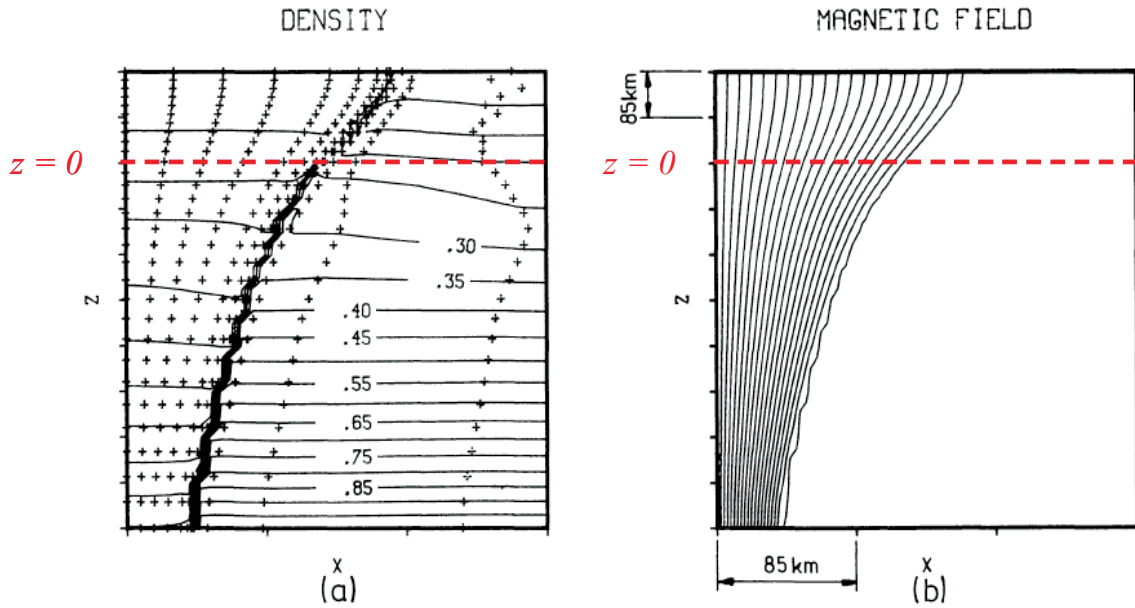
Figure 1.9: Results of a 2D calculation of flux tube in TFA (with mirror symmetry) by Deinzer et al. (1984), for which the internal density at the base has been prescribed as twice lower as the external one (the tube is inserted ad hoc here, as static calculations cannot reproduce its formation). Left: density as a function of height, with the iso-density lines normalized to $1.6 \cdot 10^{-6}$ g cm$^{-3}$. Right: magnetic field configuration. The red dashed line indicates the level $\tau = 1$, chosen as the reference $z = 0$.

Fig. 1.9 presents the results of a 2D static calculation of flux tubes in TFA (with mirror symmetry), illustrating the flux tube expansion as well as the reduced internal density depicted by the iso-density lines. To conclude, the decrease of $B(z)$ predicted by the static TFA has been shown to be consistent with the measurements (Zayer et al. 1989, Bruls and Solanki 1995, cf. Sect. 1.2.2), and the pressure balance has been closely verified in recent state-of-the-art 3D MHD simulations of magnetic elements (Vögler et al. 2005, Yelles Chaouche 2008). Hence, the TFA can be considered a valid description of magnetic elements and provides a simple model for the raw interpretation of the observations [14].

In principle, this TFA flux tube picture is not restricted to strong fields (spots, pores, magnetic elements), and could be applicable to weaker flux concentrations (e.g. in the internetwork) as long as the fields are strong enough to maintain a flux tube "identity" against the disrupting action of the flows. However, the consequences of the pressure equilibrium will differ for weaker fields, as they will be less evacuated, thus less buoyant and less vertical, and also less bright as the internal opacity drops to a lesser extent.

## 1.3.2 Thermal structure

Basically, the thermal state is a consequence of the equilibrium between the following contributions, illustrated in Fig. 1.10:

---

[14]Recent work based on diagnostics of 3D MHD simulations nevertheless revealed that a second-order expansion of the MHD equations reproduces the $B_z$ profiles of simulated features more accurately (Yelles Chaouche 2008)

1. *Quenching of convective flows*: The strong Lorentz force in the tube interior deflects the cross-field flows, which "quenches" the convective energy transport. As mentioned in Sect. 1.3.1, this domination of the magnetic field over kinetic motions is a consequence of the large ratio between the magnetic energy density and the kinetic energy density.

2. *Radiative losses*: The interior of the tube looses energy by radiation. The combination of these two effects makes the tube *cooler than its surroundings at equal geometrical depth z*, as sketched by the isotherms and the horizontal dashed lines in Fig. 1.10 (right).

3. *Lateral radiative influx*: To compensate this deficit, a radiative influx from the tube walls sets in. Because they correspond to deeper photospheric layers effectively heated by convection [15], these walls are much hotter than the tube interior where convection is quenched, with temperatures of about 7000 K (Knölker et al. 1991), and than the surroundings.

4. *Assorption in the tube*: Its small volume as well as its transparency (owing to the reduced internal density) allows the tube to absorb the radiation bath of the hot walls throughout its section. This radiation then heats the tube to the point where it becomes *hotter than the exterior at equal optical depth* (compare the $\tau = 1$ line with the isotherms in Fig. 1.10 (right).

5. *Heating of upper layers*: The hot walls and deeper layers of the tube shine through the tenuous atmosphere of the magnetic element towards upper layers, which thereby reach an equilibrium temperature larger than the gas of the quiet atmosphere at the same geometrical height. The latter indeed only receives the continuum radiation coming from layers at a temperature of $\sim$ 6400 K, further absorbed in the denser non-magnetic atmosphere. This effect is known as "radiative channeling" (Cannon 1970, Steiner and Stenflo 1990) or "radiative illumination" (Knölker et al. 1988, 1991), and leads to a *shallower temperature gradient within than without the flux tube*. In turn, this accounts for the apparent enhanced brightness contrast of magnetic elements when observed in spectral line cores (see Sect. 1.2.3).

   Note that the efficiency of the lateral heating is restricted to dimensions of the order of the photon mean free path in the photosphere, $\sim$ 100 km, as wider tubes would become laterally optically thick and thus prevent the lateral radiation to travel across. This is the reason why BPs (not necessarily faculae) are associated with small flux tubes, and larger flux concentrations like spots or pores appear dark. It should be noted that the above considerations set no lower limit on the width of flux tubes to appear bright (as for infinitesimal width the internal temperature would equal the exterior temperature at the same geometrical depth). However, lower size limits for flux tubes in concentrated form (with kG strength) can be derived from theoretical considerations concerning their formation mechanism (see for instance Venkatakrishnan 1986).

---

[15]There is a steep temperature gradient in the photosphere due to the opacity gradient caused by the $H^-$ ions, such that from the thermal point of view, a magnetic element is much like a hole in a hot and opaque material.
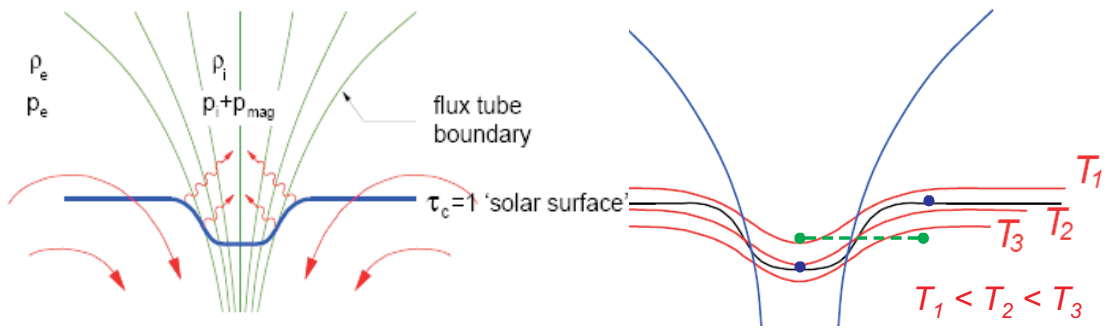
Figure 1.10: Schematics of the different factors contributing to the thermal structure of a magnetic element (left), and (right) the ensuing thermal structure (courtesy Oskar Steiner). The red lines depict isotherms. The green dots are meant to guide the eye across the isotherms at equal geometrical depth, while the blue dots are for equal optical depth.
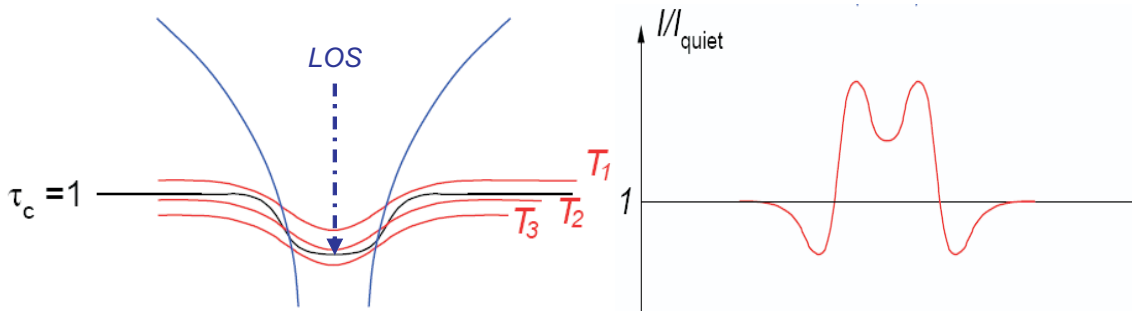


Figure 1.11: Left: Schematics of the thermal structure of the magnetic elements with a vertical line of sight. Right: The corresponding relative intensity profile showing the enhanced brightness over the magnetic element, with the double humps corresponding to the locations where the $\tau = 1$ line almost reaches the $T_3$ isotherms (hot walls) on the left panel (courtesy Oskar Steiner).

### 1.3.3 BPs vs. faculae: the "hot-wall" picture

Why do magnetic elements appear different at disk center and near the limb? To give an answer, we have to "look" at the thermal structure depicted above, while considering the effects of the line-of-sight (LOS) inclination with respect to the axis of the magnetic flux concentration.

When looking at a magnetic element from overhead, which happens mostly at disk center (assuming a vertical flux tube), the radiation we receive mainly originates from the *bottom* of the optical depth unity depression. According to Sect. 1.3.2, the magnetic element is hotter there than in its surroundings at equal optical depth. Owing to this temperature difference, the magnetic element appears brighter giving rise to a "Bright Point"[16], as sketched in Fig. 1.11.

---

[16]In observations, however, the finite spatial resolution often "blurs" the continuum contrast of BPs to neutral or even negative values. Broad-band filtergrams, in which the contrast of BPs is particularly enhanced, are thus more commonly used to observe BPs (see Sects. 1.2.3 and 1.3.4).

Figure 1.12: Illustration of the hot wall effect by Spruit (1976), with the limbward wall of the flux tube becoming visible as the observer looks out of disk center with an inclined LOS.
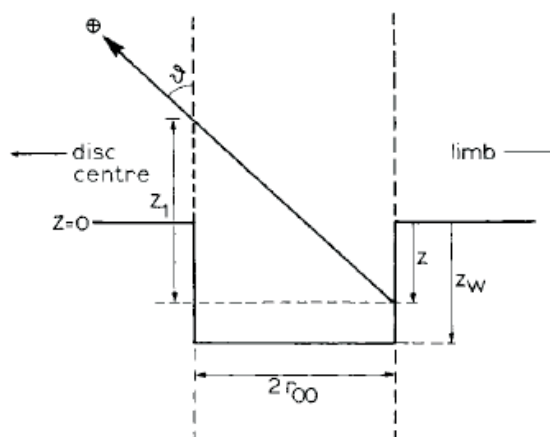
The mechanisms responsible for the phenomenon of faculae are somewhat more complex. Mainly four effects are thought to contribute to the appearance and brightness of faculae near the limb:

1. *Hot wall visibility*: As first proposed by Spruit (1976) (schematized in Fig. 1.12), when observing closer to the limb and thereby inclining the LOS with respect to the vertical flux tube, its hot wall becomes more visible while its bottom gets hidden (shadowed by the foreground granule). This bottom obscuration naturally explains the disappearance of BPs towards the limb.

2. *Wall temperature*: The wall temperature is *larger than the bottom temperature* (see e.g. Knölker et al. 1991, and Fig. 1.10, where the bottom has temperature $T_2$, while the walls reach $T_3$), since the former is heated up by convection, whereas the bottom lies in an evacuated atmosphere where convection is quenched (cf. Sect. 1.3.2).

3. *Optical depth shift*: As we look closer to the limb, our inclined LOS traverses a thicker atmosphere. As depicted in the bottom panel of Fig. 1.13, this causes the optical depth unity level to shift *upwards*, where the temperature difference between the interior and the exterior of the tube is even larger (due to the flatter temperature gradient inside). This is in fact nothing else than the *limb darkening effect* combined with the temperature structure of the magnetic element. Together with the larger temperature of the wall with respect to the surroundings, this effect qualitatively accounts for the contrast increase of faculae towards the limb.

4. *Transparency of the flux tube*: On the limbward side of the flux concentration, the granular material "sees a more transparent sky" in the direction toward the flux concentration then on the opposite one (Steiner 2005). This causes faculae to have larger apparent sizes (with sizes often larger than BPs, see Sect. 1.2.4) than the mere projection of the flux tube wall, as well as facular profiles to exhibit an extended limbward tail as in Fig. 1.13.

In short, we could summarize by stating that *faculae are the result of the enhanced view on the hot granular material behind the flux tube as the LOS peers through the latter*. Note that when observing closer to the limb, the LOS is actually directed toward
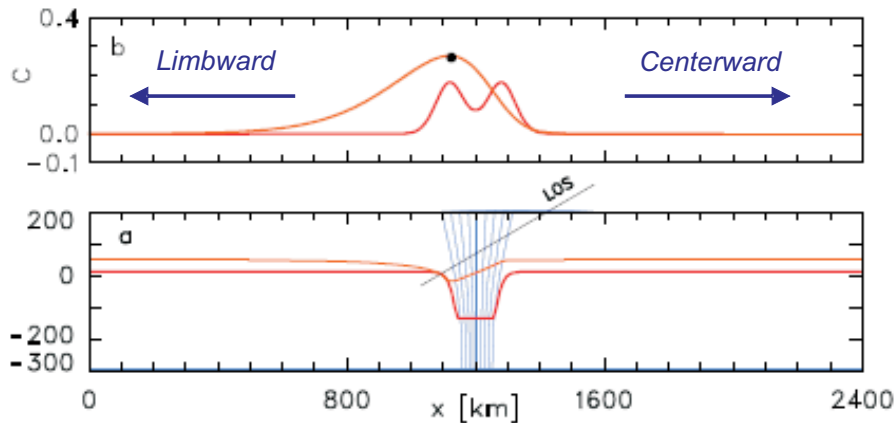
Figure 1.13: Top panel: Comparison of BP and facula contrast profile in orange and red respectively, obtained from a 2D MHS thin flux tube calculated by Steiner (2005). The contrast is defined as $I/I_{\text{quiet}} - 1$, where $I_{\text{quiet}}$ is the mean intensity outside the flux tube. The abscissa is the unprojected horizontal distance. Bottom panel: Corresponding flux tube with optical depth unity for a vertical LOS in red (BP case), and an inclined LOS in orange (facula case).

the granule on the *limb side* of the magnetic element, whence the generally observed limbward orientation of faculae.

Hence, by combining thermal and geometrical effects, the "hot-wall" picture presented above gives an explanation for most observational facts about BPs and faculae, namely their different appearances, the progressive disappearance of BPs in favor of faculae toward the limb, the CLV of facular contrast and the orientation of faculae. However, the peculiar appearance of faculae as illuminated granules (as well as the mismatch of the diverse measurements of facular contrast CLV) led to some controversies, and an alternative "hot-cloud" model was also considered, in which hot material was thought to be lifted above the photosphere by upflows in the flux tube, in order to account for the large extension of faculae close to the limb and their "hillock" diffuse appearance (Schatten et al. 1986). But as the hot-wall picture further received recent support from comprehensive 3D MHD simulations (attributing the facular brightness to a deeper view inside the hot limbward wall due to the opacity depression, Keller et al. 2004, Carlsson et al. 2004), it is the most generally accepted model of these phenomena. However, as will be pointed out in Sect. 1.3.6, we are still a long way from having a complete theory of faculae in our hands, predicting the contrast and appearance of realistic magnetic flux concentrations as a function of their size, inclination and field strength, in agreement with the observations (Steiner 2007).

### 1.3.4   Contrast in G-band and CN-band

The use of proxy magnetometry has stimulated much theoretical effort with the aim of understanding the prominent contrast enhancement of magnetic features in G-band relative to continuum. Hand-wavingly, the contrast in a given spectral band depends on the ratio between the temperatures of the magnetic element and its surroundings, at the for-

mation heights corresponding to that spectral band (assuming LTE, whereby the intensity is a function of the temperature only). The problem then consists of determining, by way of atmospheric models and radiative transport calculations, the formation heights of the G-band radiation inside and outside the flux tube and the associated temperatures, and to compare with the case of continuum radiation. Rigorously, the emerging G-band spectrum has to be calculated and further integrated to retrieve the corresponding intensities.

As discussed in Sect. 1.3.2, the magnetic element is hotter than the surrounding photosphere at equal (vertical) optical depth, which explains the positive contrast in continuum and in G-band separately. According to "conventional wisdom" (Rutten 1999), the G-band contrast enhancement (compared to continuum) could be explained by solely considering the shallower temperature gradient inside the magnetic element (due to radiative channeling, c.f. Sect. 1.3.2) than in the quiet surroundings. Assuming that the absorbtion in the many CH lines of the G-band causes the radiation to escape from higher up than for the continuum, the different temperature gradients would thus increase the temperature difference between the internal and external atmospheres at equal optical depth.

Yet another effect comes into play due to the *temperature sensitivity of the CH lines*. Radiative transfer calculations across plane-parallel and semi-empirical flux tubes atmospheres have revealed a significant *weakening of the CH lines* in the emerging G-band spectra (Steiner et al. 2001, Rutten et al. 2001). This was attributed to the *depletion of CH molecules within the deep and hot photospheric layers of the magnetic element*, caused by their dissociation (which was already conjectured by Berger et al. (1995) on the basis of his G-band observations). This conclusion was further confirmed by self-consistent three-dimensional radiative simulations, including nearly 300 CH and atomic lines and non-grey radiative transfer (see Sect. 1.3.6), showing the reduced CH density at the location of the G-band bright magnetic flux concentrations, as a consequence of their *higher temperature and lower density* compared to their weakly magnetized surroundings (Schüssler et al. 2003). These studies further demonstrated that the reduced CH abundance inside the tube yields a geometrical shift of the optical depth scale at the center of any CH line, down to almost the continuum formation height. As a consequence, the line is formed over a height range of only ∼ 40 km inside the magnetic flux concentrations (compared to 180 km outside), which implies that the effect of the reduced CH absorbtion largely dominates over the effect of different temperature gradients.

It should be noted that all the aforementioned calculations were carried out under the assumption of local thermodynamical equilibrium, whereby molecular dissociation is dominantly collisional. This was justified by Sánchez Almeida et al. (2001), who demonstrated that radiative photodissociation only plays a minor role for the CH abundance.

Hence, the enhanced contrast in the G-band is mainly due to the high temperature sensitivity of the CH lines, which in turn owes to the low dissociation potential of the CH molecule (3.5 eV). Another diatomic molecule, CN, is susceptible to behave very similarly, and observations of magnetic elements in the CN band-head can exhibit even superior contrast (see Zakharov et al. 2007, for more details). In a comparable way, the absorbtion lines of neutral atoms are more temperature sensitive than ionized species because of their low ionization and excitation potentials (Chapman and Sheeley 1968). But the considerable advantage of the G-band and CN band for proxy magnetometry lies in their relatively low formation height above the continuum formation layers, and the presence of densely packed absorbtion lines over a wide spectral window. This allows the

*same granulation pattern to be seen as in the continuum* without loss of resolution, and permits *wide-band observations* with large photon flux and short exposure times.

### 1.3.5 Formation mechanisms and dynamics

So far, we have presented the physics underlying the properties of quasi-static flux tubes assumed to be already in a "concentrated" form. But how are such strong flux concentrations produced in the photosphere?

To start with, the magnetic field can be concentrated by the action of convective plasma flows, a mechanism referred to as *flux expulsion*. Owing to the large conductivity in the photosphere (between 1 and 1000 A/Vm, see Stix 2004), the field lines indeed behave as if they were firmly attached to the fluid and the field is said to be *frozen* into the plasma. This is, strictly speaking, the statement of the "Walén's theorem" which holds in ideal MHD, i.e. neglecting magnetic diffusivity (this is justified in the photosphere, where the magnetic Reynolds number reaches values of $R_{\mathrm{m}} \sim 100-1000$, such that the diffusive decay term can be neglected compared to the advection term in the induction equation). As a consequence, *converging flows are capable of flux concentration*, and such flows occur *at the borders of granules and supergranules* due to their convective action [17], as illustrated in Fig. 1.14. The flux expulsion mechanism thus provides a qualitative explanation for the concentration of the field in the magnetic network and in the intergranular lanes. However, it can only concentrate the field until the back-reaction of the Lorentz force balances the inertial force of the flow, or equivalently until an equipartition between the magnetic energy density and the kinetic energy density is reached, namely:

$$\frac{1}{2}\rho u^2 = \frac{B_{\mathrm{eq}}^2}{8\pi} \tag{1.2}$$

where $u$ is the typical speed of the granulation flows, $\sim 2$ km s$^{-1}$, corresponding to a field strength $B_{\mathrm{eq}} \sim 400$ G...too low in comparison with the kG strengths of magnetic elements deduced from observations!

To reach kG field strengths, we need further concentration through the so-called *convective intensification* mechanism. I will describe it here in rough "hand-waving" terms, while referring to original manuscripts (e.g. Parker 1978, Webb and Roberts 1978, Spruit 1979, Venkatakrishnan 1985, Hasan 1985, Grossmann-Doerth et al. 1998, Rajaguru and Hasan 2000) and the reviews of Schüssler (1992) and Steiner (2003) for a rigorous treatment. The problem with the flux expulsion picture is that the energy balance is incomplete, as it does not take into account radiative fluxes and ensuing thermal effects. If these are considered, the flux tube atmosphere is found to cool down during its formation due to radiative losses and the progressive suppression of convective motions. This results in a cooler and denser inner material that sinks down leaving an evacuated atmosphere behind. In parallel, this engenders a decrease of the internal gas pressure and the contraction of the tube, whose field lines are pushed together under the pressure of the external gas. This intensification eventually stops when the flux tube reaches both a mechanical equilibrium

---

[17]Rigorously, we cannot neglect completely diffusive effects as the concentration proceeds in the intergranular lanes, because the field lines have to "detach" themselves from the flow if a stable flux concentration is to be formed.
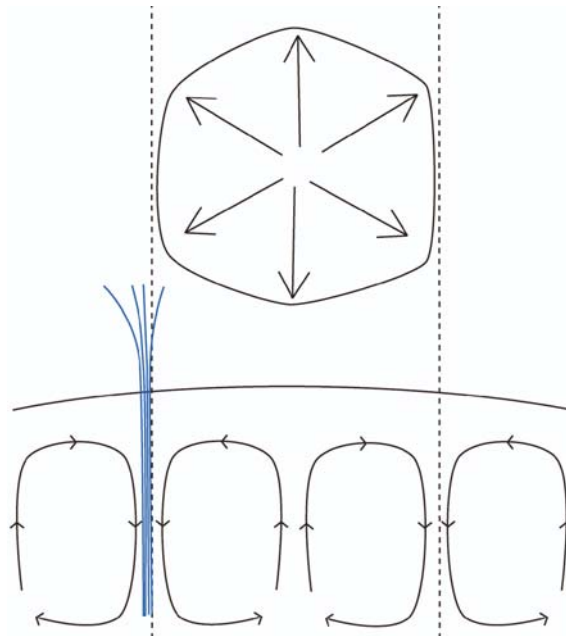
Figure 1.14: Sketch illustrating the flux expulsion mechanism by the converging flows of granulation and supergranulation cells.

(horizontal pressure balance, cf. Sect. 1.3.1) and a thermal equilibrium (steady-state between lateral heating and radiative losses).

It should be noted that the distinction between the flux expulsion and convective intensification processes is a theoretical abstraction, to better put in evidence the different aspects related to them. In the real Sun though, as well as in simulations carrying out a full momentum and energy treatment, these processes are found to act in parallel [18] (Schüssler 1990, Vögler et al. 2005). To date, there are only few observational confirmations of the predictions associated with the convective intensification phenomenon, either indirectly (by demonstrating the strong field strength-size dependence for the small flux tubes Solanki et al. 1996) or directly (on a single case though, c.f. Nagata et al. 2008). This is probably because of its short timescale, and because of the difficulty to disentangle it from the flux expulsion.

Finally, since all magnetic structures have finite lifetimes, their flux must decay. The decay of flux tubes is easily conceived by invoking magnetic diffusion due to the finite resistivity of the plasma, although other flux tube instabilities can also play a role (see Schüssler 1992). But probably the most common form of decay (in regions of mixed polarity at least, as it is often the case in the magnetic network), is the cancellation of opposite polarity fluxes through magnetic reconnection (with release of magnetic energy), creating loops below or above the surface (e.g. Spruit et al. 1991). Flux cancellation events have been observed in time series of magnetograms both in the quiet Sun and in a decaying active region, and it was deduced that it could be among the most frequent decay mechanisms (Martin et al. 1985, Livi et al. 1985). Even though these observations report a decrease of net flux, it should be stressed that reconnection cannot destroy field lines

---

[18]In this sense, the original terminology of "convective collapse" or "convective instability" can be misleading.
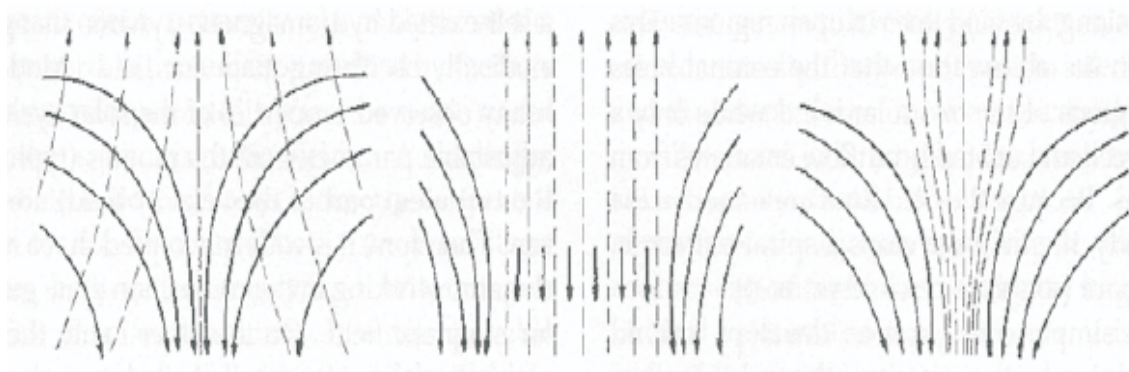
Figure 1.15: Schematics of the convective intensification process, by Schüssler (1992). Left: flux expulsion by the horizontal granular flows. Middle: inhibition of convective motions by the building-up of magnetic forces and ensuing cooling-off and downflow of cool material. Right: contraction of the flux tube under the external pressure.

but only alter the configuration of the magnetic field. Yet a destruction/removal of field lines must occur, otherwise the continuous emergence of "fresh flux" would engender an ever increasing field strength at the surface. But how exactly that happens is still an open question in solar physics (Stenflo 2008).

### 1.3.6   MHD radiative simulations

Because the only system of equations (relevant for flux tubes) that can be treated analytically are the MHS TFA equations (without radiative transfer), one has to turn to numerical treatments of the MHD equations in order to have any predictive power on the thermal structure and dynamics of flux tubes. Two approaches have been undertaken so far, namely in 2D and 3D.

2D simulations were carried out first as they are computationally less intensive, with the advantage that more grid points can be included. Such models were able to extract most of the thermal properties of flux tubes (cf. Sect. 1.3.2). Moreover, by calculating the emerging intensity for various LOS inclinations, they were able to reproduce qualitatively the observed contrast profiles of BPs and faculae and the increasing contrast toward the limb (Deinzer et al. 1984, Knölker et al. 1988, Steiner and Stenflo 1990, Knölker et al. 1991, although there was still a large discrepancy between the observed and synthetic peak contrasts). More recently, numerical developments allowed realistic non-stationary convective motions to be reproduced, and revealed a very dynamic interaction between the convection and the flux tubes (Steiner et al. 1998, Steiner 2005), provoking the bending back and forth of the latter, referred to as "swaying motion" [19]. However, the above 2D simulations did not reproduce the formation processes of the flux tubes (either due to the MHS assumption or due to the closed lower boundary of the box), as the flux sheets were

---

[19]Although the observation of bright facular striations (De Pontieu et al. 2006) indirectly supports such swaying motions, there is not yet a direct observational evidence for it. Moreover, these motions seem not as strong in 3D simulations, presumably because the mass flow in the third dimension reduces the inertial force of the flow in the direction towards the flux tube (owing to mass conservation).
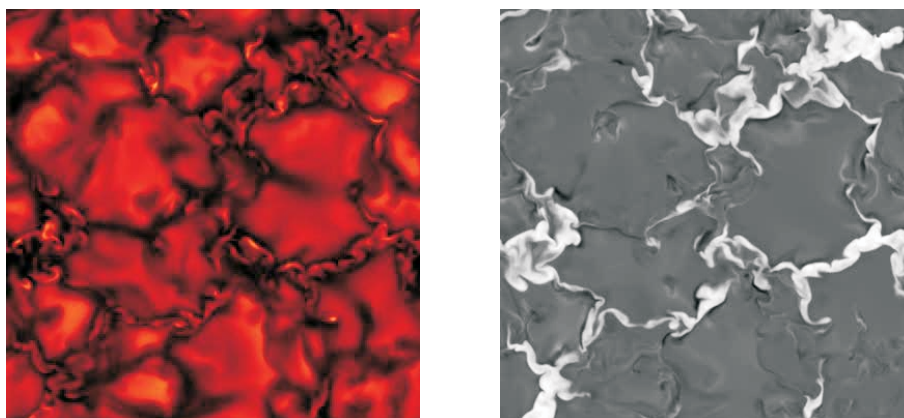
Figure 1.16: Simulation snapshots of continuum integrated intensity (left) and LOS-component of the magnetic field (right), for an initial mean field value of 200 G (courtesy Manfred Schüssler).

introduced ab initio [20].

Today's state-of-the-art MHD simulations are carried out in a 3D computational domain, covering a height range from an almost completely convective atmosphere (800 km below $\tau = 1$) to a completely radiative one up to the temperature minimum ($\sim 600$ km above $\tau = 1$), including diffusivity and non-grey radiative transfer (Vögler et al. 2005). A major success of these simulations was the ability to *reproduce self-consistently the formation of magnetic elements*, in a way that is consistent with the expected properties form the flux expulsion and convective intensification (although these processes cannot be separated in the simulations). The simulations typically start with an initial vertical unipolar homogeneous magnetic field through the box, and let the time run until a quasi-steady state is reached (in a statistical sense) after several granular turnover times. Fig. 1.16 presents snapshots of continuum integrated intensity and LOS-component of the magnetic field, for an initial mean field value of 200 G, an appropriate value to simulate active regions. Note the close correspondence between the integranular continuum bright features and the presence of magnetic field. Their complex fluid-like appearance is a consequence of the self-consistent treatment of their formation mechanisms, thereby not limiting their configuration to cylindrical or slab flux tubes.

Another success of these simulations was their ability to realistically *reproduce the appearance of disk center BPs* (Schüssler et al. 2003, Shelyag et al. 2004) *and limb faculae* (in continuum and G-band, Keller et al. 2004, Carlsson et al. 2004) by solving the radiative transfer along inclined rays. Fig. 1.17 compares such a radiative output with corresponding observations for a LOS inclination of 60°. As can be seen, the simulations and observations agree very well, confirming further the "hot-wall" model of faculae. However, quantitative disagreements remain with the observations regarding the contrast and the size of faculae, as well as their typically observed "striated appearance".

A future challenge expecting theoretical work will be to reproduce the observed magnetic features *at intermediate heliocentric angles* between the disk center and the limb, their CLV of contrast and the variation of their appearance, as well as the observed mix-

---

[20]Except in one study dedicated to reproduce the convective intensification (Grossmann-Doerth et al. 1998), where the lower boundary condition was relaxed to permit free in- and outflow of gas.
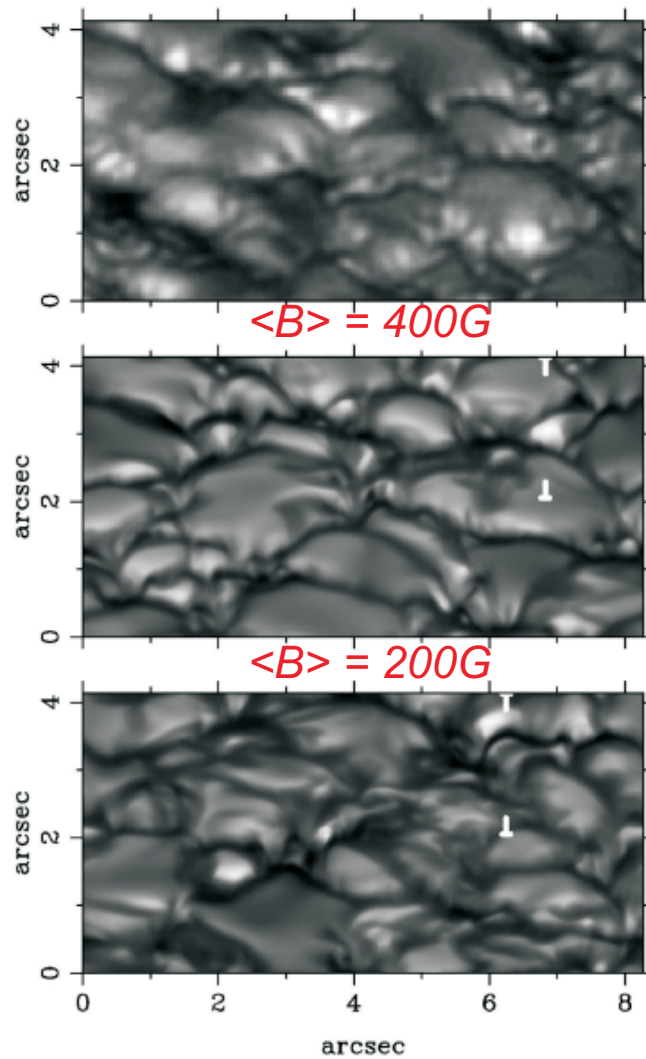
Figure 1.17: Comparison of simulated images of faculae with observations for an helio-centric angle of 60°, at a continuum wavelength of 488 nm (Keller et al. 2004). Upper panel: Observed image of Lites et al. (2004). Middle: Simulated image for an average vertical field of 400 G. Bottom: average vertical field of 200 G.

ture of BP-like and faculae-like features at intermediate heliocentric angles (see Sect. 1.4 and Chapter 2).

## 1.4    Observational contraints and goals: more CLV !

The challenging vision in the physics of magnetic elements is to determine the physical parameters (atmospheric and observing conditions) responsible for the observed contrast and appearance (whether BP or facula) of a magnetic element: e.g. flux tube size and topology, granule geometry, field strength and inclination, spatial resolution, wavelength and heliocentric angle. The way towards such an understanding necessarily resides in an interplay between observation and theory.

On one hand, the 3D simulations briefly described in Sect. 1.3.6 seem to contain most of the physics to mimic the observations qualitatively and reproduce realistic magnetic structures at disk center and near the limb. Yet they still fail in matching the observed contrast values, and there has been no attempt to compare the appearance of simulated features with observed ones at intermediate heliocentric angles. Likewise, there has been to our knowledge only one study computing the apparent contrast CLV from simulation snapshots so far (Zakharov 2006). On the other hand, these models require more constraints in order to be validated, to compare between different alternatives, and thereby to make progress. To do so, we must extract more observational constraints, in particular at different heliocentric angles (since quantitative comparisons have been mostly performed at disk center and at $\mu \sim 0.6$). To obtain such constraints was the major goal of this thesis.

We can think about a quantitative constraint as the measurement of an observable under given conditions (e.g. the mean field stength in an active region at a given resolution), or better, the retrieval of a relationship between two observables. In this respect, the CLV of contrast represents a valuable constraint, inasmuch as it suits the vision discussed above, can be computed for flux tube models (cf. Sect. 1.3.6), and provides a simple *relationship between emergent intensity and emission angle*. Therefore the measurement of contrast CLVs has been and is still a standard problem of solar physics. However, these measurements are subtle as the contrast depends on almost all atmospheric parameters! Statistical approaches would thus be required, in which the contrast is measured and averaged for a fixed range of atmospheric parameters (e.g. in active regions, for a given range of field strength, filling factor etc.). The output would then be comparable to a simulated one under the same conditions.

The problem with previous CLV measurements, besides their mutual discrepancies (cf. Sect. 1.2.4), is the lack of information about atmospheric parameters. Up to now, only few studies have sorted the contrast in ranges of magnetic flux (Topka et al. 1997, Ortiz et al. 2002, Berger et al. 2007), but there is no CLV yet that benefits from a more complete characterization of the atmosphere, e.g. by inverting simulateously observed polarimetric maps. In addition, the observing conditions are often not specified or only partially known: the spatial resolution is often poor and is fluctuating in ground-based data, and the images suffer from unkown amounts of straylight. All this leads to a problem of reliability for quantitative comparison with simulations.

As the appearance of magnetic elements also varies from center to limb (Sect. 1.2.4), a new type of constraint one can think of is a CLV of the relative distribution of BPs and faculae, which would quantify the general change of appearance of magnetic elements with heliocentric angle. As simulations are now able to realistically reproduce the appearance of magnetic elements at disk center and near the limb, this would provide an appropriate constraint to compare the appearances and the distribution of BPs and faculae at intermediate heliocentric angles as well. By the same token, it would contribute to clarify the relationship between BPs and faculae, a question that was never completely resolved (cf. Sect. 1.2.4 and Chapter 2). Such a constraint has not been obtained before, as it requires the development of statistical methods to sort BPs and faculae in images.

## Goals of this work

This thesis work has been dedicated to work towards the constraints mentioned above, i.e.:

1. a CLV of the relative distribution of BPs and faculae in high-resolution images, through the development of an appropriate statistical technique (Chap. 2),

2. a statistical analysis of the contrast and morphology of the obtained populations of BPs and faculae at various heliocentric angles (Chap. 3),

3. a CLV of contrast in seeing-free images (free of straylight) at a given visible continuum wavelength, as a function of magnetic parameters (inclination, field strength and filling factor) inferred by inversions of Stokes spectra (Chap. 4).

While doing so, this work also attempted to indirectly shed light on two related fundamental questions:

- Do bright features near the limb (i.e. faculae) correspond to the same flux concentrations as BPs near disk center?

- Over the range of heliocentric angles in which the presence of BPs and faculae overlap, what physical phenomena cause the apparent mixture of BPs and faculae?

The first question is indeed tightly related to the topic of Chap. 4, namely the dependence of the brightness of the magnetic features on their physical parameters, at different heliocentric angles. While Chap. 2 presents a framework in view of studying the properties of BPs and faculae separately, Chap. 3 provides some clues to the relationship between BPs and faculae via the study of their photometric properties.

# 2 Discriminant analysis and classification of bright points and faculae

While photospheric magnetic elements appear mainly as Bright Points (BPs) at disk center and as faculae near the limb, high-resolution images reveal the coexistence of BPs and faculae over a range of heliocentric angles. This is not explained by a "hot wall" effect through vertical flux tubes, and points that the transition from BPs to faculae needs to be quantitatively investigated. To achieve this and in view of studying the properties of BPs and faculae separately, we made the first attempt to discriminate BPs and faculae, by developing a statistical classification approach based on Linear Discriminant Analysis (LDA). This Chapter gives a detailed description of our method, and shows its application on high-resolution images of active regions to retrieve a Center-to-Limb Variation (CLV) of the relative number of BPs and faculae.

## 2.1 Introduction

When imaged at high spatial resolution, the solar photosphere discloses a myriad of tiny bright features, primarily concentrated in active regions and outlining the borders of supergranules in the quiet Sun (forming the "magnetic network"). Near disk center, they appear mainly as "Bright Points" (BPs) or "filigree" (Dunn and Zirker 1973, Mehltretter 1974), i.e. roundish or elongated bright features located in the intergranular downflow lanes (Title et al. 1987), particularly bright when observed in the Fraunhofer's G-band (Muller and Roudier 1984, Berger et al. 1995, Langhans et al. 2002). Near the limb, they resemble more side-illuminated granules called "faculae" or "facular grains" (e.g. Muller 1975), herein considered as individual small-scale elements (Hirzberger and Wiehr 2005), as opposed to facular patches visible on the white light full disk (see Rogerson 1961, for instance). The close association of BPs and faculae with magnetic-field indicators such as chromospheric Ca II emission suggests that they are related phenomena (Mehltretter 1974, Wilson 1981), both associated with small-scale kG flux concentrations (Stenflo 1973). These so-called "magnetic elements" are considered as the basic building blocks of the photospheric magnetic activity (see Schüssler 1992, Solanki 1993, for reviews), whence the importance of understanding their fundamental physics. High-resolution imaging of BPs and faculae is an essential tool in this respect, inasmuch as localized bright features can be used as "proxies" of these magnetic elements (Solanki et al. 2006). Besides, much of the interest in faculae has been justified by their major role in producing

the total solar irradiance variation (Lean and Foukal 1988, Fligge et al. 1998, Walton et al. 2003, Krivova et al. 2003).

The peculiar appearance of BPs and faculae as well as their different distribution on the disk raises questions about their physical origin and mutual relationship. The standard models accounting for both these phenomena describe BPs and faculae as distinct radiative signatures of strongly evacuated thin flux tubes (to maintain horizontal pressure balance in the "thin flux tube approximation", Schüssler 1992), arising from different viewing angles. When the line of sight is nearly vertical, the radiation mainly escapes from the laterally-heated "floor" of the optical depth depression, giving rise to a BP, whereas an inclined line of sight provides an enhanced view on the "hot wall" of the tube, leading to the bright granular appearance of faculae ("hot-wall" model, Spruit 1976, Knölker et al. 1988, 1991, Steiner 2005). This simplified picture has been verified in its salient points by recent comprehensive 3D MHD simulations including diffusivity and non-grey radiative transfer, with computational boxes of 6 Mm side length covering a height range from an almost fully convective regime up to the temperature minimum (Vögler et al. 2005). A major success has been the ability to qualitatively reproduce BPs near disk center (Schüssler et al. 2003, Shelyag et al. 2004) and faculae closer to the limb (Keller et al. 2004, Carlsson et al. 2004), thereby confirming the basic hot-wall model to first order. However, quantitative disagreements with observations still remain regarding the contrast, the size and the striated appearance of faculae (Keller et al. 2004, Steiner 2007). Furthermore, images with the highest spatial resolution reveal the presence of BPs away from disk center, and of facular elements even close to disk center (Hirzberger and Wiehr 2005, Berger et al. 2007). Such mixtures of BPs and faculae at several heliocentric positions is not explained by the hot-wall picture considering vertical flux tubes, and seems not apparent in the simulated synthetic images (cf. Discussion in Keller et al. 2004). Although granular brightenings at disk center have been partially associated with parcels of rising material (Berger and Title 2001), some of them definitely exhibit facular appearances. Further, it is not clear either whether the BPs and faculae seen at different heliocentric angles are associated with similar magnetic structures, or rather with different structures prone to selection effects (Lites et al. 2004, Solanki et al. 2006). This shows that the transition from BPs to faculae is not clearly understood, and current models aiming at reproducing BPs and faculae would benefit from a quantitative study of the distribution of these features on the disk.

To tackle these issues, a necessary step is to sort the BPs and faculae observed at various disk positions, in order to treat them separately. The approach proposed here is the first attempt in this direction, and relies on Linear Discriminant Analysis (LDA) (Fischer 1936) as a basis to "classify" features as BPs or faculae. Our method makes use of purely photometric information, so that it only distinguishes the features *appearing* as BPs or as faculae. We applied this method to high-resolution images of active regions, covering a range of heliocentric angles where the transition from BPs to faculae is expected. This allowed us to retrieve, for the first time, an estimate of the center-to-limb variation of the relative amount of both features, and thereby to quantitatively grasp how the appearance of magnetic elements varies from center to limb.

Multivariate classification techniques have been earlier fruitfully applied in astronomy to stellar spectra (Kurtz 1984, Egret et al. 1984, Heck et al. 1984, Rampazzo et al. 1988) and faint objects (Jarvis and Tyson 1981), for the star-galaxy separation in im-

ages (Kurtz 1983, Sebok 1979, Malagnini et al. 1985), the interpretation of photometric catalogs (Heck 1976), the discrimination of pulsar types (Fracassini et al. 1984) and of Gamma Ray Burst classes (Mukherjee et al. 1998), the detection of cosmic ray hits on the HST CCDs (Murtagh and Adorf 1992) and the taxonomy of galaxy morphologies (Huertas-Company et al. 2008) (see also the general review by Heck and Murtagh 1989). In the framework of solar physics, although multivariate techniques such as Principal Component Analysis (PCA) and Cluster Analysis have been used for the denoising of Stokes spectra and for sunspots, the application of Discriminant Analysis itself has been up to now restricted to identify the set of conditions triggering solar flares (in the aim of "probablistic flare forecasting" Smith et al. 1996, Leka and Barnes 2003, Barnes et al. 2007), and in terrestrial connection to assess the reality of the response at the Earth's surface to the solar cycle (Tung and Camp 2008). But in none of these cases the purpose was to perform classification of features. Therefore, this paper gives a detailed description of our classification method, and by the same token provides a concrete example of linear discriminant analysis to solar data. Among other potential applications in solar physics, we mention the taxonomy of flares and the separation of chromospheric BPs and cosmic ray spikes on wavelet-analyzed images (Antoine et al. 2002).

The structure of this Chapter reflects the path taken to resolve the classification problem. Section 2.2 describes the original dataset processing, and the automated segmentation method by which bright features were detected at each disk position. Section 2.3 contains an outline of the classification scheme while briefly presenting the principles of LDA, and gives a detailed report of how this technique can be applied to a selected sample of BPs and faculae in order to derive a single discriminant variable, based on which a simple classification rule can be built. Section 2.4 then deals with the actual classification of all the segmented features and justifies the approach from a methodological standpoint, while Sect. 2.5 interprets the results physically and discusses the pros and cons of the method as well as its applicability. Finally, Sect. 2.6 summarizes the obtained results and gives future directions for such work.

## 2.2   Image processing and segmentation

### 2.2.1   Dataset processing

The original dataset consists of simultaneous G-band (430.5 ± 0.5 nm) and nearby continuum (436.3 ± 0.5 nm) images recorded at the 1m Swedish Solar Telescope (SST, La Palma), on 7th and 8th September 2004. They cover active regions at seven disk positions in the range $0.56 \leq \langle \mu \rangle \leq 0.97$, where $\mu \equiv \cos\theta$, $\theta$ is the heliocentric angle and $\langle \mu \rangle$ corresponds to the center of the respective field of view (FOV), equivalent to the mean $\mu$ over the whole FOV (cf. Table 2.1). This range of disk positions contains both BPs and faculae, and is thus well-suited to investigate their transition. Note that the highest latitude of our images is 17°, thereby excluding polar faculae from the present analysis (Okunev and Kneer 2004, Blanco Rodríguez et al. 2007). Because our study requires the highest spatial resolution in order to resolve individual BPs and faculae, the dataset was restricted to the one to three best image pairs at each disk position (obtained at peaks of seeing), which were kept for further processing and analysis (see Table 2.1).

Table 2.1: Dataset specifications: $(\mu_{min}, \mu_{max})$ indicates the $\mu$ coverage of the images, after their rotation along the disk radius vector pointing towards the closest limb. $FOV_{eff}$ is the effective field of view once the spots and pores have been masked out. The number of image pairs selected for processing and analysis is given in the last column.

| Date | NOAA | $\langle \mu \rangle$ | $(\mu_{min}, \mu_{max})$ | $FOV_{eff}$ [arcsec$^2$] | # of pairs |
|---|---|---|---|---|---|
| 07-Sept-2004 | 0669 | 0.97 ± 0.003 | (0.963, 0.977) | 2034 | 1 |
| 07-Sept-2004 | 0671 | 0.78 ± 0.008 | (0.75, 0.8) | 2135 | 1 |
| 08-Sept-2004 | 0670 | 0.97 ± 0.003 | (0.963, 0.976) | 1906 | 1 |
| 08-Sept-2004 | 0667 | 0.937 ± 0.003 | (0.928, 0.945) | 1027 | 2 |
| 08-Sept-2004 | – | 0.9 ± 0.005 | (0.882, 0.916) | 2400 | 1 |
| 08-Sept-2004 | 0671 | 0.63 ± 0.01 | (0.58, 0.67) | 1923 | 3 |
| 08-Sept-2004 | 0671 | 0.6 ± 0.01 | (0.55, 0.64) | 1763 | 2 |
| 08-Sept-2004 | 0671 | 0.56 ± 0.01 | (0.51, 0.6) | 1904 | 1 |
| 13-Aug-2006 | 0671 | 0.77 ± 0.008 | (0.763, 0.776) | 566 | 1 |

For the selected image pairs, phase-diversity reconstruction allowed a roughly constant angular resolution to be achieved, close to the diffraction limit ($\sim 0\rlap{.}''1$ at 430 nm). The reconstructed simultaneous image pairs (G-band and continuum) were aligned and destretched using cross-correlation and grid warping techniques (courtesy P. Sütterlin). The direction of the closest limb was found by comparison with roughly co-temporal SOHO/MDI full disk continuum images, and the images were divided by the limb darkening $\mu$-polynomial of Neckel and Labs (1994) at the nearest tabulated wavelength (427.9 nm). For each image pair, the contrast $C$ was then defined relative to the mean intensity $\langle I \rangle_{QS}$ of a quasi-quiet Sun subfield (of area ranging from 44 to 114 arcsec$^2$, depending on the image) as $C = (I - \langle I \rangle_{QS})/\langle I \rangle_{QS}$. The G-band and continuum contrast are hereafter denoted $C_G$ and $C_C$, respectively. To enhance the segmentation process (see Sect. 2.2.2), we applied a high-pass spatial frequency filter to remove medium and large-scale fluctuations of the intensity (with observed spatial scales between 5 and 30″), presumably attributable to p-modes, supergranular cell contrasts, straylight and residual flat-field effects. The Fourier filter was of the form $f(k) = 1 - e^{-a^2 k^2}$, where $k$ is the modulus of the spatial frequency, and the parameter $a$ was set to have a cut-off frequency ($F(k) = 0.5$) of 0.2 arcsec$^{-1}$ and full power ($F(k) = 1$) at 0.65 arcsec$^{-1}$ (in accordance with Hirzberger and Wiehr 2005). Finally, sunspots and large pores featuring umbral dots were masked out, together with their immediate surrounding granules. This prevents the contamination of BPs/faculae statistics by features of a different physical nature. Figures 2.1 and 2.2 show examples of G-band images at $\langle \mu \rangle = 0.97$ and $\langle \mu \rangle = 0.6$, respectively, in which the quiet Sun contrast reference and the masked out sunspot and pore areas are outlined.

## 2.2.2 Magnetic brightenings segmentation

Prior to their classification as BPs or faculae, bright magnetic features at the different disk positions of our dataset were first detected by a segmentation algorithm. The aims of our algorithm were twofolds:
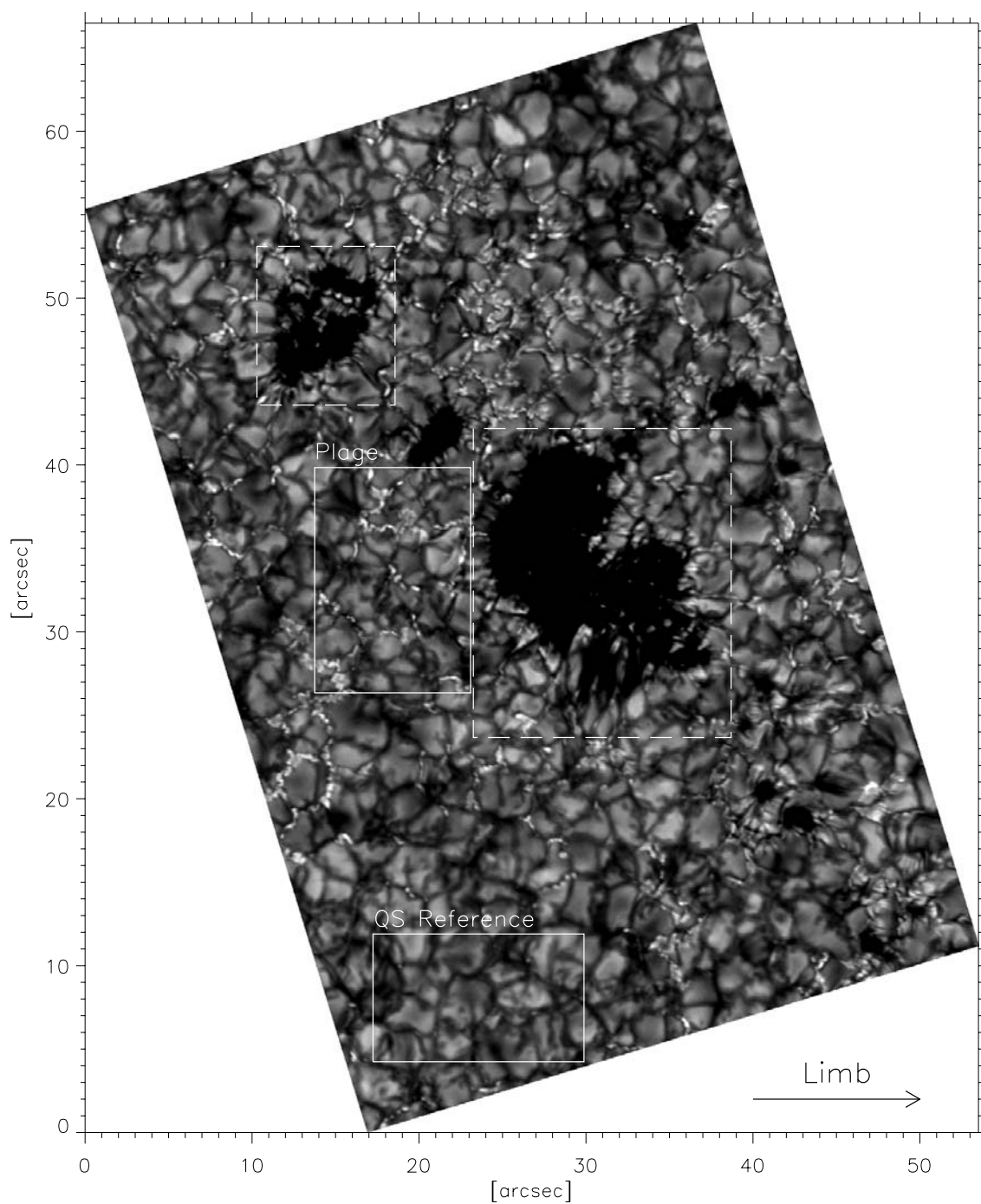
Figure 2.1: G-band image of NOAA 0669 at $\langle \mu \rangle = 0.97$ recorded on the 7th September 2004. The dashed lines outline the spot and pore areas masked out for the segmentation. The "QS Reference" indicates the quasi-quiet Sun subfield chosen as reference for the contrast. The "Plage" subfield is the one selected for the $C_G$ *vs.* $C_C$ diagram shown in Fig.3.10. The arrow indicates the direction of the closest limb
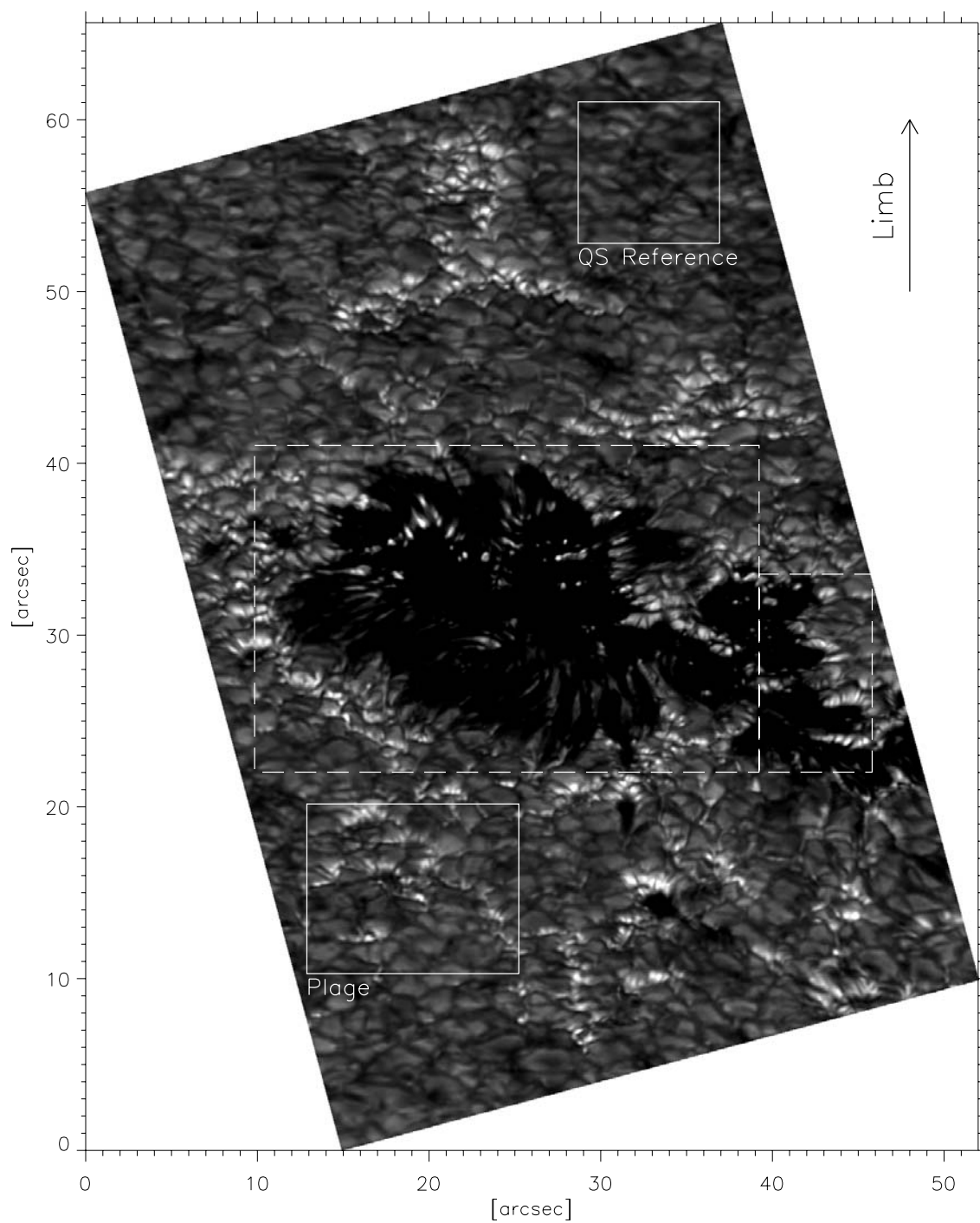
Figure 2.2: G-band image of NOAA 0671 $\langle \mu \rangle = 0.6$ recorded on the 8th September 2004. The "Plage" area was used for the $C_G$ *vs.* $C_C$ diagram plotted in Fig. 3.10.

1. Detect magnetic brightenings photometrically by comparison of their contrast in G-band and continuum.

2. Decompose groups of BPs and striated faculae into individual elements by using Multi-Level-Tracking (MLT, Bovelet and Wiehr 2001, 2003, 2007).

The second point significantly increases the statistics of the study, and relies on the assumption that these elements correspond to distinct magnetic features. This has been justified for disk center BPs (Berger and Title 2001), while observations of the dynamic behavior of striated faculae suggest a correspondance with those features (De Pontieu et al. 2006), the dark striations being associated with sites of lower magnetic field strength (Berger et al. 2007, Carlsson et al. 2004).

The principle behind point 1 is best illustrated by $C_G$ *vs.* $C_C$ scatterplots of a plage area, shown in Fig. 2.3 (see Figs. 2.1 and 2.2 for the location of the chosen plage subfields). As can be seen in Fig. 2.3, the scatterplot splits into two clearly distinct pixel distributions. A similar pattern appears in the diagnostics of radiative MHD simulations of Shelyag et al. (2004), where the upper distribution is shown to be associated with strong flux concentrations, whereas the lower one corresponds to weakly magnetized granules (see also Sánchez Almeida et al. 2001, for the comparison of different 1D LTE atmospheres). Moreover, this "non-magnetic" branch has roughly a slope equal to unity at all disk positions, as granulation does not show any brightness excess in G-band. We can thus select pixels which are G-band bright and likely to be of magnetic origin by imposing two thresholds: a G-band threshold $C_{G,t}$ selecting the bright portion of the diagram (dashed lines in Fig. 2.3), and a threshold $C_{diff,t}$ on the contrast difference $C_{diff} \equiv (C_G - C_C)$ (see Berger et al. 1998, for more details), defining a straight line with slope unity that cuts out the "non-magnetic" distribution (inclined solid lines in Fig. 2.3). This method is particularly suited for the detection of bright magnetic features, as the separation between the "magnetic" and "non-magnetic" branches increases with brightness.

To achieve point 2., we chose a set of closely-spaced MLT levels between $C_{G,t}$ and $C_G = 0.7$. The interlevel spacing was tuned to 0.02 (similar to Bovelet and Wiehr 2007, for BPs at disk center) by visual comparison of the segmentation maps with the original images. This spacing allowed chains of BPs and faculae striations to be resolved, while avoiding over-segmentation. The structures were then extended down to $C_G = 0$ with two intermediate levels at $C_G = 0.1$ and $C_G = 0.05$. The extension of structures increases the segmented area of faculae compared to BPs, allowing its further use as discriminant parameter (see Sect. 2.3.3). The intermediate levels prevent the merging of BPs with adjacent granules and the clumping of granular fragments when the contrast of intergranular lanes does not drop below $C_G = 0$. Since a necessary condition for a feature to be selected is to have its contrast maximum above $C_{G,t}$, no other levels were included between $C_G = 0.0$ and $C_{G,t}$ to avoid oversegmentation. Likewise, structures of less than 5 pixels were removed at each MLT level (given the platescale of the images, 0.″041/pixel, 5 pixels correspond to the area of a roundish feature with a diameter of 0.″1, i.e. roughly equal to the diffraction limit).

The segmentation algorithm then proceeded in two steps: First, MLT was applied to the spatially-filtered G-band images. In a second step, structures corresponding to "magnetic" features were selected by requiring them to *contain* a minimum of 5 pixels
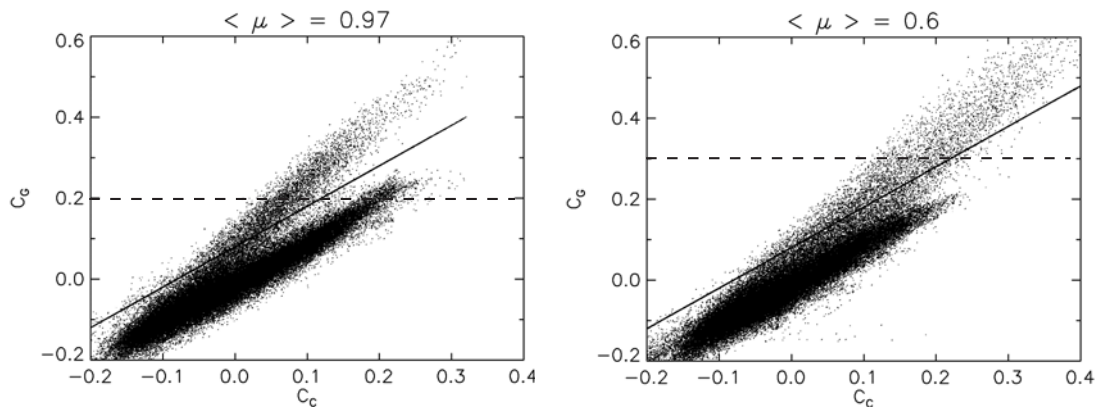
41

Figure 2.3: $C_G$ vs. $C_C$ scatterplots for selected plage subfields of area approximately $10 \times 12$ arcsecs$^2$ at $\langle \mu \rangle = 0.97$ (*left*) and $\langle \mu \rangle = 0.6$ (*right*). The exact locations of these subfields within their respective images are outlined in Figs. 2.1 and 2.2 (rectangles denoted "Plage"). The solid line corresponds to the difference threshold $C_{\mathrm{diff,t}}$ and the dashed line to the G-band threshold $C_{\mathrm{G,t}}$.

satisfying $C_G > C_{\mathrm{G,t}}$ and $C_{\mathrm{diff}} > C_{\mathrm{diff,t}}$. A binary map of segmented features was ultimately obtained for each G-band/continuum image pair.

From Fig. 2.3, one notices that the "magnetic" and "non-magnetic" pixel distributions overlap more at $\langle \mu \rangle = 0.6$ than at $\langle \mu \rangle = 0.97$, a tendency that was generally observed for decreasing $\langle \mu \rangle$. To avoid the false detection of granules, the G-band threshold must then be raised as $\langle \mu \rangle$ decreases, inasmuch as the "magnetic" pixel distribution extends towards larger values of $C_G$ while the "non-magnetic" one reaches lower values (as the rms contrast of granules decreases towards the limb). To do this consistently, we determined a CLV of maximum G-band contrasts $C_{\mathrm{G,max}}$ of features segmented *independently* of the G-band threshold. Specifically, taking one image pair at each disk position, the features were segmented solely by a safe difference threshold $C_{\mathrm{diff,t}} = 0.1$, and the ones having less than 20 pixels above this threshold were removed (as most non-magnetic detections contain only a few pixels, Berger and Title 2001). A visual count over a portion of the images yielded an estimate of the remaining fraction of false detections, approximatively 4 %. Under the reasonable assumption that these false detections were as well the faintest, we adjusted the G-band threshold consistently at all $\langle \mu \rangle$ to eliminate the $\sim 4$ % faintest features (the chosen value of the threshold was actually rounded up, and was constant throughout the field of view at each $\langle \mu \rangle$). The values of the features maximum G-band contrast $C_{\mathrm{G,max}}$ as well as the $\langle \mu \rangle$-dependent G-band thresholds are plotted *vs.* $\langle \mu \rangle$ in Fig. 2.4. Hence, at each disk position, the value of the G-band threshold corresponds to the approximate peak contrast of the faintest features which can safely be considered magnetic.

Unlike the G-band threshold, the difference threshold $C_{\mathrm{diff,t}}$ can be set to a unique value for all disk positions, provided that the slope of the non-magnetic distribution does not vary with $\langle \mu \rangle$ in the $C_G$ vs. $C_C$ diagram. To set $C_{\mathrm{diff,t}}$ properly, we made use of "test" data consisting of a single G-band/continuum image pair obtained with the same setup as our original dataset, but supplemented with SOUP (Lockheed Solar Optical Universal Polarimeter) Stokes $V$ and $I$ maps, recorded in the wing of the Fe I 6302.5 Å line with a

Figure 2.4: Maximum G-band contrast values (small crosses) of all features segmented only with a difference threshold ($C_{\text{diff,t}} = 0.1$) at each disk position. The dashed line corresponds to the chosen G-band threshold removing approximately the 4% faintest features, which are delimited exactly by the large crosses.
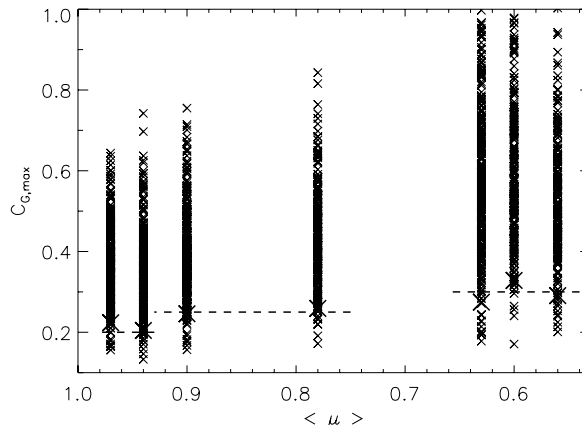
detuning of 75 mÅ. Except for its speckle reconstruction, the test data were processed as described in Sect. 2.2.1. Given the value of the G-band threshold for that disk position, the difference threshold was tuned such as to minimize the fraction of "false" detections. By considering false detections as having less than 5 pixels with $|V/I| \geq 0.075$ (well above the noise level $\sim 10^{-2}$), the optimal difference threshold was found as $C_{\text{diff,t}} = 0.08$. The corresponding fraction of false detections amounts to roughly 2 %. These test images were, however, not used further because they were focused on a large sunspot and hence contain a very small effective field of view (see Table 2.1, 13-Aug-2006). Note that the imposition of the difference threshold was the only use of the continuum images in this work. The subsequent analysis was carried out only on the basis of G-band contrast.

Without information about the magnetic field proper, our segmentation has to rely on purely photometric thresholds, and hence cannot pretend to detect *all* the magnetic features. The combined thresholds only aim at detecting a sample of bright features that is *least biased* by non-magnetic ones. However, the use of thresholds always implies the drawback of selection effects. In particular, the G-band threshold will neglect fainter features, especially low-contrast BPs near disk center (see Title and Berger 1996, Bovelet and Wiehr 2007, Shelyag et al. 2004), and this effect might be more important as this threshold is raised towards the limb.

## 2.3   Discriminant analysis

### 2.3.1   General scheme and training set

To develop an algorithmic classification method for BPs and faculae, we adopted the following scheme, that uses Linear Discriminant Analysis (LDA, a statistical technique first introduced by Fischer 1936) on a reference sample of features:

1. *Training set selection*: Extraction of a reference sample of features, visually identified as BPs and faculae.

2. *Discriminant parameters definition*: Choice of observables taking sufficiently different values for the BPs and faculae of the training set, in order to be of use for the further discrimination of the rest of features.

43

3. *LDA*: Determination of a unique variable by linear combination of the chosen parameters, such that it best discriminates the two classes of the training set.

4. *Assignment rule*: Imposition of an adequate threshold on the discriminant variable defined by LDA, separating the BPs and the faculae of the training set.

Ultimately, *all* the magnetic brightenings detected by the segmentation algorithm can be classified according to the assignment rule, by measuring their value of the variable defined by LDA. Note that within the presented scheme, the actual role of LDA is "only" to provide that discriminant variable, from which a genuine assignment rule can be derived. As such, it is thus a purely *descriptive* dimensionality reduction technique, and its application requires prior knowledge of the classes membership. Therefore this whole scheme is based on a selected sample of known classification, commonly referred to as "training set" or "design set". In this process, the training set is thus taken as a reference for the practical definition of the classes, in the sense that all the features are classified as BPs or as faculae upon their similarity with the training set classes (which is basically what the threshold assignment rule does). Comprehensive manuscripts about the general topic of classification can be found in Murtagh and Heck (1987) and Hand (1981) (including LDA and other multivariate methods, the use of training sets, and the design of assignment rules).

Our training set was chosen as a sample of 200 BPs and 200 faculae, obtained by manual selection of 40 features of each at each of five disk positions: $\{\langle\mu\rangle = 0.56, 0.63, 0.78, 0.9, 0.97\}$ for faculae and $\{\langle\mu\rangle = 0.63, 0.78, 0.9, 0.94, 0.97\}$ for BPs. Because it is used as a reference for the classes, the selected sample should be statistically representative of the actual populations of BPs and faculae (such as would be identified by eye). At each disk position, care was thus taken to select the most homogeneous mixture of features with various contrasts and sizes, distributed over the whole field of view.

It should be kept in mind that the problem we are facing is more subtle than a standard classification one, in that BPs and faculae are possibly not two distinct types of objects, but the radiative signatures of more or less similar physical entities (magnetic flux concentrations) viewed under different angles. Consequently, there may well be no sharp boundary between the two classes, but rather a continuous transition with a spectrum of "intermediate features", having various degrees of "projection" onto the adjacent limbward granules (see Hirzberger and Wiehr 2005, and Sect. 3.3). In addition, we cannot exclude the presence in our dataset of bright features resulting from different magnetic flux structures ("flowers, ribbons" etc.), and hence unclassifiable as BPs and faculae (Berger et al. 2004). The concept of classes (and of training set thereof) can nonetheless be introduced to represent the populations of features that would be reasonably identified as BPs and faculae upon visual inspection. In this sense, the discriminant analysis approach presented here is only a statistical shortcut to the work of the eye alone, and cannot claim to classify the intermediate features mentioned above.

### 2.3.2   Characteristic profiles

As a basis to define discriminant parameters, we considered the spatial variation of the G-band contrast along a cut made through a BP or a facula. Small-scale magnetic features are indeed known to exhibit more pronounced signatures in the G-band than in continuum,

and such contrast profiles have characteristic shapes when BPs and faculae are cut along specific directions: radially for limb faculae, and accross the intergranular lane for disk center BPs (Berger et al. 1995, Hirzberger and Wiehr 2005). The following procedure was developed to retrieve *one* characteristic profile per feature, independently of the feature type and disk position :

First, each feature was oriented in a local coordinate frame $x/y$ as illustrated in Fig. 2.5. The $x/y$ axes were defined such as to minimize the $y$-component of the feature's G-band "contrast moment of inertia" $M_{G,y} \equiv \sum C_G(x,y)(x - x_{max})^2$, where $x_{max}$ is the $x$-location of the contrast maximum $C_{G,max}$. To give optimal results on the orientation, the summation only ran over pixels having $C_G \geq 0.5\, C_{G,max}$, thus involving only the "core pixels" of the features [1]. In practice, the $x/y$ frame was fixed and the minimum of $M_{G,y}$ was found by iteratively rotating a small window surrounding the feature with 5° steps (smaller steps did not yield better results, due to the finite number of pixels considered). Next, contrast profiles were obtained along $x$ and $y$ by averaging the rows and columns of that window having pixels with $C_G \geq 0.9\, C_{G,max}$ (delimited by black lines in Fig. 2.5c). Such $x/y$ profiles are displayed in Fig. 2.6 in the case of a typical BP (*right*) and a typical facula (*left*). These profiles were further restricted to the contrast range $C_G > 0$ about $C_{G,max}$ (delimited by the lower "+" marks), such that all profiles share a consistently-defined reference level $C_G = 0$. Finally, the single *characteristic profile* for each feature was found to be the smoothest of the positive contrast-restricted $x/y$ profiles (overplotted in thick). To quantify the smoothness of the profiles, we counted the number of their local extrema, eventually adding the number of inflexions in case the number of extrema was equal in $x$ and $y$. It should be pointed out that the use of MLT segmentation (by opposition to a single-clip) is an essential prerequisite for obtaining these characteristic profiles, by avoiding that pixels from adjacent features contaminate the contrast moment of inertia and thus spoil the feature's orientation process.

Owing to the previous orientation of the features (via their contrast moment of inertia), the characteristic profiles exhibit different shapes for BPs and faculae, and consequently proved very useful for the extraction of valuable discriminant parameters (see Sect. 2.3.3). By contrast, profiles retrieved along the disk radius vector (as performed in early stages of this work) have less characteristic shapes and thus less power to distinguish BPs from faculae, due to the scatter in the orientation of these features with respect to the radial direction. As can be seen in the examples of Fig. 2.6, the characteristic profile of the typical BP is narrower and steeper than the profile of the typical facula. In particular, the characteristic profile of the facula is indistinguishable from the adjacent granule, as the contrast varies monotonously from one to the other. We mention the resemblance of the characteristic profiles of the BP and facula with the observations of Berger et al. (1995) and Hirzberger and Wiehr (2005), respectively, as well as with the synthetic profiles of Knölker et al. (1988) and Steiner (2005). It can be noted that the underlying average profile of the facula features a narrow "dark lane", theoretically predicted and often present in facular profiles (Keller et al. 2004, Steiner 2005, Lites et al. 2004, Hirzberger and Wiehr 2005). However, these were not ubiquitous in our observations and did not allow us to derive any useful discriminant parameter, whence the choice to restrict the characteristic profiles to $C_G > 0$.

---

[1] involving pixels with lower contrast yields poorer results, as these are often associated to granulation in the case of faculae, and thus do not carry information about the orientation of the facular brightening itself.
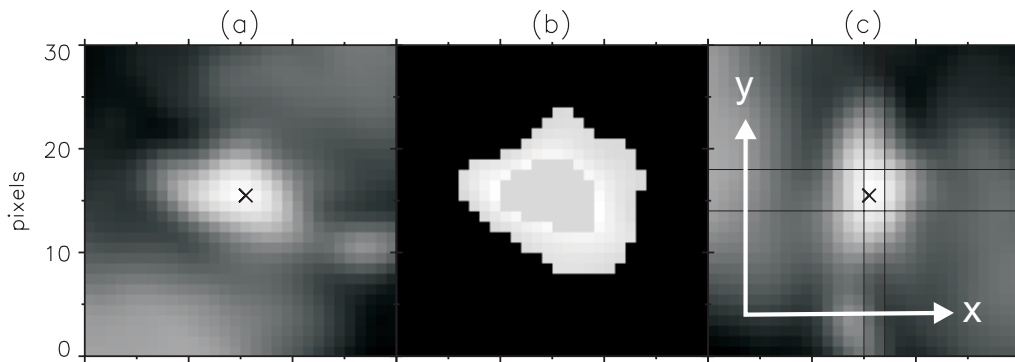
Figure 2.5: Orientation of an individual feature in its local $x/y$ coordinate frame. **a)** Zoom window surrounding the feature in the original G-band image. The cross indicates the location of the contrast maximum. **b)** Isolated feature as delimited by the segmentation map. The pixels having $C_G \geq 0.5\,C_{G,max}$ are highlighted in grey, and are used to compute the G-band contrast moment of inertia. **c)** Window rotated such that the $y$-component of the G-band contrast moment of inertia $M_{G,y}$ is minimum, thereby defining the local $x/y$ coordinate frame. The rows and columns used to retrieve the average profiles along $x$ and $y$ are contained between the straight black lines.

Due to finite resolution, straylight, and the partial compensation of spatial intensity fluctuations by the filter (see section 2.2.1), it is common to find BPs embedded in "grey" lanes with positive contrast (Bovelet and Wiehr 2007). Upon careful visual analysis of grey lane-BPs profiles, we identified these grey lanes as contrast depressions with a low minimum ($C_{G,min} \leq 0.1$), separating the BP profile from the adjacent granule profile (having a width larger than $0\rlap{.}''8 \cdot \mu$, and a maximum contrast above $C_{G,min} + 0.07$). These identification criteria were found by trial-and-error, and are consequently tailored for our particular dataset. As most normal BPs profiles have quasi-linear slopes at their edges, the sides of profiles featuring grey lanes were linearly extrapolated down to $C_G = 0$. Only after this could the $x$ and $y$ average profile be properly restricted to positive contrast values, and their smoothness compared for the adequate retrieval of the characteristic profile. This linear extrapolation is illustrated in Fig. 2.7 for characteristic profiles of both BPs and "intermediate features", indicating at the same time the variety of feature profiles that can be obtained.

### 2.3.3   Discriminant parameters

In search of adequate discriminant parameters, we carried out a pilot study by defining of set of parameters, among which: the peak-to-width ratio, are asymmetry and second moment of the characteristic profiles, the local contrast relative to the immediate surroundings (similar to Bovelet and Wiehr 2003), and the contrast of adjacent lanes. By looking at the distribution of the parameter values for the BPs and faculae of the training set (mean values and standard deviation at each $\langle \mu \rangle$, see below) as well as their correlation, three roughly mutually independent parameters were eventually found to be good discriminants for the training set classes. Their definitions are illustrated in Fig. 2.6:

- $\Delta$ := width of the characteristic profile at the reference level $C_G = 0$ [arcsecs].
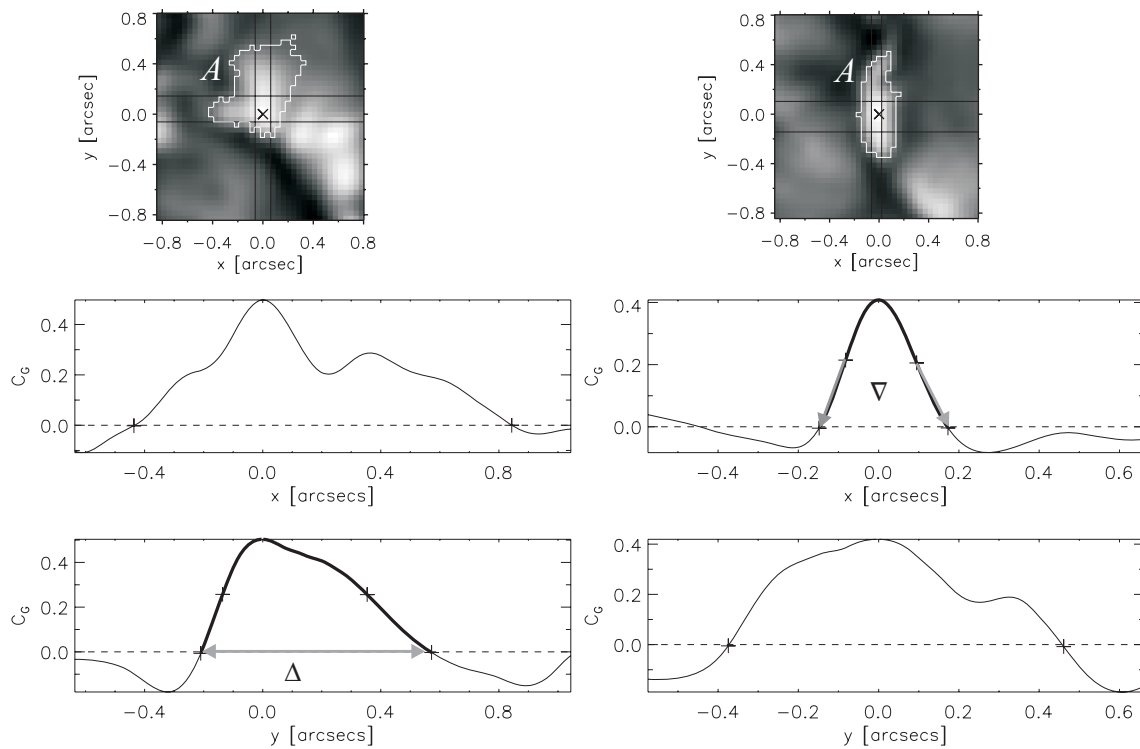
Figure 2.6: Local frame orientation and G-band contrast profiles and of a typical facula (*left*) and a typical BP (*right*). (*Top windows*) Orientation of the features in their local $x/y$ coordinate frames, where the black lines delimit the pixels having $C_G \geq 0.9 C_{G,\max}$ used for profile averaging. The white contours obtained from the segmentation map enclose the area $A$ of the features. (*Lower panels*) Average G-band contrast profiles along $x$ and $y$. The retrieved *characteristic profile* for the BP and the facula is indicated by the thick lines. The "+" marks intersecting the reference level $C_G = 0$ (dashed line) delimit the positive contrast portion of the profiles, and the upper "+" marks indicate the half-max level $C_G = 0.5 C_{G,max}$ on the characteristic profiles. The parameters $\Delta$ and $\nabla$ are illustrated on the characteristic profiles of the facula and the BP, respectively. All the $x/y$ profiles were cubic spline-interpolated by a factor 10, in order to avoid the artificial roughness due to sampling when choosing the characteristic profile (as the smoothest of the $x/y$ profiles, see Sect. 3.3).

- $\nabla :=$ average slope (from both sides) of the characteristic profile below the half-max level $C_{G,HM} = 0.5 C_{G,\max}$ [arcsecs$^{-1}$].

- $A :=$ apparent area of the feature defined by the segmentation binary map [arcsecs$^2$].

We emphasize that the three chosen parameters are defined using *relative* contrast levels ($C_G = 0$ and $C_G = 0.5 C_{G,\max}$). This allows the comparison and classification of features having different absolute contrast values, in particular avoiding the bias of the classification results at various disk positions by the contrast CLV (a crucial requirement if we consider a common training set providing the same classes reference for all disk positions, see end of this Section).

Fig. 2.8 (left column) shows the mean values and standard deviation of the parameters $A$, $\Delta$ and $\nabla$ at the different $\mu$-values of the training set. These parameters describe well the
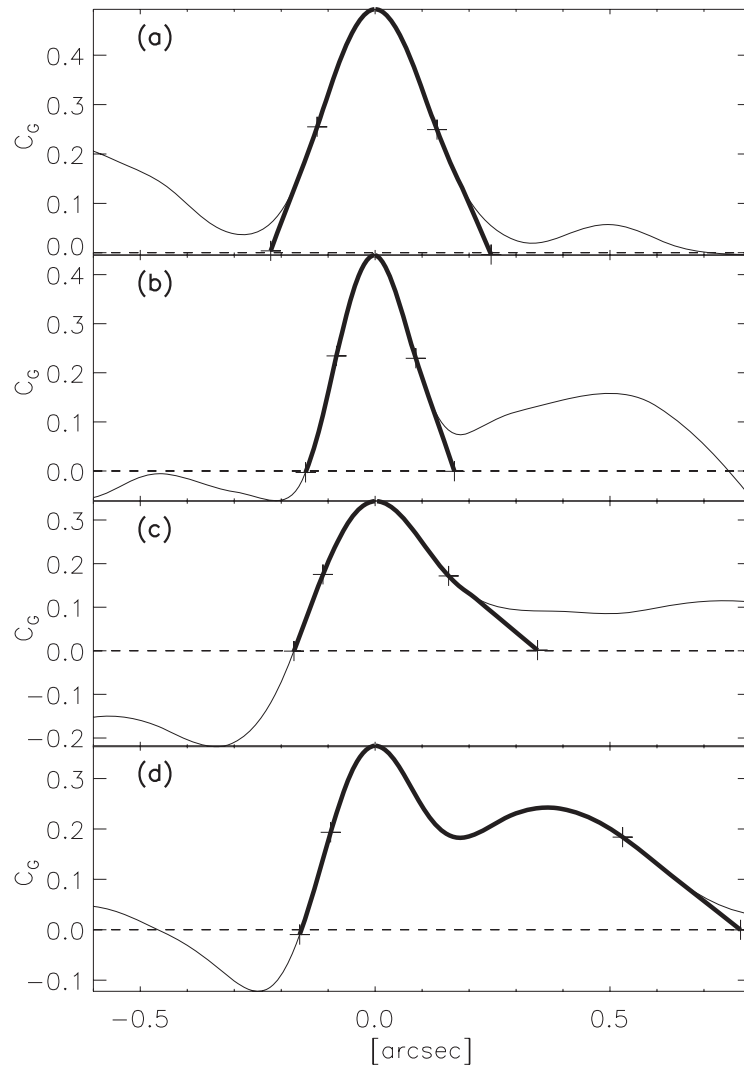
Figure 2.7: Characteristic profiles (thick lines) of BPs **(a, b)** and intermediate features **(c, d)** surrounded by one or two "grey" lanes. On the grey lane sides, the characteristic profiles have been linearly extrapolated from the half-max level ("+") to $C_G = 0$. From **a)** to **d)**, these profiles illustrate the continuous transition between the typical BPs and typical faculae, for which examples are shown in Fig. 2.6.

different appearances of BPs and faculae for the following reasons. The best discriminant parameter, $\Delta$, takes greater values for faculae as it encompasses the width of the adjacent granular profile (as the facular and granular profile are merged together, cf. Fig. 2.6), whereas BPs are limited to the width of intergranular lanes. The parameter $\nabla$ describes how steep the contrast drops towards the edges of the profile and has typically larger values for BPs, which show steep and symmetric contrast enhancements squeezed between the adjacent granules. To supplement these two profile parameters, the segmented feature area $A$ has been added to avoid that faculae with small widths (typically lying on small abnormal granules frequently found in active regions) are classified as BPs. In area these faculae appear significantly larger.
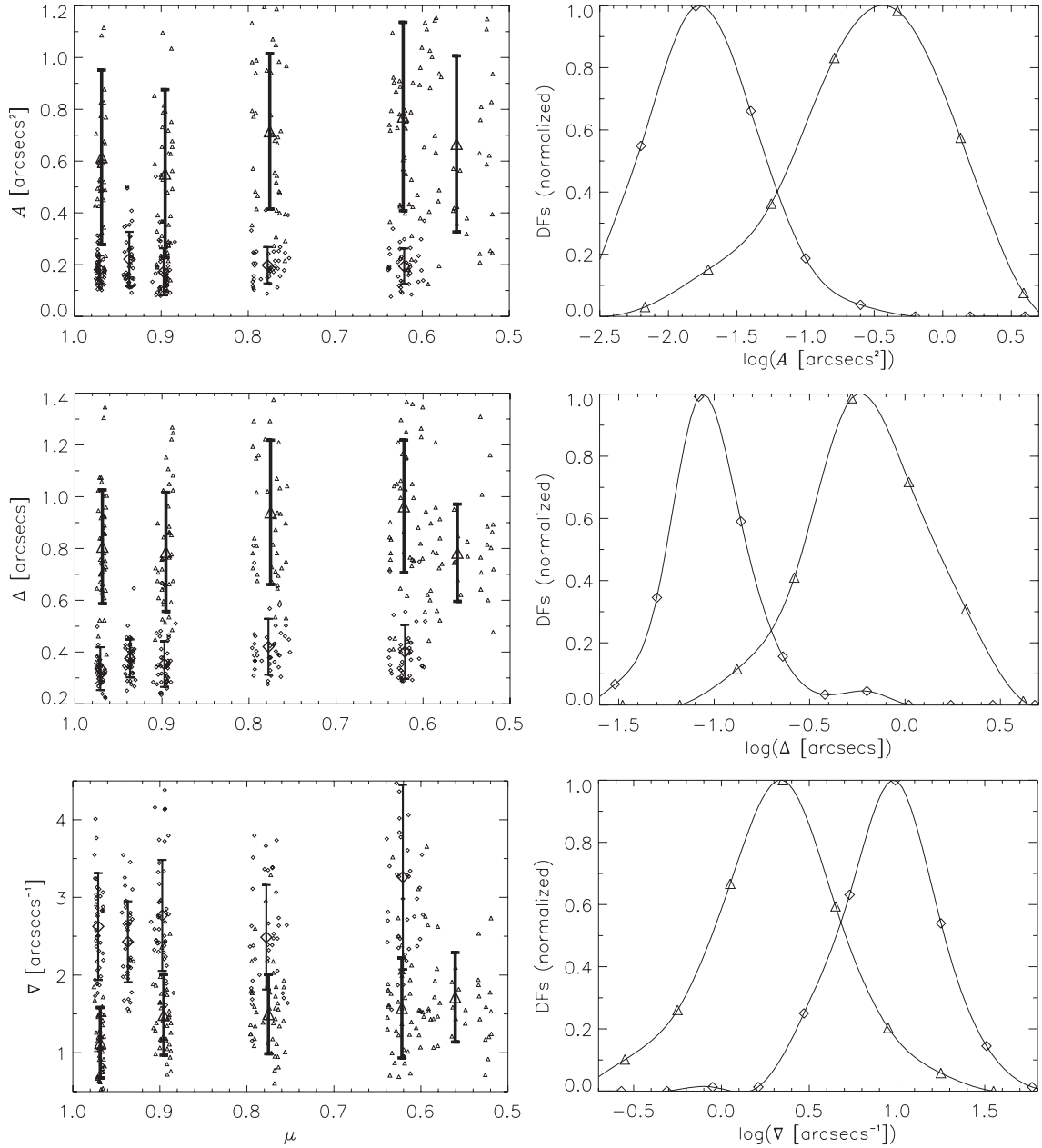
Figure 2.8: *Left column*: Mean values and standard deviations of the three parameters for the BPs ("⬦" and thin bars) and faculae ("△" and thick bars) of the training set *vs.* disk position ⟨μ⟩. The training set does not contain BPs at ⟨μ⟩ = 0.56 nor faculae at ⟨μ⟩ = 0.94. To give an idea of the outliers and the μ distribution of the training set features at each disk position, individual features values were overdrawn (little "⬦" for BPs and little "△" for faculae). The μ values of the individual features was computed by using the ⟨μ⟩ (center of FOV) of the corresponding images as reference. *Right column*: Normalized density functions (DFs) histograms of the log-transformed parameters for BPs ("⬦") and faculae ("△"), obtained by combining all disk positions of the training set together. Cubic splines are overplotted for visual clarity and their maxima were used for the normalization of the histograms.

As can be seen from Fig. 2.8 (left column), the parameter values do not vary significantly with $\langle\mu\rangle$, as the difference between the largest and smallest mean values over the whole $\mu$ range barely exceed their standard deviations. The relative constancy of width and area is particularly surprising for faculae, and could be due to a compensation of granular foreshortening by enhanced radiative escape (Steiner 2005), as well as to the distribution in the orientation of faculae (to be discussed in a forthcoming paper). The relative invariance of the parameters is nevertheless advantageous, as it justifies performing LDA on the whole training set at once (all $\langle\mu\rangle$ together), thus allowing to find a single linear combination of parameters and a single BPs/faculae threshold valid for all the disk positions of our dataset. Moreover, combining all the training set features together enhances the sampling of the classes and yields a more accurate threshold. For these reasons, no "deprojection" of the parameters was performed, as this would then induce a variation of the parameters with $\mu$.

### 2.3.4   Linear Discriminant Analysis

Because LDA distinguishes classes based solely on means and covariances (see Equation 2.1), it works best for parameters that are normally or at least symmetrically distributed (Murtagh and Heck 1987). To verify this condition, we studied the density functions (DFs) of our three parameters by producing histograms of the training set, and estimated the skewnesses via the third standardized moment[2] (Kenney and Keeping 1962). Taking the natural logarithm was found to reduce the skewness of all parameters (Limpert et al. 2001), and therefore they were replaced by their log-transforms. This was partly expected, as the width of magnetic bright points has been previously observed to be lognormally distributed (Berger et al. 1995). The density functions of $\log(A)$, $\log(\Delta)$ and $\log(\nabla)$ are displayed in Fig. 2.8 (right column).

Having the right parameters in hand, LDA could then be carried out to find their linear combination that best discriminates the training set classes. From a geometrical viewpoint, this problem is formally equivalent to finding the direction of the parameter space $\{x = (\log(A), \log(\Delta), \log(\nabla))\}$ along which the "separability" between the training set classes is maximum. Explicitely, we searched for the axis vector $\widehat{a}$ that maximizes Fischer's separability criterion (as introduced in the original work of Fischer 1936):

$$J(a) = \frac{[a^{\mathrm{T}}(m_{\mathrm{bp}} - m_{\mathrm{fac}})]^2}{a^{\mathrm{T}}(S_{\mathrm{bp}} + S_{\mathrm{fac}})a}, \tag{2.1}$$

where the superscript T denotes transpose, $m_{\mathrm{bp}}$ and $m_{\mathrm{fac}}$ are the class mean vectors and $S_{\mathrm{bp}}, S_{\mathrm{fac}}$ the covariance matrices. In this form, $J(a)$ is actually a trade-off between the separation of class means (between-class separation) and the compactnesses of the classes (within-class scatter), both viewed along $a$. In practice, maximizing the Fischer criterion as $\frac{\partial}{\partial a}J(a)|_{\widehat{a}} = 0$ yields the simple relation $\widehat{a} \propto (S_{\mathrm{bp}} + S_{\mathrm{fac}})^{-1}(m_{\mathrm{bp}} - m_{\mathrm{fac}})$ (Hand 1981). The original parameters could then be projected onto $\widehat{a}$, thereby obtaining the desired linear combination defining the single variable $F \equiv \widehat{a}^{\mathrm{T}}x$ (for "Fischer" variable). The 2D projections of the 3D training set vectors are represented in Fig. 2.9a-c, with an overlaid

---

[2]Although the third moment tends to be dominantly affected by outliers, this effect is only minor for large samples like our training set.

Table 2.2: $J$ values associated with each discriminant parameter, and for the variable $F$ obtained by linear combination of the three parameters. The $a$'s are the coefficients of the linear combination (absolute values).

|   | $\log(A)$ | $\log(\Delta)$ | $\log(\nabla)$ | $F$(3D) |
|---|---|---|---|---|
| $J$ | 3.17 | 4.71 | 1.8 | 6.27 |
| $a$ | 0.27 | 0.59 | 0.14 | |

axis corresponding to the direction of maximum separability $\widehat{a}$. Fig. 2.9d displays the density function histogram of the obtained variable $F$. The maximal value of $J$ associated with the variable $F$ (projection onto $\widehat{a}$) and the values of $J$ associated to each parameter (projection onto the parameters' axes) are listed in Table 2.2. These values give an idea of the relative "discriminant power" of the three parameters, and the larger $J$ value of the variable $F$ demonstrates the advantage of their optimal linear combination provided by LDA.

The DFs of the discriminant parameters (Fig. 2.8 right column) and of the variable $F$ (Fig. 2.9d) also give a good visual estimate of the amount of overlap between the training set classes. An intuitive measure of the discriminant power of a parameter could then be given by the ratio between the number of features contained in the overlapping part of the DFs in Fig. 2.8 and the total number of training set features. This ratio takes already a fairly low value of 0.07 for $\log(\Delta)$, and goes down to 0.042 for $F$. However, such a measure is statistically poor compared to $J$, since it mostly relies on the outliers contained in the tails of the DFs (only 28 and 17 features for $\log(\Delta)$ and $F$, respectively), whereas $J$ takes advantage of the full parameter distributions.

The overlap of the DF of $\log(A)$ and the particular skewness of the DF of faculae towards small areas arises from our MLT segmentation. To investigate the influence of the MLT levels on the DFs of the dicriminant parameters and on LDA, we carried out tests with fewer MLT levels over the same training set (see App. A for more details). We found that the skewness of the DF of $\log(A)$ for faculae is in major part due to their segmentation into fine striations. It should be noticed that the DF of $\log(\Delta)$ is less skewed, because the characteristic profiles of these striated faculae are mostly retrieved along the long dimension of the striations (owing to their individual orientation, see Sect. 3.3), which makes $\Delta$ a robust parameter to distinguish them from BPs. However, the coarser segmentation of the tests has the undesired effect that a part of the features are undersegmented, which leads to lower values of $J$ for all parameters as well as for the discriminant variable $F$. Due to the merging of BPs into chains and ribbons, their DFs are particularly affected and become skewed towards larger $A, \Delta$ and smaller $\nabla$. For $\Delta$ and $\nabla$, this is probably a consequence of the misorientation of merged features when retrieving the characteristic profiles. We believe that those tests confirm our appropriate choice of MLT levels for the purpose of further discriminating between individual BPs and faculae.

We stress that the procedure of orienting the features prior to the retrieval of their contrast profiles, as described in Sect. 3.3, is an essential ingredient for obtaining discriminant parameters based on those profiles. In early stages of this work, profiles were only retrieved along the direction perpendicular to the closest limb, and the ensuing overlap of the DFs was significantly larger.
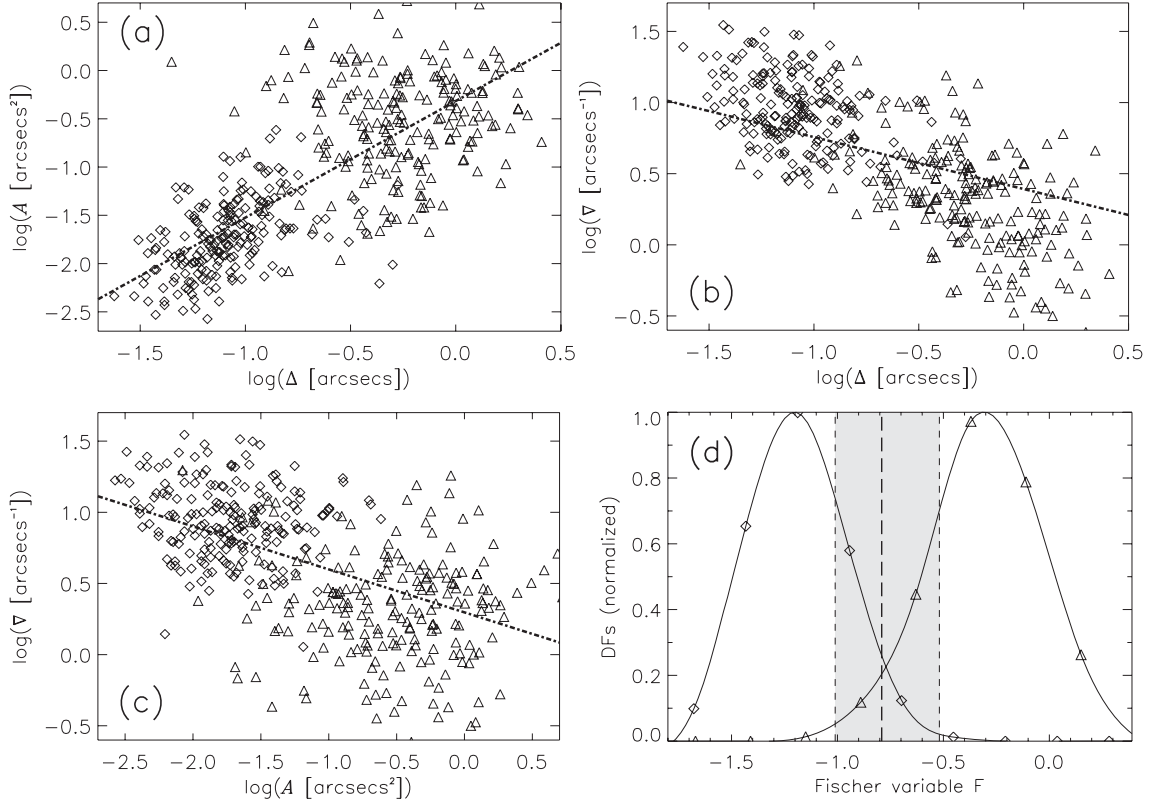
Figure 2.9: **(a-c)** 2D projections of the 3D training set vectors $\{\log(A), \log(\Delta), \log(\nabla)\}$ for the BPs ("$\diamond$") and faculae ("$\triangle$") classes of the training set, together with an axis indicating the projected direction of maximum separability $\widehat{a}$ (dashed-dot line). **d)** Spline-interpolated density function histogram of the variable $F$, with the BP-faculae threshold $F_t$ (long dashed line) and the rejection range corresponding to the apparent rejection rate $\alpha = 0.2$ (grey zone).

Finally, it should be noted that the values of these photometric discriminant parameters all depend to some extent on the spatial resolution. $\nabla$ is probably the most sensitive in that respect, but it has the least weight in the variable $F$ due to its lower value of $J$ (see $a$ values in Table 2.2). This points to the requirement of having a dataset of roughly constant resolution, a condition met by our selection of images (Sect. 2.2.1).

## 2.4   Classification

To build an assignment rule for the subsequent classification of all features, we made the usual choice of a threshold value $F_t$ at equal "standardized" distance from the classes means (i.e. distance to the mean divided by the standard deviation, or "Mahalanobis" distance) (Mahalanobis 1936, Murtagh and Heck 1987), namely:

$$\frac{(\widehat{a}^T m_{bp} - F_t)^2}{\widehat{a}^T S_{bp}\widehat{a}} = \frac{(\widehat{a}^T m_{fac} - F_t)^2}{\widehat{a}^T S_{fac}\widehat{a}}. \tag{2.2}$$

This threshold $F_t$ is drawn on the density function histogram of $F$ in Fig. 2.9d.

### 2.4.1 Classification with hard threshold

In a first step, a single hard threshold equal to $F_t$ was used to classify *all* the segmented features as BPs or faculae by measuring their values of $F$.

As already stated at the end of Sect. 2.3.1, there is a continuous spectrum of intermediate features between BPs and faculae, that cannot be reasonably identified as belonging to one class or the other. Hence, a hard threshold classification is self-contradictory, as these intermediate features are assigned to classes whose reference (the training set) does not represent them.

Explicitly, at each disk position, the relation between the number of BPs and faculae $N_{bp}, N_{fac}$ classified using the threshold $F_t$ and the *true* numbers $N_{bp}^*, N_{fac}^*$, i.e. such as would be found by eye, is given by:

$$\begin{aligned}
N_{bp} &= N_{bp}^* + \epsilon^* N_{fac}^* - \xi^* N_{bp}^* + 1/2 N_{int}, \\
N_{fac} &= N_{fac}^* + \xi^* N_{bp}^* - \epsilon^* N_{fac}^* + 1/2 N_{int}, \\
N_{tot} &= N_{bp} + N_{fac} = N_{bp}^* + N_{fac}^* + N_{int},
\end{aligned} \tag{2.3}$$

where $\epsilon^*, \xi^*$ are the "true" misclassification rates, i.e. the fractions of *actual* faculae and BPs populations that are misclassified, and $N_{int}$ is the number of intermediate features, from which we assume that half is assigned to each class. Because we are not interested in absolute numbers, but rather in the relative distribution of BPs and faculae, we define the classified $X_{bp}$ and true $X_{bp}^*$ fractions for BPs as:

$$X_{bp} \equiv \frac{N_{bp}}{N_{bp} + N_{fac}}, \quad X_{bp}^* \equiv \frac{N_{bp}^*}{N_{bp}^* + N_{fac}^*} \tag{2.4}$$

and likewise for faculae. The CLV of the classified fractions $X_{bp}$ and $X_{fac}$, obtained by using the threshold $F_t$ defined by equation (2.2) is depicted in Fig. 2.10a.

But because $N_{int}$ is unknown and not negligible (as shown in Sect. 2.4.2), we cannot recover a direct relation between classified and true fractions in order to estimate the latter. Moreover, as the intermediate features tend to be assigned equally to both classes, their effect tends to equalize $X_{bp}$ and $X_{fac}$. Although this CLV qualitatively represents the transition from BPs to faculae, it is open to criticism from the methodological point of view, and underestimates the difference between the fraction of BPs and faculae by an unknown amount.

### 2.4.2 Classification with reject option

The only way to recover a relation between the classified and true relative fractions is to exclude the intermediate features from the statistics by introducing a so-called "reject option" (Hand 1981), in the form of a rejection range in $F$ centered about $F_t$. At the same time, this will significantly reduce the misclassification errors. Assuming that all intermediate features fall within the rejection range, the relation between classified and true numbers at each disk position becomes:

$$\begin{aligned}
N_{bp} &= N_{bp}^*(1 - \beta^*) + \epsilon^* N_{fac}^* - \xi^* N_{bp}^*, \tag{2.5} \\
N_{fac} &= N_{fac}^*(1 - \alpha^*) + \xi^* N_{bp}^* - \epsilon^* N_{fac}^*, \tag{2.6}
\end{aligned}$$

$$N_{rej} = \alpha^* N_{fac}{}^* + \beta^* N_{bp}{}^* + N_{int}, \tag{2.7}$$

$$N_{tot} = N_{bp} + N_{fac} + N_{rej} = N_{bp}{}^* + N_{fac}{}^* + N_{int}, \tag{2.8}$$

where $\alpha^*$ and $\beta^*$ stand for the "true" rejection rates, i.e. the fractions of the actual faculae and BPs populations that fall in the rejection range. The boundaries of our rejection range were tuned to have equal "apparent" rejection rates, $\alpha = \beta$, defined as the fractions of the *training set* contained in that range. Assuming that the training set adequately represents the true BPs and faculae populations, namely $\alpha^* \sim \alpha$ and $\beta^* \sim \beta$, this precaution equalizes the true rejections as well ($\alpha^* \sim \beta^*$), and thus prevents the introduction of bias in the number statistics. The apparent rejection rate was set to a reasonable value for the rejection of intermediate features, $\alpha = 0.2$ (see below), yielding the shaded rejection range on the histogram of $F$ in Fig. 2.9d. With the chosen rejection range, we can compute the apparent misclassification rates by reclassifying the training set: $\epsilon, \xi = 0.005$. Although these values are only optimistic estimates of the true misclassification rates, the rejection has lowered them by more than a factor 10 (the apparent misclassification rates in the hard threshold case are $\sim 0.05$), which should be reflected in the true rates as well.

Under the full rejection of intermediate features, the relative classified fractions then become:

$$X_{bp} = \frac{N_{bp}{}^*(1 - \beta^*) + \epsilon^* N_{fac}{}^* - \xi N_{bp}{}^*}{N_{bp}{}^*(1 - \beta^*) + N_{fac}{}^*(1 - \alpha^*)} \tag{2.9}$$

for BPs and similarly for faculae. Assuming that the rejection yields negligible misclassification rates, and that the training set is representative ($\alpha^* \sim \beta^*$), the relation (2.9) simplifies to $X_{bp} \sim X_{bp}{}^*$, so that under these assumptions the classified fractions closely approximate the true ones. The CLV of classified fractions $X_{bp}$ and $X_{fac}$, obtained by adding a rejection range with $\alpha = 0.2$, is shown in Fig. 2.10b.

Compared with the CLV of $X_{bp}$ and $X_{fac}$ obtained with a hard threshold, the difference between $X_{bp}$ and $X_{fac}$ at each $\langle \mu \rangle$ is now systematically larger (except for $\langle \mu \rangle = 0.9$). This is probably an effect of the contamination by intermediate features in the hard threshold case, as these tend to equalize $X_{bp}$ and $X_{fac}$ (see Sect. 2.4.1). The difference is particularly large for $\langle \mu \rangle = 0.97$ and for the limbward data points at $\langle \mu \rangle \leq 0.64$. This is likely to be attributed to the larger misclassification errors in the hard threshold method than with the reject option. Indeed, as can be seen from relation (2.3), the misclassification errors also tend to overestimate the number of BPs near the limb where faculae dominate, while underestimating it near disk center, and *vice versa* for faculae.

We shall now elaborate on the validity of the aforementioned assumptions, and further justify the use of a reject option as opposed to the hard threshold classification. A subtle source of error is the departure of the actual populations from the trainig set ones, causing $\alpha^* \neq \beta^*$. To evaluate the importance of this effect, we have varied $\alpha$ in the range (0.2, 0.5), which should induce unequal variation of $\alpha^*$ and $\beta^*$ and consequently different variations of $X_{bp}$ and $X_{fac}$ (cf. Eq. 2.9). By the same token, this allowed us to check as well if intermediate features were still wrongly classified as BPs or faculae for $\alpha = 0.2$, as the separation between $X_{bp}$ and $X_{fac}$ should then increase with $\alpha$. But we observed both positive and negative fluctuations of $X_{bp}$ and $X_{fac}$, indicating that most intermediate features were indeed rejected, and that the true rejection rates were nearly equal for BPs and faculae. As those fluctuations were always less than 0.05, we chose this value as an upper limit on the error induced by eneven actual rejection rates, and represented it by
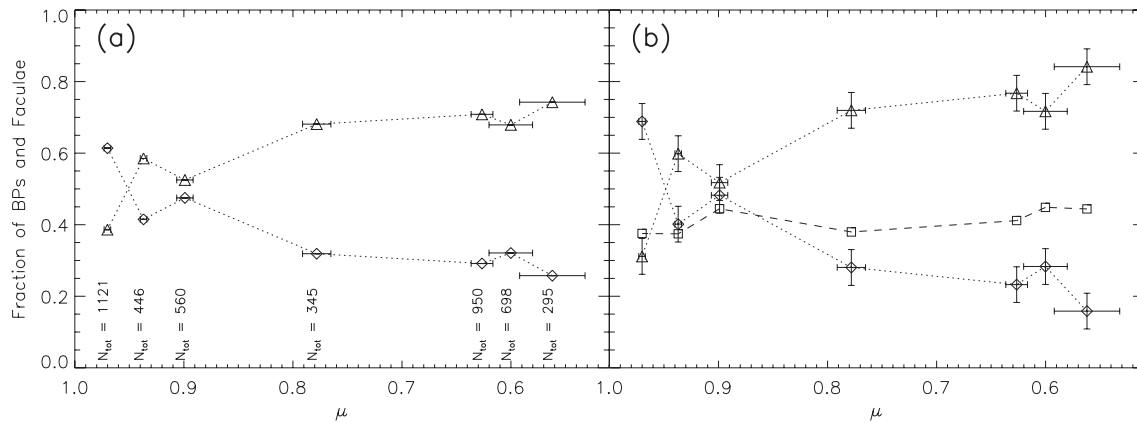
Figure 2.10: **a)** CLV of relative fractions of BPs ("⋄") and faculae ("△") obtained by classifying all the segmented features using a hard threshold $F_t$ defined via equation (2.2). The abcissa of the points are the $\langle\mu\rangle$ of the analyzed images, and the horizontal error bars correspond to the standard deviation of the individual features' $\mu$ values with respect to $\langle\mu\rangle$. $N_{\text{tot}}$ gives the total number of features at each disk position, which depends on the effective FOV of the images and the number of available image pairs at each disk position (see Table 2.1). The dotted lines are only plotted to guide the eye. **b)** Relative fractions of BPs ("⋄") and faculae ("△") after the introduction of a rejection range such that the apparent rejection rates of BPs and faculae are equal to 0.2. The vertical error bars (±5%) are upper limit estimates of the errors induced by uneven true rejections rates (see main text for details). The fraction of rejected features with respect to the total number of features is also plotted, as squares ("□") joined by a dashed line.

the symmetric error bars in Fig. 2.10b. Second, even by using a reject option, the true misclassification rates might not be negligible. In the hope of obtaining less optimistic estimates of the misclassification rates, we implemented a "leave-one-out" method on the training set (Hand 1981, Murtagh and Heck 1987). This method basically consists of taking maximum advantage of the training set: for each of the N elements of the training set, LDA is carried out on the remaining N-1 elements and the element left out (the test one) is classified, thus yielding N independent classification tests. The "leave-one-out" basically gave the same results as the simple reclassification (probably due to the fairly large size of the training set). To compare the effect of rejection at the various disk positions, we overplotted in Fig. 2.10b the fraction of rejected features with respect to the total number of features $N_{\text{rej}}/N_{\text{tot}}$. The relative constancy of $N_{\text{rej}}/N_{\text{tot}}$ is reassuring, and reflects the self-similarity of the actual BPs and faculae populations at various $\langle\mu\rangle$ (as far as $F$ is concerned). It also gives an indication about the number of intermediate features, as in absence of them we would have $N_{\text{rej}}/N_{\text{tot}} \simeq \alpha$, using as before $\alpha^* \sim \beta^* \sim \alpha$ together with the relation 2.7. As can be seen, the fraction of rejected features fluctuates around 0.4, indicating a significant fraction of intermediate features $N_{\text{int}}/N_{\text{tot}} \simeq 0.2$, which further justifies the introduction of the rejection range.

Lastly, the results obtained here do not only depend on the choice of the training set, but also on the choice of the classification method. Fischer's LDA implicitly assumes similar covariance matrices for the classes, which is not quite true in our case, as can be seen from the different shapes of the BPs and faculae "clouds" in their 2D projections (Fig.

55

2.9). We then implemented a "class-dependent" LDA, taking into account the difference in covariance matrices and deriving different discriminant axes for the two classes (Balakrishnama and Ganapathiraju, Balakrishnama et al. 1999). However, the difference in the obtained relative fractions was insignificant, thereby indicating that the covariance matrices of our chosen parameters were suited enough for Fischer's LDA. Other alternative multivariate statistical methods could be Quadratic (also called Bayesian) Discriminant Analysis or Cluster Analysis. The former has the inconvenience of assuming explicitly multinormal probability distributions for the classes, and the latter does not aim at classifying but rather at identifying groups within a population (which is not optimally suited for BPs and faculae due to the spectrum of intermediate features). For a short review of these techniques, refer to Murtagh (1994).

## 2.5   Discussion

In the preceding section we compared the hard threshold with the reject option from a *methodological* point of view, thus illustrating the advantage of the latter when the classes are not completely distinct, or when other types of features may contaminate the classification. But even with a judicious reject option, the obtained fraction CLV still presents error bars that are hardly quantifiable and is based on the assumption that the training set is representative. For solar physics purposes though, the achieved precision may be sufficient, as the results are anyway dependent on the particular dataset and its nature (active region plage, network, etc.), as well as the definition of the classes through the choice of the training set.

To help the comparison with the literature as well as to give a visual idea of which features were classified as BPs and faculae, Fig. 2.11, Fig. 2.12 and Fig. 2.13 show their contours overlaid on the G-band images at $\langle \mu \rangle = 0.97$, $\langle \mu \rangle = 0.6$ (same images as in Figs. 2.1 and 2.2), and $\langle \mu \rangle = 0.9$ respectively. Our results are consistent with recent high-resolution observations from Berger et al. (2007), who noticed the presence of disk-center faculae at $\langle \mu \rangle = 0.97$, very few intergranular BPs at $\langle \mu \rangle = 0.6$, and a mixture of both features at $\langle \mu \rangle = 0.89$. The presence of some "intergranular brightenings" around $\langle \mu \rangle = 0.55$ has been also reported by Lites et al. (2004), and Hirzberger and Wiehr (2005) have clearly observed the coexistence of BPs and faculae at $\mu \sim 0.78$. This suggests the validity of our classification method, although this should be confirmed in the future by using datasets with co-temporal magnetic vector information.

Although our CLV cannot be generalized due to the limited statistics of the present dataset and the coarse sampling of the $\mu$ range, it allows us to constrain the $\mu$ interval where the transition from BPs to faculae occurs. In this respect, The CLV also exhibits a kind of plateau in the range $0.6 < \mu < 0.78$, indicating that BPs may still be found in that range, but progressively disappear closer to the limb, probably affected by the foreground granular obscuration (Auffret and Muller 1991). This plateau can also be attributed to the slower variation of the heliocentric angle in that $\mu$ range ($36° < \theta < 54°$) compared to the centerward range $0.78 < \mu < 0.97$ ($13° < \theta < 41°$). Conversely, faculae appear to be present at all disk positions, except for the inner third of the disk where $\mu > 0.9$. Hence, by contrast to full-disk images in which faculae patches are only prominent closer to the limb, at high resolution faculae are conspicuous features of active-region plages at all disk
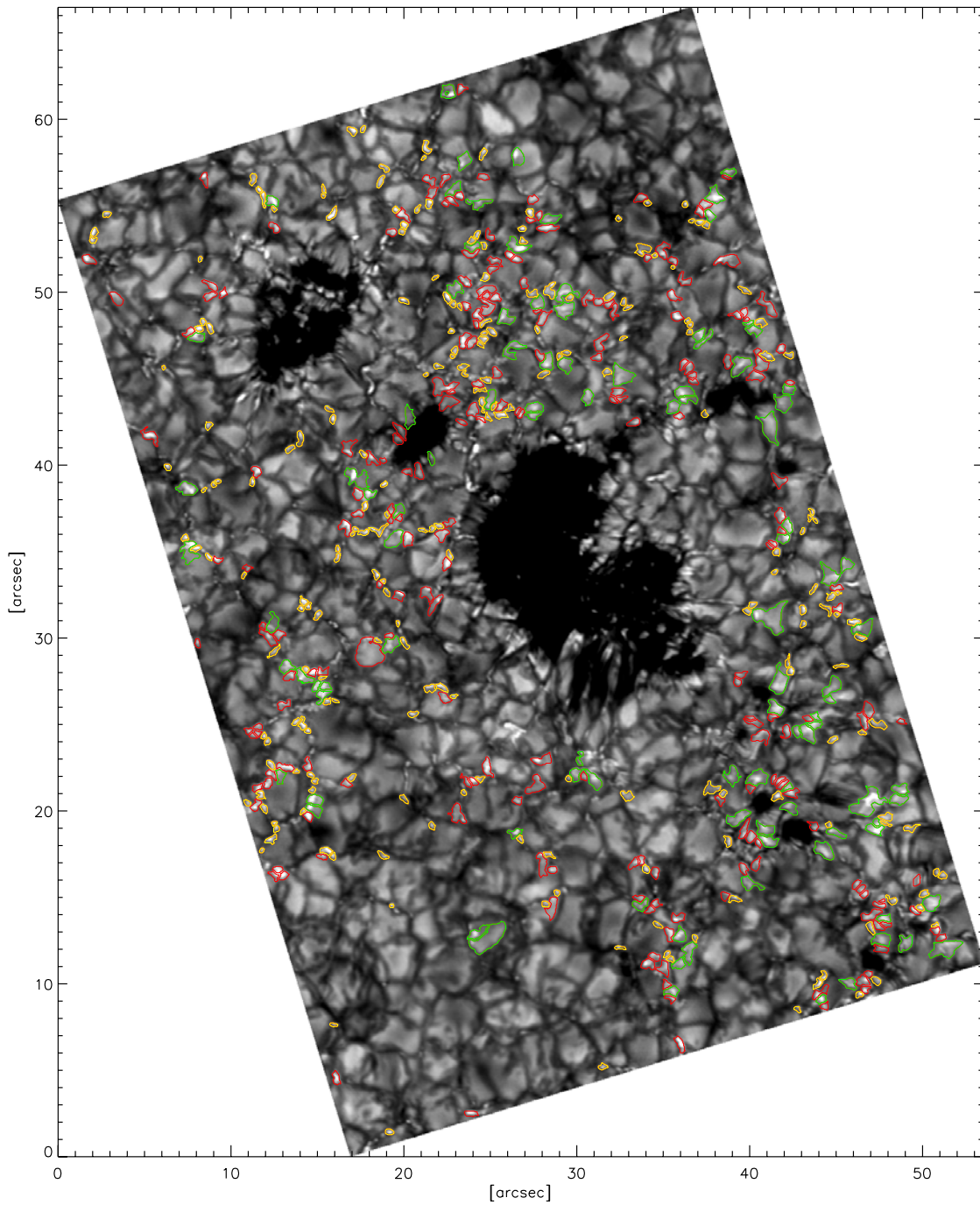
Figure 2.11: G-band image at $\langle\mu\rangle = 0.97$ (the same as in Fig. 2.1), with the overlaid contours of the features classified using the reject option. The faculae are contoured in green, the BPs in yellow and the rejected features in red. The contours correspond to the border of the features as defined by the segmentation map (corresponding to the lowest MLT level $C_G = 0$). Tickmarks are in arcseconds.
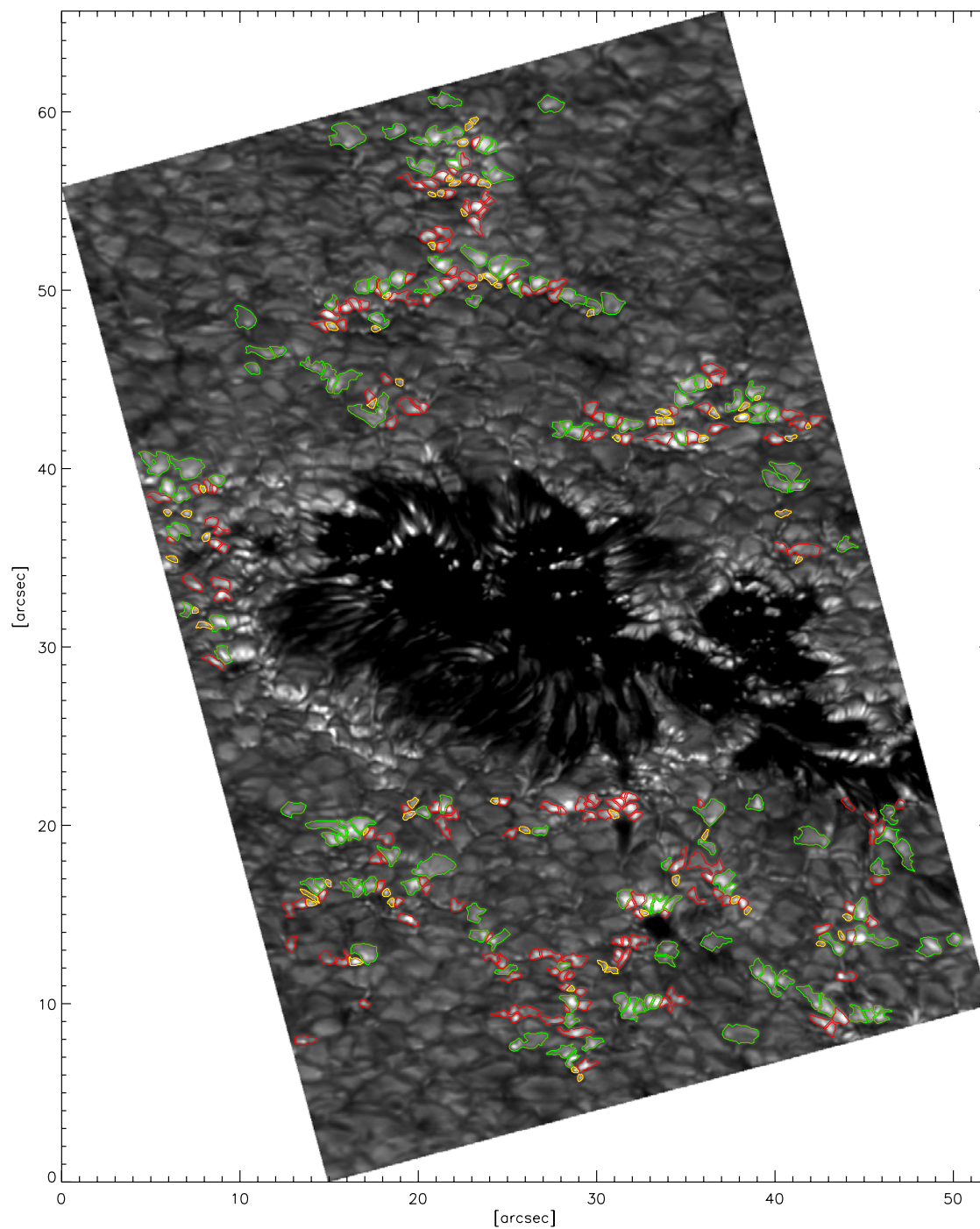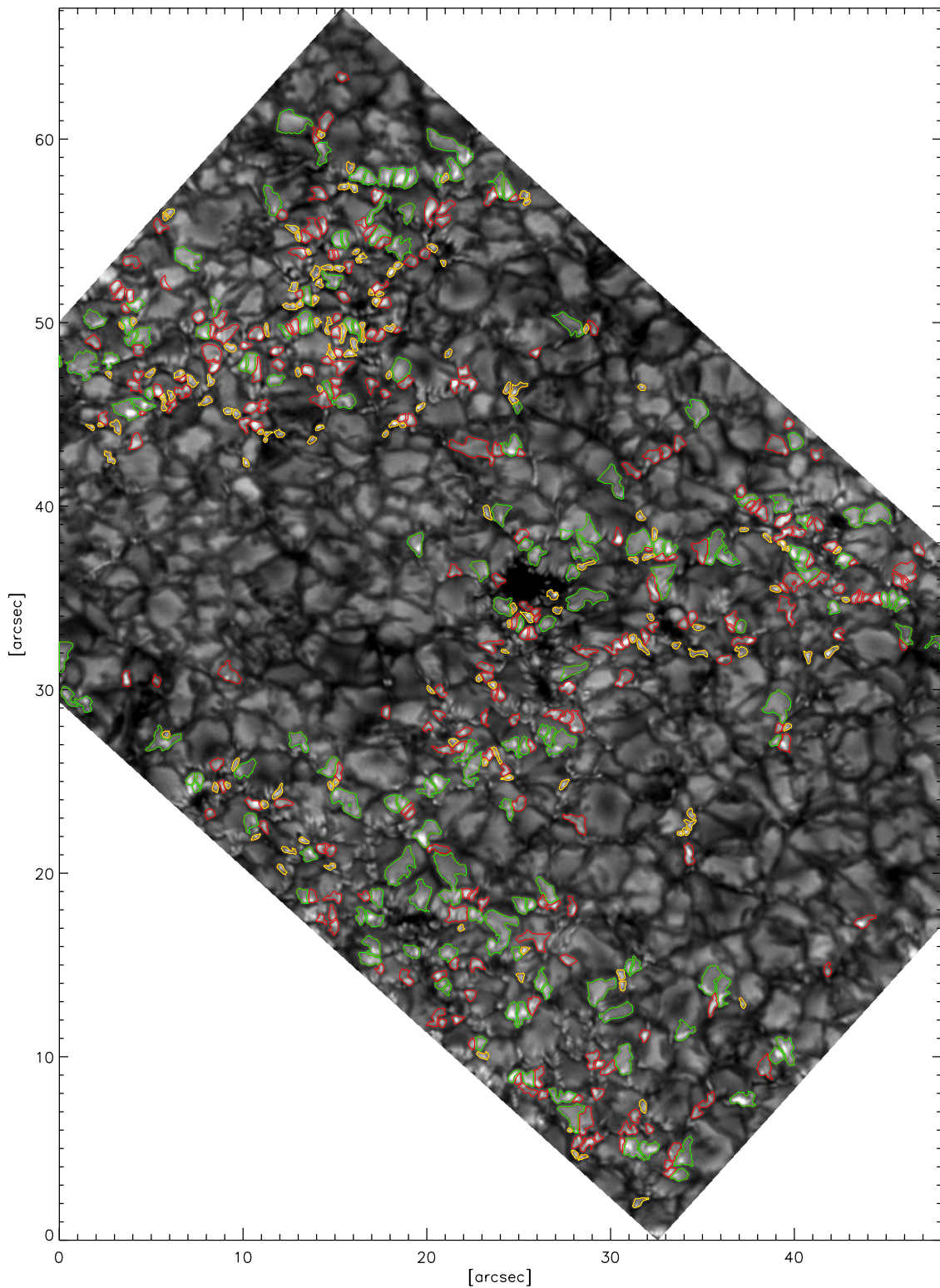
Figure 2.12: G-band image at $\langle \mu \rangle$ = 0.6 (the same as in Fig. 2.2), with the overlaid contours of the features classified using the reject option (see caption of Fig. 2.11).

Figure 2.13: G-band image at $\langle\mu\rangle = 0.9$, with the overlaid contours of the features classified using the reject option (see caption of Fig. 2.11). The original field of view has been slightly cropped horizontally for this display.

positions.

Surprisingly, even close to disk center at $\langle\mu\rangle = 0.94$, one of our images displays a large number of faculae. Faculae at large $\mu$ are sometimes seen next to pores or micropores, presumably due to the rapidly expanding field lines of these structures (see images of Berger et al. 2007 and Hirzberger and Wiehr 2005 for instance). But a closer look at this image reveals no particular presence of pores and micropores next to the faculae. Rather, it suggests that this large density of faculae relates to the presence of a prominent spot covering about two-thirds of the field of view. Its low-lying canopy field probably causes the field lines of the neighboring small-scale flux concentrations to bend away, thereby inducing faculae as the line-of-sight peers through these inclined fields and sees the hot granular material below (as pointed out by Solanki et al. 1987). Hence, this particular data point in Fig. 2.10 should be treated with caution.

The overall dominance of faculae in our dataset as well as the presence of BPs at relatively small $\mu$ values ($\mu \sim 0.6$) cannot be understood in terms of the conventional "hot wall" picture, if we consider only vertical flux tubes and varying viewing angles with disk position. The most straightforward alternative is to invoke inclined fields, whereby BPs would arise from flux tubes aligned along the line of sight and faculae from flux tubes inclined with respect to it. Assuming that the features classified as BPs around $\mu \sim 0.6$ are indeed the signatures of flux concentrations roughly aligned along the line of sight, this suggests that in addition to a large population of magnetic features inclined by $5 - 15°$ to the vertical (giving rise to the dominance of BPs at $\mu \sim 0.97$), there is an extended tail of magnetic features with a larger inclination (possibly reaching up to $\sim 50°$, according to Fig. 2.10). For comparison, Stangl and Hirzberger (2005) obtained field inclination angles as large as $37°$ for BPs in a network region, deduced from static measurements of the radial displacement between the maxima of the Fe I 6302.5 Å magnetic field map and line core intensity (assuming straight magnetic field lines). Note that larger angles are not excluded from their statistics, but could not be distinguished from misinterpretations of differential image distortions. Using Milne-Eddington inversions of active regions plages spectra, Martínez Pillet et al. (1997) determined the distribution of the magnetic field vector zenith angle. Their distribution features a mode value close to $10°$, with a tail of highly inclined fields. The authors claimed that these high inclinations mostly correspond to weak fields, yet the inclination maps were not compared with continuum brightness to check the eventual correspondence with bright features. This tail may partly copprespond to the BPs seen at small $\mu$. Recently, magnetic field vector LOS-inclinations have been retrieved specifically for a sample of BPs in a sunspot moat, using height-independent polarimetric inversions of IR and visible lines (Fe I, Ti I) , compared with a G-band BP segmentation map (Beck et al. 2007). The results are nevertheless similar to Martínez Pillet et al. (1997): the obtained distribution also has a mode around $10°$, and a long tail covering all angles up to horizontal fields is still present. All these results indicate that magnetic flux concentrations are prone to a rather wide range of inclinations, thus allowing faculae to be observed at all disk positions. Conversely, the alignment of flux tubes along the line of sight is less likely off-disk center, and is less subject to give rise to BPs due to the increasing foreground granular obscuration when the limb is approached.

As mentioned above, strongly inclined fields could be induced by the divergent field lines of larger flux structures, forcing the surrounding smaller ones to bend. However, this effect appears minor in our images, as one notices no clear influence of large pores

or spots on the number and preferential direction of surrounding faculae near disk center (see Fig. 2.11). In addition, the image at $\langle\mu\rangle = 0.9$ (Fig. 2.13) is free of spots, but nonetheless contains a large number of faculae. Finally, we are not observing either faculae concentrations at the periphery of plages, that would indicate the repulsive action of clustering small flux tubes. Rather, faculae seem rather homogeneously distributed in the images where $\langle\mu\rangle > 0.78$ (for smaller $\langle\mu\rangle$, faculae dominate in the whole FOV because of the inclination of the line-of-sight). As a plausible mechanism to produce inclined fields, we are led to consider the swaying motion of flux tubes. The movies of faculae dynamics obtained by De Pontieu et al. (2006), showing their consecutive fading and brightening on the granular evolution timescale, sometimes even taking BP-like appearances, support this idea. Such swaying motions have been reproduced in the 2D magnetoconvection simulations of Steiner et al. (1998), with flux sheets bending back and forth with angles up to 30°. This value as well as the vigor of the simulated buffeting motions are dependent on the ratio of the kinetic energy density of the convective flow to the magnetic energy density, and are influenced by the chosen boundary conditions (impermeable box with vertical flux at the boundaries). However, these strong swaying motions have not yet been reported in 3D MHD simulations, such as those of Vögler et al. (2005). Finally, large field inclinations could also be related to the recently-observed "transient horizontal fields" emerging in plage regions (Ishikawa et al. 2008).

From here on, we discuss the assets and weaknesses of the proposed mehod, as well as its applicability. A key point of the method resides in the orientation of individually segmented features to retrieve characteristic profiles (see Sect. 3.3). This procedure makes the method applicable at different $\langle\mu\rangle$ (due to the diverse orientations of BPs and faculae), and thereby offers the possibility of studying the transition from BPs to faculae as $\mu$ varies. For its optimal efficiency, the orientation procedure requires the preliminary segmentation of groups of BPs and striated faculae into individual components (here by the use of MLT). With the aim of studying the transition between both types of features, such a decomposition implicitely relies on the assumption that these individual components correspond to different single magnetic features, and the resulting CLV is meaningful under this assumption only. In the considered $\mu$ range at least, the orientation process makes the discriminant parameters roughly $\mu$-invariant, thus allowing LDA to be applied to the whole dataset at once (cf. Sect. 2.3.3). LDA itself has the advantage to be fairly simple to implement, and to assume little on the distribution properties of the discriminant parameters (except the rough symmetry of the density functions and similarity of the covariant matrices, see Sect. 2.3.4). However, it requires the careful preselection of a training set (and thus the manual classification of part of the features). This is a crucial step, for it can potentially bias the classification if the training set is not representative of the actual populations. In particular, if the method is to be applied on another dataset, the training set selection must be repeated (as well as the subsequent steps of the method thereof), unless the new dataset has been obtained under similar conditions (spatial resolution, wavelength, $\mu$ range). But the principal weakness of the current method lies in the use of mere photometric information, allowing only a limited number of discriminant parameters to be defined. This induces the following pitfall: faculae "sitting" on very small granules (fragments, abnormal granulation) are basically indistinguishible from BPs as far as our parameters are concerned. Several instances appear in Figs. 2.12 and 2.13, where such small faculae are either rejected or misclassified. The method could be improved by

the inclusion of discriminant parameters coming from polarimetric maps, provided that BPs and faculae exhibit sufficiently different magnetic properties. Care should be taken, however, if the aim is to investigate the magnetic properties of BPs and faculae, as the results would then be biased by a classification relying on similar properties.

We conclude by drawing the attention on precautions that should be taken in applying our method to other datasets. Having a fairly homogeneous and high spatial resolution is an essential requirement, as the values of all parameters $A$, $\Delta$ and $\nabla$ depend on it. A variable resolution would cause the values of the parameters to vary throughout the dataset (between different images or even across the field of view), thus preventing a well-defined discriminant variable and a unique BP/faculae threshold to be obtained. We mention that for a dataset with a constant but different resolution, the method would in principle still be valid, but the values of the parameters and of the class threshold would differ. However, degrading datasets of variable resolution to a constant lower one would reduce the contrast of features (loss of statistics due to the contrast threshold), and blur the local contrast depressions, so that it would become difficult to separate adjacent BPs and faculae striations. The method would also loose in efficiency due to the misorientation of merged features (cf. Sect. 3.3). Therefore, our photometric method is best suited for seeing-free high-resolution datasets (such as will be provided by the SUNRISE mission, Gandorfer et al. 2007). Finally, care should be taken in applying unchanged the herein-derived discriminant $F$ and its threshold value to other datasets. If the current method is applied to a dataset of slightly different resolution (or with a different amount of straylight), wavelengths (e.g. CN-band, Zakharov et al. 2007) or $\mu$ range, the values of the segmentation thresholds should first be adapted (the same holds for the identification criteria of the "grey-lane" BPs), and the training set selection must then be repeated (as well as the subsequent steps of the method thereof). Under different conditions, the ensuing values of the discriminant parameters will be different, and consequently LDA will yield a different linear combination for the discriminant variable and a different threshold.

## 2.6   Summary

We have developed a photometric method based on Linear Discriminant Analysis (LDA) to discriminate between individual Bright Points (BPs) and faculae, observed at high resolution over a range of heliocentric angles. We first demonstrated the feasibility of an automated segmentation for both individual BPs and faculae at various disk positions, based on joint G-band and continuum photometric information only. For each segmented feature, a "characteristic G-band contrast profile" was retrieved along a specific direction, by properly orienting the feature using its "contrast moment of inertia". Three physical parameters were then identified to be good discriminants between BPs and faculae at all disk positions of our dataset: the width and slope of the contrast profiles, as well as the apparent area defined by the segmentation map. Linear discriminant analysis was then performed on a visually-selected reference set of BPs and faculae, yielding a single linear combination of the parameters as discriminant variable for all disk positions. Using an appropriate threshold and rejection range on this variable, all the segmented features were ultimately classified and the relative fractions of BPs and faculae at each disk position of our dataset were computed. The resulting CLV of these fractions is mostly faculae-

dominated except for $\mu > 0.9$, i.e. close to disk center. This is in agreement with previous observations, thus suggesting the validity of the presented method. We propose that these ubiquitous faculae are produced by a hot-wall effect through *inclined fields*. As we do not observe a significant influence of pores and spots on surrounding faculae, but rather a homogeneous distribution of faculae in the images, we speculate that these inclined fields could be produced by swaying motions, or could be related to the horizontal fields detected by Ishikawa et al. (2008) in active regions.

# 3 Contrast and morphology analysis of bright points and faculae

Near the highest present-day spatial resolution ($\sim 0.''1$), Bright Points (BPs) are found to coexist with faculae in images, while the latter are often resolved as adjacent striations. Understanding the properties of these different features is fundamental to carry out proxy magnetometry. To shed light on the relationship between BPs and faculae, we studied them separately after the application of our classification method (described in Chap. 2) on active region images at various heliocentric angles. In this Chapter, we explore different aspects of the photometric properties of BPs and faculae, namely their G-band contrast profiles, their peak contrast in G-band and continuum, as well as morphological parameters.

## 3.1 Introduction

Solar photospheric Brights Points (BPs) and faculae are known to be the bright radiative signatures of small-scale kilo-Gauss (kG) magnetic flux concentrations near disk center and near the limb (Mehltretter 1974, Wilson 1981), respectively. Since they can be observed in broad spectral bands with short exposure times ($\sim 10$ ms), so that the atmospheric aberrations are frozen in the image, BPs and faculae play an important role in indirectly tracing those flux concentrations at high spatial and temporal resolution (Schüssler 1992). Yet the interpretation of these observations requires a deeper understanding of the phenomena responsible for the appearance of BPs and faculae, in view of performing actual "proxy magnetometry".

According to the basic "hot-wall" picture (Spruit 1976), BPs are seen when the line of sight (LOS) is parallel to the flux tube axis, i.e. directed toward the depressed "bottom" of the optical depth unity surface inside the tube, whereas faculae arise from an inclined view on the hot granular "wall" of that surface (see Chap. 2 for more details). Provided that most kG flux tubes are vertical due to buoyancy, they are mostly viewed from overhead at disk center and obliquely near the limb. Recently, this basic picture has been confirmed in its salient points by 3D radiative MHD simulations, which were able to reproduce BPs at disk center (Schüssler et al. 2003, Shelyag et al. 2004), and faculae near the limb (Keller et al. 2004, Carlsson et al. 2004). However, the diagnostics of the resulting synthetic images reveal remaining quantitative discrepancies with the observations regarding the peak contrast values, sizes and "striated appearance" of faculae (Keller et al. 2004, Steiner 2007).

On the observational side, the classical approach to test and constrain the "hot-wall"

model of BPs and faculae has been to study the Center-to-Limb Variation (CLV) of the contrast. According to that model, the contrast varies from center to limb as the hot wall becomes ever more visible (Spruit 1976), but the many measurements of "facular contrast" CLVs (meant as the contrast of all photospheric brightenings, i.e. of BPs and faculae together) give rather controversial results (see Steiner 2007, for a review). The presence of different proportions of BPs and faculae in the datasets could possibly play a role. Except for the "extreme limb" (heliocentric angles > 60°), high-resolution images indeed disclose mixtures of BPs and faculae (Hirzberger and Wiehr 2005, Berger et al. 2007), with increasing fraction of faculae toward the limb (see Chap. 2). The coexistence of BPs and faculae at the same disk position could be explained by the inclination of the fields with respect to LOS, whereby BPs would be induced by flux tubes aligned along the LOS and faculae by inclined flux tubes.

Moreover, it is not clear either whether the BPs and faculae seen at different heliocentric angles are manifestations of similar magnetic features (field strength, sizes). Early high-resolution observations raised the suspicion that faculae (referred to as "facular granules") were the signatures of bigger magnetic features than BPs (see review of Muller 1985). Such a suspicion was supported by 2D MHD calculations which showed that small flux tubes were mainly bright at the center of the disk (Deinzer et al. 1984) while larger ones brightened mainly near the limb (Knölker and Schüssler 1988). At the highest achievable spatial resolution of close to 0.″1, however, facular granules are found to break into smaller "striations", seemingly associated with gaps of reduced field strength (De Pontieu et al. 2006, Berger et al. 2007). This morphological change of faculae at higher resolution raises new doubts, and to our knowledge, there has been no systematic comparison of the properties of these facular elements with those of BPs.

To bring new clues about their observational properties, we propose to tackle the problem of BPs and faculae separately, using the following approach on high-resolution images of active regions at several heliocentric angles. First, previously segmented bright "magnetic" features are sorted as BPs or faculae. Then, their contrast and morphology is analyzed separately. While Chap. 2 gave a detailed account of our classification method, we here focus on the second point and address the following specific questions:

- How do the contrast and morphology of BPs and faculae differ?

- How do the photometric properties of these two classes of features vary from center to limb?

The goal of this Chapter is not to provide definite answers, but rather to take different approaches to study the relationship between BPs and faculae, in order to suggest directions for future research. We first analyzed the information contained in G-band contrast profiles of BPs and faculae in Sect. 3.3. Then, we considered and compared the values of G-band and continuum contrast of those features in Sect. 3.4. Finally, Sect. 3.5 presents a characterization of the morphology of individual BPs and faculae elements. Although our photometric-based classification method is not yet fully calibrated (in absence of magnetogram data, see Chap. 2), the statistical results do provide fresh information, allow a comparison with literature values and provide new constraints on models and MHD simulations.

# 3.2   Detection and discrimination of BPs and faculae

## 3.2.1   Dataset

Our dataset consists of simultaneous G-band ($430 \pm 0.5$ nm) and continuum ($436 \pm 0.5$ nm) filtergrams of active regions, recorded at the 1m–Swedish Solar Telescope (SST). They cover seven disk positions in the range $0.56 \leq \langle \mu \rangle \leq 0.97$ (see Table 3.1), where $\langle \mu \rangle$ denotes the center of their fields of view (FOV). At each disk position, only one to three image pairs recorded at instants of best seeing were selected, and reconstructed by phase-diversity. The resulting images reach almost diffraction-limited quality (angular resolution $\sim 0.''1$, see Chap. 2 for examples). For each image pair, the brightness contrast was defined relative to the mean intensity $\langle I \rangle_{\mathrm{QS}}$ of a selected "quasi-quiet" area, cospatial in G-band and continuum, as $C = (I - \langle I \rangle_{\mathrm{QS}}) / \langle I \rangle_{\mathrm{QS}}$. The G-band and continuum contrast are herein subscripted $C_{\mathrm{G}}$ and $C_{\mathrm{C}}$.

## 3.2.2   BPs and faculae segmentation

The principles and details of the segmentation algorithm are presented in Chap. 2. In brief, a Multi-Level-Tracking (MLT) segmentation (Bovelet and Wiehr 2001) was first carried out on the G-band images, after the application of a high-pass spatial filter. The MLT levels were finely spaced in order to resolve groups of BPs and faculae striations into *individual elements*. Then, we removed the segmented features that did not contain a minimum of 5 pixels with $C_{\mathrm{G}}$ above a given threshold, $C_{\mathrm{G,t}}$, and $C_{\mathrm{G}} - C_{\mathrm{C}}$ above another threshold, $C_{\mathrm{diff,t}}$. The choice of these thresholds relies on the brightness excess of bright "magnetic" features in G-band compared to continuum (Berger et al. 1998, Shelyag et al. 2004). Because this G-band brightness excess decreases towards the limb while the absolute contrast increases, $C_{\mathrm{G,t}}$ was raised in a systematic way for lower $\langle \mu \rangle$ (see Chap. 2). In contrast, $C_{\mathrm{diff,t}}$ was kept constant for all disk positions, as granulation shows only little G-band contrast excess regardless of $\langle \mu \rangle$.

## 3.2.3   Classification as BPs and Faculae

In order to classify the segmented features as BPs and faculae, we developed a method based on *Linear Discriminant Analysis* (LDA, Fischer 1936), using a selected reference sample of features ("training set") with chosen discriminant parameters (see Chap. 2 for details). The training set consisted of 200 BPs and 200 faculae, selected by visual inspection at 5 different disk positions.

   To obtain discriminant parameters for LDA, we retrieved G-band contrast profiles along directions specific to each feature, such that these profiles well characterize BPs and faculae. To this end, each feature was oriented in a local coordinate frame $x/y$, corresponding to the principal axes of its "G-band contrast moment of inertia" (see Chap. 2 for details). Averaged G-band contrast profiles were then extracted along $x$ and $y$, restricted to their positive contrast values, and the smoothest of these profiles was designated as the *characteristic profile*. We emphasize that these profiles were retrieved *from the spatially-filtered images*, to allow the definition of the same reference level ($C_{\mathrm{G}} = 0$) for the characteristic profiles of all features. Figure 3.1 gives an example of a feature oriented in its $x/y$

Table 3.1: Classification results at each $\langle\mu\rangle$ of our dataset, where $\langle\mu\rangle$ refers to the value at the center of the field of view of the images. $N_{tot}$ and $N_{rej}$ are the total number of segmented features and the number of rejected ones (not classified). $N_{bp}$ and $N_{fac}$ stand for the number of classified BPs and faculae, while $N_{bp}^{\dagger}$ and $N_{fac}^{\dagger}$ are the numbers of BPs and faculae used for the contrast CLVs (see Sect. 3.4.1).

| $\langle\mu\rangle$ | $N_{tot}$ | $N_{rej}$ | $N_{bp}$ | $N_{fac}$ | $N_{bp}^{\dagger}$ | $N_{fac}^{\dagger}$ |
|---|---|---|---|---|---|---|
| $0.97 \pm 0.003$ | 1123 | 421 | 484 | 218 | 385 | 180 |
| $0.94 \pm 0.003$ | 447 | 167 | 113 | 167 | 80 | 139 |
| $0.9 \pm 0.005$ | 561 | 249 | 150 | 162 | 148 | 158 |
| $0.78 \pm 0.01$ | 346 | 132 | 60 | 154 | 59 | 154 |
| $0.63 \pm 0.01$ | 947 | 389 | 130 | 428 | 130 | 428 |
| $0.6 \pm 0.01$ | 697 | 312 | 109 | 276 | 109 | 276 |
| $0.56 \pm 0.01$ | 294 | 131 | 25 | 138 | 25 | 138 |
| all | 4415 | 1801 | 1071 | 1543 | 936 | 1473 |

frame, as well as the retrieved averaged profiles in $x$ and $y$ and its characteristic profile. The width and the mean slope at the edges of these characteristic profiles were found to be suitable discriminant parameters, together with the feature area defined by segmentation (see Chap. 2 for the definition and "discriminant power" of these parameters).

LDA was then carried out in order to find a unique discriminant variable as linear combination of the above parameters, and such that it would best discriminate the training set classes according to Fischer's criterion (Fischer 1936). By choosing a judicious threshold on that variable, all the segmented features at each disk position of our dataset were ultimately classified as BPs or faculae. To lower the rate of misclassifications and eliminate "intermediate features" (i.e. those which are hardly identifiable as BPs or faculae), the features whose value of the discriminant variable were contained within a given range about the threshold were left unclassified (this range was chosen such as to reject an equal fraction 0.2 of the BPs and faculae of the training set).

The results of this classification with rejection are summarized in Table 3.1. As a complement, Fig. 3.2 shows the contours of classified features in subfields extracted at various $\langle\mu\rangle$, thereby giving a visual impression of which features were classified as BPs and faculae, and the variation of their appearance with $\langle\mu\rangle$. It should be stressed that our classification relied on purely photometric parameters, and therefore can only sort features *appearing* rather as BPs or as faculae.

## 3.3   Analysis of contrast profiles

To begin with, we investigated the orientation, width and shape of the G-band *characteristic profiles* of the classified BPs and faculae. These profiles have the particularity to characterize the spatial variation of the contrast along a *feature-specific* direction (after orienting the features according to their "contrast moment of inertia", see Sect. 3.2.3). As this direction was chosen to yield characteristic profile shapes for BPs and faculae, the characteristic profiles are good candidates for comparison with radiative transfer cal-
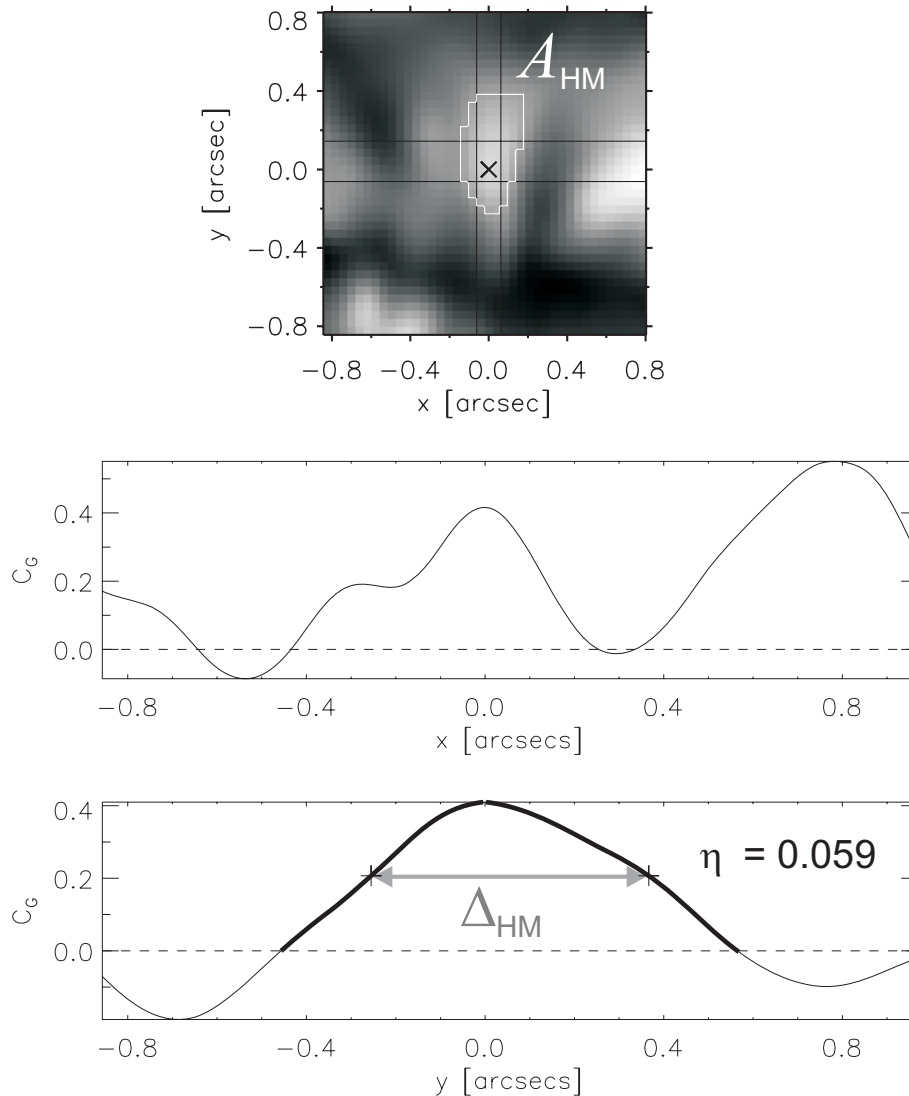
Figure 3.1: Example of local frame orientation and G-band contrast profiles of a facula located at $\mu \sim 0.9$. Top window: Orientation of the feature in its local $x/y$ coordinate frame. The black lines delimit the pixels having $C_G \geq 0.9C_{G,max}$ used for profile averaging. The pixels having $C_G \geq 0.5C_{G,max}$, with total area $A_{HM}$ (see Sect. 3.4.3), are contoured in white. Lower panels: Average G-band profiles along $x$ and $y$. All the $x/y$ profiles were cubic spline-interpolated by a factor 10 for the correct comparison of their smoothnesses in the choice of the characteristic profile. The retrieved *characteristic profile*, in this case chosen along y, is overplotted in thick. $\Delta_{HM}$ represents its width at half-maximum ($C_G = 0.5C_{G,max}$). The value of the skewness $\eta$ of the characteristic profile is indicated (see Sect. 3.3.3).
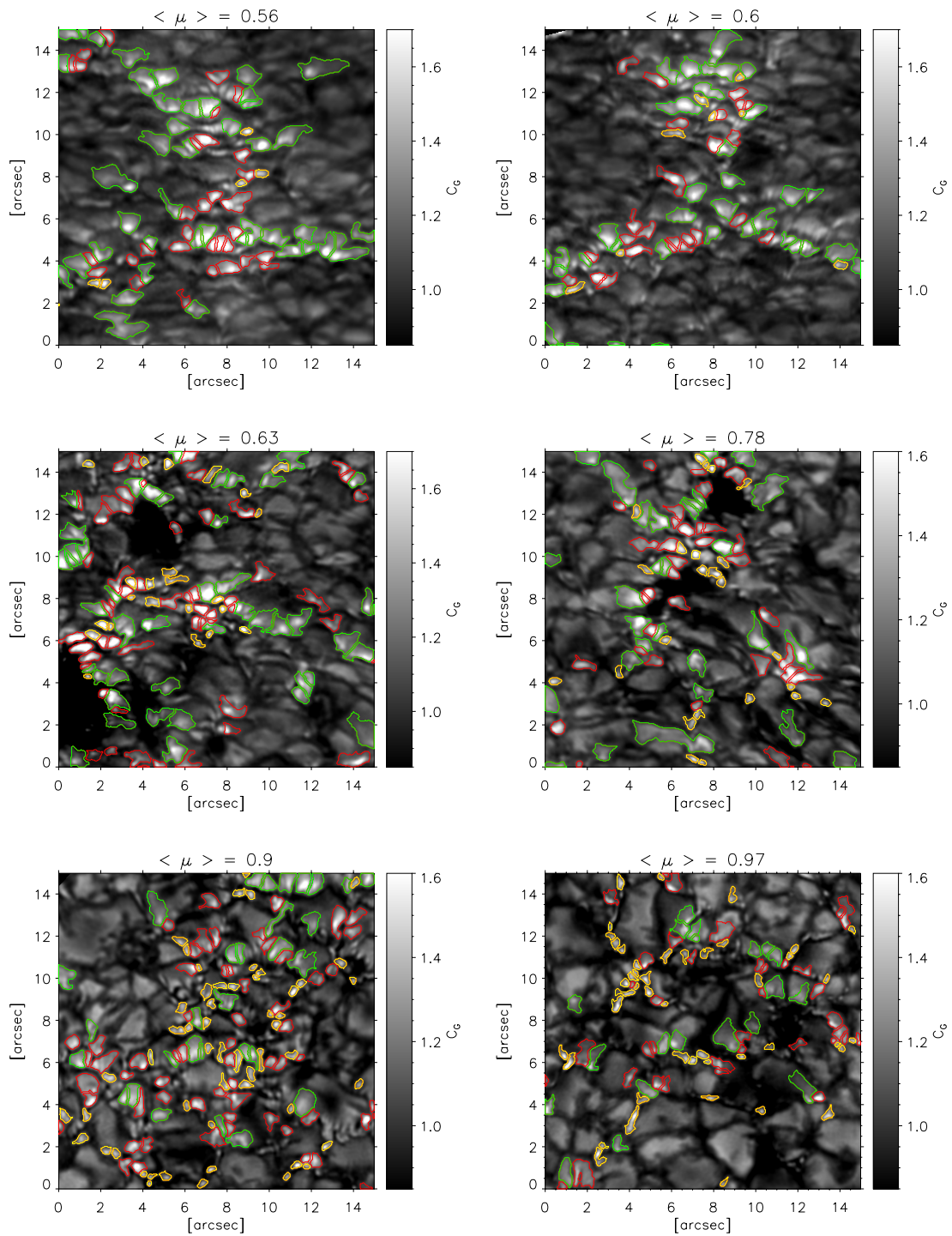
Figure 3.2: Subfields extracted from the G-band images at various $\langle \mu \rangle$, illustrating the CLV of the appearance and relative proportion of the features classified using the reject option. The faculae are contoured in green, the BPs in yellow and the rejected features in red. The contours correspond to the border of the features as defined by the segmentation map (corresponding to the lowest MLT level $C_G = 0$). The direction of the closest limb is towards the top for all subfields.
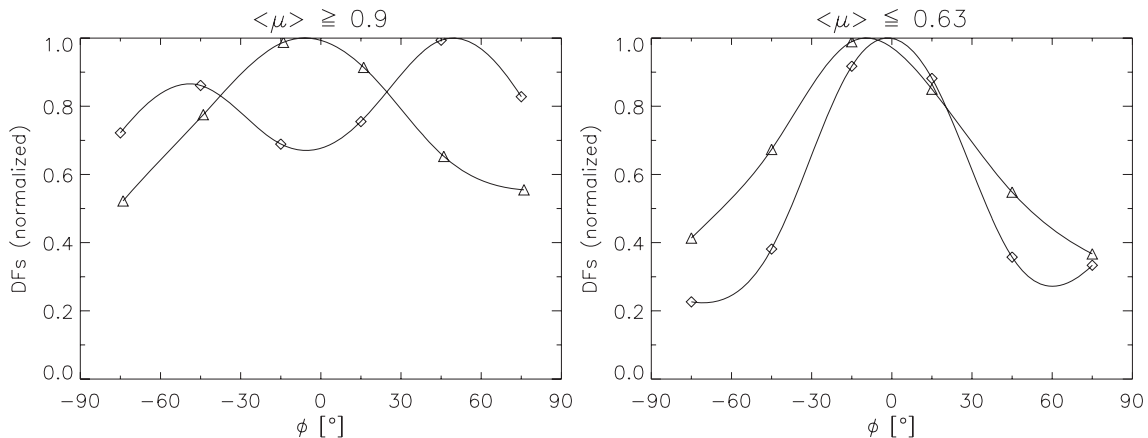
Figure 3.3: Left: Density function (DF) of the angle $\phi$ between the chosen axis of the characteristic profile ($x$ or $y$) and the radial direction for BPs ($\diamond$) and faculae ($\triangle$) in the "center" data ($\langle\mu\rangle \geq 0.9$). Right: Same for the "limb" data ($\langle\mu\rangle \leq 0.63$). The symbols are plotted centered in the bins. Cubic spline interpolations are overplotted as guides, and used to normalize the DFs.

culations accross 2D flux sheets (Deinzer et al. 1984, Knölker et al. 1988, 1991, Steiner 2005). In general, this direction was such that the profiles were retrieved across the short dimension of elongated BPs, and along faculae striations.

### 3.3.1   "Orientation" of BPs and faculae

To understand the coming results related to such profiles, it is instructive to determine how the direction of these characteristic profiles is distributed around the "radial" direction, i.e. the direction parallel to the radius vector joining the disk center to the closest limb. For this purpose, we defined $\phi \in (-90°, 90°)$ as the angle between the chosen direction of the characteristic profiles ($x$ or $y$ axis of its oriented local frame) and the radial direction, as illustrated in Fig. 3.6. The radial direction in our images is defined with an accuracy of 1° to 2°.

As the orientation of BPs and faculae differs at disk center and near the limb, we separated the data into a "center" group (images with $0.9 \leq \langle\mu\rangle \leq 0.97$, see Table 3.1) and a "limb" group ($0.56 \leq \langle\mu\rangle \leq 0.63$). The normalized density functions (DFs) of the BPs and faculae in these two groups are shown in Fig. 3.3.

The DF of faculae peaks close to 0° for the limb gruop, which was expected since facular brightenings are on average radially oriented near the limb due to the inclination of the line of sight (LOS). Yet, their DF exhibits a similar but broader peak for the center group. The preference for radial orientation of the profiles near disk center is probably induced by the LOS inclination as well, since the "center" data actually covers a range of heliocentric angles between 14° and 28°. The broader wings of the distribution are probably induced by inclined fields (cf. Sect. 3.1), whose orientation is unrelated to the radial direction.

The BPs near disk center have a wide distribution of orientation. The noticeable peaks at $\phi \sim \pm 50°$ here are in fact not systematic, as we verified that the shape of the DF varies from one image to the next. Surprisingly though, the characteristic profiles of

71

the BPs are dominantly radially oriented near the limb. Although this could be induced by selection effects due to the foreshortening of the intergranular lanes (elongated BPs would be preferably found in lanes perpendicular to the radial direction), it strongly hints at possible misclassifications. A careful look at the classified BPs in the images near the limb (see Fig. 3.2, $\langle\mu\rangle \leq 0.63$) reveals that despite their apparent resemblance with BPs, many of them appear to lie on the edge or on a fragment of a granule. This suggests that these limbward BPs are in fact small faculae having a BP-like appearance due to the lack of resolution. They could thus be misclassified by our purely photometric segmentation algorithm (see the Discussion in Chap. 2).

### 3.3.2   Width of BPs and faculae

Next, we investigated the width at half maximum of the characteristic profiles, $\Delta_{HM}$ (illustrated in Fig. 3.1), in order to obtain a measure of the sizes of BPs and faculae and to compare its values with the literature.

   We first retrieved the average $\Delta_{HM}$ at each $\langle\mu\rangle$, in order to obtain a CLV for BPs and faculae. As shown in Fig. 3.4 (left), the average $\Delta_{HM}$ take clearly distinct values for BPs and faculae at all $\langle\mu\rangle$, the latter being roughly twice as wide. Also, these averages are rather independent (within the standard deviations) of $\langle\mu\rangle$ (however, a slight positive trend can be noted for the BPs toward decreasing $\mu$, which can be possibly attributed to some misclassifications for $\mu < 0.63$, see Sect. 3.3.1). The difference between the BP and faculae values as well as their $\mu$-invariance stems from both our classification method and from the orientation of the characteristic profiles. The discriminant variable, on the basis of which the features are classified, is indeed essentially based on the width of the characteristic profiles of the training set, and the classification threshold on that variable was the same for all $\langle\mu\rangle$ (see Chap. 2). To illustrate the effect of the orientation of the characteristic profiles relative to the radial direction, Fig. 3.4 (right) shows the analogous CLV of the full width at half maximum (FWHM, defined as well at $C_G = 0.5C_{G,max}$) obtained from *radial* profiles. It can be seen that the $\Delta_{HM}$ values of BPs and faculae are much more constant and have less dispersion than the FWHM of radial profiles. The characteristic profiles thus allow a more robust measurement of the size of the features.

   The apparent $\mu$-invariance of $\Delta_{HM}$ justifies plotting single DFs for BPs and faculae by combining the features from all $\langle\mu\rangle$ (Fig. 3.5). The histogram of BPs can be compared to the one of Berger et al. (1995), who also retrieved G-band profiles along feature-specific directions (in their case chosen such as to minimize the width of BPs) for BPs in active regions at disk center. Interestingly, whereas the mode of our BP distribution corresponds to $\Delta_{HM} = 0\rlap{.}''18$, their histogram peaks at around $0\rlap{.}''3$. The discrepancy by almost a factor 2 is explained by the ratio of the spatial resolution between both studies (the data of Berger et al. 1995, were recorded at the 50 cm Swedish Vacuum Solar Telescope, SVST). Likewise, a recent multi-level tracking study of network BPs in the quiet Sun observed with the Dutch Open Telescope (angular resolution  $0\rlap{.}''23$ in G-band) yielded BPs "diameters" of about $0\rlap{.}''3$ (diameter of a disk equivalent to the segmented area, Bovelet and Wiehr 2008). At equal resolution than ours, Wiehr et al. (2004) and Puschmann and Wiehr (2006) retrieved the distribution of BP diameter by a MLT segmentation of G-band images from the SST. Despite their different definitions of "size", they obtain modal values of $0\rlap{.}''22$ and $0\rlap{.}''15$ respectively, similar to ours.
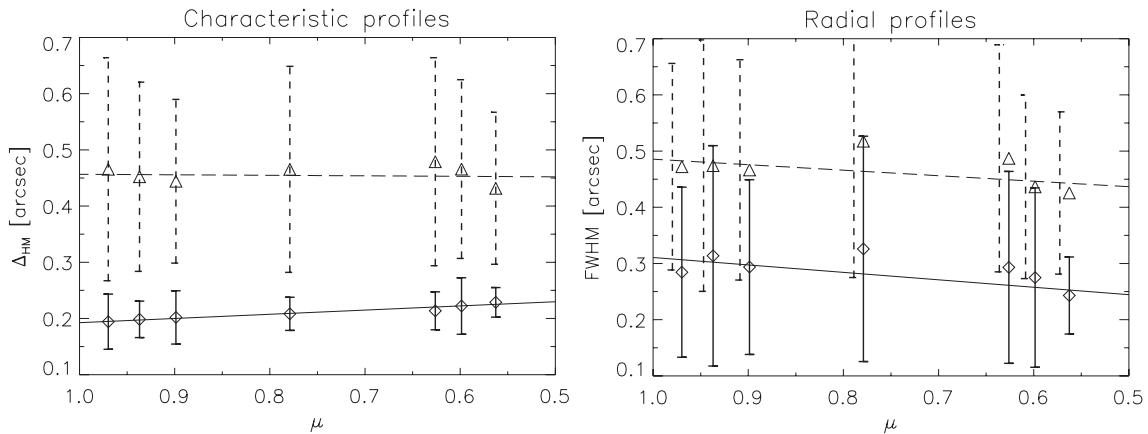
Figure 3.4: Left: Center-to-limb variation (CLV) of the average $\Delta_{HM}$ of BPs ($\diamond$) and faculae ($\triangle$), retrieved from the characteristic profiles. Right: CLV of the average full-width at half maximum (FWHM) retrieved from radial profiles. The error bars represent the standard deviations of BPs (solid) and faculae (dashed) at each $\langle\mu\rangle$. Linear regressions have been overplotted for BPs (solid) and faculae (dashed).



Figure 3.5: Normalized DFs of $\Delta_{HM}$ for all BPs ($\diamond$) and faculae ($\triangle$). For comparison, the normalized DF of all segmented features (BPs, faculae and rejected features) in the "limb" data is plotted as well (+) with a dotted cubic spline.
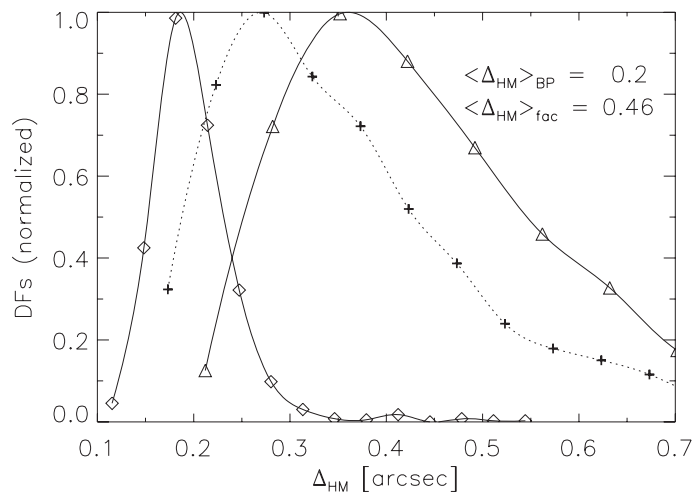
The $\Delta_{HM}$ distribution of faculae peaks at larger values of about $0\rlap{.}''36$ with an average of $\sim 0\rlap{.}''46$, which is consistent with the large extent of facular brightenings (up to $0\rlap{.}''5$ or more) reported by Lites et al. (2004). However, our average value is larger than the average value of $0\rlap{.}''37$ obtained by Berger et al. (2007), using radial cuts at $\langle\mu\rangle = 0.6$. We verified that this difference is accounted for by the inclusion of only the classified faculae in our statistics (about one quarter of all the features at $\langle\mu\rangle = 0.6$, see Table 1), whereas their measurements were performed on all their detected features. When including all segmented features of the limb data in the statistics (BPs, faculae, and rejected features), yielding the additional DF in Fig. 3.5, we obtain a similar average $\Delta_{HM}$ of $\sim 0\rlap{.}''37$.

The consistency of our distributions of $\Delta_{HM}$, obtained for the *classified* BPs and faculae at all the $\langle\mu\rangle$ of our dataset, with other studies performed exclusively on BPs (at disk center) or faculae (near the limb) indirectly supports the validity of our classification method.

73

Figure 3.6: Illustration of the sign convention for $\eta$. The $r$ and $t$ axes indicate the radial direction and the transverse one. The $x$ and $y$ axes represent the local reference frame of a given feature. Whether the characteristic profile of that feature is retrieved along $x$ or $y$, $\eta$ is counted positive is the profile is skewed toward the limb (dashed arrows). The angle $\phi$ is also represented, for the case in which the characteristic profile si along $x$.
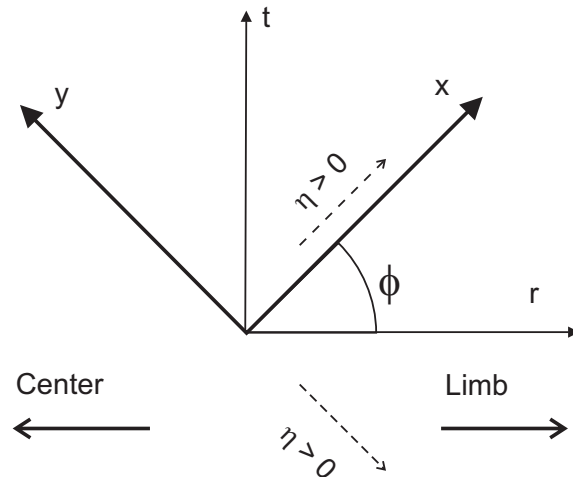
### 3.3.3   Asymmetry of facular profiles

Of particular interest for the comparison with theoretical models are the asymmetries of contrast profiles over the length of the faculae. These would pose new constraints that "any model of faculae must satisfy" (Steiner 2007). 2D flux tube models indeed predict asymmetric facular intensity profiles, with a steep intensity rise induced by the hot wall and a gentle fading on the limb side (Deinzer et al. 1984, Knölker et al. 1988, 1991, Steiner 2005). Even though radial contrast profiles of limb faculae have been earlier retrieved (Hirzberger and Wiehr 2005, Berger et al. 2007), there has been no quantitative investigation of their asymmetry.

To quantify the asymmetry of the characteristic profiles, we measured their *skewness* as the third standardized moment of these profiles:

$$\eta = \frac{\int ds \tilde{C}(s)(s - \langle s \rangle)^3}{[\int ds \tilde{C}(s)(s - \langle s \rangle)^2]^{3/2}}, \tag{3.1}$$

$$\tilde{C}(s) = \frac{C(s)}{\int ds C(s)}, \tag{3.2}$$

$$\langle s \rangle = \int ds \tilde{C}(s) s, \tag{3.3}$$

where $C(s)$ stands for the G-band characteristic profile and $s$ for the chosen coordinate of this profile ($x$ or $y$ axis of its local frame, cf. Sect. 3.2.3). To compare with flux tube models predicting a limbward asymmetry, we counted the skewness $\eta$ as positive in the direction of the characteristic profile pointing limbward (as illustrated in Fig. 3.6).

As for the study of the orientation, the "center" and "limb" data were treated separately, inasmuch as the contrast profiles suffer from different degrees of projection onto the plane of the sky. The DFs of the obtained $\eta$ of faculae and BPs are displayed in Fig. 3.7. In the limb data, the faculae profiles are clearly positively skewed (i.e. toward the limb) with an average value (and similar modal value) of 0.16 [1]. In contrast, the BPs

---

[1]We mention that similar DFs and skewnesses are obtained if using radial contrast profiles instead, since the characteristic profiles in the limb data are mostly radially oriented (see Fig. 3.3).
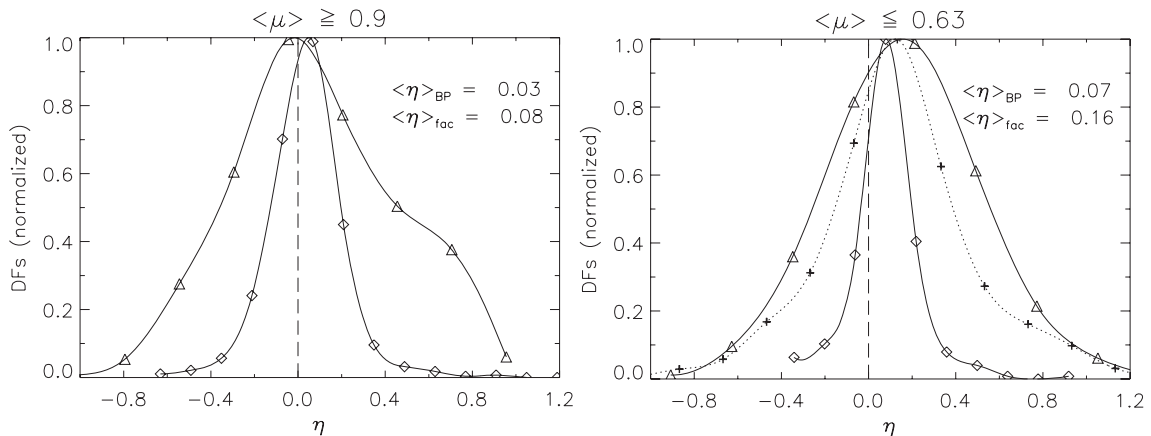
Figure 3.7: Left: Normalized DFs of $\eta$ for BPs ($\diamond$) and faculae ($\triangle$) of the center data ($\langle\mu\rangle \geq 0.9$). Right: Idem for the limb data ($\langle\mu\rangle \leq 0.63$). For comparison, the normalized DF of all features (BPs, faculae and rejected features) in the limb data is plotted as well (+) with a dotted cubic spline. As a guide, a vertical dashed line ($\eta = 0$) separates positive and negative skewness.

identified near the limb have an average value of 0.07 only. The fact that their profiles are slightly limbward skewed as well further suggests that part of these BPs are misclassified small faculae. As indication, we overplotted the DF obtained if no classification is performed, i.e. including the faculae, the BPs and the rejected features. Even without classification, the profiles are positively skewed with an average value of 0.13.

In contrast to the limb data, the faculae of the center data exhibit positive and negative values of $\eta$ in similar proportions, with an average value of 0.08. This suggests that the sign of the asymmetry of facular profiles depends the orientation of their characteristic profiles, as the latter have a wider distribution of orientation relative to the radial direction in the center data than in the limb data (see Fig. 3.3). The slight excess of positive skewness can be explained by the rather wide range of $\mu$ of the "center" images (see Table 3.1), so that the faculae are still preferably radially oriented in these images (see Sect. 3.3.1). The BPs exhibit a rather narrow distribution with a low mean value of 0.03, lower than the corresponding value near the limb. As a remark, we verified that if radial profiles are used instead of the characteristic ones, similar conclusions are obtained for faculae at disk center, but the DF of BPs becomes wider as the consequence of the random orientation of elongated BPs.

Finally, we looked at the absolute values of $\eta$ at the different $\langle\mu\rangle$ of our dataset, and compared with the case of radial profiles. The CLV of the average $|\eta|$ is given in Fig. 3.8 for both cases. It is striking that both BPs and faculae reveal remarkably constant values of $|\eta|$ with $\langle\mu\rangle$ when measured on the characteristic profiles, whereas these values fluctuate much and have larger standard deviations when measured on the radial profiles. The former are thus more robust observables to use as constraint for models. Note that for faculae near the limb ($\mu \leq 0.63$ in Fig. 3.8), the similarity between the values of $|\eta|$ of the characteristic and radial profiles is easily explained by the preferred radial orientation of the profiles. Near disk center, however, the $|\eta|$ from radial profiles are surprisingly large, which indicates that granules contribute significantly to the asymmetry
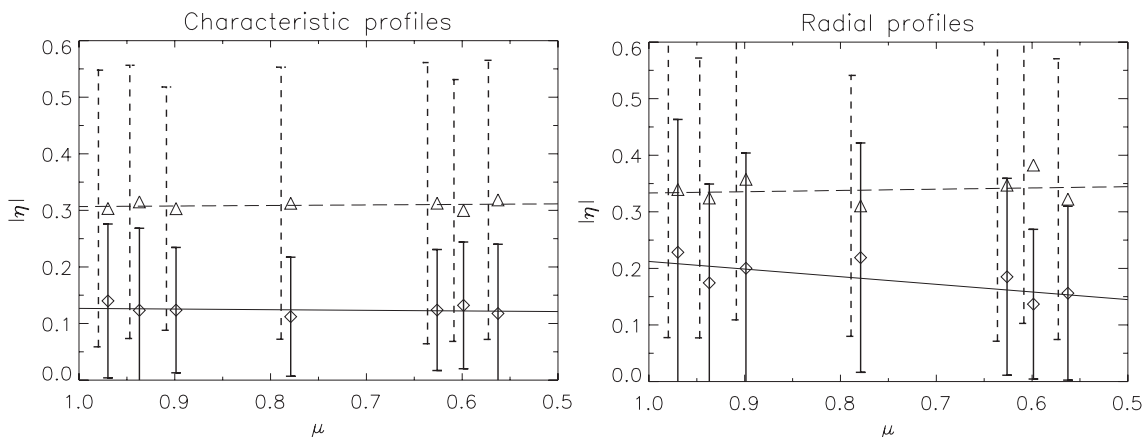
Figure 3.8: CLV of the average absolute values of $\eta$ for BPs ($\diamond$) and faculae ($\triangle$), evaluated on the characteristic profiles (left) and on radial profiles (right). Error bars: Standard deviations of BPs (solid) and faculae (dashed). The latter are left-shifted for readability. Solid and dashed linear regressions have been overplotted for faculae and BPs, respectively.

of these profiles. For BPs, the visibly decreasing trend of $|\eta|$ from radial profiles reflects the random orientation of BPs near disk center and their preferred radial orientation near the limb (possibly due to misclassifications).

## 3.4   G-band and continuum contrast

In this Section, we examine the behaviour of the G-band and continuum contrast of BPs and faculae by considering the peak values of the features, $C_{G,max}$, and $C_{C,max}$ [2] (taken at the same pixel location and measured in the non-filtered images). Quantifying the contrast of the features via their peak values rather than using averages minimizes the smearing of the BP contrast within intergranular lanes (Title and Berger 1996), and avoids mixing granulation pixels in the faculae contrast.

### 3.4.1   Center-to-limb variation

We first looked for trends in the center-to-limb variation (CLV) of the peak contrast values of BPs and faculae, averaged at each $\langle\mu\rangle$ (Fig. 3.9). To avoid a bias due to the progressive increase of the G-band threshold with decreasing $\langle\mu\rangle$ in our segmentation (see Sect. 3.2), we imposed here an equal threshold for all disk positions by requiring $C_{G,max} > 0.3$ (corresponding to the highest value of the $C_{G,t}$ threshold used in the segmentation, see Chap. 2).

Whereas the peak contrast of faculae increases towards the limb as expected in our $\mu$ range (enhanced view on the hot wall), the BPs surprisingly follow the trend of faculae, both in G-band and continuum. A straightforward explanation for this common behaviour

---

[2]In this Chapter, we used the symbol $C_{G,max}$ to refer both to the peak contrasts of the G-band characteristic profiles, measured from the spatially filtered images, and the actual peak contrast of the features used in this Section, measured in the non filtered images. The difference can be understood from the context and will be always clearly stated.
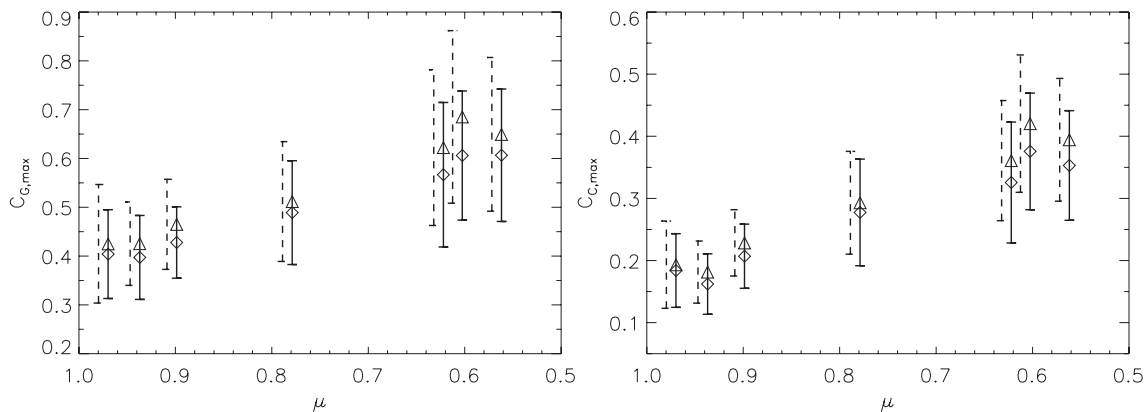
Figure 3.9: Left: CLV of the averaged G-band peak contrast $C_{G,max}$ of BPs ($\diamond$) and faculae ($\triangle$). Right: Idem in continuum, where $C_{C,max}$ was taken at the same pixel location as $C_{G,max}$. To avoid bias (see main text), only features having $C_{G,max} > 0.3$ were considered. The vertical bars represent the standard deviations of BPs (solid) and faculae (dashed), the latter being artificially left-shifted for readibility.

would be the misclassification of small faculae in the limb images ($\langle\mu\rangle \leq 0.63$). However, such misclassifications cannot account for the common contrast increase of BPs and faculae at larger $\mu$ values ($\langle\mu\rangle \geq 0.78$). Finally, note that faculae have systematically larger contrast than BPs at all $\mu$ (both in G-band and continuum), especially in the limb images, which can be due both to the hot-wall effect and the finite spatial resolution.

The similar behaviours of BPs and faculae implies that a distinction between these features would have a negligible influence in the contrast CLV of magnetic elements, at least in the considered $\mu$ range and wavelengths.

## 3.4.2   G-band–continuum relation

BPs are known to exhibit a brightness excess in G-band compared to continuum, which has been explained by the lower CH abundance in the hot and tenuous atmosphere of magnetic elements (Shelyag et al. 2004, Schüssler et al. 2003). Although faculae do exhibit larger contrasts in G-band as well, there has been no comparison of their G-band–continuum contrast relation with the one of BPs.

The relation between G-band and continuum contrast is best described by scatterplots of $C_G$ vs. $C_C$, such as performed at disk center (without BPs/faculae distinction) by Berger et al. (1998) and Shelyag et al. (2004), using observations and simulated synthetic images, respectively. As before, we divided the data between "center" ($0.9 \leq \langle\mu\rangle \leq 0.97$) and "limb" ($0.56 \leq \langle\mu\rangle \leq 0.63$), whose scatterplots of $C_{G,max}$ vs. $C_{C,max}$ are shown in Fig. 3.10 [3]. Linear regressions of the form:

$$C_{G,max} = sC_{C,max} + o \tag{3.4}$$

---

[3]Since we are not interested in directly comparing the magnitude of the contrast between different $\mu$ (unlike in Sect. 3.4.1), we included here all the data points without imposing $C_{G,max} > 0.3$. The same holds for Sect. 3.4.3.
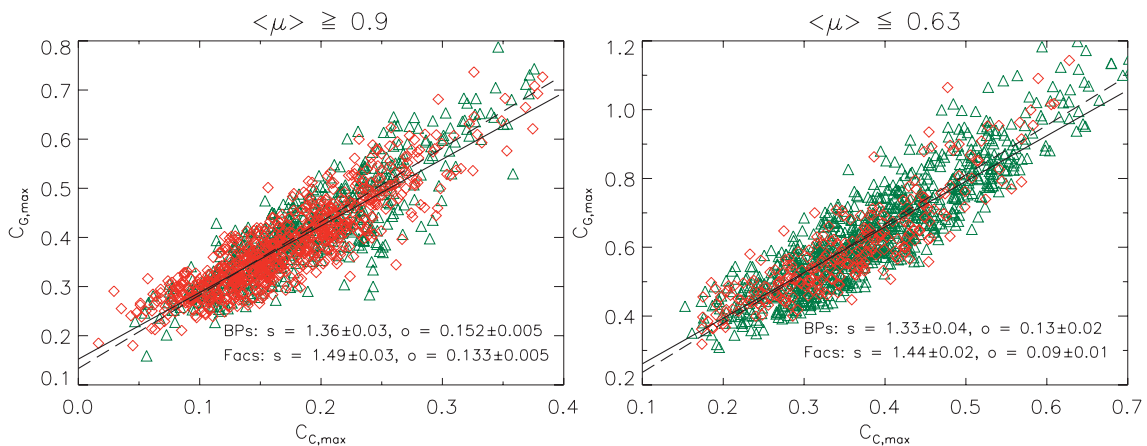
Figure 3.10: Scatterplot of $C_{G,max}$ vs. $C_{C,max}$ for BPs ($\diamond$) and faculae ($\triangle$) in the "center" images ($0.9 \leq \langle\mu\rangle \leq 0.97$) and for the "limb" images ($0.56 \leq \langle\mu\rangle \leq 0.63$). The data points of BPs and faculae were linearly-fitted separately (solid line for BPs and dashed for faculae), yielding the slopes $s$ and offsets $o$, together with their 1-$\sigma$ uncertainties (indicated by $\pm$).

were applied separately to BPs and faculae. The best fit values of the slope $s$ and the offset $o$ are indicated in Fig. 3.10, together with their 1-$\sigma$ uncertainties.

Comparing the trends of the BPs and faculae reveals that BPs have lower $s$ and larger $o$ than faculae by more than 3 $\sigma$ in both the center and limb data. Care should be taken, however, as the peak contrasts of BPs are more affected by the finite spatial resolution (Possible physical effects will be discussed in Sect. 3.6.1). The differences between the center and limb data are less obvious: both for BPs and faculae, $s$ and $o$ seem lower in the limb data, but by 1-2 $\sigma$ and 1-4 $\sigma$ only, respectively.

### 3.4.3  Size-dependence of the contrast

Because high-resolution imaging can provide "direct" measurements of the size of re-solved magnetic features (arguable off-disk center), it offers a way to directly probe the dependence of the contrast on the size of these features. By comparison with flux tube models and/or studies of contrast as a function of magnetogram signal, such measure-ments could provide valuable constraints as well as deliver a "proof-of-principle" of proxy magnetometry.

As a measure of the "size" of a feature, we considered the apparent area (projected onto the plane of the sky) of the set of pixels whose G-band contrast in the spatially filtered images exceeds half of its maximum contrast, $A_{HM}$, illustrated in Fig. 3.1 [4]. Like for $\Delta_{HM}$, using the half-maximum level for the measurement makes it independent of the peak contrast of the features.

Because of the CLV of the contrast and the geometrical foreshortening affecting $A_{HM}$ with decreasing $\mu$, we have divided the data into four intervals of $\mu$. Fig. 3.11 shows the scatterplots of $C_{G,max}$ and $C_{C,max}$ vs. $A_{HM}$ for the BPs and faculae in the four $\mu$ intervals.

---

[4]Measuring $A_{HM}$ in the filtered images reduces the dispersion due to the medium and large-scale fluctu-ations of the intensity.

In each interval, the contrast values of *all* the features (BPs, faculae and rejected) were averaged in bins of $A_{HM}$ in order to identify an overall trend. This is justified by the relatively distinct ranges of $A_{HM}$ of BPs and faculae (owing to our classification), which allow a single trend to represent both contrast behaviours.

In all $\mu$ intervals, the trends of the average $C_{G,max}$ exhibit more pronounced concave shapes than $C_{C,max}$. This is particularly visible near disk center for $0.94 < \mu < 0.98$, where the G-band trend reaches a clear peak, while the continuum trend is almost flat. Nearer the limb ($\mu < 0.65$), both the G-band and continuum trends are qualitatively more similar, and seem to differ essentially by a proportionality factor. This is consistent with the lower value of the offset $o$ of the $C_{G,max}$ vs. $C_{C,max}$ relation (making it closer to proportionality) for the limb data compared to the center data (cf. Sect. 3.4.2) [5].

Despite our segmentation of bright features only (see Sect. 3.2.2), the obtained trends bear a striking resemblance with the analogous trends of contrast as a function of "magnetogram signal" (calibrated measure of the Stokes $V$ amplitude) and apparent flux density (see Chapter 4). This similarity seems to hold both for the continuum (see Topka et al. 1992, Lawrence et al. 1993, Ortiz et al. 2002, despite the differences in wavelength) and the G-band (see Berger et al. 2007). Alike those trends, the concave shape of the trends as a function of $A_{HM}$ becomes ever more pronounced as $\mu$ decreases. In addition, the present trends peak at larger $A_{HM}$ for lower $\mu$ intervals, in the same way as the peak shifts to larger magnetogram signals. To our knowledge, such an analogy has not been unveiled before. These new results lend credit to the use of proxy magnetometry of BPs and faculae at high resolution, at least in the $\mu$ range considered here.

We shall now have a closer look exclusively on the BPs of the center data ($\langle\mu\rangle \geq 0.9$). Since BPs near disk center are thought to be the signatures of flux concentrations seen from overhead, it is expected that their contrast–size relation closely follows the predictions of flux tube models. Such models predict a decrease of the contrast with the size of the flux tubes (assuming a constant field strength), mainly because of the increasing ratio between their internal volume and the heating surface of their "walls" (Spruit 1976, Deinzer et al. 1984, Fabiani Bendicho et al. 1992). To verify this prediction, we have investigated the dependence of the $C_{G,max}$ and $C_{C,max}$ of the BPs on both $A_{HM}$ and $\Delta_{HM}$, as presented in Fig. 3.12. The latter can be considered a good proxy of the underlying flux tube/sheet width, since it is generally measured along the short dimension of the BPs (owing to the orientation of the characteristic profiles).

The behaviour of the BP peak contrasts partly deviates from the theoretical expectations, both as a function of $A_{HM}$ and $\Delta_{HM}$. Except the notable decrease of $C_{G,max}$ and $C_{C,max}$ as a function of $A_{HM}$ for the large BPs ($A_{HM} > 0.06$ arcsec$^2$), the contrast rather exhibits an increase with $A_{HM}$ for the smaller BPs. This "anomaly" could be due to the spatial resolution, affecting the $C_{G,max}$ and $C_{C,max}$ values of small BPs. This is supported by the fact that as a function of $A_{HM}$, the contrast trends are again reminiscent of the relation contrast–magnetogram signal. And since the magnetograms have a much poorer spatial resolution, the initial increase of contrast with magnetogram signal is reasonably explained by the increasing "filling factor" (fractional area of the resolution element) of unresolved features. However, true physical effects cannot be entirely discarded, in particular the possible dependence of the field strength on the size of the flux concentrations

---

[5]It can be verified that each of the present average values of $C_{G,max}$ and $C_{C,max}$ relate according to the linear relations presented in Sect. 3.4.2.

(see Sect. 3.6.2). The trends as a function of $\Delta_{HM}$ are especially intriguing, in that the contrast monotonously rises over the whole range of size (with a slight cubic shape). It is probable that the decrease of contrast toward larger cross–sectional areas of the BPs is "hidden" when viewing the data as a function of $\Delta_{HM}$, because the latter is limited to the width of intergranular lanes while the area is free to vary in the perpendicular dimension. Finally, we note that irrespective of being examined as a function of $A_{HM}$ or $\Delta_{HM}$, the shape of the contrast trends seem to be amplified in G-band with respect to continuum. As a function of $A_{HM}$, the difference between continuum and G-band is not unlike the difference between continuum and line core contrast as a function of magnetogram signal observed by Frazier (1971) (at 525 nm) and Title et al. (1992) (at 676.8 nm), and is consistent with the G-band high-resolution measurements of Berger et al. (2007) (obtained at SST).

## 3.5   Morphology

To study the morphological properties of BPs and faculae, we considered the 2D "figures" formed by the set of pixels having G-band contrast values above half of the local maximum of the segmented features (in filtered images), i.e. with $C_G > 0.5C_{G,max}$ [6]. These figures are naturally simply connected by virtue of the MLT segmentation, and their outline is by definition independent of absolute contrast values, and thus of any threshold. To minimize the spurious effect of pixellation (artificial roughness of the outline, erroneous areas and perimeters) particularly affecting small BPs, the segmented features were bilinearly-interpolated by a factor three in each direction with an additional contour smoothing, prior to the extraction of the figures. The outline of such a figure is shown in Fig. 3.13, superposed on the corresponding bilinearly interpolated feature.

In the framework of geometrical set theory, the form of figures is adequately described by a variety of "form parameters", defined as ratios independent of the position, scaling and orientation (Stoyan and Stoyan 1994). In this study, we were only interested in form parameters characterizing the "overall" and "small-scale" deviations from circularity. To characterize the global ellipticity of each feature, we considered the ellipse whose semi-major axis $a$ is given by the maximal chord length $D_F$ of its associated figure, the so-called "Ferret diameter", and whose semi-minor axis $b$ is deduced from the figure area $A$ [7]:

$$a = \frac{D_F}{2}; b = \frac{A}{\pi a} \tag{3.5}$$

The ellipticity can then be defined as:

$$f_E = 1 - \frac{b}{a} \in (0, 1) \tag{3.6}$$

This definition is indeed independent of the orientation and barely influenced by the irregularity (non-convexity) of the figure contour. Fig. 3.14a displays the mean values of $f_E$ for

---

[6]Following Stoyan and Stoyan (1994), these figures were treated as simple two-dimensional objects, thus neglecting the fact that their pixels have different contrast values.

[7]Due to the interpolation of the feature, the area $A$ of the figures considered here is not equivalent to the area $A_{HM}$ considered in Sect. 3.4.3.
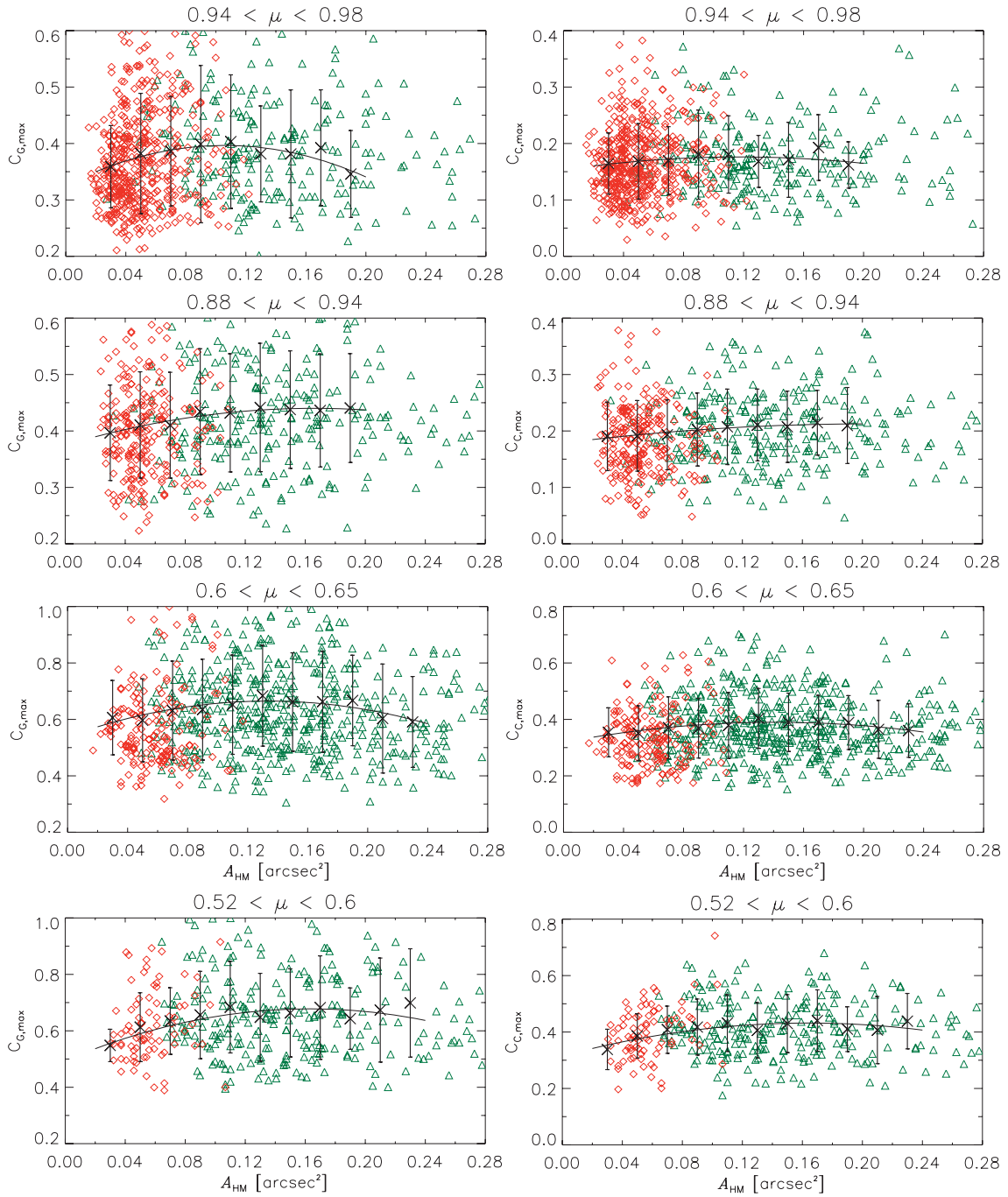
Figure 3.11: Left column: Dependence of $C_{\mathrm{G,max}}$ on $A_{\mathrm{HM}}$ in four distinct intervals of $\mu$ near disk center (upper two panels) and nearer the limb (bottom two panels). Right column: Same for $C_{\mathrm{C,max}}$. Crosses and error bars: Average and standard deviation of the peak contrast of *all* features (BPs, faculae and rejected) in bins of $A_{\mathrm{HM}}$ of width 0.02 arcsec$^2$, restricted to bins having more than 10 contrast points. Solid curve: Least-square quadratic fit of the average values (weighted by the inverses of the standard deviations). The individual data points corresponding to BPs ($\diamond$) and faculae ($\triangle$) have been overplotted.
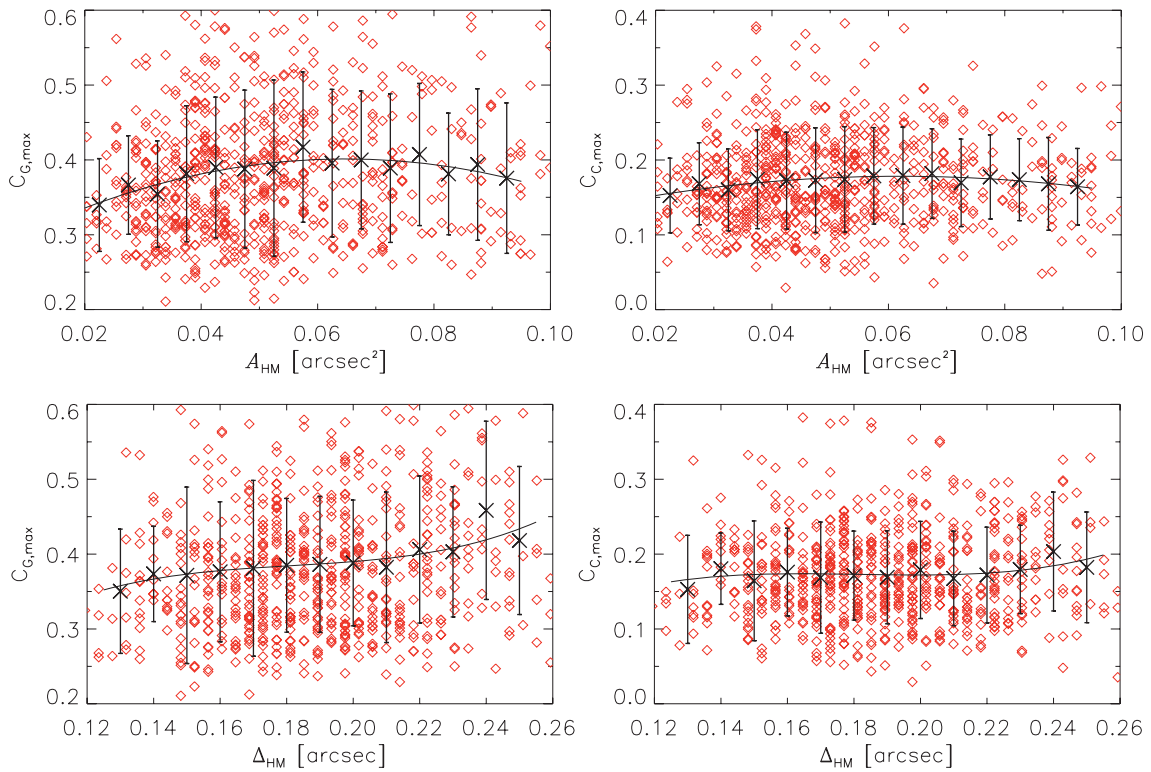
Figure 3.12: Dependence of $C_{G,max}$ (left) and $C_{C,max}$ (right) on $A_{HM}$ (upper panels) and $\Delta_{HM}$ (lower panels) for BPs in the "center" images ($\langle\mu\rangle \geq 0.9$). Crosses and error bars: Average and standard deviation of the BP peak contrasts into bins of $A_{HM}$ of 0.005 arcsec$^2$ and bins of $\Delta_{HM}$ of 0.01 arcsec. Quadratic polynomials and cubic polynomials have been fitted to the average contrasts in bins of $A_{HM}$ and $\Delta_{HM}$, respectively. Individual contrasts of BPs are overplotted ($\diamond$).

Figure 3.13: Illustration of a 2D figure used for the morphology studies. The feature is in its local $x/y$ reference frame, and its contrast spatial distribution was bilinearly-interpolated by a factor three in each direction. The boundary of the feature is defined by the segmentation map, with additional contour-smoothing. The inner contour outlines the relevant figure composed by the pixels satisfying $C_G > 0.5C_{G,max}$, and the oblique chord line corresponds to the "Ferret" diameter $D_F$.
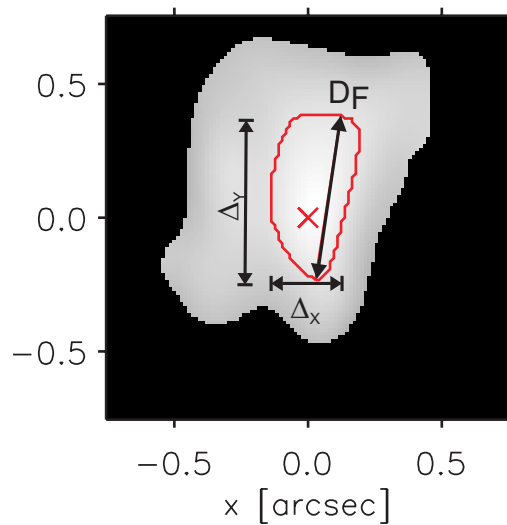
BPs and faculae at each $\langle\mu\rangle$. The values are roughly constant with $\langle\mu\rangle$, although a slight decrease towards the limb can be noticed for both BPs and faculae (possible foreshortening or spatial resolution effect). Also, whereas the average values of BPs and faculae are rather similar, the former have larger standard deviations and thus can exhibit a larger variety of global shapes.

For comparison with other studies, we computed the DFs of the "center" BPs and "limb" faculae, as shown in Fig. 3.14b. The faculae histogram can be directly compared with the one of Bovelet and Wiehr (2001), who used an identical definition of ellipticity, applied to MLT-segmented facular grains in a 658 nm continuum image at $\langle\mu\rangle = 0.54$ recorded at the SVST. Although not specified in their paper, the authors used as well a normalized threshold at 0.5 for their figures (private communication). Despite their lower statistics (only 638 faculae) extracted from only one $\langle\mu\rangle$ and their lower spatial resolution (of little influence on large structures as faculae though), their histogram is very similar to ours. The mode also corresponds to $f_E \sim 0.4$ and the distribution spans values from $f_E = 0$ to 0.8. A closer look at their results indicates that our distribution is closer to their histogram of "larger-than-average" faculae, which are more elliptical than the smaller ones. This can be due to several factors: small faculae are likely to be rejected or misclassified in our treatment, while their lower spatial resolution cause small faculae to appear more circular. The ellipticities of disk center BPs in active regions have been investigated previously by Berger et al. (1995), on G-band images from SVST. These authors used a slightly different definition, as the semi-axes ratio $a/b$ of a best-fitting ellipse to the BP shape given by their segmentation map. They thus obtained distribution with a mean value of 1.5 and a severe drop for ellipticities larger than 2. If we transform our previous definition of $f_E$ into $a/b$, we then obtain a larger mean value of 1.88, and a more extended distribution tail as well. Although the discrepancy can be partly due to the different definitions of the ellipse and the threshold-dependence of their definition (their BP contours are limited by their segmentation threshold whereas our "figures" are defined by the half-maximum level), it is most probably related to the lower spatial resolution of the SVST. Hence, whereas the ellipticities of faculae did not significantly change by increasing the spatial resolution, BPs appear more elliptical than in earlier studies, so that their ellipticities become comparable to the faculae ones.

Another useful shape ratio to quantify the deviations from circularity is the "area-perimeter ratio" defined as:

$$f_{AU} = \frac{4\pi A}{U^2} \in (0, 1) \qquad (3.7)$$

where $U$ stands for the perimeter of the figure, and $f_{AU} < 1$ for all figures other than a perfect disc. But while this definition characterizes as well the global circularity as $f_E$, it is very sensitive to small-scale deviations of convexity in the figure outline, through the second power of $U$. Having already examined the global ellipticity of BPs and faculae via $f_E$, we can then use $f_{AU}$ to address the convexity of their contour shape. The larger average values of BPs compared to faculae at each $\langle\mu\rangle$ (see Fig. 3.14c) indicates that BPs have more convex and regular shapes. This is probably a consequence of the finite spatial resolution, as BPs have much smaller sizes. In addition, the figure contours of the faculae can be more complex due to the clustering of fine striations, which are not always properly resolved by the MLT segmentation. Also, the finite resolution is probably responsible for the common increase of the average $f_{AU}$ of BPs and faculae toward lower $\mu$.

The two shape ratios presented above are strict "form parameters" through their independence on the feature's orientation. However, treating BPs and faculae as simple 2D figures neglects the distribution of contrast within the features, which contains meaningful information about their individual orientation (see Sect. 3.3.1). As all our BPs and faculae have already been oriented in a local $x/y$ frame according to their "contrast moment of inertia", we can define an new shape ratio in that frame:

$$f_{\mathrm{XY}} = 1 - \frac{\Delta_{\mathrm{x}}}{\Delta_{\mathrm{y}}} \qquad (3.8)$$

where $\Delta_{\mathrm{x}}$ and $\Delta_{\mathrm{y}}$ are the widths of the figure along $x$ and $y$, measured through the location of maximum contrast $C_{\mathrm{G,max}}$ (see Fig. 3.13). Unlike for $f_{\mathrm{E}}$, BPs do exhibit slightly larger values of $f_{\mathrm{XY}}$ than faculae (Fig. 3.14d). This difference can be attributed to the narrow contrast distribution of elongated BPs about their $y$ axis, while faculae have a flatter, more diffuse distribution (this is also the case for adjacent faculae striations due to the relatively weak contrast depressions between them). This difference was probably hindered in $f_E$, since the latter does not take into account the "orientation" of the features. Moreover, the $f_{\mathrm{XY}}$ values of faculae have much more dispersion than the BP ones, whereas it is the opposite for $f_{\mathrm{E}}$. This can be again attributed to the proper orientation of BPs (reducing their dispersion) and to the more complex shape of the faculae (as revealed by $f_{\mathrm{AU}}$), causing discrepancies between the axes of the ellipse used in the definition of $f_{\mathrm{E}}$ (3.5) and $\Delta_{\mathrm{x}}, \Delta_{\mathrm{y}}$. Hence, whereas the global ellipticity of BPs and faculae is very similar when looking at it independently of their orientation, BPs appear slightly more elongated when using a shape ratio that takes into account their contrast distribution.

## 3.6 Discussion

### 3.6.1 On the relationship between BPs and faculae

We shall here discuss some aspects of the differences and similarities between the features classified as BPs and faculae, as revealed by our analysis.

It was found that near the limb ($0.56 < \langle \mu \rangle < 0.63$), faculae are preferably radially oriented and their profiles exhibit a limbward skewness ($\eta > 0$). This was partly expected, as a limbward asymmetry was predicted by 2D calculations (Deinzer et al. 1984, Knölker et al. 1988, 1991) as a signature of the hot-wall effect. Earlier observational studies of facular profiles nevertheless gave inconsistent results, although they did not statistically quantify the asymmetry of the profiles. Indeed, even though some isolated cases of asymmetric facular profiles were observed (Lites et al. 2004, Hirzberger and Wiehr 2005), a recent study found that the profile resulting from the average of the "radial cuts" of all detected bright features at $\mu \sim 0.6$ was rather symmetric (Berger et al. 2007). However, these authors did not perform a "classification" of faculae, and it is very likely that averaging all profiles smears out the asymmetry of individual facular profiles. Interestingly, the three radial profiles of faculae computed from the 3D MHD simulations of Keller et al. (2004) do not exhibit a visible asymmetry either. It should be beared in mind that the observed profiles are *projected onto the plane of the sky*, as the ones of Keller et al. (2004), whereas the profiles computed from 2D models are always shown as a function
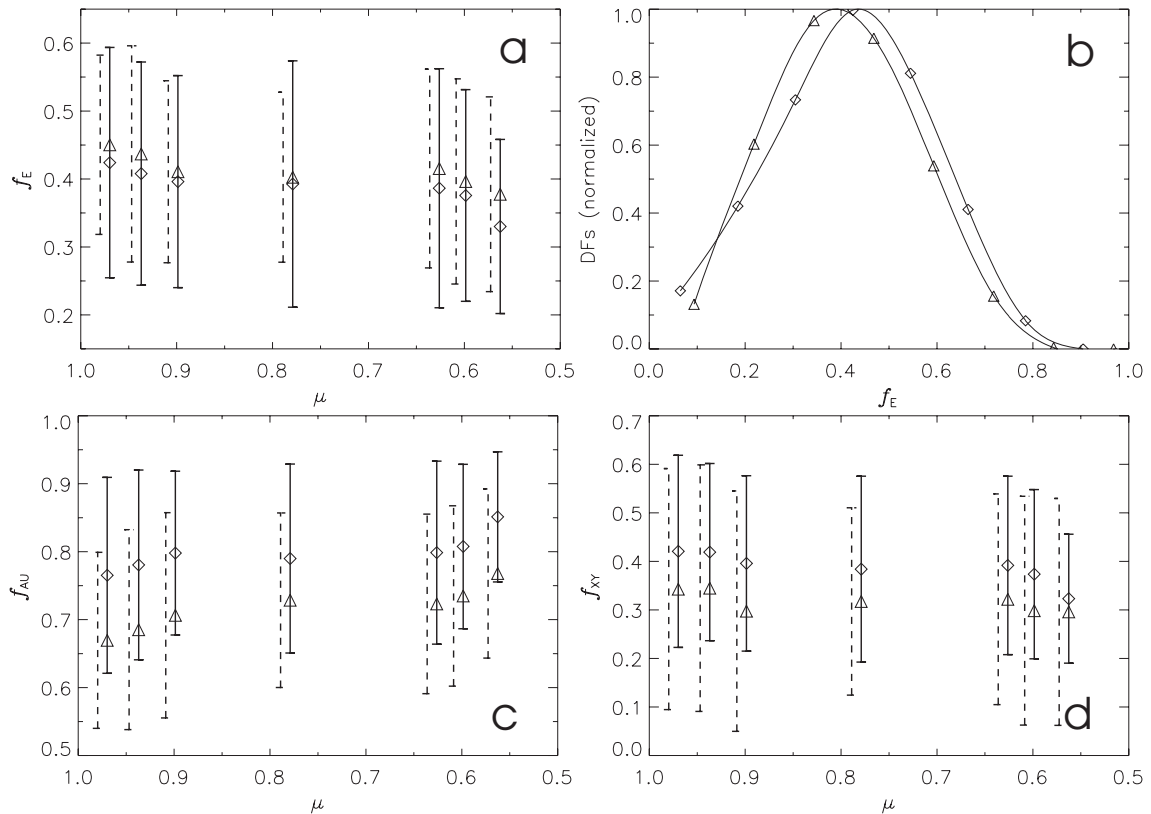
Figure 3.14: a) CLV of the average ellipticities $f_E$ of BPs ($\diamond$) and faculae ($\triangle$). b) Normalized DFs of $f_E$ for the BPs of the "center" data and the faculae of the "limb" data. c) CLV of the average area-perimeter ratio $f_{AU}$. d) Idem for the width ratio $f_{XY}$ in the local reference frame $x/y$. For all CLVs, the standard deviations of faculae (dashed) have been left-shifted for readibility.

of the horizontal coordinate. However, our facular profiles exhibit an asymmetric shape *despite their projection onto the plane of the sky*, and thus pose a novel constraint for the 3D simulations.

Near disk center, we found faculae to have a wider distribution of orientation (relative to the radial direction) and to exhibit both limbward and centerward skewness. But interestingly, the "degree of asymmetry" of their profiles (quantified through $|\eta|$) is very similar to the limb faculae. This suggests that faculae near disk center are also produced by a "hot wall effect", but induced by the inclination of the fields (see also Discussion in Chap. 2). Therefore the orientation of their brightenings appears unrelated to the radial direction (although our "center" images covers a wide range $0.9 < \langle\mu\rangle < 0.97$ and contains as well LOS effects). That faculae could be induced by inclined fields has been already proposed by Keller et al. (2004) on the basis of their 3D MHD simulations, although they did not actually check their existence near disk center. We note that if the apparent orientation of the facular brightenings indeed reflects physical information about the azimuthal direction of inclined fields, this would justify to retrieve profiles by taking into account the individual orientation of these brightenings (e.g. the herein "characteristic profiles") instead of radial cuts.

As expected, BPs near disk center have a large spectrum of orientation with very

symmetric characteristic profiles. Near the limb, surprisingly, the orientation of their characteristic profiles is preferably radial while their profiles exhibit a slight limbward skewness. This suggests that the features appearing as BPs near the limb are manifestations of the same hot wall effect as limb faculae. But unlike large faculae, they take a BP-like appearance because they do not benefit from a large granule on their limbward side, and due to the finite resolution. The appearance of faculae was indeed shown by Keller et al. (2004) to depend on the presence of a "well-formed" granule next to the flux concentrations. Such very small facular brightenings have been already reported by Lites et al. (2004), and Keller et al. (2004) also argued that they arise from the limited spatial resolution and ensuing remaining speckles in the observations.

The BP-like appearance of small faculae is also understandable in the light of our morphology study. The statistics of the shape ratios indeed revealed that at the highest achievable resolution, at which adjacent BPs and faculae striations can be resolved by MLT segmentation, these elements bear only minor morphological differences (in spite of their large difference of size on average). This similarity between BPs and faculae, in particular the relatively low ellipticity of BPs, can be surprising when having in mind the often very complex structure of intergranular BPs in active regions (see Berger et al. 2004), appearing like a "magnetic fluid" in MHD simulation snapshots (Schüssler et al. 2003, Shelyag et al. 2004). However, a close look at the subfields shown in Fig. 3.2 (for $\langle \mu \rangle = 0.9, 0.97$) reveals that many of these complex structures are broken up into smaller adjacent ones by the MLT segmentation, while others are rejected from the classification [8]. Moreover, even if the definitions of the shape ratios are scale-independent, their values depend very much on the spatial resolution, especially for BPs. Further increase in spatial resolution is thus expected to reveal further morphological differences.

When analyzing the contrast of BPs and faculae, we surprisingly found them to have a similar CLV of their peak contrast, which cannot be explained solely by the misclassification of small faculae. An alternative explanation is that in the $\mu$ range considered here, the variation of contrast is not dominated by the visibility of the hot wall, but by a "limb darkening" effect common to BPs and faculae. This could be due to the geometrical shift of the optical depth combined with the larger temperature gradient outside than inside the flux concentrations, causing a similar darkening of the quiet environment of BPs and faculae. In addition, the geometrical shift could be more important outside than inside the flux tubes, due to their partial evacuation.

Further hints on the different physical nature of BPs and faculae could be provided by their different linear relations (slope $s$ and offset $o$) between their G-band and continuum contrast [9]. We can speculate the following interpretation for the distinct G-band–continuum trends of BPs and faculae. Assuming that BPs correspond to magnetic elements aligned with the LOS, whereas faculae arise from an oblique view through such elements, we can qualitatively compare the CH opacity along a line of sight (LOS) that is parallel to the axis of a flux tube (BP case) and along an inclined LOS (facula case). Nu-

---

[8]We note that the adoption of a coarser MLT segmentation would probably yield more morphological differences between BPs and faculae, as the former would clump into complex shapes and the latter would appear rather like "facular granules" (instead of finer striations). However, the classification would loose in efficiency (as shown in Appendix A).

[9]These different behaviours should be considered carefully near the limb due to the plausible misclassified faculae.

merical radiative transfer calculations have shown that inside the flux tube, the low density and the collisional dissociation of CH molecules lead to a reduced CH opacity (Steiner et al. 2001, Sánchez Almeida et al. 2001, Schüssler et al. 2003, Shelyag et al. 2004). While a vertical look fully captures this CH-depleted atmosphere, an inclined LOS travels through some non-magnetic region in front of the flux tube, and thus integrates more CH opacity. Therefore, the CH lines should be somewhat stronger (relative to continuum) for the inclined LOS than for the vertical one. The BPs should thus have larger contrasts than faculae in G-band, which translates in a larger $o$. And if the CH lines are stronger for the inclined LOS, they should be more sensitive to temperature variations. The G-band contrast of faculae should thus be more affected by variations of the continuum emission (related to temperature), which accounts for a larger $s$. Of course, in real data, the limited spatial resolution may have a significant effect on the observed trend (Sánchez Almeida et al. 2001, even proposed that the G-band–continuum relation of BPs is entirely dictated by the limited resolution) by reducing the values of $s$ and $o$, as demonstrated by the diagnostics of Shelyag et al. (2004) on degraded simulation snapshots.

### 3.6.2   Possible prospects for proxy magnetometry

The obtained trends of the peak contrasts (in G-band and continuum) as a function of the area of the features in different intervals of $\mu$ strikingly resemble the trends of the variation of the contrast as a function of magnetogram signal (Frazier 1971, Topka et al. 1992, Lawrence et al. 1993, Ortiz et al. 2002).

In magnetogram sudies, the spatial resolution is in general much poorer, so that the magnetic features are mostly unresolved and their magnetogram signal (which scales with their magnetic flux) can be roughly interpreted as a measure of their cross–sectional area (assuming a roughly constant field strength). The contrast is then seen to increase with small magnetogram signals as the features become larger and better resolved, until the contrast decreases for larger signals associated with darker features (e.g. micropores).

The fact that the peak contrasts as a function of the area behave similarly comes as a surprise for several reasons. First, our measurements of contrast and areas are performed at a much higher spatial resolution (a factor 5 to 50 better, depending on the magnetogram study), and except for the smallest BPs, the BPs and faculae considered here have dimensions far exceeding the diffraction limit (see Sect. 3.3.2). Second, we are considering only bright features whose G-band contrast exceed a rather large threshold (see Sect. 3.2.2). Third, studies of the contrast as a function of magnetogram signal average the contrast of unrelated pixels in the images having magnetogram signals within given bins ("magnetogram-binning method"), and thus bear no information about the identity of the magnetic features. The obvious similarity between our results and magnetogram studies has thus important implications: (1) the finite spatial resolution still affects the measured peak contrast values, (2) there must be some correlation between the observed area of the segmented features and the associated magnetic flux, and (3) in a statistical sense, magnetogram-binning studies can be interpreted in terms of single features.

That the finite spatial resolution plays an important role in our measurements is clear, as even when restricting the case to BPs near disk center, the theoretical decrease of contrast with area is only recovered for large BPs. This is not in contradiction with the fact that most BPs considered here have dimensions largely exceeding the diffraction limit, as

the point spread function (PSF) could significantly smear the contrast at the core of the BPs. In addition, observational indications exist that the "true" (i.e. corrected for resolution effects) contrast-size relation of BPs matches the theoretical expectations. A decrease of contrast with size was indeed found by Spruit and Zwaan (1981) by correcting their BP diameters for the effects of finite resolution, and suggested by Ortiz et al. (2002) when relating the contrast per unit of flux (contrast divided by the magnetogram signal, which was interpreted as some measure of the features' intrinsic contrast) to the magnetogram signal. Physical effects could also come into play to explain that an increase of contrast with size (instead of the expected decrease) is found in the low size range. As will be seen in Chap. 4, the contrast of magnetic elements behaves similarly as a function of filling factor (fraction of resolution element occupied by the magnetic feature) and as a function of field strength. It could then be that the features having small sizes also harbour weaker fields (therefore less opacity depression and lower contrast). That small concentrations of flux can have weaker field strength could be accounted for by some inhibition of their "convective intensification" (Parker 1978, Grossmann-Doerth et al. 1998) through lateral heating (as theoretically predicted by Venkatakrishnan 1986, Rajaguru and Hasan 2000). In particular, Venkatakrishnan (1986) deduced that slender tubes (of diameter < 100 km) should show a strong dependence of their intrinsic field strength on their size, which has been supported by the infrared polarimetric observations of Solanki et al. (1996).

The possible correlation between the projected area of bright features and the flux of the associated magnetic elements is at first sight intriguing. Especially near the limb, one would expect the facular brightness to be rather a simple "cumulative function of their projected area" (Berger et al. 2007), related to the incidence of the line of sight (LOS) onto the hot wall. Berger et al. (2007) indeed found a linear relation between the facular contrast and the area of the features, which surprisingly has a similar slope at all their disk position [10] There could nevertheless be a relation between the visibility of the bright granular walls of facular features and the associated magnetic flux. Namely, the larger the flux concentrations the more visible the walls are (and the larger the projected area) but the cooler is the atmosphere traversed by the LOS, which could contribute to reduce the contrast of larger features. The relation between the extent of the facular brightness and the amount of flux is also supported by the cuts across magnetograms and faculae of Berger et al. (2007), showing that even at $\mu \sim 0.6$, both quantities are roughly co-spatial.

Hence, through their similarity with magnetogram studies, our results seem to validate the use of proxy magnetometry at high resolution and thus offers promising prospects. However, a true assessment of the relation between the measure of area used in our study and the magnetic flux of the features requires a dataset with joint magnetograms, and this area measurement should be properly calibrated for its use as a proxy.

To conclude, we would like to raise the attention on the use of one-dimensional measurement of sizes to verify the theoretical contrast-size relation. When measuring the size of the features via the width of their "characteristic" contrast profiles ($\Delta_{HM}$), we found no sign of a decrease of the contrast even toward large sizes (unlike the contrast dependence on the features' area). Berger et al. (1995) found a similar trend by measuring the FWHM of BPs across their short dimension, and Wiehr et al. (2004) by using their "equivalent diameters". The absence of contrast decrease can be explained by the fact that the degree

---

[10]However, their area is defined differently from ours, as their definition relies on a "blob-finding" segmentation, whereas we use MLT and further take care to measure the area in a feature-independent way.

to which flux concentrations are heated depends in first order on their volume, which can be better "grasped" by their cross-sectional area (assuming constant optical depth depression) than by a one-dimensional width measurement (especially for elongated sheet-like flux tubes). In addition, the telescope PSF spreads the contrast in two dimensions, which cannot be adequately captured when relating the contrast to a one-dimensional size measurement. Since the predictions of the contrast–size relation arose from early 2D flux tube models, it comes almost natural to seak for a contrast–size relation using 1D measurement of the size. The above suggests that a 2D area measurement is likely to be more appropriate, and should be compared with 3D simulations correspondingly.

## 3.7    Summary

In the present study we followed the classification approach developed in Chap. 1 to sort BPs and faculae in high-resolution images of active regions at various heliocentric angles, and statistically analyzed their photometric properties (contrast and morphology), as well as their variation with heliocentric distance. Here we briefly summarize the obtained results:

1. The statistical distribution of the width of BPs and faculae classified with our method is consistent with previous studies, performed on disk center-BPs (Berger et al. 1995, Wiehr et al. 2004, Puschmann and Wiehr 2006, Bovelet and Wiehr 2008) or limb-faculae only (Lites et al. 2004, Berger et al. 2007), which indirectly supports our classification.

2. Limb faculae ($0.52 < \mu < 0.65$) are mostly radially oriented and their contrast profiles are limbward-skewed (both in mode and average), as predicted by 2D MHD calculations (Deinzer et al. 1984, Knölker et al. 1988, 1991, Steiner 2005). Nearer the disk center, their orientation is more widely distributed and the profiles exhibit both limbward and centerward skewness in similar proportions, but with absolute values comparable to the ones near the limb. This indicates that faculae near disk center are induced by inclined fields, and that the orientation of the facular brightenings is related to the azimuthal direction of their inclination. The skewness of facular profiles sets a novel constraint for 3D MHD simulations of faculae.

3. BPs observed near the limb are most probably very small faculae having a BP-like appearance due to the rather small granule on their limbward side.

4. In the $\mu$-range considered here, the G-band and continuum contrast of BPs and faculae increases similarly from center to limb.

5. BPs and faculae exhibit different linear relations between their G-band and continuum contrast. It is unclear whether the different trends are artefacts of the finite resolution or are due to real radiative transfer effects related to CH opacity.

6. At the current spatial resolution allowing to resolve adjacent BPs and faculae striations, the morphological parameters investigated here take rather similar values for BPs and faculae.

7. The relation between the peak contrasts and the apparent (projected) areas of BPs and faculae has a trend which is qualitatively very comparable to the studies of contrast as a function of magnetogram signal, both for the continuum (Ortiz et al. 2002, Topka et al. 1992, Lawrence et al. 1993, see as well Chapter 4) and the G-band (Berger et al. 2007). These trends seem to vary in a similar way within different $\mu$ intervals, and are more pronounced in G-band than in continuum. This similarity implies some relation between the areas of the features observed in high resolution images and the flux of the associated magnetic elements, and thus opens an interesting avenue for proxy magnetometry.

# 4 Center-to-Limb Variation of the continuum contrast as a function of inferred magnetic parameters

The center-to-limb variation (CLV) of the continuum contrast of magnetic features represents an important constraint for flux tube models, as well as a useful input to reproduce the total solar irradiance. However, precise measurements are difficult because the contrast depends on the atmospheric and magnetic parameters of those features, and is severely affected by the observing conditions (seeing). In this chapter, I present the first measurements of the continuum contrast CLV of magnetic features as a function of different magnetic parameters (field strength, filling factor and inclination), inferred by inversions of seeing-free spectropolarimetric maps with high spatial resolution (provided by the Hinode satellite).

## 4.1 Introduction

The center-to-limb variation (CLV) of the continuum contrast of magnetic features is a standard problem of solar physics, for it provides a "simple" constraint for flux tube models in the form of a relationship between the emerging intensity and the emission angle. Moreover, the CLV of contrast (and most importantly at continuum wavelengths) of magnetic features is a necessary input to reproduce the fractional change of irradiance with disk position and by integration over $\mu$ the total solar irradiance (see introduction of Lawrence et al. 1993). Yet the contrast is a subtle observable, as it depends on almost all atmospheric and magnetic parameters (field strength, amount of flux, surrounding granulation etc), as well as the observing conditions (seeing, wavelength).

As mentioned in Chap. 1 (Sect. 1.2.4), there exists a long list of "facular contrast CLVs" (meant as the contrast of all photospheric brightenings, BPs and faculae together) with rather controversial results, notably due to the many factors influencing the contrast measurements and the difficulty to control these factors (e.g., different spectral ranges, resolutions, selection effects, statistics, amount of flux, see e.g. Criscuoli and Rast 2008, Ortiz et al. 2002). In particular, most of them lack information about the magnetic parameters and the observing conditions (e.g. fluctuating spatial resolution in ground-based studies). A parameter known to influence the CLV of continuum contrast is the size of the flux tube (Spruit 1976), as the ratio of the Wilson depression to the tube diameter affects the relative visibilty of tube "wall" and "bottom" (at optical depth unity). To probe this dependence, relatively few studies have investigated the CLV as a function of "magne-

togram signal", which roughly scales with the size and number density (in the resolution element) of the unresolved magnetic features (assuming that their intrinsic field strength does not vary much, Stenflo and Harvey 1985). A first series of studies was carried out by Topka et al. (1992), Lawrence et al. (1993), and Topka et al. (1997) (hereafter referred to as TL), using continuum filtergrams of active regions at various visible wavelengths and nearly simultaneous magnetograms recorded at the 50-cm Swedish Vacuum Solar Telescope (SVST). Although TL obtained very consistent measurements of contrast vs. magnetogram signal at a few discrete heliocentric angles (by selecting data with good seeing conditions in time series), they needed to fight the variable seeing conditions when comparing their data at different heliocentric angles. To obtain a CLV, they indeed had to combine observations made on different days under different seeing conditions, different wavelengths, and average all data points in a large magnetogram signal range (what they refer to as "faculae", between 188 Mx cm$^{-2}$ to 612 Mx cm$^{-2}$). One of their major conclusions was that not only the average facular contrast (average between 188 Mx cm$^{-2}$ to 612 Mx cm$^{-2}$) is negative at disk center (i.e. darker than the average quiet Sun), but the contrast is negative over their whole range of magnetogram signal. They estimated that the average facular contrast turns positive for heliocentric angles larger than $\theta \sim 20°$, and that the highest contrasts observed at large $\theta$ are associated with pixels of large magnetogram signals that appear dark at disk center, i.e. with micropores. The seeing limited the spatial resolution of their data to about 0$\farcs$6, blending the contrast of features with their surroundings (which can easily smear out the brightness of features in intergranular lanes, as demonstrated by Title and Berger 1996), which could explain their low contrast near disk center (cf. Solanki 1993). Stimulated by this issue, Berger et al. (2007) repeated the study of TL at a higher spatial resolution using simultaneous magnetograms (resolution $\sim$ 0$\farcs$3) and G-band images (resolution $\sim$ 0$\farcs$1) from the 1-m Swedish Solar Telescope, with the help of post-facto reconstruction techniques (unlike TL). For the data at $\langle\mu\rangle = 0.97$ (mean $\mu$ across the field of view, $\mu = \cos\theta$), magnetogram signals in the range between 500 Mx cm$^{-2}$ and 1100 Mx cm$^{-2}$ exhibited positive contrast values. However, the results of Berger et al. (2007) are not directly comparable since the contrast of magnetic elements is known to be enhanced in G-band (due to their internal evacuation and larger temperature, Steiner et al. 2001, Rutten et al. 2001, Sánchez Almeida et al. 2001, Shelyag et al. 2004, Schüssler et al. 2003).

For a fully consistent and comparable study of contrast at different $\mu$ and under identical conditions, space-based measurements are necessary. These allow for vast amounts of data to be collected and a much more complete range of heliocentric positions to be covered. Following this line of thought, Ortiz et al. (2002) used SOHO/MDI to provide systematic reference curves of contrast vs. magnetogram signal in various intervals of $\mu$, and vice-versa. Although these space-based results are much more reliable, the much poorer resolution of SOHO ($\sim 5''$) hampers the interpretation of their results in terms of individual magnetic elements.

The Hinode Solar Optical Telecope (SOT) opens new perspectives owing to its much higher resolution of 0$\farcs$3 (Tsuneta et al. 2008). In particular, its spectropolarimeter instrument (SP) allows for the full Stokes vector to be recorded in the visible Fe line pair around 630 nm. By carrying out proper inversions, one can thus systematically investigate for the first time the dependence of the continuum contrast on the inferred magnetic parameters (inclination, intrinsic field strength, filling factor) of the underlying flux concentrations.

In this study, I present an assessment of the dependence of the continuum contrast on inferred magnetic parameters (using the VFISV code, see Sect. 4.2.3) in the quiet Sun, over a continuous range of $\mu$ down to $\mu = 0.2$. Despite its low number density of magnetic elements, the advantage of the quiet Sun is to largely exclude micropores, and therefore focus on the study of smaller features. This prevents the mixture of structures having different contrast (dark micropores and bright elements) when averaging the contrast as a function of the magnetic parameters.

In a first step, I repeated the work of TL and Ortiz et al. (2002) to see how the results compare when the spatial resolution increases (Sect. 4.3.1). In order to obtain a "step-by-step" view of the dependence of the contrast on the magnetic parameters, I considered first the dependence on the apparent flux density (Sect. 4.3.2) and the inclination (Sect. 4.3.3), then on the field strength and filling factor (Sect. 4.3.4).

## 4.2   Dataset analysis

### 4.2.1   Hinode/SP scans

To obtain full Stokes vector information at various heliocentric angles across the solar disk, I selected an ensemble of 22 spectropolarimetric scans of the Hinode/SP instrument (Tsuneta et al. 2008), recorded between December 2006 and April 2007. These scans cover network and internetwork regions near the equator (with the exception of one scan at the south limb).

The SP instrument delivers profiles of the four Stokes parameters (along its slit) in a visible wavelength range covering both the Fe I 630.15 nm and 630.25 nm lines, at a constant high spatial resolution of 0.″3 (see e.g. Lites et al. 2008, for more details). The field of view (FOV) along the slit is approximately 160″, and all our maps had a total FOV of 160″ × 160″, with the exception of 2 scans with FOV of 160″ × 320″. The scans were performed in the so-called "normal mode", with an exposure time of 5.8 s, resulting in typical noise levels at disk center of $1.1 \times 10^{-3}$ and $1.2 \times 10^{-3}$ for Stokes $V$ and $Q, U$, respectively (in units of continuum intensity $I_c$). All the profiles were calibrated via the `sp_prep` routine of the SolarSoft package [1]. As it was noticed that the 10 first and last pixels along the slit contain spurious CCD effects, the corresponding pixel rows of the spectropolarimetric maps were cropped to avoid erroneous inversion results and continuum intensity values at these pixel locations.

### 4.2.2   Maps of continuum intensity and heliocentric distance

Maps of the continuum intensity $I_c$ were provided by the `sp_prep` procedure, by calculating the mean of Stokes $I$ in the red continuum of the Fe I 630.2 nm line. Since these maps are exactly co-spatial with the spectropolarimetric maps by construction, any destretching and related errors are avoided.

Owing to the short exposure times compared to the granulation turnover timescale ($\sim 10$ min), these continuum maps can be thought of as quasi-instantaneous images. They

---

[1] `http://www.lmsal.com/solarsoft/sswdoc/index_menu.html`

are thus appropriate to study magnetic features, whose evolution timescales are roughly comparable with those of the granulation (Berger and Title 1996, Berger et al. 1998).

Knowing the pointing coordinates, the slit position within the scan and its tilt angle relative to the solar NS axis, `sp_prep` also calculates maps of the right ascension $x$ and declination $y$ (heliocentric cartesian), and thereby the $\mu$ value at each pixel of the maps.

Provided these "$\mu$ maps", the limb darkening of the continuum maps could be removed by dividing them by the 5th-order polynomial in $\mu$ of Neckel and Labs (1994) (hereafter NL).

For the scans nearest to the limb ($\mu < 0.4$), we noticed that the apparent limb in the continuum maps (drop-off of the intensity) was lying at positive $\mu$ values. This mismatch was enough to cause a departure of the actual limb darkening of the continuum map from the NL polynomial for $\mu \leq 0.3$. The correlation tracker of the SP instrument is indeed known to drift along gradients of the intensity (Lites, private communication), such as to cause an ever increasing mismatch between the pointing coordinates and the observed intensity as the slit approaches the visible limb [2]. To correct for this systematic error and properly remove the limb darkening as close to the limb as possible, I applied a linear stretch of the $x$ coordinate (perpendicular to the slit), so that the corrected $\mu$ value equals zero at the "visible limb". The intensity value corresponding to this visible limb was chosen such that it yielded a smooth $\mu = 0$ borderline in the corrected $\mu$ maps, and such that this correction allowed an accurate limb darkening removal down to $\mu = 0.1$ (in the sense that the NL polynomial well superposes onto any spatial cut of the continuum map). The precise match between averaged intensity cuts and the NL polynomials calculated from the $\mu$ maps made me confident that the latter are correct up to the second decimal.

The contrast in each map was then defined as the intensity excess relative to a chosen subfield of pure quiet granulation of area $20'' \times 20''$ :

$$\text{Contrast} = \frac{I_c - \langle I_c \rangle_{\text{QS}}}{\langle I_c \rangle_{\text{QS}}} \, , \tag{4.1}$$

where $\langle I_c \rangle_{\text{QS}}$ is the mean continuum intensity of the chosen quiet area.

It should be noted that in absence of time series, the contrast precision is limited by large-scale fluctuations of the intensity, contributing to the statistical scatter in the measurements.

### 4.2.3   Inversions

The magnetic parameters at each pixel location of the maps were inferred using VFISV (Very Fast Inversion of the Stokes Vector), a *one-component* Milne-Eddington inversion code developed by Borrero et al. (2009). This code is optimized for speed (it can invert $10^6$ spectra in about 3 min), and is thus particularly suited for statistical studies on large datasets.

In its current state of development, this code only fits the profiles of the Fe I 630.25 nm line, whereas other Milne-Eddington codes generally invert the profiles of both Fe lines. Although some information is lost when inverting only one line, I compensated

---

[2]The source of this error is unknown, but I noticed a similar behavior in scans at the west limb, showing that the CT apparently moves limbward

by choosing rather conservative polarization amplitude thresholds for the pixels to be considered in this study, in order to obtain reliable results (see below).

Although Milne-Eddington inversions also yield thermodynamic parameters and other kinematic parameters, I will herein consider only the field strength $B$, the field inclination $\gamma$ with respect to the line of sight (LOS), the filling factor $\alpha$ and the LOS-component of the velocity $v_{los}$ in the magnetized plasma. As the model atmosphere possesses one component only, these quantities can be considered as averaged over the resolution element. I will refer to $\{B, \alpha, \gamma\}$ as "magnetic parameters", upon which the dependence of the contrast shall be investigated.

To solve the problem of simultaneously fitting the Stokes $I$ and the polarization profiles in case of unresolved fields or stray-light contamination, we adopted the treatment of "local stray light" developed by Orozco Suárez et al. (2007b). Explicitely, at each pixel location, we considered that the Stokes $I$ profile results from a superposition of a "magnetic profile" $I_m$, and a "non-magnetic" one $I_{nm}$ treated as non-polarized stray light contamination by the neighbouring pixels: $I = \alpha I_m + (1 - \alpha)I_{nm}$. The $I_{nm}$ profile was obtained in the same manner as Orozco Suárez et al. (2007b), i.e. by averaging the Stokes $I$ profiles in a surrounding square region of $1'' \times 1''$ area (excluding the central pixel).

Since this straylight is purely non-polarized ($V, Q, U$ are not affected), the parameter $\alpha$ can equivalently account for unresolved fields, and is then related to the fraction of the pixel atmosphere that effectively harbours magnetic fields. But care should be taken with this interpretation, as VFISV does not invert for a second non-magnetic component, and both the physical contributions of the filling fraction and stray light are mixed in $\alpha$. It has nevertheless been shown by Orozco Suárez et al. (2007a) that at the spatial resolution of Hinode, the field strength could be reliably inferred using a single-component atmosphere only and such a "local stray light" treatment, the latter accounting both for the effects of telescope diffraction (the strict straylight contribution of the Hinode/SP PSF was shown to be only minor, Danilovic et al. 2008) and for the presence of unresolved fields. By convention, I simply refer to the parameter $\alpha$ as "magnetic filling factor"

As it was noticed that inverting directly for $\alpha$ as free parameter was yielding an artificial peak at values very near to $\alpha = 1$ (not physical since the stray light contamination cannot be null), the free parameter was chosen as $\beta = 1/(1 + \alpha) \in (0, \infty)$ instead, which was found to remove this artefact.

Finally, in the weighting scheme, we took into account the realistic spatial variation of the noise in the polarization profiles in the $\chi^2$ definition:

$$\chi^2 \propto \sum_S \sum_{\lambda_i} (S_{obs}(\lambda_i) - S_{syn}(\lambda_i))^2 w_S^2, \quad S = I, Q, U, V, \qquad (4.2)$$

$$w_S = \frac{1}{\sigma_S}, \quad S = Q, U, V, \qquad (4.3)$$

$$w_I = 0.2 \frac{\sum_{S=Q,U,V} w_S}{3}, \qquad (4.4)$$

where $S_{obs}$ and $S_{syn}$ stand for the observed and synthetic Stokes profiles, $\lambda_i$ for the wavelength at the pixel $i$ of the spectra and $\sigma_S$ for the noise level of the Stokes profiles (standard deviation of 13 pixels in the red continuum of the Fe I 630.25 nm line, further averaged with a boxcar of 5 pixels along the slit). The weights $w_S$ were thus allowed to vary across the map to account for the spatial variation of the photon noise due to limb darkening (the

level of noise in units of $I_c$ increases towards the limb, particularly for $\mu < 0.7$, see Fig.
4.2) and local variations due to granulation. Note that $w_I$ was not derived from the noise
in Stokes $I$, because the latter is strongly affected by CCD residual flat-fielding effects
(Lites, private communication) and not by the photon noise itself. To account only for the
photon noise, $w_I$ was set to the average of the weights of $Q, U, V$ multiplied by a factor of
0.2, which was earlier found by Borrero (private communication) to give optimal results
for inversions in the quiet Sun.

To quantify the signal-to-noise ratio in each pixel of the spectropolarimetric maps,
co-spatial maps of the "rms" noise level (in units of $I_c$) for $Q, U, V$ were constructed [3]. To
reduce the graininess of these "noise maps", the latter were smoothed with a boxcar of 5
pixels, such that the variation of noise due to the variation of granulation brightness was
still visible.

In the subsequent analysis, I only considered pixels whose Stokes $V$ amplitude was
higher than 8 rms, or whose $Q$ or $U$ amplitudes were above 4.5 rms. The reason behind
these polarization thresholds is that for lower Stokes amplitudes, the solutions of the in-
versions tend to become degenerate in $B, \gamma, \alpha$. Second, the critical polarization amplitude
at which this degeneracy occurs differs for $V$ and $Q, U$, requiring a larger threshold in $V$.
This degeneracy is illustrated in Fig. 4.1 by scatterplots of $\gamma, \alpha, B$ as a function of the
$V$ and $Q$ amplitudes (the situation is similar for $U$) at disk center (taking pixels from all
maps where $\mu > 0.99$). To emphasize the degeneracy for low signals, pixels where all
Stokes amplitudes are below 3 times their respective noise rms are overplotted in orange.
As can be seen, a threshold of 3 rms almost removes the degeneracy in $Q, U$, but it is too
low to remove it in $V$. This can be explained by the fact that the profile shape of Stokes
$Q, U$ is much more field strength-dependent than Stokes $V$ (due to the ratio of the $\pi$ to $\sigma$
components). Therefore, I chose rather conservative thresholds at 4.5 rms in $Q, U$ and 8
rms in $V$, indicated by the dashed red line. I mention that the threshold level in $Q, U$ is
the same as chosen by Orozco Suárez et al. (2007b), while their $V$ threshold was set at 4.5
rms only. Since these authors inverted for both Fe lines, it is possible that their inversion
results were less affected by the degeneracy of the solutions for low V signals.

To give an idea of the Stokes signals selected with the above thresholds, probability
density functions (PDFs) of the Stokes $Q, U, V$ amplitudes obtained over all selected pix-
els are shown in Fig. 4.2 for six intervals of $\mu$ between $\mu = 1$ and $\mu = 0.2$ (the same
$\mu$ intervals were chosen throughout this study, such as to cover an equal range of helio-
centric angle $\Delta\theta = 14°$ in each of them and thereby sample an equal portion of the solar
surface). All PDFs are normalized to the total number of selected pixels in each $\mu$ inter-
val. The secondary peaks in the PDFs are due to the different thresholds for $V$ and $Q, U$,
as indicated by the superpositon of the PDFs of the pixels having $Q$ or $U$ above 4.5 rms
(red). The variation of the PDFs with $\mu$ is essentially an effect of the increasing level of
the noise rms, whose CLVs (for $Q, U, V$) are plotted in the bottom right panel of Fig. 4.2.

The PDFs of the inferred magnetic parameters $\gamma, \alpha, B$ and the unsigned "apparent flux
density" $B_{app} = B\alpha$ are given in Fig. 4.3 for the same $\mu$ intervals. These PDFs are not

---

[3]I distinguish between the noise level used for the weighting scheme, $\sigma_S$, and the values of the noise
maps denoted simply "rms" (and referring either to $Q, U$ or $V$ depending on the context). These two noise
levels indeed differ because the Stokes profiles were normalized differently (in the inversions, the profiles
were normalized by a constant number of counts corresponding to disk center, instead of by $I_c$) and because
of the different boxcars applied.
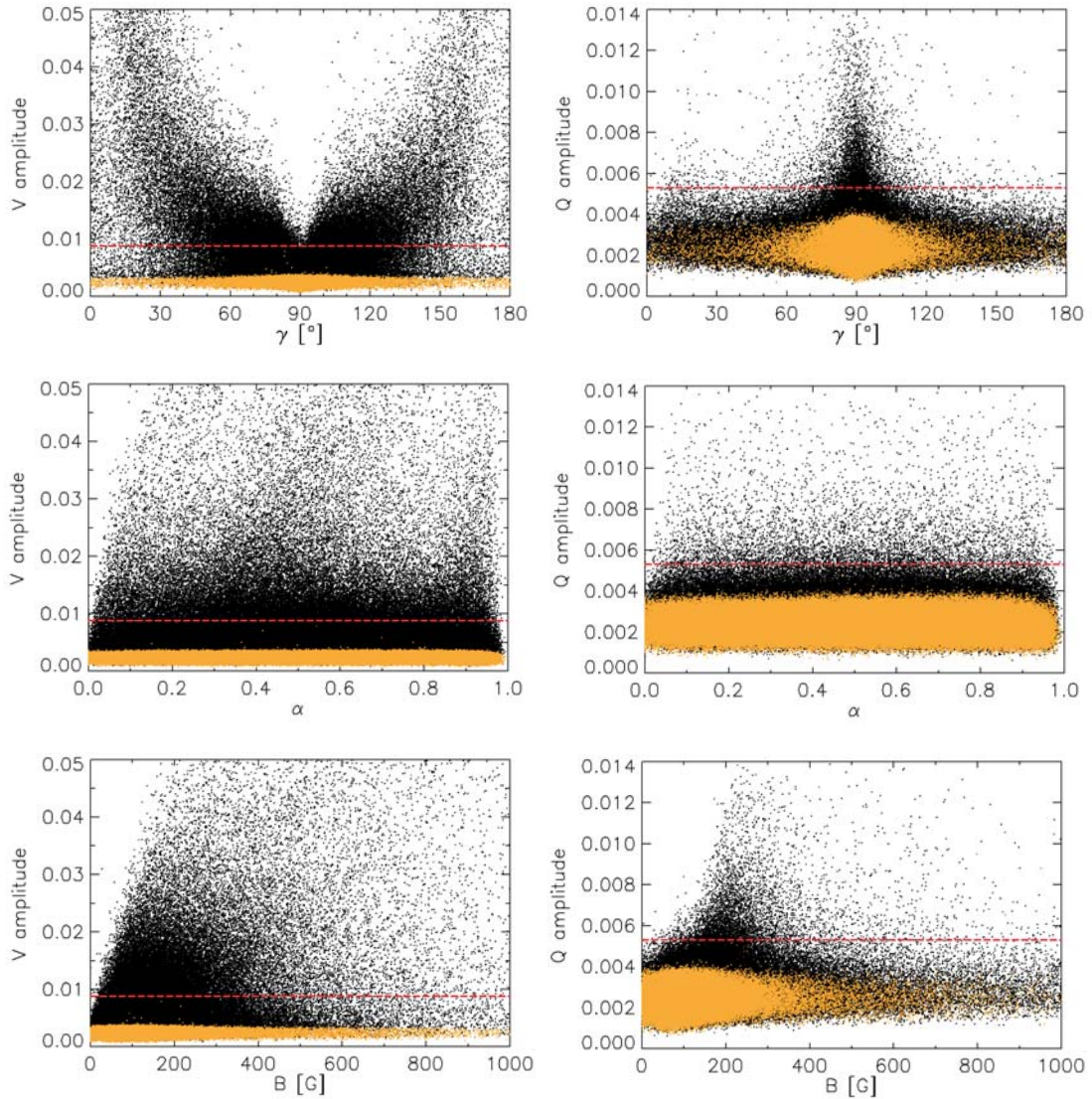
Figure 4.1: Scatterplots of Stokes $V$ amplitude (left column) and Stokes $Q$ amplitude (right column) vs. $\gamma, \alpha, B$ for all analyzed maps at disk center, $\mu > 0.99$. The polarization amplitudes are in units of $I_c$. Pixels where all Stokes amplitudes were below 3 times their respective rms noise levels are overplotted in orange. The red dashed lines indicate the chosen polarization threshold of 8 rms in $V$ and 4.5 rms in $Q, U$ (for this purpose I averaged the noise map in $V$ and in $Q$).
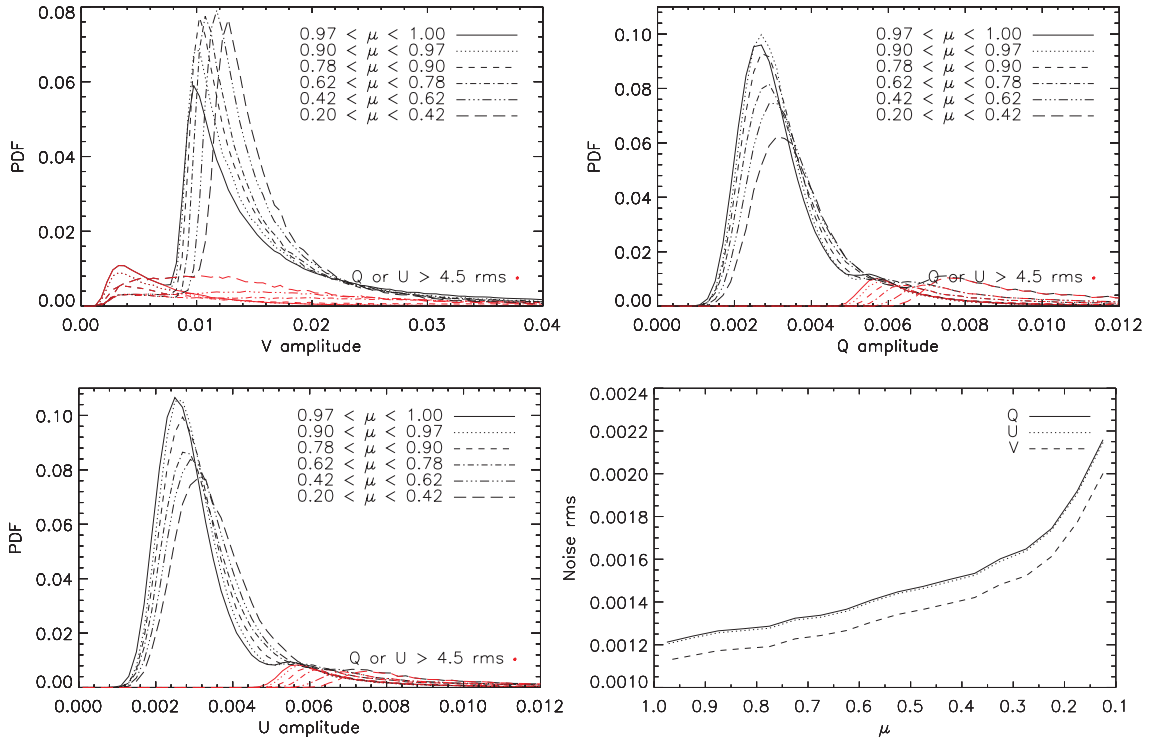
Figure 4.2: Probability density functions of the Stokes $V, Q, U$ amplitudes for all pixels selected by our polarization thresholds, in six intervals of $\mu$ between $\mu = 1$ and $\mu = 0.2$. Red PDFs: same for pixels having Q or U above 4.5 rms. All PDFs are normalized to the total number of pixels in each $\mu$ interval. Bottom right: CLV of the noise rms of the $Q, U, V$ amplitudes (obtained from the "noise maps") for all selected pixels.

meant to show how the magnetic parameters actually distribute at different $\mu$ (most of the variation is caused by the CLV of our polarization thresholds following the noise rms) but rather to indicate how the *selected* magnetic parameters distribute at different $\mu$. Previous investigations of the PDFs of magnetic parameters in the quiet Sun were carried out by Martínez González et al. (2007), who reported that the PDFs were self-similar at different $\mu$, thus suggesting an isotropic distribution of the orientation of weak fields. Unlike us, however, IR lines were used (better sensitivity to Q,U) and a single polarization threshold was considered at all $\mu$. Since our polarization thresholds vary from center-to-limb, we cannot say anything here about the isotropy of the field distribution. Whereas the variation of our thresholds allows us to invert profiles with equal reliablity at different $\mu$, it does introduce a bias in the population of fields considered. Throughout this study I followed the convention of noting the units of apparent flux density (and magnetogram signal) in Mx cm$^{-2}$ and the units of intrinsic field strength in G.

   In spite of the varying polarization thresholds with $\mu$, note that the mode of PDF($B_{\mathrm{app}}$) is roughly constant. Conversely, the PDF of $\gamma$ varies much with $\mu$, with a decrease of the amount of longitudinal fields (progressive inclination of strong vertical fields) and a decrease of the transverse fields at $\gamma \sim 90°$ (increasing polarization thresholds).

   Note that the PDF($\gamma$) in the interval $0.97 < \mu < 1$ compares well with the one retrieved by Orozco Suárez et al. (2007c), with its broad triple peak of inclined fields between 70° and 140° (our PDF has somewhat broader wings of vertical fields due to the larger $V$

threshold). However, beware that except for the central peak of $\gamma \sim 90°$, the two "horns" peaking at about 70° and 110° are dominated by signals having both $Q$ and $U$ below 4.5 rms. This suggests that part of the retrieved large inclinations are induced by fitting $Q$ and $U$ profiles dominated by noise (this is still under investigation). If they were induced by a true excess of horizontal fields, a broadening of these horns would be expected as $\mu$ decreases due to the azimuthal distribution of these fields, but it is not observed.

The shape of the PDF($B$) in the interval $0.97 < \mu < 1$ is reassuring, as the tail toward kG fields with a sharp drop for $B > 1500$ G is similar to the PDFs derived from 3D MHD simulations (see 10G run shown in Sánchez Almeida 2007), and to the one retrieved by the Milne-Eddington inversions of the Fe I lines of Sánchez Almeida et al. (2003) and Orozco Suárez et al. (2007b). The PDF($\alpha$) in the interval $0.97 < \mu < 1$, however, differs significantly from the one obtained by Orozco Suárez et al. (2007b). Instead of a sharp peak at $\alpha \sim 0.2$, our PDF has a broad peak centered about $\alpha \sim 0.5$ and a smaller one at $\alpha$ close to 1. As $\mu$ decreases, two effects can be noticed. Firstly, the broad main peak seems to shift toward lower $\alpha$ values, which could be due to a geometrical effect, as an increasing area of solar surface is sampled by each pixel. Secondly, the peak at $\alpha$ close to 1 amplifies, mostly as a contribution of the transverse fields (in red). I argue that this increase of $\alpha$ relates to the progressive inclination of vertical magnetic elements with respect to the LOS, giving rise to increasing filling fractions (due to the increasing amount of transverse fields which cover larger portions of the pixels). In turn, the decrease of kG field strengths with decreasing $\mu$ is likely to be related to this increasing peak of large $\alpha$, as the PDF($B_{app}$) does not vary much and neither does the range of $B_{app}$ (see Fig. 4.9). These two assertions will receive further support in Sect. 4.3.4.

Finally, Fig. 4.4 gives a glimpse at the maps of the inferred magnetic parameters for three chosen subfields at $\mu \sim 0.98, 0.7, 0.31$, containing both network and internetwork features.

## 4.3   Center-to-limb variation of the contrast...

In the present study I followed a "magnetic parameter-binning method" (as TL did for their magnetogram signal), in which the contrast and the magnetic parameters are compared pixel per pixel (independently, without information about magnetic "structures"), and investigated statistically after being binned together according to values of the magnetic parameters. Except for some particular illustrations, no distinction between the different SP scans are made and the pixel data are distinguished based solely upon their $\mu$ value.

### 4.3.1   ...As a function of "magnetogram signal"

To begin with, I repeated the investigation of continuum contrast as a function of magnetogram signal undertaken by TL and Ortiz et al. (2002), to see how the results would differ at the spatial resolution of Hinode (0″3), compared with the spatial resolution of the magnetograms of TL (0″6 at best), and of Ortiz et al. (2002) (5″). Note that these authors considered different wavelengths (525.0, 557.6, 630.2 and 676.8 nm for TL and 676.8 nm for Ortiz et al. (2002)), and when possible the comparisons with TL will always refer to
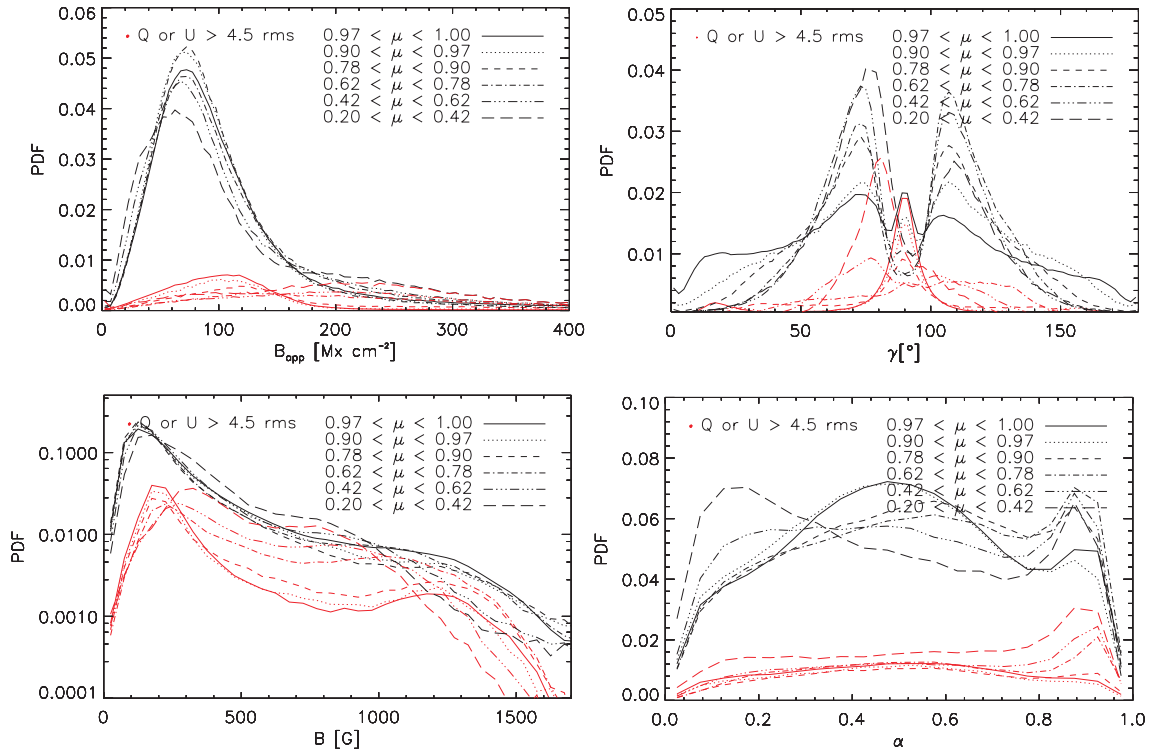
Figure 4.3: Probability Density Functions (PDFs) of the inferred magnetic parameters for six intervals of $\mu$: apparent flux density $B_{app}$, inclination with respect to the LOS $\gamma$, filling factor $\alpha$ and intrinsic field strength $B$. Red PDFs: same for pixels having Q or U above 4.5 rms. All PDFs are normalized to the total number of pixels in each $\mu$ interval.

630.2 nm (although their results at other wavelengths are similar).

As anologon to the proper magnetogram signal derived from the calibration of the Stokes $V$ amplitude, I used here the unsigned *apparent longitudinal flux density* $B_{app,los} = B\alpha|\cos\gamma|$ (i.e. absolute value of the net average of the longitudinal component of the field) directly inferred from the inversions [4]. Following TL and Ortiz, $B_{app,los}$ was corrected by a factor $1/\mu$ to compensate for the decrease of signals due to the progressive inclination of strong vertical fields with $\mu$, and in the following I denote this "corrected magnetogram signal" with the symbol $M$: $M = B_{app,los}/\mu$. Note that for vertical fields at fixed $\mu$, $M$ directly scales with the net flux (normal to the solar surface) in the resolution element.

The PDFs of $B_{app,los}$ and $M$ are compared in Fig. 4.5. As shown by the overplotted PDFs of signals with $Q$ or $U$ larger than 4.5 rms, the accumulation of signals at very low $B_{app,los}$ and $M$ is due to transverse fields. Note also that the modal value of the PDF($B_{app,los}$) only slightly increases with lower $\mu$ (due to the increase of our polarization thresholds), so that the modal value of the PDF($M$) progressively shifts to larger values of $M$ as $\mu$ decreases. This shows that one should be careful in using $M$ for weak fields, as the $1/\mu$ factor assumes purely vertical fields [5]. The rough self-similarity (up to the

---

[4]The correspondence between $B_{app,los}$ and the amplitude of Stokes $V$ holds only in the weak field regime, which is the dominant case for the quiet Sun.

[5]This problem was already pointed out by Berger et al. (2007), as resulting in "rather large magnetogram signals and subsequently high dispersion in the near-limb datasets".
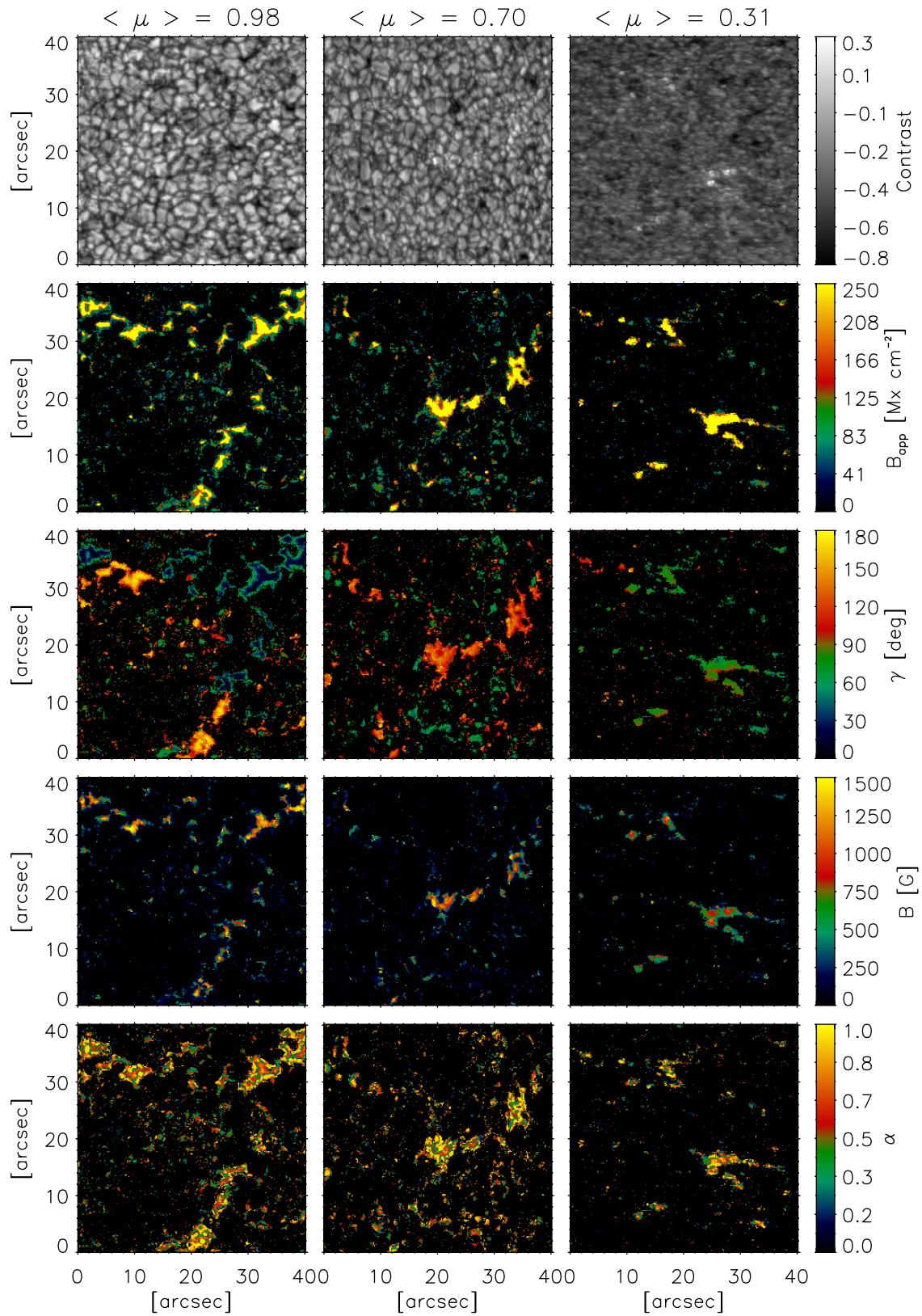
Figure 4.4: Chosen subfields from continuum maps and inversion maps at three different $\mu$, covering both network and internetwork regions. $\langle\mu\rangle$ stands for the average $\mu$ over the subfields. The pixels where all Stokes amplitudes are below the respective polarization thresholds are set to black. These correspond to almost 90 % of the field of views.

101
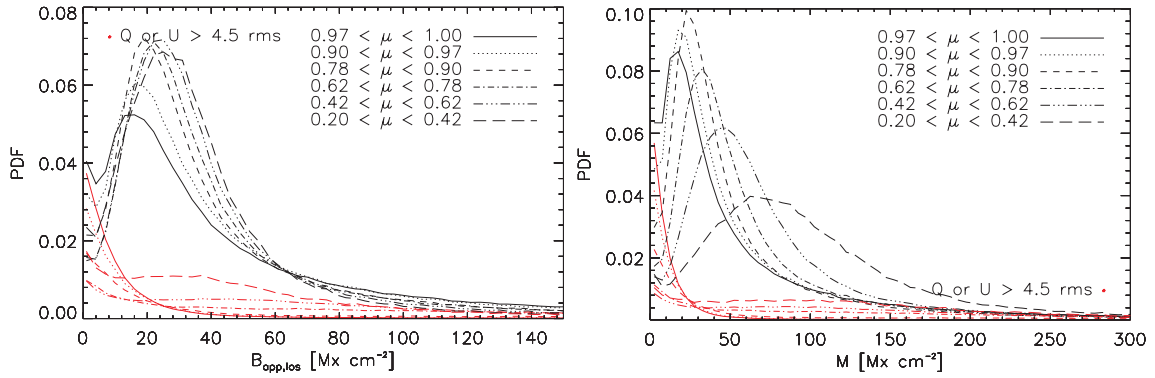
Figure 4.5: PDF of the apparent longitudinal flux density $B_{\rm app,los}$ (left) and $M = B_{\rm app,los}/\mu$ (right) in intervals of $\mu$. Red curves: PDFs restricted to signals having $Q$ or $U$ above 4.5 rms. All PDFs are normalized to their area (i.e. total number of pixels) in each $\mu$ interval.

threshold-induced variation) of the PDF of $B_{\rm app,los}$ in the different $\mu$ intervals is in favor of a quasi-isotropic distribution of the orientation of the weak fields dominating the PDF (an excess of horizontal or vertical fields should induce a shift of the PDF toward larger and lower values, respectively). An isotropic distribution for the internetwork fields was suggested by Martin (1988), and was strongly supported by the spectropolarimetric work of Martínez González et al. (2008) using IR lines.

Because one of the major conclusions of TL concerned the negative contrast of magnetic features at disk center, I first restricted the study of contrast vs. $M$ to $\mu > 0.99$, as presented in Fig. 4.6. To perceive a trend within the scatter of the data points, the contrast values were averaged into bins of $M$, and a third-order polynomial was fitted to the average values.

First, whereas TL reported negative average contrasts at disk center (in fact up to $\theta = 14°$) for all values of magnetogram signal (at all their wavelengths), the present values of the contrast trend do turn positive in the $M$-range between 400 and 900 Mx cm$^{-2}$. This shows that the conclusion of TL does not hold anymore when increasing the spatial resolution. Moreover, the range of contrast of our trend is much larger, extending from -0.08 to 0.035, whereas the average values of TL range between 0 and -0.04 (exluding the "knee"-like abrupt drop of contrast for large magnetogram signals in their data, attributed to micropores and small pores in active regions). The shape of the trend also differs from the one of TL (even at 630.2 nm, cf. Lawrence et al. 1993). Whereas their contrast monotonically drops with $M$, our trend has a clear concave shape for $M > 200$ Mx cm$^{-2}$ with a peak contrast at about 0.035 for $M \sim 700$ Mx cm$^{-2}$. Note that there are still many individual data points with negative contrast in Fig. 4.6, especially in the range $M < 200$ Mx cm$^{-2}$. As will be clarified below and in Sect. 4.3.2, these do not correspond to magnetic elements but rather to weak fields located in intergranular lanes.

I then investigated how the relation between the contrast and $M$ varies with $\mu$, by tiling the data points into the previously defined six $\mu$ intervals, as shown in Fig. 4.7. For $M > 200$ Mx cm$^{-2}$, the trends of the average values exhibit a concave shape in all $\mu$ intervals (like at disk center). Note that TL found concave trends only for $\theta > 14°, \mu < 0.97$, while for $\theta < 14°$ their trend is monotonously decreasing. Further, whereas the contrast curves of Topka et al. (1992) only reach positive values for $\theta > 27°, \mu < 0.89$ (at 630.2 nm), our
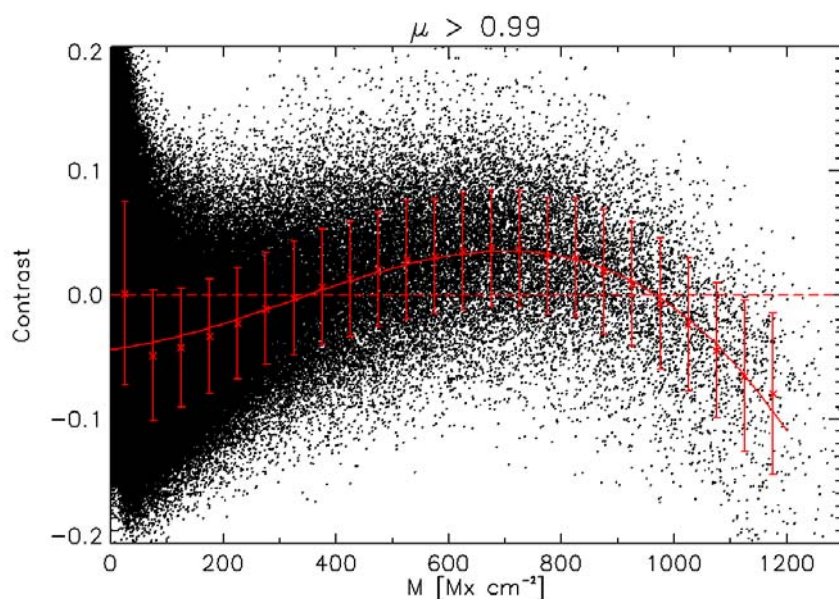
Figure 4.6: Contrast vs. corrected magnetogram signal $M$ at $\mu > 0.99$. Each data point corresponds to one pixel. Red crosses: average values of contrast inside $M$-bins of 50 Mx cm$^{-2}$ from 0 to 1200 Mx cm$^{-2}$. The red error bars are the standard deviations inside each bin. Solid red curve: third-order weighted polynomial fit. Dashed red: guideline for neutral contrast.

trends reach positive values in all $\mu$ intervals, with larger peak contrasts. For example, the data of Topka et al. (1992) (at 630.2 nm) reach a peak contrast of 0.01 and 0.03 at $\mu = 0.89$ and $\mu = 0.73$ respectively, whereas the peak of our contrast trends reach 0.015 for the interval $0.9 < \mu < 0.97$, 0.05 for $0.78 < \mu < 0.9$ and 0.08 for $0.62 < \mu < 0.78$. For comparison, at the much lower spatial resolution of MDI, Ortiz et al. (2002) could not detect any increase of the contrast as a function of magnetogram signal for $\mu > 0.88$ (like TL for $\mu > 0.97$), but the shape of their contrast trends becomes concave as well for lower $\mu$ values. Because the spatial resolution of Ortiz et al. (2002) is considerably lower, their peak contrasts are much lower in all $\mu$ intervals. Particularly for $\mu < 0.42$, our peak reaches 0.15 whereas theirs lies at 0.045. The above shows that the spatial resolution not only affects the contrast values, but also alter the shape of the contrast trend, becoming more concave and with a larger peak as the resolution increases.

Finally, similar to the results of TL and Ortiz et al. (2002), the magnetogram signal at which the peak contrast is reached increases at lower $\mu$, which can be understood by a rough relation between $M$ and the size of underlying flux tubes, assuming the latter vertical and with constant field strength (larger flux tubes have maximum contrast at lower $\mu$ as the LOS must incline more for their "cool floor" to disappear, and reach higher contrasts due to their larger "hot wall" area Spruit 1976, Deinzer et al. 1984, Knölker and Schüssler 1988). However, the assumption of purely vertical fields is doubtful, especially at low $\mu$ values (see Sect. 4.3.2).

Having a closer look to the data points and fitted trends for low $M$ values, one can notice that for values inferior to $M \sim 200$ Mx cm$^{-2}$, the data points seem to concentrate in a "blob" extending over a large contrast range between -0.2 and 0.2 at disk center,
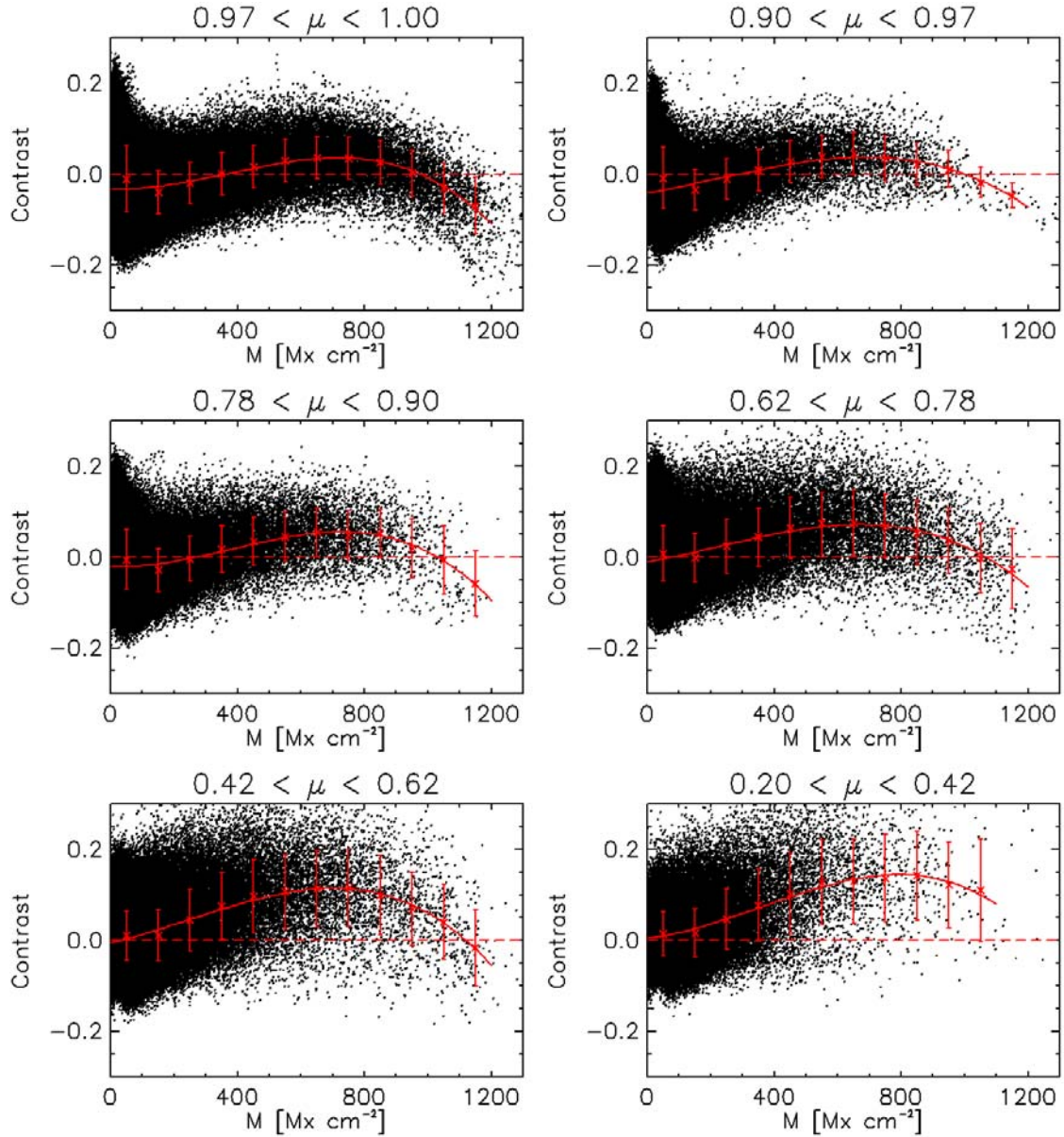
Figure 4.7: Contrast vs. corrected magnetogram signal $M$ for six $\mu$ intervals between $\mu = 1$ and $\mu = 0.2$. Each data point corresponds to one pixel. Red crosses and error bars: average and standard deviations of contrast data in bins of 100 Mx cm$^{-2}$. Solid red curve: third-order polynomial fit. The average values and standard deviations are only calculated for the bins containing more than 10 data points (meaningful standard deviation). Dashed red: guidelines for neutral contrast.

while this range is progressively reduced with $\mu$. This contrast range is typical of pure granulation, with decreasing rms contrast for lower $\mu$. As $\mu$ decreases, this blob extends to larger $M$, and a careful comparison with the PDF($M$) given in Fig. 4.5 convinced me that this blob of weak signals corresponds to the main peak of this PDF, which progressively shifts to larger $M$ because of the $1/\mu$ factor (in the definition of $M$). More information about this blob of weak fields will be obtained in the next subsections.

As in the study of Ortiz et al. (2002), the binning of the data can be reversed to obtain the CLV of contrast for intervals of $M$ (this was impossible in the ground-based study of TL because their data was recorded at a few discrete $\mu$), displayed in Fig. 4.8. Care should be taken when interpreting such plots, however, because a given magnetic feature (even a vertical magnetic element) would probably have different values of $M$ at different $\mu$ (due to varying filling factors), so that the intervals of $M$ cannot be strictly interpreted as given populations of magnetic features. For $M > 250$ Mx cm$^{-2}$, the polynomial trend of the contrast CLV does reach a maximum like the one of Ortiz et al. (2002), but our statistics for large $M$ is too poor to confidently claim that the corresponding $\mu$ values shift to lower $\mu$ as $M$ increases (as expected for vertical flux tubes, and reported in Ortiz et al. 2002). For $M < 150$ Mx cm$^{-2}$, one clearly notices how the contrast range of the data points reduces with the decrease of the granulation contrast rms.

### 4.3.2   …As a function of apparent flux density

From this point on, I will take advantage of the inversion of the full Stokes vector to disentangle the different magnetic parameters $(\gamma, B, \alpha)$ coupled in the definition of $M$, beginning with the unsigned *apparent magnetic flux density* $B_{\mathrm{app}} = B\alpha$ (i.e. net average of the flux density within the resolution element). The PDF($B_{\mathrm{app}}$) has already been presented in Fig. 4.3.

Fig. 4.9 shows the variation of the contrast as a function of $B_{\mathrm{app}}$ for the six usual intervals of $\mu$, analogous to Fig. 4.7 for $M$. Like for $M$, the range of $B_{\mathrm{app}}$ for which the contrast is positive becomes ever larger for lower $\mu$: from 500 to 900 Mx cm$^{-2}$ near disk center, between 350 and 1050 Mx cm$^{-2}$ for $0.78 < \mu < 0.9$, and for all $B_{\mathrm{app}} > 250$ Mx cm$^{-2}$ when $\mu < 0.78$. However, the behaviour of the contrast as a function of $B_{\mathrm{app}}$ differs from its behaviour as a function of $M$ for $\mu < 0.78$. Whereas the contrast as a function of $M$ systematically reaches a clear maximum, the peak is less pronounced as a function of $B_{\mathrm{app}}$. For the interval $0.42 < \mu < 0.62$, the average contrasts rather reach a plateau for $B_{\mathrm{app}} > 900$ Mx cm$^{-2}$, and for $\mu < 0.42$ the contrast even monotonically increases. Further, the maximum values reached by the average contrast in bins of $B_{\mathrm{app}}$ are larger than in bins of $M$, particularly for the two lowest $\mu$ intervals (contrast up to 0.14 vs. 0.12 in $0.42 < \mu < 0.62$, and 0.26 vs. 0.14 in $0.2 < \mu < 0.42$). The shift of the peak contrast toward larger $B_{\mathrm{app}}$ as $\mu$ decreases is also stronger than the corresponding shift as a function of $M$. These differences stem from non-vertical fields, as for purely vertical ones $M = B_{\mathrm{app}}$. At low $\mu$ in particular, the values of $M$ differ from the ones of $B_{\mathrm{app}}$ because non-vertical fields can have a larger longitudinal component than vertical ones (and are subject to have large $M$ due to the $1/\mu$ factor, cf. shift of PDF($M$) in Fig. 4.5). To check the importance of this effect, I plotted the PDF($B_{\mathrm{app}}$) for the pixels having $M > 200$ Mx cm$^{-2}$ (avoiding the blob at weak $M$) in the different $\mu$ intervals, shown in Fig. 4.10. As $\mu$ decreases, the PDF discloses a "contamination" by low $B_{\mathrm{app}}$, particularly for $\mu < 0.42$.
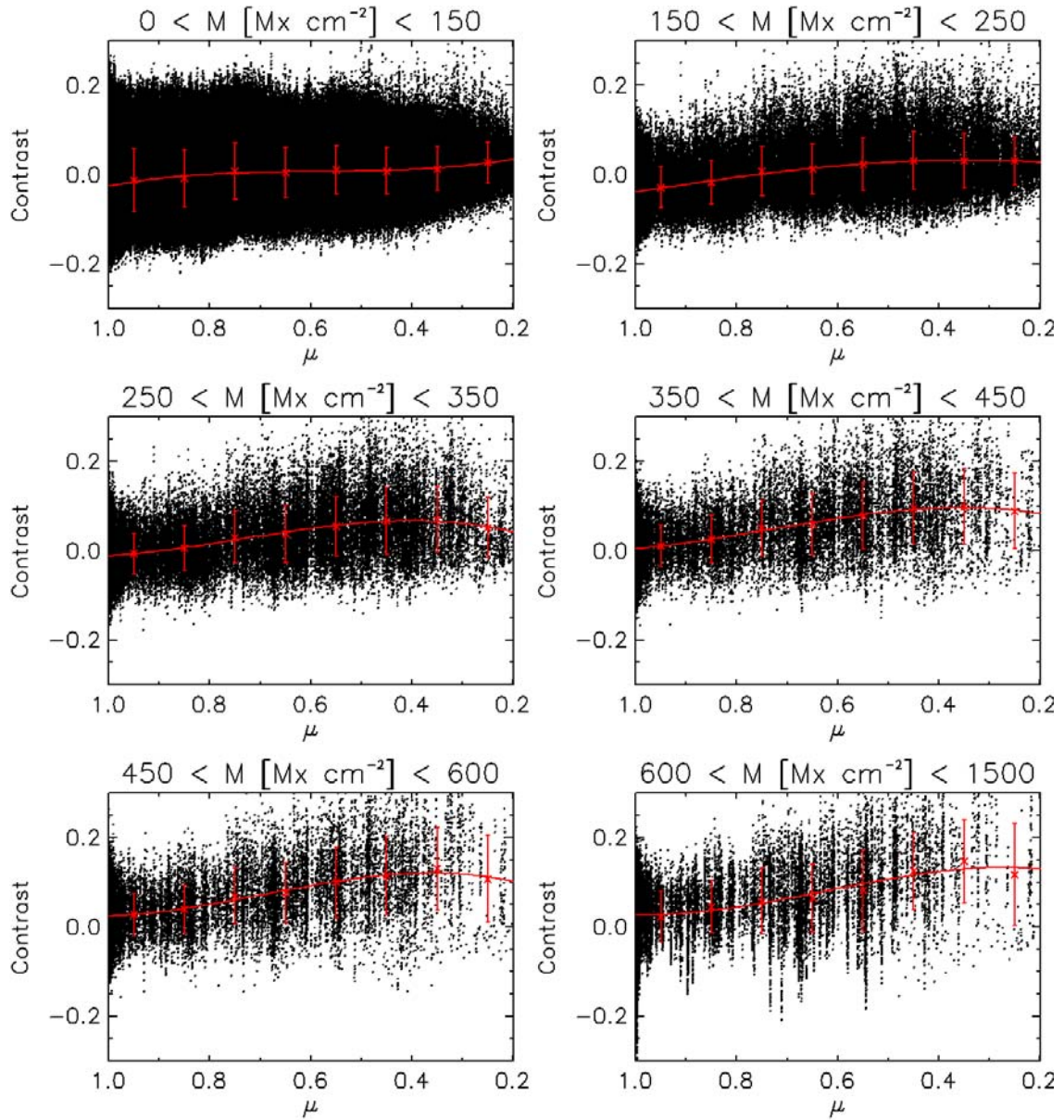
Figure 4.8: CLV of contrast for various intervals of corrected magnetogram signal $M$. Red crosses and error bars: average and standard deviations of the contrast in $\mu$ bins spaced by 0.1. Red curve: third-order polynomial fit.

When $\mu < 0.62$, the PDF indeed peaks at rather low values $B_{app} \sim 100$ Mx cm$^{-2}$. And as we shall confirm below, the fields in the range $B_{app} < 250$ Mx cm$^{-2}$ are essentially tied to granulation, and not to flux concentrations. Assuming that the inference of $B_{app}$ is correct, these weak $B_{app}$ fields thus spoil the contrast vs. $M$ relation at low $\mu$, because their contrast reflects the one of granulation and not of flux concentrations. Regarding the discrepancy between $M$ and $B_{app}$ due to the $1/\mu$ correction factor included in $M$, one can notice that the blob of data points at low signals occupies now a roughly constant range $B_{app} < 250$ Mx cm$^{-2}$, whereas the same blob was extending to larger $M$ values for lower $\mu$ intervals. As mentioned in Sect. 4.3.1, this blob well corresponds to the main peak of the PDF($M$) (Fig. 4.5) including all selected pixels, and whereas the peak shifts to larger $M$ for lower $\mu$ due to the $1/\mu$ factor, the corresponding peak of PDF($B_{app}$) (cf. Fig. 4.3) stays remarkably constant. This constant range $B_{app} < 250$ Mx cm$^{-2}$ of the blob helps to keep a clear distinction between the contrast behaviour of weak fields (tied to granulation) and of stronger flux concentrations.

Let us now examine the CLVs of contrast in intervals of $B_{app}$ displayed in Fig. 4.11. For low signals $B_{app} < 150$ Mx cm$^{-2}$, the CLV has a quasi flat trend, and the decreasing scatter of the data points with decreasing $\mu$ clearly reflects the variation of the granulation contrast rms. The interval $150 < B_{app} < 250$ Mx cm$^{-2}$ seems to be a transition in which the decrease of granulation rms can still be recognized, but with a positive trend nevertheless. Finally, for all intervals $B_{app} > 250$ Mx cm$^{-2}$, the contrast exhibits a clearly positive trend toward the limb, as expected for concentrated flux features. Comparing with the corresponding plots in intervals of $M$ (Fig. 4.8), a striking difference is that there is no clear indication of a maximum in the polynomial fits. And just as the contrast was reaching larger values as a function of $B_{app}$ than as a function of $M$ in $\mu$ intervals, the contrast reaches larger values in the $B_{app}$ intervals than in the $M$ intervals.

We shall now have a closer look at the weaker fluxes and the apparent "blob" in Fig. 4.12, showing the scatterplots of the contrast and the inferred LOS-component of the velocity $v_{los}$ vs. $B_{app}$ at disk center. Note that all the $v_{los}$ of this study were corrected for the gravitational redshift (inducing an offset of 636 m $s^{-1}$ in $v_{los}$, which is deduced assuming a Doppler effect only), but not for the convective blueshift (of $-0.2$ to $-0.5$ km $s^{-1}$ Balthasar 1984, playing only a minor role at Hinode's resolution). Roughly, one can separate the behaviour of the contrast and $v_{los}$ into three ranges of $B_{app}$. The range $B_{app} < 150$ Mx cm$^{-2}$ contains most of the blob points. The decrease of the average contrast is accompanied by an increase of the average $v_{los}$, indicating that the fields progressively shift to intergranular lanes as $B_{app}$ increases. As mentioned previously, the range $B_{app} \in (150, 250)$ Mx cm$^{-2}$ is a kind of transition where the average contrast reaches a minimum while the average $v_{los}$ reaches a maximum. Finally, for $B_{app} > 250$ Mx cm$^{-2}$, the blob is no longer visible and the contrast increases monotonously while $v_{los}$ slowly decreases. In the following, the two first ranges of $B_{app}$ will often be considered without distinction, as both contain blob points. Further hints about the nature of the fields in the range $B_{app} < 250$ (blob) and $B_{app} > 250$ Mx cm$^{-2}$ can be obtained by considering their scatterplot relations between the contrast and the inferred LOS-component of the velocity $v_{los}$ at disk center (Fig. 4.13). As already visible in Fig. 4.12, the contrast and $v_{los}$ are clearly correlated for $B_{app} < 250$ Mx cm$^{-2}$ (the Pearson correlation coefficient is $-0.64$): the contrast tends to have positive values for $v_{los} < 0$ km s$^{-1}$ (upflows, granules) and negative values for $v_{los} > 0$ km s$^{-1}$ (downflows, intergranular lanes). Hence, the range $B_{app} < 250$ Mx cm$^{-2}$ is dominated by
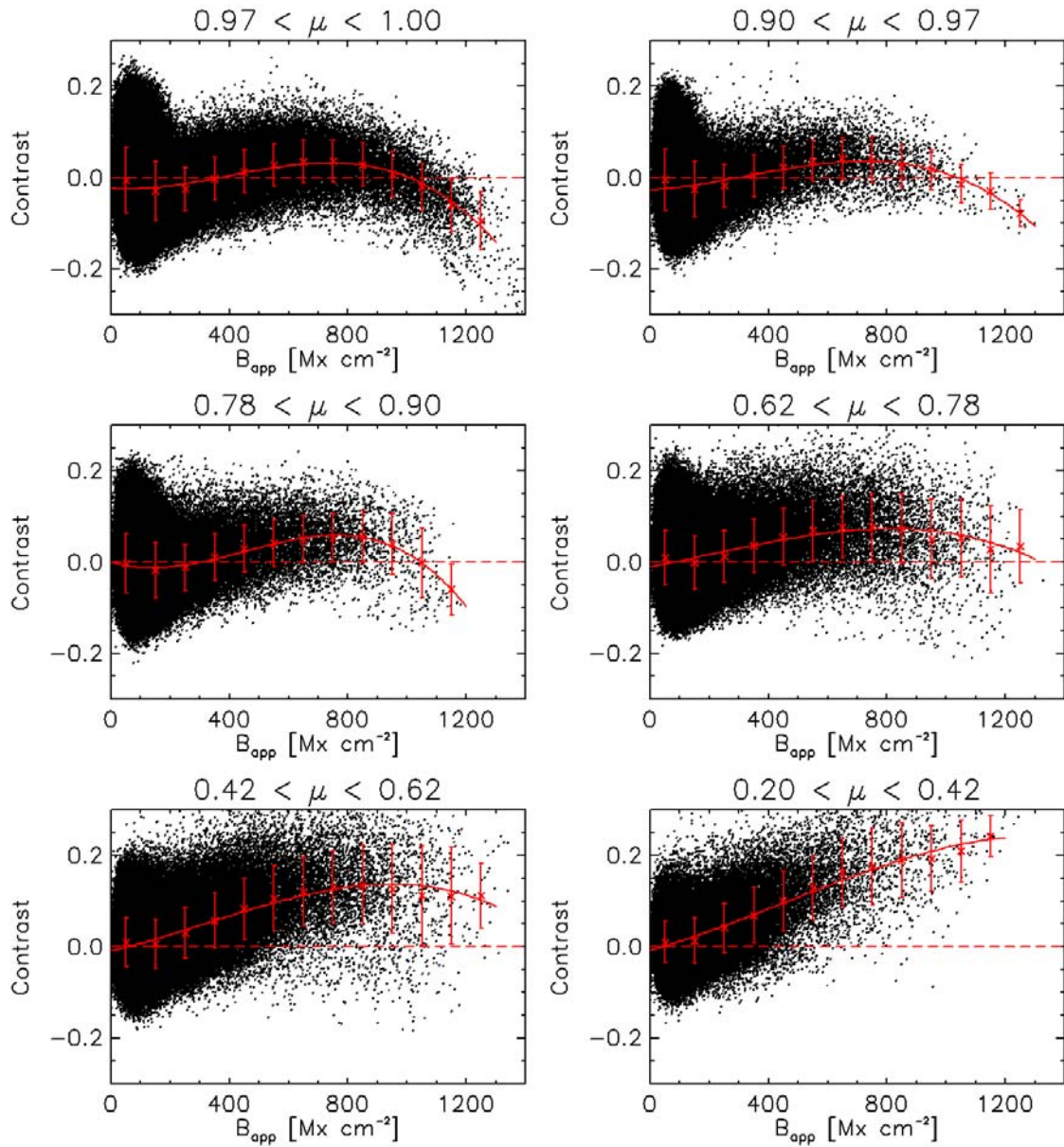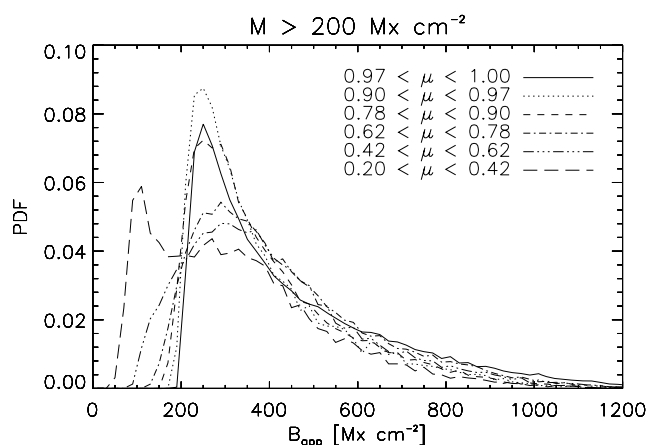
Figure 4.9: Contrast vs. unsigned apparent flux density $B_{app}$ for six $\mu$ intervals between
$\mu = 1$ and $\mu = 0.2$. Red crosses and error bars: average and standard deviations of contrast
data into bins of 100 Mx cm$^{-2}$ (only for bins containing more than 10 data points). Solid
red curve: third-order polynomial fit.

Figure 4.10: PDFs of $B_{\mathrm{app}}$ for $M$ in the range $M > 200$ Mx cm$^{-2}$ for the six intervals of $\mu$.

weak fields occuring in and in between granules, whose contrast simply corresponds to the one at these locations (the fields are too weak to modify the contrast of these regions). Conversely, the range $B_{\mathrm{app}} > 250$ Mx cm$^{-2}$ is dominantly associated with $v_{\mathrm{los}}$ around 0 km s$^{-1}$ (although probably mainly $> 0$ km s$^{-1}$ if correcting for the convective blueshift) with a faint tail toward positive $v_{\mathrm{los}}$, without obvious correlation between the contrast and $v_{\mathrm{los}}$. These fields thus correspond to stronger flux concentrations with inhibited flows. This can be seen as well in Fig. 4.14, showing subfields of the continuum maps roughly centered within the six usual $\mu$ intervals, where the locations $B_{\mathrm{app}} > 250$ Mx cm$^{-2}$ have been contoured. Note that the contrasts of these contoured regions become evidently superior to the granular contrast only in the three subfields closest to the limb. Having a look at the values of $B_{\mathrm{app}}$ within the same subfields (Fig. 4.4, saturated at $B_{\mathrm{app}} = 250$ Mx cm$^{-2}$) reveals that these locations essentially coincide with the network, as well as with some strong internetwork elements. In what follows I will thus refer to the interval $B_{\mathrm{app}} < 250$ Mx cm$^{-2}$ as the *granulation field regime* (either due to small filling factors or small field strengths, see Sect. 4.3.4) and to the interval $B_{\mathrm{app}} > 250$ Mx cm$^{-2}$ as the *concentrated field regime*.

### 4.3.3   ...As a function of apparent flux density and inclination

As we just have decoupled $B_{\mathrm{app}}$ from $M$, the next step is to consider the dependence of the contrast on both $B_{\mathrm{app}}$ and the inclination $\gamma$ with respect to the LOS. This is also motivated by the concerns raised by TL about the extent to which their results depend on the inclination of the magnetic fields, since they were only characterizing the variation of contrast as a function of magnetogram signal, assuming the fields vertical (see Topka et al. 1997).

We shall first have a look at how $\gamma$ distributes for the two regimes of "granulation fields" ($B_{\mathrm{app}} < 250$ Mx cm$^{-2}$) and "concentrated fields" ($B_{\mathrm{app}} > 250$ Mx cm$^{-2}$), which is illustrated in Fig. 4.15 by the PDFs of $\gamma$ for the usual $\mu$ intervals. The PDFs of the granulation fields resemble the one shown in Fig. 4.3 for all selected pixels, except that it does not exhibit the "wings" of vertical fields near disk center. As expected for inter-granular flux concentrations, the PDFs of the concentrated fields reveal them to be close to vertical. Near disk center ($0.97 < \mu < 1$), the PDF peaks at 15° and 165° for the two polarities, and the two peaks come closer together as $\mu$ decreases.
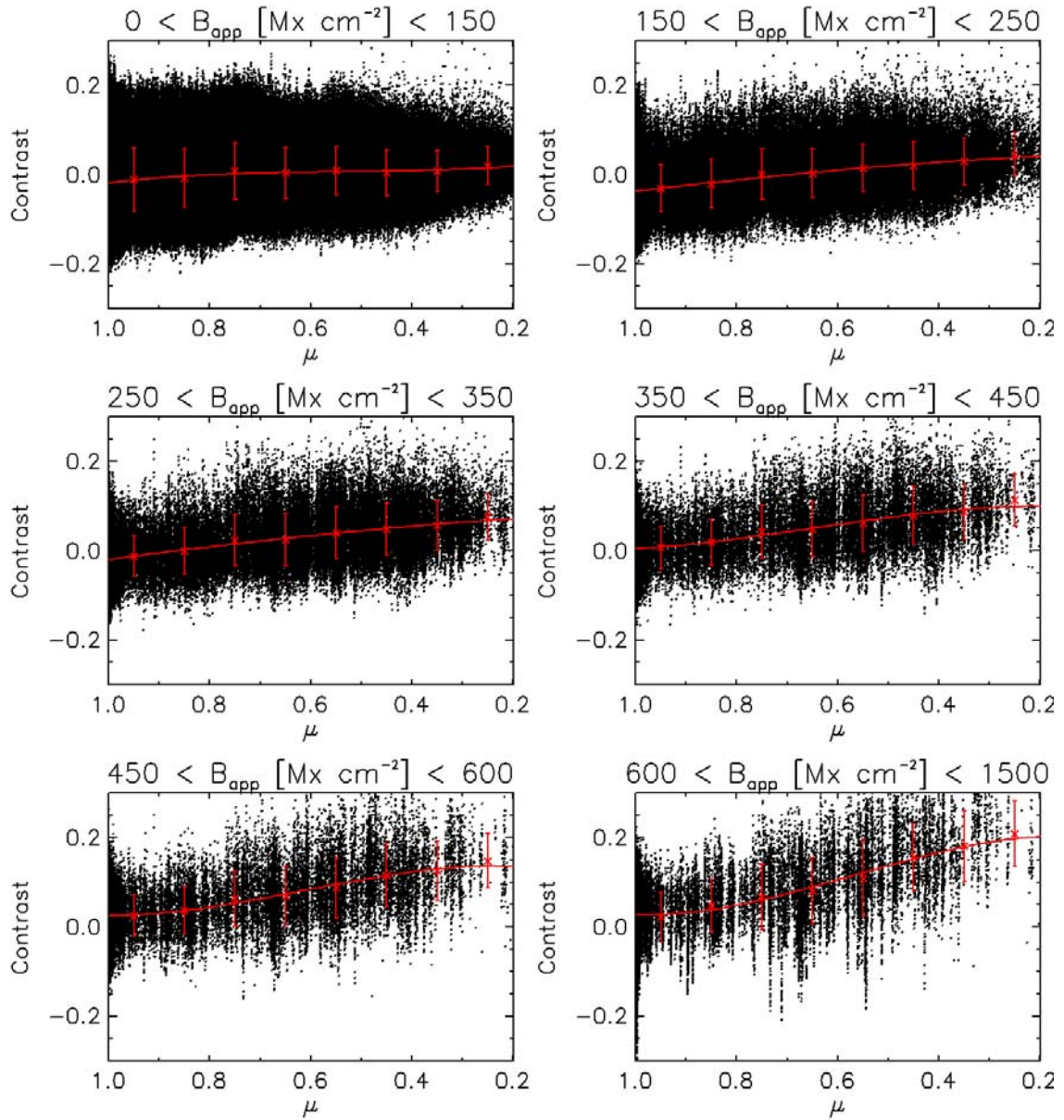
Figure 4.11: CLV of contrast for various intervals of apparent flux density $B_{\mathrm{app}}$. Red crosses and error bars: average and standard deviations of the contrast in $\mu$ bins of 0.1. Red curve: third-order polynomial fit.
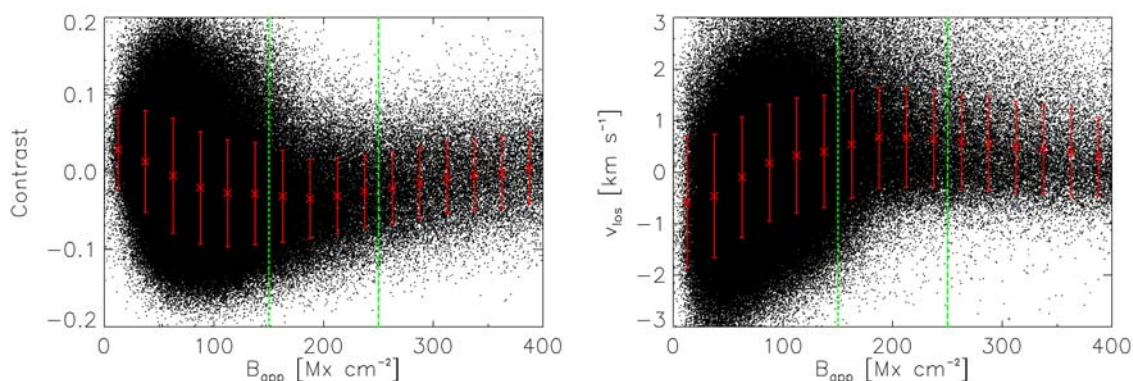
Figure 4.12: Scatterplot of the contrast (left) and $v_{los}$ (right) vs. $B_{app}$ at disk center ($\mu > 0.99$). Red crosses and bars: average values and standard deviations in bins of $B_{app}$ of width 25 Mx cm$^{-2}$. Dashed green: Guidelines separating the fields with $B_{app} > 250$ Mx cm$^{-2}$ and $B_{app} < 150$ Mx cm$^{-2}$.
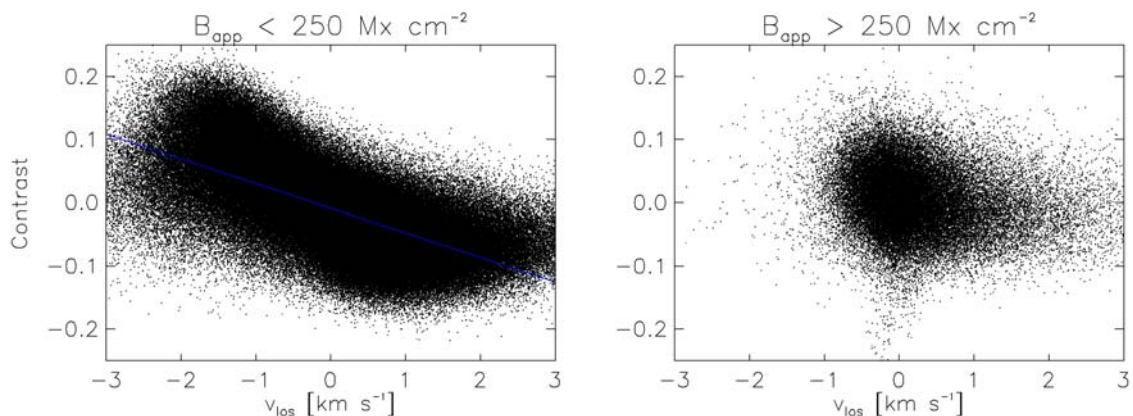


Figure 4.13: Left: Scatterplot of the contrast vs. LOS-component of the velocity $v_{los}$ for $B_{app} < 250$ Mx cm$^{-2}$ and $\mu > 0.99$ (disk center). Solid blue: linear regression. Right: Same for $B_{app} > 250$ Mx cm$^{-2}$.

As the parameter $\gamma$ adds a dimension to the contrast dependence, we shall first restrict the problem to the dependence of the contrast on $\gamma$ for intervals of $B_{app}$ at disk center ($\mu > 0.99$), in Fig. 4.16. As indication, pixels where the amplitudes in $Q$ or $U$ is larger than 4.5 rms (corresponding to inclined fields) are plotted in green.

In the interval of $B_{app}$ between 50 and 150 Mx cm$^{-2}$, the average contrast values in bins of $\gamma$ exhibit a clear trend, as the largest average contrast lies above the standard deviation bars of the lower contrasts. The contrast is largest for the more horizontal fields ($60° < \gamma < 130°$), then the contrast lowers as the fields become less inclined ($20° < \gamma < 60°, 130° < \gamma < 160°$), and finally increases again while reaching some plateau of slightly negative values around $-0.02$ for the more vertical fields with $\gamma < 20°$ and $\gamma > 160°$. As pointed out in the previous Section, this interval of $B_{app}$ is completely dominated by the contrast of granulation, so that the more horizontal fields (brighter pixels) can be associated to granules, and the more vertical ones (darker pixels) to intergranules (see
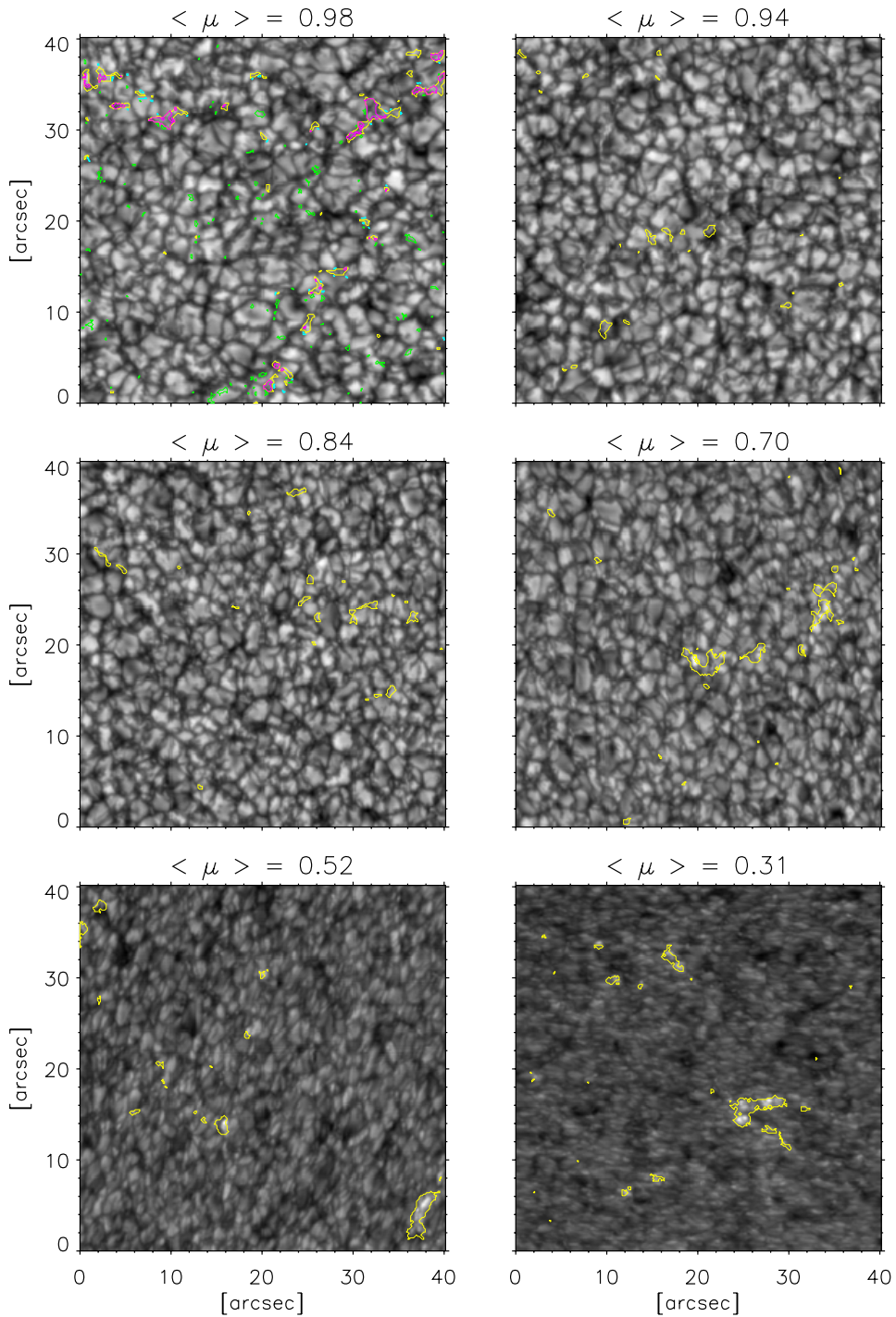
Figure 4.14: Chosen subfields from continuum maps at six different $\mu$ within the usual $\mu$ intervals. $\langle\mu\rangle$ indicates the average $\mu$ over the subfield. Yellow contours: concentrated fields $B_{app} > 250$ Mx cm$^{-2}$. Pink contours ($\langle\mu\rangle = 0.98$): inclined concentrated fields $B_{app} > 250$ Mx cm$^{-2}$ and $Q$ or $U$ exceeding 4.5 rms. Green contours ($\langle\mu\rangle = 0.98$): weak inclined fields with $B_{app} < 250$ Mx cm$^{-2}$ and $Q$ or $U$ exceeding 4.5 rms. Cyan contours ($\langle\mu\rangle = 0.98$): weak vertical fields with $B_{app} < 250$ Mx cm$^{-2}$ and $\gamma < 20°$ or $\gamma > 160°$.
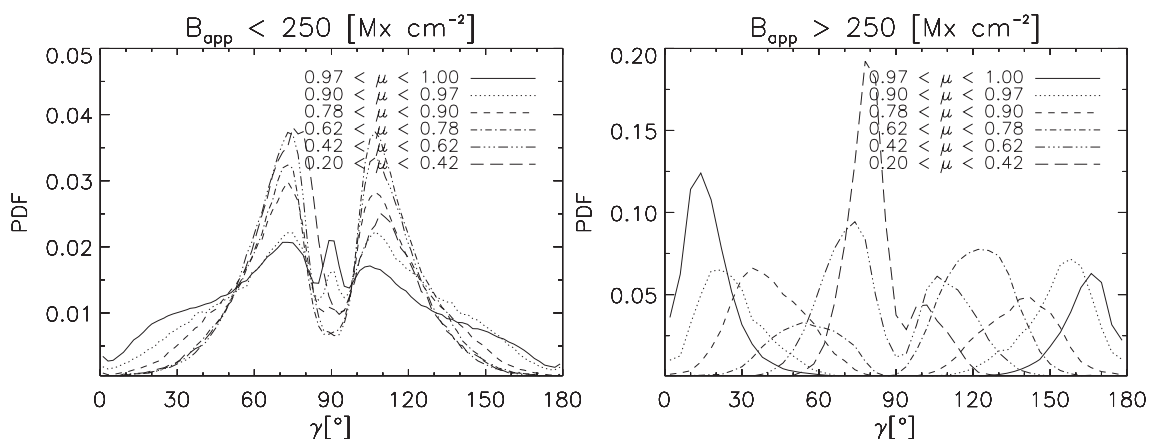
Figure 4.15: Left: Same for the fields with $B_{app} < 250$ Mx cm$^{-2}$ ("granulation fields") in the usual $\mu$ intervals. Right: PDF of the inclination $\gamma$ for pixels where $B_{app} > 250$ Mx cm$^{-2}$ ("concentrated fields").

below and Fig. 4.17 as well).

The same trend is noticeable for $B_{app}$ in the range 150 to 250 Mx cm$^{-2}$, where we can perceive some kind of dichotomy between horizontal fields ($Q, U$ signals near $\gamma = 90°$) and more vertical fields. As noted already in Sect. 4.3.2, in spite of being still dominated by granulation fields, this range of $B_{app}$ represents some transition between the granulation field regime and the concentrated field regime (see previous Sect.) In the concentrated field regime, the interval of $B_{app}$ between 250 and 350 Mx cm$^{-2}$ contains more vertical fields, but there are still pixels with $\gamma$ up to 60° and 140° (with $Q$ or $U$ signals). And in both polarities, the contrast decreases as the fields become more transverse. The locations of these inclined concentrated fields where $B_{app} > 250$ Mx cm$^{-2}$ and $Q$ or $U$ exceed 4.5 rms have been contoured in the subfield at $\langle\mu\rangle = 0.98$ in Fig. 4.14 (pink). The contours show that these fields are either associated with large network features (e.g. large structure at $x = 31''$, $y = 31''$), or are located close to the boundaries of smaller features. This could then be attributed to the expansion of magnetic flux concentrations with height, causing the field lines to bend radially away from the center of the flux concentrations, the effect being stronger for larger features. Finally, for $B_{app}$ between 350 and 450 Mx cm$^{-2}$, the fields are even more vertical, but the decreasing trend of the average contrast values with the transversality of the fields is still visible.

As it was previously shown that the fields in the range $B_{app} < 250$ Mx cm$^{-2}$ are associated with granulation, the variation of their contrast with the inclination can be clarified by examining the relation between $v_{los}$ and $\gamma$ in Fig. 4.17. It is remarkable that the trend of the average $v_{los}$ is similar to the reverse of the trend of the contrast as a function of $\gamma$ (cf. Fig. 4.16), owing to the negative correlation between the contrast of these fields and $v_{los}$ (cf. Sect. 4.3.2). We can see that for $\gamma < 50°$ and $\gamma > 140°$, the average values of $v_{los}$ are close to 1 km s$^{-1}$ and most data points have positive $v_{los}$, meaning that in this range of $\gamma$ the fields are mostly located in the intergranular lanes. For $50° < \gamma < 140°$, the average $v_{los}$ decreases as the fields becomes more horizontal and more pixels aquire negative values of $v_{los}$. For $80° < \gamma < 110°$, the average values are near to $-0.6$ km s$^{-1}$ while individual pixels span a range of $v_{los}$ between $-2$ and $+1$ km s$^{-1}$, and almost all the pixels have $Q$ or $U$ larger than 4.5 rms. Horizontal fields thus
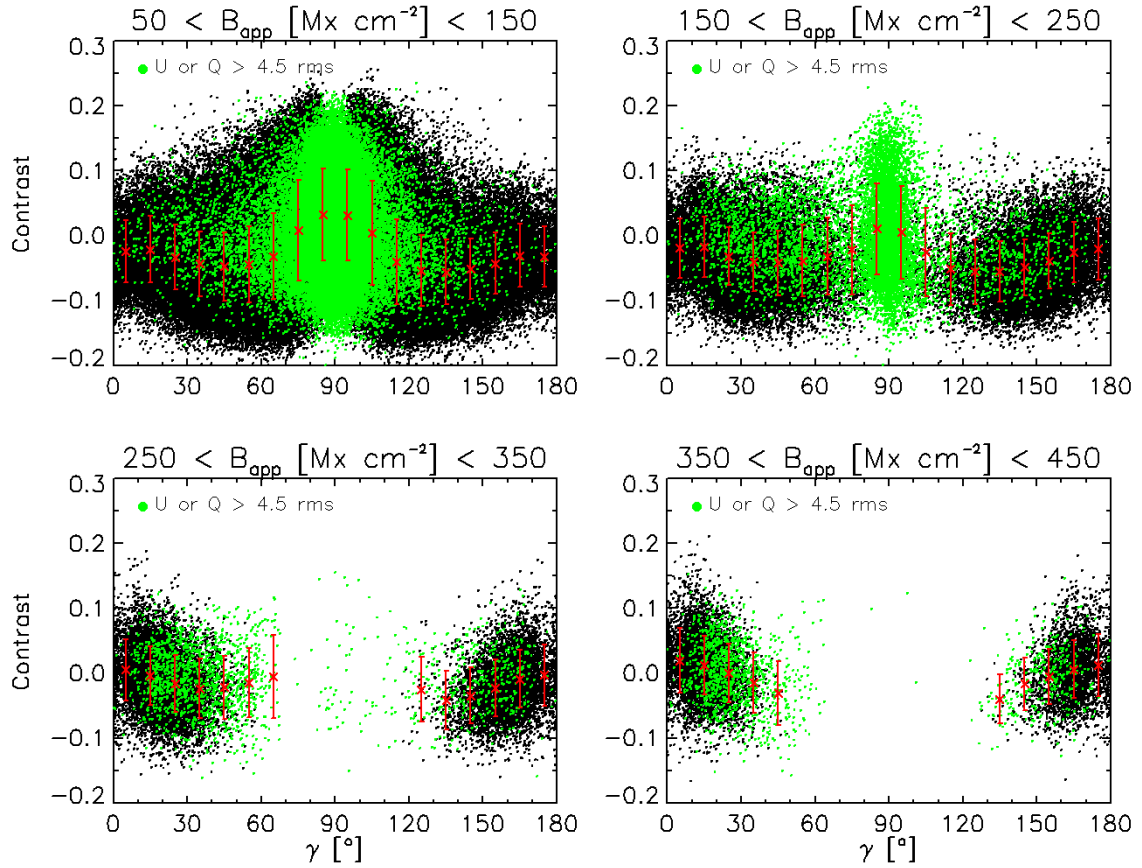
Figure 4.16: Contrast as a function of the inclination $\gamma$ for various intervals of $B_{\mathrm{app}}$ at disk center ($\mu > 0.99$). Green data points: pixels where the Stokes $Q$ or $U$ amplitude is larger than 4.5 rms. Red crosses and bars: Averages and standard deviations of the contrast in bins of $10°$ of $\gamma$, only for the bins with more than 50 pixels.

have a preference for granules. This can be visualized as well by contouring the regions where $B_{\mathrm{app}} < 250$ Mx cm$^{-2}$ and $Q$ or $U$ is above 4.5 rms in the subfield $\langle\mu\rangle = 0.98$ of Fig. 4.14 (green). It can be noticed that among these fields, the ones lying onto granules are preferably located near the granular edges. This is consistent with previous results by Lites et al. (2007) and Lites et al. (2008) (obtained by their calibration of the "fractional net linear polarization"). Hence, granules seem to be "wrapped" by weak fields, with rather horizontal fields at their top and progressively more vertical ones at their border and in the intergranular lanes.

The information presented above can be condensed in one plot by performing a two-dimensional binning of the contrast and $v_{\mathrm{los}}$ as a function of $B_{\mathrm{app}}$ and $\gamma$, as shown in Fig. 4.18. For all $B_{\mathrm{app}} < 250$ Mx cm$^{-2}$, one sees even more clearly how the contrast varies with $\gamma$, first with the zone of neutral and slightly negative contrasts ($\gamma < 20°$, $\gamma > 160°$), then the decrease to negative values before increasing again to large positive values for horizontal fields (onto granules). Note the remarkably similar pattern of the contrast and $v_{\mathrm{los}}$ in this granulation field regime: as the contrast increases, the downflows decrease. One can also differentiate between the range $B_{\mathrm{app}} < 150$ Mx cm$^{-2}$, where the horizontal fields are on average associated with large contrasts and upflows (due to their location

Figure 4.17: Scatterplot of the LOS-component of the velocity $v_{los}$ vs. inclination $\gamma$ in the granulation field regime $B_{app} < 250$ Mx cm$^{-2}$ and at disk center ($\mu > 0.99$).
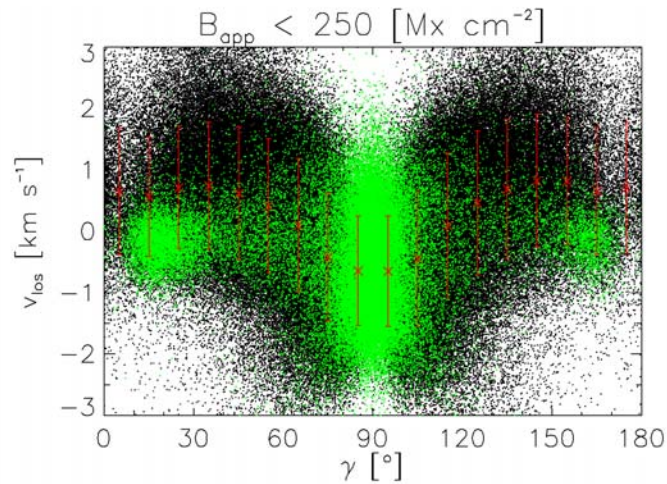
on bright granules), and the range $B_{app}$ between 150 and 250 Mx cm$^{-2}$ (between dashed lines), where the contrast is rather neutral for horizontal fields and the upflows weaker. It was checked that the corresponding pixels occupy tiny parts of granular edges or nearby parts of the intergranular lanes (their contours are not shown because there are very few cases in one map only). It is thus possible that these pixels are slightly darker simply due to their locations. It should be noted that the range $B_{app} < 50$ Mx cm$^{-2}$ (excluded from Fig. 4.17) contains large contrasts spreading over all $\gamma$, a sign that the inference of $\gamma$ is probably unreliable for such weak fields. Moreover, the standard deviations of $v_{los}$ become excessively large in this range of $B_{app}$.

The rather vertical fields in the range $B_{app} < 250$ Mx cm$^{-2}$ for which the contrast is almost neutral deserve some attention. Contouring these weak vertical fields ($B_{app} < 250$ Mx cm$^{-2}$, $\gamma < 20°$, $\gamma > 160°$) in the $\langle \mu \rangle = 0.98$ subfield of Fig. 4.14 (cyan contours) provides additional evidence for concentrated fields. The contours often lie at the immediate vicinity of strong concentrated elements ($B_{app} > 250$ Mx cm$^{-2}$), or are located in intergranular lanes. These fields could thus correspond to some boundary layers between the stronger elements and their surroundings, or simply to smaller magnetic elements. Their field strength indeed ranges between 400 and 1000 G (see corresponding subfield for $B$ in Fig. 4.4 and PDF($B$) for vertical fields with $B_{app} \in (150, 250)$ Mx cm$^{-2}$ in Fig. 4.24).

For $B_{app} > 250$ Mx cm$^{-2}$, the contrast is almost everywhere positive, except for the most inclined weak fields and the strong fields with negative contrast (in the positive magnetic polarity). The contrast increases quickly with $B_{app}$, and reaches its largest values in the range between 500 and 800 Mx cm$^{-2}$, for the fields that are most vertical. These fields are associated with $v_{los}$ close to 0 km s$^{-1}$ or slightly negative. Even in this range of $B_{app}$, the contrast drops quickly back to neutral as the fields incline. For $B_{app} > 1000$ Mx cm$^{-2}$, the contrast decreases again (in the positive polarity) to negative, probably due to the presence of some micropores not removed from the images.

Using the same 2D-binning representation, we can further grasp how the contrast depends on both $B_{app}$ and $\gamma$ in the six $\mu$ intervals usually considered, the first three ($0.78 < \mu < 1$) in Fig. 4.19 and the other three ($\mu < 0.78$) in Fig. 4.20. In the regime $B_{app} < 250$ Mx cm$^{-2}$, the variation of contrast with $\gamma$ is less and less pronounced as $\mu$ decreases. This is not surprising since this regime is dominated by the granulation contrast, which exhibits a decreasing rms for decreasing $\mu$.
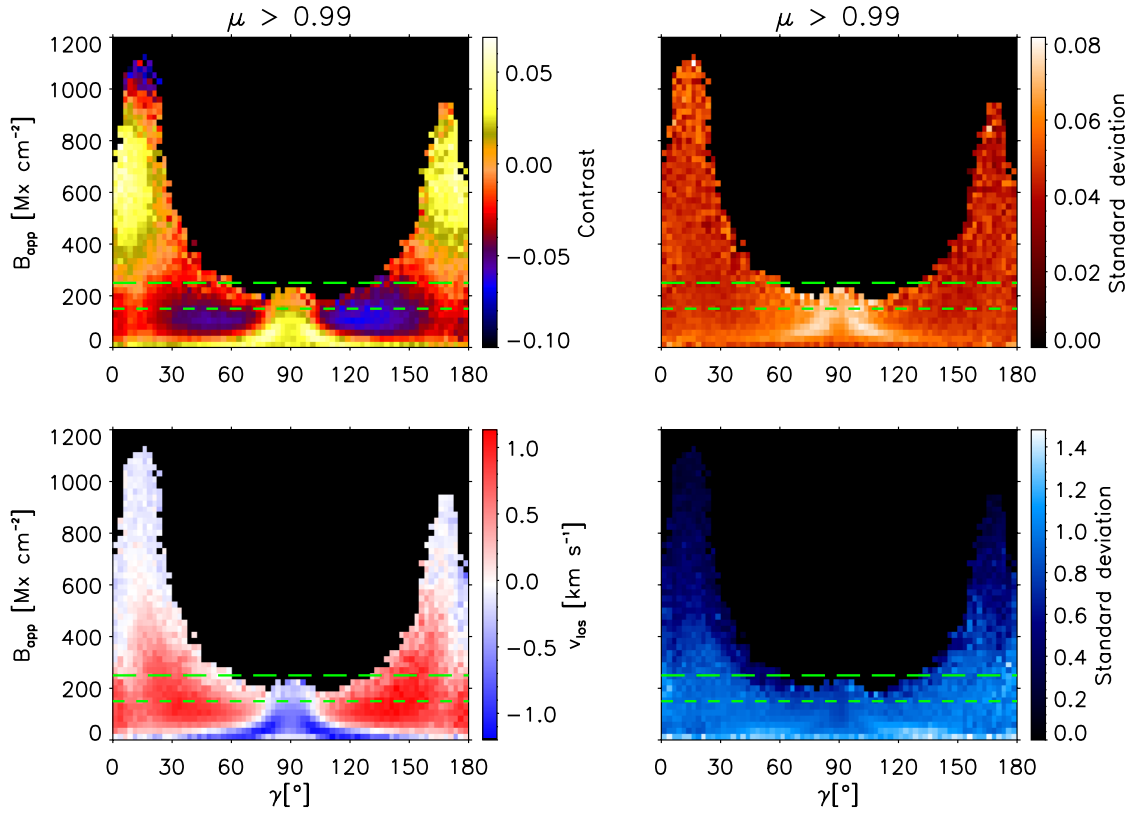
Figure 4.18: Variation of the contrast (upper panel) and $v_{los}$ (lower panel) as a function of both $B_{app}$ and $\gamma$ at disk center ($\mu > 0.99$) in a 2-dimensional binning representation. Left: Average of the contrast into bins of 2.5°-width in $\gamma$ and 25 Mx cm$^{-2}$-width in $B_{app}$. Right: Standard deviation of the contrast and $v_{los}$ in the same bins. Dashed green: limit $B_{app} = 250$ Mx cm$^{-2}$ between the granulation field regime and the concentrated field regime (long dashed), and limit $B_{app} = 150$ Mx cm$^{-2}$ (short dashed). The full color scale of the contrast varies between the minimum and maximum average values. Bins with less than 10 data points (pixels) are set to black.

For the concentrated fields $B_{app} > 250$ Mx cm$^{-2}$, the contrast mostly depends on $B_{app}$ in the same way as discussed in Sect. 4.3.2. For $\mu < 0.78$, the contrast is entirely positive regardless of $\gamma$. Note that the contrast increases abruptly in the last two $\mu$ intervals. Interestingly, the somewhat weak dependence on inclination varies with $\mu$. Whereas at disk center the most longitudinal fields were the brightest, as $\mu$ decreases below 0.78, the contrast becomes largest for larger inclinations. As the $\mu$ intervals are rather wide, this variation with $\gamma$ could be simply explained by the contrast CLV of magnetic elements. Quasi-vertical magnetic elements located at a lower $\mu$ will have a larger contrast and be attributed a larger $\gamma$ roughly equal to their heliocentric angle. To give an idea, the average contrast of the fields with 600 Mx cm$^{-2} < B_{app} < 1500$ Mx cm$^{-2}$ increases by about 0.06 between $\mu = 0.4$ and $\mu = 0.6$ (see Fig. 4.11).
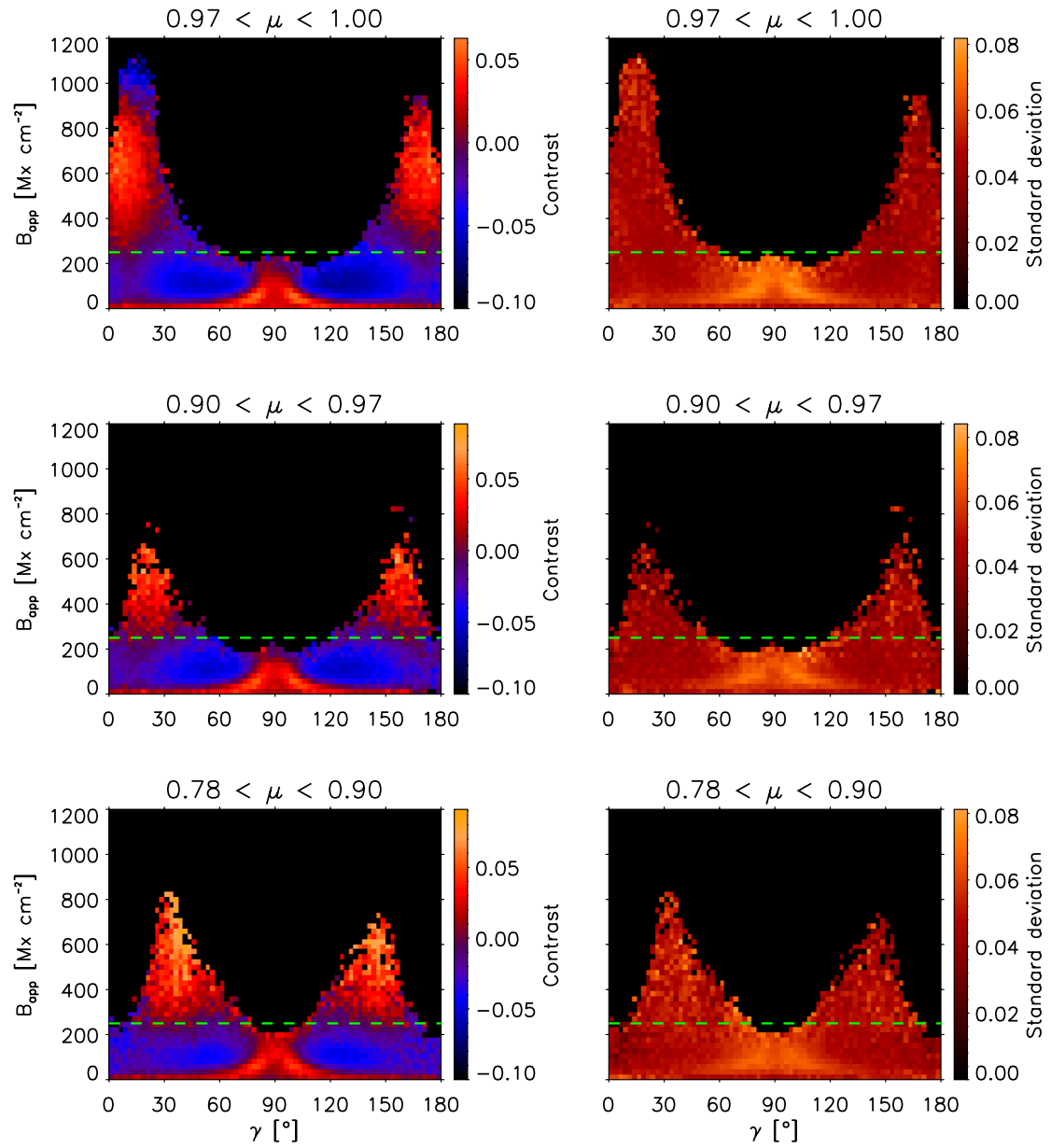
Figure 4.19: Same as Fig. 4.18 for three intervals of $\mu$ with $\mu > 0.78$. A common colour scale is used for the average contrasts in all $\mu$ intervals including those plotted in Fig. 4.20. This colour scales differs from that employed in Fig. 4.18.
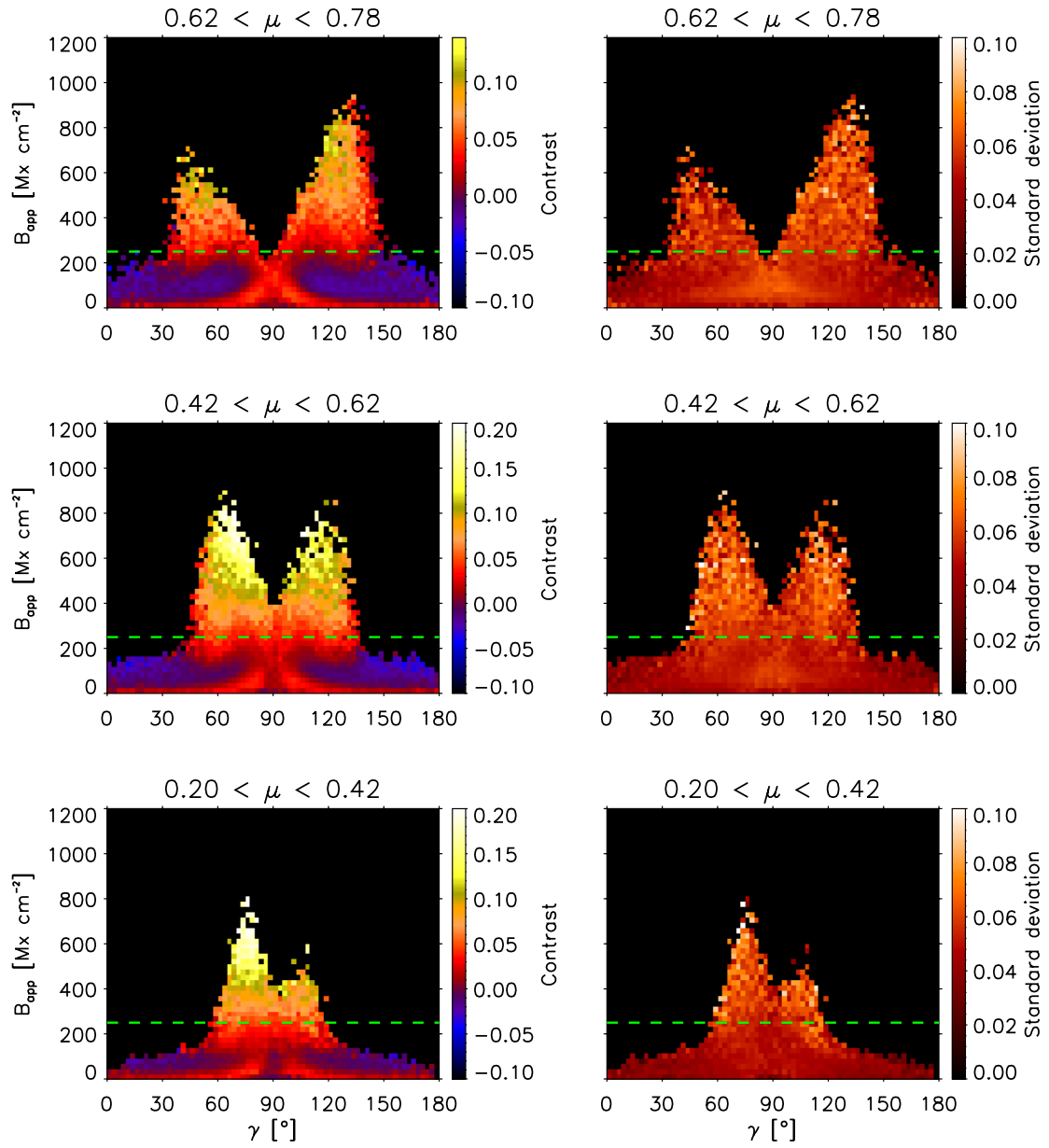
Figure 4.20: Same as Fig. 4.19 for three intervals of $\mu$ in $0.2 < \mu < 0.78$. The same color scale is used as in Fig. 4.20.

### 4.3.4   ...As function of field strength and filling factor

In this Section, I further decouple $B_{\mathrm{app}}$ into the inferred filling factor $\alpha$ and its associated intrinsic field strength $B$, which at the same time brings us closer to the limit of reliability of the inversions.

   As in the preceding Sections, we shall first examine the PDFs of $\alpha$ and $B$ in Fig. 4.21, distinguishing the granulation field from the concentrated field regime. For the granulation fields, we can notice the strong increase of low $\alpha$ (peak between 0.1 and 0.2) in the two lowest $\mu$ bins. This could be already noticed in the PDF of Fig. 4.3 when considering all pixels (above polarization thresholds), and can now be attributed to the weak granulation fields. This increase of low filling factors close to the limb could be induced by various effects: the increasing area of solar surface projected in the pixels, the loss of detected flux due to cancellation of mixed polarities in this larger effective resolution element, and possibly the increasing diffraction and stray light contamination of the intergranular lanes due to the decrease of the granulation contrast rms. The PDF of the inferred intrinsic field strength is roughly self-similar at all $\mu$, with peaks between 100 and 150 G and a long tail toward larger field strengths.

   For the concentrated field regime, the increase of the peak of $\alpha$ close to 1 is striking, although it was already visible to a lesser extent in the PDF of all selected pixels (cf. Fig. 4.3). This could be due to the progressive inclination of the strong fields with respect to the LOS (filling an ever larger portion of the pixels), and/or to the expansion of the flux concentrations with height. However, the interpretation of $\alpha$ as a geometrical filling factor is not straightforward as it also accounts for the effects of telescope diffraction (see Sect. 4.2.3). Note that since the maximum field strength in our data is of about 2000 G, the minimum filling factor in the range $B_{\mathrm{app}} > 250$ Mx cm$^{-2}$ is 0.125. The PDF($B$) near disk center presents a double peak, with a population of equipartion fields (peak around 500 G) and of kG magnetic elements (peak around 1100 G). This distribution is reminiscent of the PDF obtained by Lites (2002), using a threshold on the apparent longitudinal flux density corresponding to "network-like" elements. This is not surprising as we saw that the range $B_{\mathrm{app}} > 250$ Mx cm$^{-2}$ indeed isolates mostly network-like features in the subfields of $B_{\mathrm{app}}$ (Fig. 4.4). However, the population of inferred kG elements strongly decreases in favor of the equipartition one as $\mu$ lowers, in a strikingly similar fashion as the peak of $\alpha$ close to 1 amplifies. This observation raises doubts about the reliability of the inference of $B$ and $\alpha$ as $\mu$ varies, since they are strongly interdependent and the interpretation of $\alpha$ at different $\mu$ is unclear. For these rather strong fields, we can indeed assume that the distribution of $B_{\mathrm{app}}$ is reliable (the signals are well above the polarization thresholds), and since the range of $B_{\mathrm{app}}$ does not vary significantly in the different $\mu$ intervals (see Fig. 4.3 and Fig. 4.9), an increase of the inferred $\alpha$ must consequently be accompanied by a decrease of the associated $B$. Although this could be physically explained by a decrease of $B$ associated with the expansion of the flux concentrations with height (Frazier and Stenflo 1972, Stenflo et al. 1987, Solanki et al. 1987, Zayer et al. 1989, Bruls and Solanki 1995), care should thus be taken in interpreting these last results, at least the ones off-disk center [6].

   At disk center, the dependence of the contrast on $\alpha$ and $B$ can be well captured by directly examining a 2D-binning representation of the contrast and $v_{\mathrm{los}}$ as functions of

---

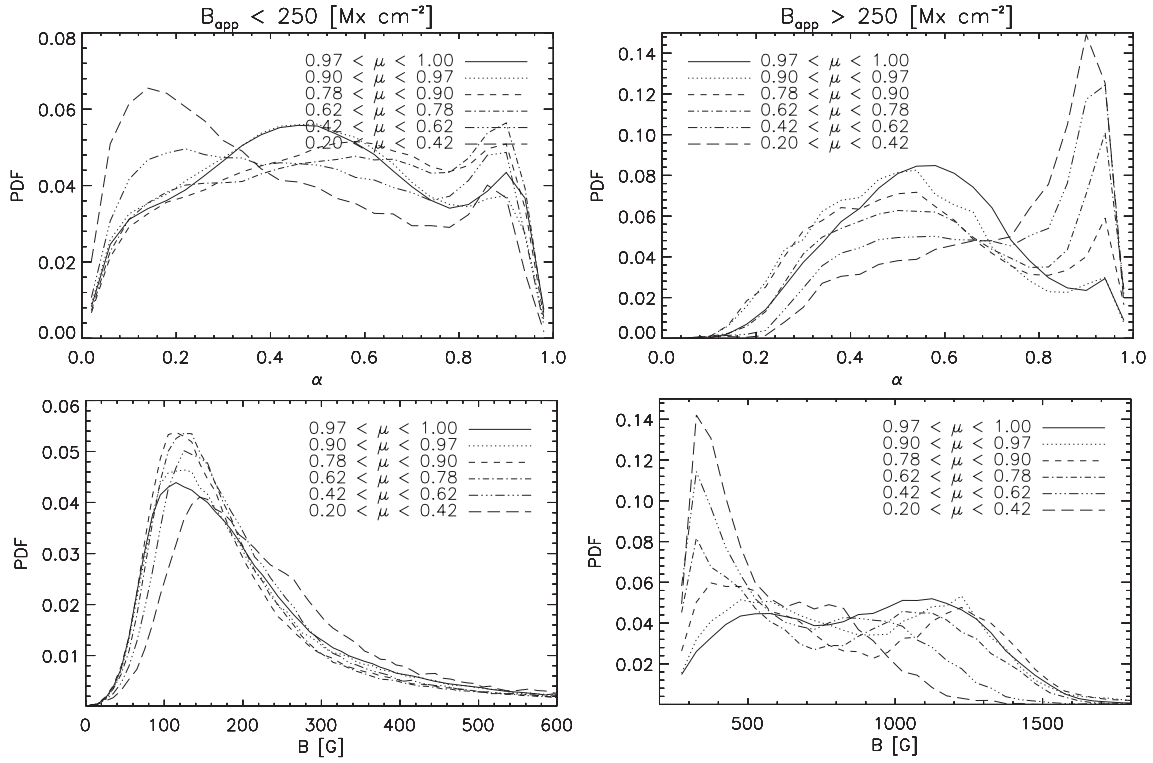[6]This could possibly be due to the inversion of a single line.

Figure 4.21: Left column: PDFs of filling factor $\alpha$ and intrinsic field strength $B$ for the granulation field regime, in the six $\mu$ intervals usually considered. Right column: Same for the concentrated field regime.

these two magnetic parameters, cf. Fig. 4.22. Qualitatively, it can be noticed that the contrast behaves similarly whether we follow a variation in $\alpha$ at constant $B$ or vice-versa. In other words, Fig. 4.22 illustrates that there is some symmetry in $B$ and $\alpha$ and that as a general rule, the variation of contrast is dictated by $B_{app}$. For instance, in the range $B_{app} < 250$ Mx cm$^{-2}$, an increase in $B$ or $\alpha$ leads to a general decrease of contrast and a shift from granules to intergranules, as indicated by the associated increase of $v_{los}$ (cf. variation with $B_{app}$ in Fig. 4.18). Passed the limit of 250 Mx cm$^{-2}$, the contrast becomes increasingly brighter with $B_{app}$, until eventually decreasing in the micropore region.

Quantitatively, however, the contrast is not constant at fixed $B_{app}$. In the concentrated field regime, the parameter region around $\alpha \sim 0.5$ and $B \sim 1500$ G has the largest contrast. It can be noticed that $v_{los}$ is slightly negative in this region, but would possibly increase to $\sim 0$ km s$^{-1}$ after removing the granular blueshift of 0.2-0.5 km s$^{-1}$. In the dark downflow region for $B_{app} < 250$ Mx cm$^{-2}$, the largest downflows coincide with the darkest pixels around $\alpha \sim 0.4$ and $B \sim 400$ G (see below).

More insight into the granulation field regime can be obtained by visualizing the scatterplots of $v_{los}$ vs. $\alpha$ and $B$ shown in Fig. 4.23. As in Fig. 4.22, the dependence of the average $v_{los}$ on $B$ and $\alpha$ is qualitatively very similar: $v_{los}$ increases first with $\alpha$ and $B$ until reaching a maximum around $\alpha \sim 0.4, B \sim 400$ G, after which $v_{los}$ decreases slowly. This indicates that the very weak fluxes ($\alpha < 0.2, B < 200$ G) are on average located on granules, and reflects the well-known fact that progressively more intense fields tend to have an increasing preference for intergranular lanes. I note that most of these granulation
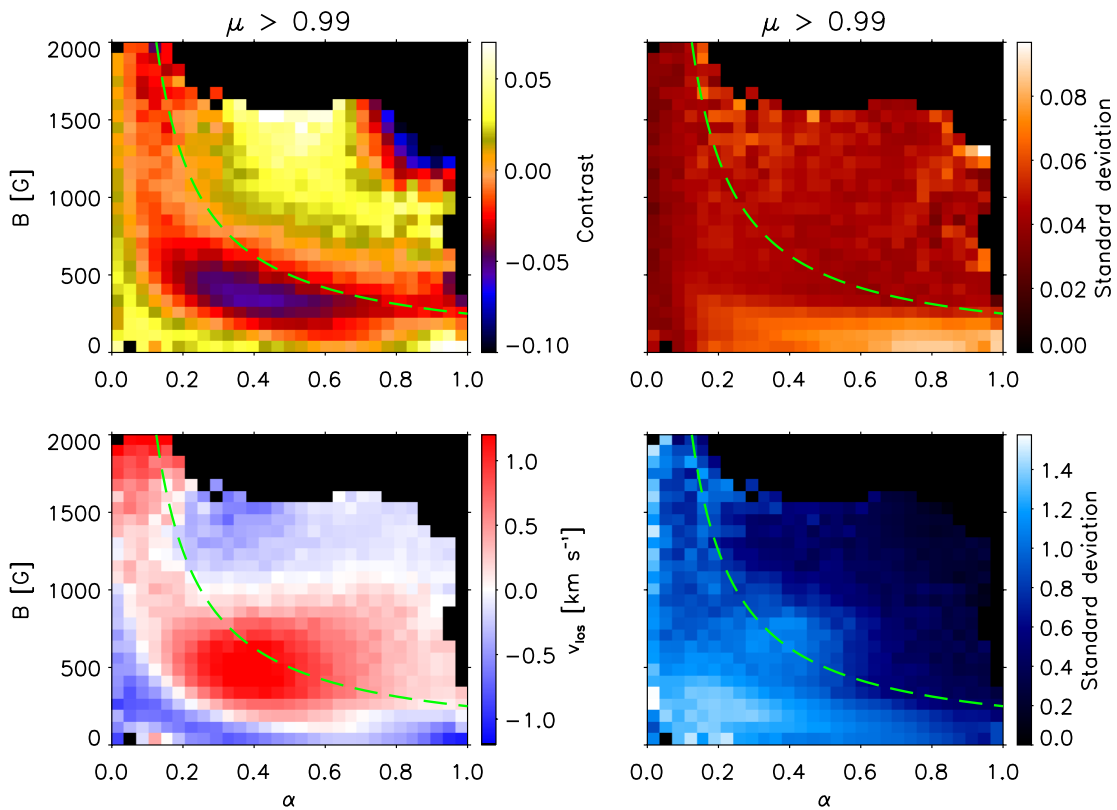
Figure 4.22: Variation of the contrast (upper panel) and $v_{los}$ (lower panel) as a function of both $B$ and $\alpha$ at disk center ($\mu > 0.99$) in a 2-dimensional binning representation. Left: Average of the contrast in bins of 0.035-width in $\alpha$ and 75 G-width in $B$. Right: Standard deviation of the contrast and $v_{los}$ in the same bins. Dashed green: limit $B_{app} = 250$ Mx cm$^{-2}$ between the granulation field regime and the concentrated field regime. The full color scale varies between the minimum and maximum average contrasts. Bins with less than 10 data points (pixels) are set to black.

fields have intrinsic field strengths $B < 400$ G, i.e. they are dominated by equipartition fields (cf. PDF in Fig. 4.21). This range of $B$ corresponds both to positive and negative $v_{los}$, which can be associated with the blobs of granulation contrast in Fig. 4.9, characterizing the granulation field regime (see also Fig. 4.13). All these observations could be consequences of the "flux expulsion" process (although it cannot be followed using scans). Namely, the "blob" could be related to the intensification of the field strength and increase of the filling factor by the granular flows, which leads stronger fields to be located in the downflow lanes. The following reduction of the downflows with increasing $\alpha$ or $B$ could then be attributed to the "quenching" of those flows by the opposing Lorentz force of the intensified fields. We have thus more evidence that the granulation field regime contains some strong fields as well, but in minority. It is interesting to see that this minority of intense fields ($B > 400$ G) actually corresponds to the rather vertical fields with neutral contrast in the range $B_{app} \in (150, 250)$ Mx cm$^{-2}$ (visible as prolongations of the two "horns" of strong vertical fields in Fig. 4.18). This is shown by the PDF($\gamma$) restricted to the pixels having $B > 400$ G and $B_{app} \in (150, 250)$ Mx cm$^{-2}$ (Fig.
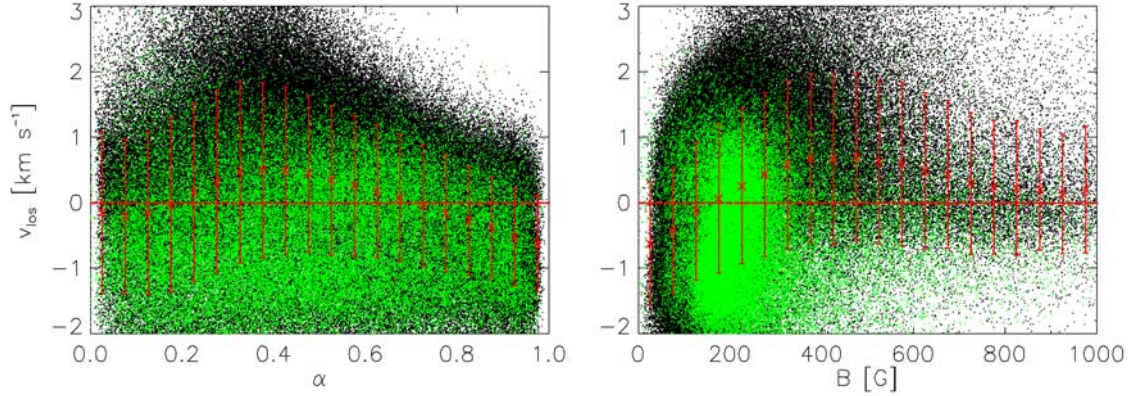
Figure 4.23: Left: Scatterplot of the LOS velocity $v_{los}$ vs. filling factor $\alpha$ for the pixels with $B_{app} < 250$ Mx cm$^{-2}$ at disk center ($\mu > 0.99$). Red crosses and bars: average values and standard deviations in bins of $\alpha$ of width 0.005. Green: Pixels where the $Q$ or $U$ amplitude exceeds 4.5 rms. Red dashed: guideline for $v_{los} = 0$ km s$^{-1}$. Right: Same for the scatterplot of $v_{los}$ vs. intrinsic field strength $B$, in bins of 50 G.

4.24 right), indeed revealing quasi-vertical fields. If looking instead at the PDF($B$) for these "weak vertical fields" ($B_{app} \in (150, 250)$ Mx cm$^{-2}$ and $\gamma < 20°$ or $\gamma > 160°$, Fig. 4.24 left), one notices a mode at roughly 400 G, followed by a long tail towards kG field strengths. These vertical fields with $B_{app} \in (150, 250)$ Mx cm$^{-2}$ are thus "half-way" between weak equipartition fields and intense kG fields. It can be seen in Fig. 4.14 that these fields (cyan contours) are often located in the immediate vicinity of the stronger flux elements, although they also appear as isolated elements in the internetwork. Of particular interest also are the strong fields with low $\alpha$, e.g. the region $B > 1000$ G, $\alpha < 0.1$ in Fig. 4.22. As revealed by their PDF($\gamma$) in Fig. 4.25, these fields are rather vertical, indicating that they very probably belong to "true" magnetic elements. But unlike the quasi-vertical fields with $B_{app} \in (150, 250)$ Mx cm$^{-2}$ discussed above, they mainly appear as isolated small flux concentrations within supergranular cells (this was checked over a whole map of $320'' \times 160''$ at disk center, but the corresponding locations were not contoured in Fig. 4.14 because they represent less than 0.4% of the map).

Finally, we can see how the dependence of the contrast on $B$ and $\alpha$ evolves from the center to the limb in the six usual $\mu$ intervals, as presented in Fig. 4.26 and Fig. 4.27. Leaving aside the decrease of the range of $B$ as $\mu$ decreases (cf. beginning of this Section), the qualitative symmetry in $B$ and $\alpha$ is very similar at all $\mu$. In all intervals of $\mu$, the region of darker contrasts is located at roughly the same portion of the plots, and the division $B_{app} = 250$ Mx cm$^{-2}$ seems to well represent the limit between the granulation fields and the concentrated ones. For $B_{app} < 250$ Mx cm$^{-2}$, the variation of contrast attenuates with lower $\mu$ due to the decrease of the granulation contrast rms. For the concentrated fields, while the brightest parameter region always corresponds to $B$ in the kG regime, the corresponding $\alpha$ increases together with an associated decrease in $B$ (from $B \sim 1600$ G near disk center to $B \sim 1200$ G near the limb). This variation thus seems related to the increase of the peak close to 1 in the PDF($\alpha$) (see Fig. 4.21) and the corresponding decreasing amount of inferred kG fields (see remarks at the beginning of this Section).
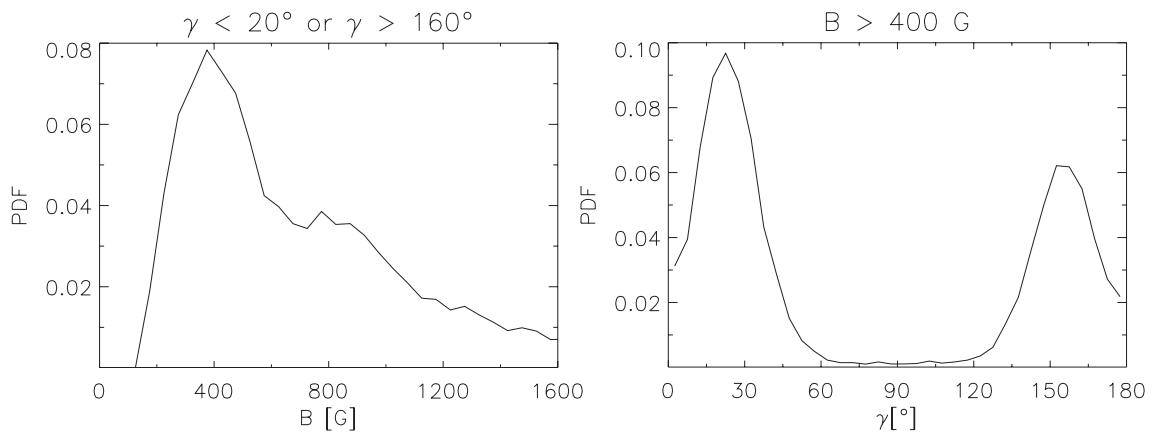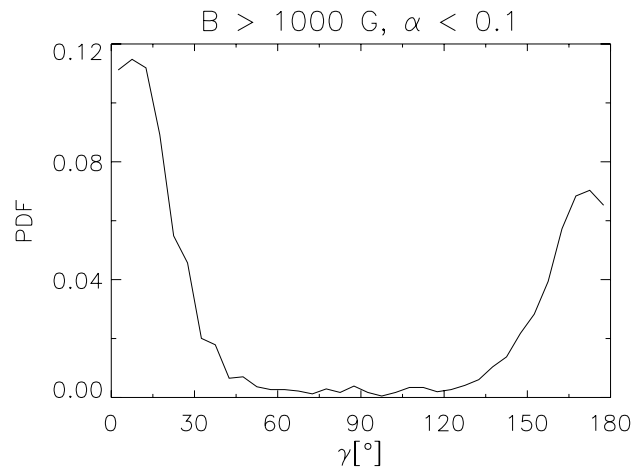
Figure 4.24: Left: PDF of the field strength $B$ for pixels with $B_{\text{app}} \in (150, 250)$ Mx cm$^{-2}$, and $\gamma < 20°$ or $\gamma > 160°$. Right: PDF of $\gamma$ for pixels with $B_{\text{app}} \in (150, 250)$ Mx cm$^{-2}$ and $B > 400$ G.



Figure 4.25: PDF of $\gamma$ for for pixels with $B > 1000$ G and $\alpha < 0.1$ at disk center ($\mu > 0.99$).

Thus the shift of the peak contrast toward stronger $B_{\text{app}}$ (cf. Fig. 4.9) is primarily related to an increase of $\alpha$. This could be explained by the "hot wall picture", if we consider that larger filling factors correspond to bigger features, which have their hot wall visible closer to the limb, and that this wall also appears brighter because it is better resolved.

## 4.4 Summary and open questions

Finally, I summarize here the main results presented in this Chapter, and raise the attention on some remaining open questions.

　　1. *Contrast as a function of "magnetogram signal"* $M = B\alpha\cos\gamma/\mu$: At the resolution of Hinode, the trends of the average contrast as a function of $M$ exhibit a peaked shape reaching positive values (i.e. brighter than the average quiet Sun) at all $\mu$, including at the very disk center. This contradicts previous studies performed at lower resolution, which reported a monotonous decrease of the contrast with magnetogram signal near disk center, with negative average contrasts for all magnetogram signals (Topka et al. 1992, Lawrence et al. 1993). Away from disk center, the herein obtained peak contrasts as a function of
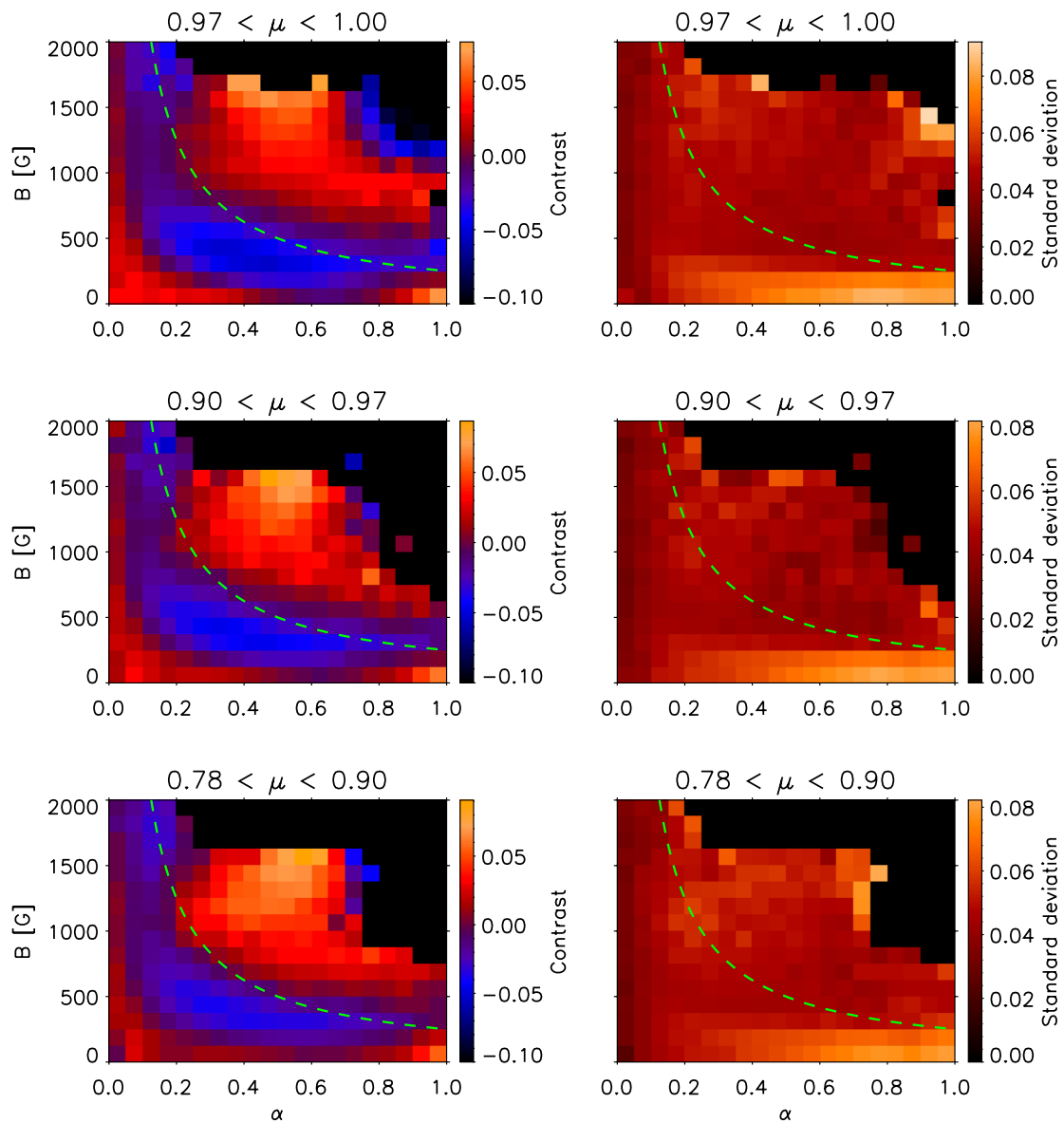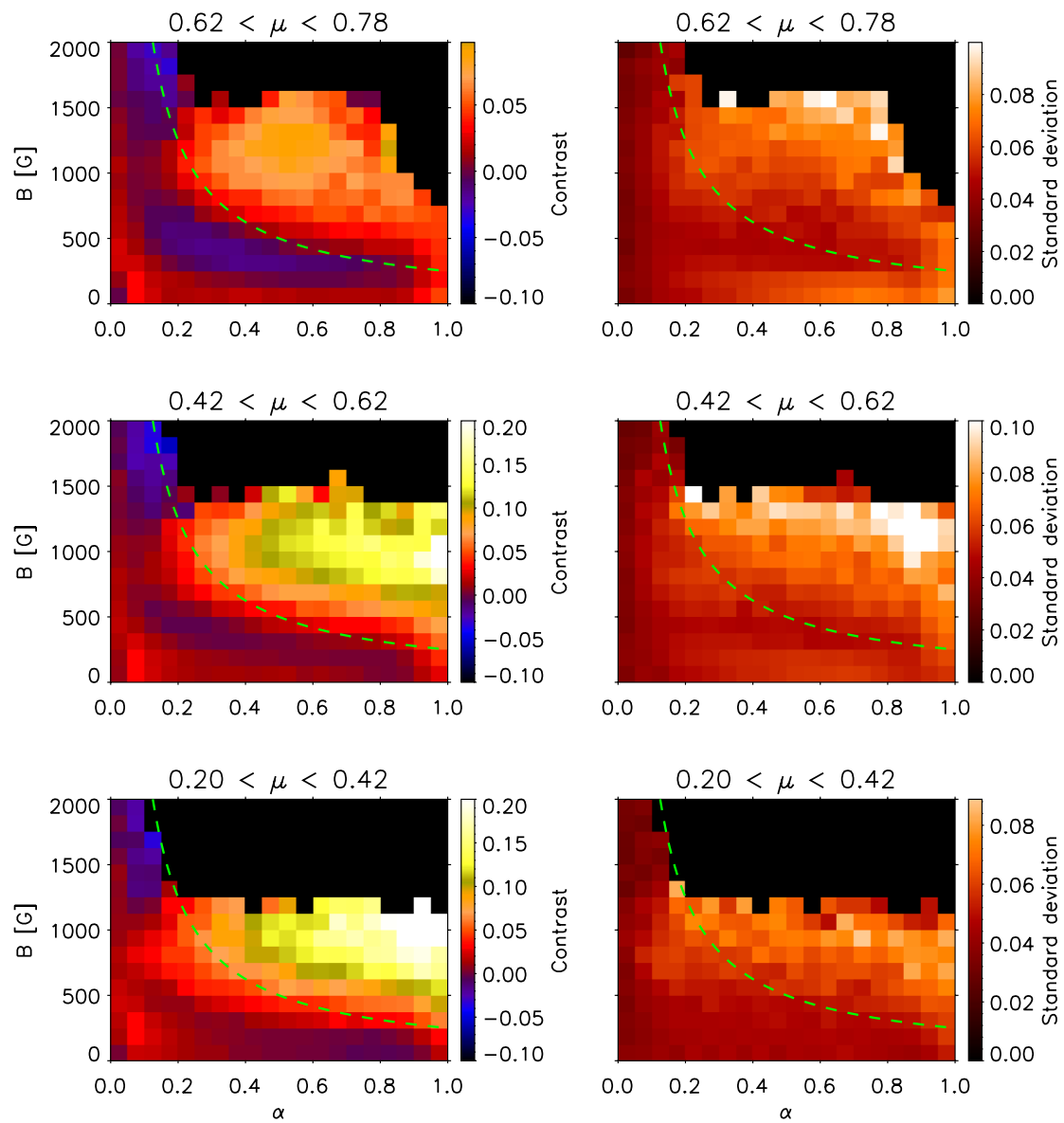
Figure 4.26: Same as Fig. 4.22 for three intervals of $\mu$ with $\mu > 0.78$. The average contrasts for all $\mu$ intervals have been set to the same unique color scale common with Fig. 4.20, but differing from Fig. 4.22.

Figure 4.27: Same as Fig. 4.26 for the three intervals of $\mu$ with $\mu < 0.78$.

*M* are significantly larger than those of previous studies (Topka et al. 1997, Ortiz et al. 2002), and the trend of the average values spans a larger contrast range. It is thus expected that further progress in telescope resolution will reveal more pronounced contrast peaks.

2. *Contrast as a function of apparent flux density* $B_{\mathrm{app}} = B\alpha$: It was found that for $\mu$ lower than $\sim 0.8$, the behaviour of the contrast as a function of $B_{\mathrm{app}}$ deviates from its behaviour as a function of *M*. At these $\mu$, the contrast increases to larger values and decreases more slowly toward large $B_{\mathrm{app}}$. In particular, the contrast is entirely positive for $B_{\mathrm{app}} > 250$ Mx cm$^{-2}$ (whereas it drops back to negative for large *M*). The different dependence of the contrast on $B_{\mathrm{app}}$ and *M* becomes more obvious as $\mu$ decreases and for $\mu < 0.42$, the contrast increases monotonously with $B_{\mathrm{app}}$. I argued that at low $\mu$, the relation between contrast and *M* was spoiled by non-vertical fields with low $B_{\mathrm{app}}$ but larger *M*. Hence, at low $\mu$, the variation of the contrast with *M* cannot be interpreted in terms of magnetic elements only, and the contrast as a function of $B_{\mathrm{app}}$ should be used instead for comparison with flux tube models. However, whereas the center-to-limb variation (CLV) of the average contrast was reaching a maximum in all intervals of *M*, there is no evidence of such a maximum in intervals of $B_{\mathrm{app}}$, even for low $B_{\mathrm{app}}$. The CLVs rather seem to reach some plateau, indicating a possible maximum for $\mu$ values lower than the range investigated here ($\mu < 0.2$).

3. *"Granulation field regime" and "Concentrated field regime"*: Two distinct regimes of $B_{\mathrm{app}}$ were identified, in which the contrast varies differently with $B_{\mathrm{app}}$ and $\mu$. At the resolution of Hinode, these two regimes can be roughly segregated by $B_{\mathrm{app}} = 250$ Mx cm$^{-2}$. The regime $B_{\mathrm{app}} < 250$ Mx cm$^{-2}$ is dominated by pixels located both in and in-between granules, whose contrast is close to the one at these locations. In this regime, the CLV of contrast is induced by the decrease of the granulation contrast rms. Therefore this regime was referred to as the "granulation field regime". The pixels with $B_{\mathrm{app}} > 250$ Mx cm$^{-2}$ essentially correspond to network elements and similar strong flux concentrations in intergranular lanes. The contrast CLV should thus be dictated by the geometry of the features. This regime was therefore referred to as the "concentrated field regime".

4. *Dependence of contrast on inclination $\gamma$ (with respect to the line of sight)*: In the regime $B_{\mathrm{app}} > 250$ Mx cm$^{-2}$, the fields are quasi-vertical and thus the contrasts depend only weakly on $\gamma$. For more inclined fields, the contrast decreases either because they are associated with larger magnetic structures or are located near the boundary of magnetic features. For $B_{\mathrm{app}} < 250$ Mx cm$^{-2}$, the dependence of the average contrast on $\gamma$ is tied to granulation (as revealed by the similar dependence of the contrast and of the line of sight-velocity $v_{\mathrm{los}}$ on $\gamma$ at disk center). Pixels with horizontal fields are on average located within granules and are brighter, while pixels with more vertical fields are preferably located in the intergranular lanes and are thus darker. This dependence on $\gamma$ is extremely similar at all $\mu$, but less pronounced as $\mu$ decreases and as the contrast difference between granules and intergranules attenuates.

5. *Dependence on field strength $B$ and filling factor $\alpha$*: Qualitatively, at all $\mu$, the contrast depends in a very symmetric fashion on $B$ and $\alpha$, for both the granulation field and the concentrated field regime. To first order, it thus seems that the contrast is mainly dictated by $B_{\mathrm{app}}$. Quantitatively, in the concentrated field regime, the contrast reaches its largest values for kG fields. But as $\mu$ decreases, the filling factor associated to these brightest pixels increases, while the field strength slightly decreases. Although this could be related to larger magnetic features whose hot walls brighten closer to the limb, it should

be kept in mind that the inferences of $B$ and $\alpha$ are completely interdependent, and the interpretation of the filling factor close to the limb is unclear. Finally, in the granulation field regime, the contrast similarly decreases (correlated with an increase of $v_{\mathrm{los}}$ at disk center) with larger $\alpha$ and $B$ until reaching a parameter range where the contrast reaches a minimum (and $v_{\mathrm{los}}$ a maximum). In this regime, both $B$ and $\alpha$ thus seem to increase from granules to intergranules.

6. *Flux expulsion*: The granulation field regime is dominated by $B < 400$ G, but also contains a minority of fields with $B > 400$ G (including kG fields). Interestingly, the contrasts decrease and the downflows increase with $B$ until $B \sim 400$ G, after which the downflows reduce and the contrast increases, while the fields become quasi-vertical. These fields of intermediate strength are often located in the immediate vicinity of stronger flux concentrations ($B_{\mathrm{app}} > 250$ Mx cm$^{-2}$). Hence the granulation field regime seems to correspond to the regime where the flux expulsion operates, and further discloses a range of fields between the equipartion fields and the kG fields.

I conclude with some remaining open questions:

- Why does the CLV of contrast in intervals of $B_{\mathrm{app}}$ not reach a maximum even for low $B_{\mathrm{app}}$? Assuming some relation between $B_{\mathrm{app}}$ and the size of flux concentrations, smaller flux tubes should reach a maximum contrast at larger $\mu$ (Spruit 1976, Deinzer et al. 1984, Knölker and Schüssler 1988)...

- Why is the dependence of contrast on $B$ and $\alpha$ so symmetric? It could be explained by an effect of the spatial resolution. For magnetic features to turn bright in the concentrated field regime, they need enough field strength to engender a sufficient depression of the optical depth scale toward deeper and hotter layers. But they also need a sufficient size in order not to be smeared out. The resulting contrast could be the consequence of both factors.

- How does the inference of $B$ and $\alpha$ depend on the treatment of stray-light?

- How do the obtained results depend on the target, how would they differ for active regions? The study of the contrast as a function of magnetogram signal should probably be repeated for active regions, to rule out that the differences with previous studies (mostly performed in active regions) are not related to the target alone (For instance, Lawrence et al. 1993, obtained some positive contrast as well in quiet Sun).

- How reliable are the results of the inversions near the limb, in particular the treatment of the filling factor (and its interpretation) and the value of the associated field strength?

- What is the error due to neglecting the vertical geometrical structure of the flux concentrations close to the limb (Solanki et al. 1998)?

- How is the contrast affected by the PSF (Danilovic et al. 2008)?

# 5 Outlook

The novel classification method of BPs and faculae presented in Chap. 2 allowed the extraction of constraints for simulations (center-to-limb variation of the fraction of BPs and faculae, contrast profiles), and the obtention of some hints about the nature of the observed BPs and faculae (Chap. 3). To fully use the potential of this method and further elucidate the relationship between BPs and faculae, this work should be extended along the following two directions:

- Firstly, the classification method shall be applied to a dataset of high-resolution images with joint spectro-polarimetric information. This would allow on one hand the validation and improvement of the method, and on the other hand the determination of the magnetic properties of BPs and faculae. In particular, we shall verify the hypothetical association of faculae near disk center with inclined fields (Chap. 2,3). Such investigations are already foreseen using data from IBIS (Cavallini 2006) and SUNRISE (using both SuFi and IMaX, see Gandorfer et al. 2007). Through their seeing-free quality, SUNRISE images will be particularly suited for the application of the classification method (requiring a homogeneous spatial resolution).

- Secondly, the method should be applied to MHD simulations for different viewing angles. Complemented by the retrieval of the magnetic properties of BPs and faculae (cf. above), the results herein obtained would then provide powerful constraints to enhance the models.

The analogy between the contrast–area (projected onto the plane of the sky) relation of the bright features (see Chap. 3) and the results of magnetogram studies seem promising for proxy magnetometry, but require some additional intermediate steps:

- The association of the apparent area of the features in images and the flux of the corresponding magnetic elements should be verified and calibrated (e.g. using the aforementioned datasets).

- Using SUNRISE data, the contrast–area relation of BPs shall be probed at an unprecedented spatial resolution and compared with model predictions (e.g. Spruit 1976, Deinzer et al. 1984, Fabiani Bendicho et al. 1992). By relating the BP contrast to the inferred field strength (Stokes inversions), one could check to which extent the contrast is affected by the finite resolution, and whether the inhibition of convective collapse plays a role (Venkatakrishnan 1986, Rajaguru and Hasan 2000, see Sect. 3.6.2).

Finally, Chap. 4 presented a first assessment of the dependence of the contrast of magnetic features on their magnetic parameters at different heliocentric angles, which also raised a number of open questions.

- An obvious extension would be to repeat this study using scans of active regions, in particular to rule out that differences with previous studies using magnetograms (mostly performed in active regions) are due to the different targets (for instance, different results were obtained by Lawrence et al. 1993, for the quiet Sun and for active regions).

- We are currently comparing the inversion results with other codes inverting the profiles of both Fe lines (the code used herein inverted only one line), in particular the treatment of stray light (especially near the limb) and the robustness against the noise in the spectra.

- Although the obtained results provide some indications about the "kind" of magnetic features appearing bright at different heliocentric angles (cf. questions in Sects. 1.2.4 and 1.4), the employed method ("magnetic parameter binning") conveys no information about the identity of the features. To effectively determine the properties of bright magnetic features and how their visibility is affected at different heliocentric angles, these features should be segmented in G-band images (composites) co-spatial with the spectropolarimetric scans, and their magnetic parameters retrieved *per feature*.

# Bibliography

Adjabshirizadeh, A., Koutchmy, S., 2002, Center-limb and shape-factor variations of facular elements, in Solar Variability: From Core to Outer Frontiers, (Ed.) J. Kuijpers, vol. 506 of ESA Special Publication, pp. 415–418

Ahern, S., Chapman, G. A., 2000, An analysis of full-disk observations of facular contrast in the blue and red, Sol. Phys., 191, 71–84

Antoine, J.-P., Demanet, L., Hochedez, J.-F., Jacques, L., Terrier, R., Verwichte, E., 2002, Application of the 2-D wavelet transform to astrophysical images, Physicalia, 24, 93–116

Auffret, H., Muller, R., 1991, Center-to-limb variation of the network bright points in the solar photosphere, A&A, 246, 264–279

Balakrishnama, S., Ganapathiraju, A., Linear Discriminant Analysis-A Brief Tutorial

Balakrishnama, S., Ganapathiraju, A., Picone, J., 1999, Linear discriminant analysis for signal processing problems, in Proceedings IEEE Southeastcon'99. Technology on the Brink of 2000., pp. 78–81

Balthasar, H., 1984, Asymmetries and wavelengths of solar spectral lines and the solar rotation determined from Fourier-transform spectra, Sol. Phys., 93, 219–241

Barnes, G., Leka, K. D., Schumer, E. A., Della-Rose, D. J., 2007, Probablistic forecasting of solar flares from vector magnetogram data, Space Weather, 5

Beck, C., Bellot Rubio, L. R., Schlichenmaier, R., Sütterlin, P., 2007, Magnetic properties of G-band bright points in a sunspot moat, A&A, 472, 607–622, `arXiv:0707.1232`

Bellot Rubio, L. R., Collados, M., 2003, Understanding internetwork magnetic fields as determined from visible and infrared spectral lines, A&A, 406, 357–362

Berger, T. E., Title, A. M., 1996, On the Dynamics of Small-Scale Solar Magnetic Elements, ApJ, 463, 365

Berger, T. E., Title, A. M., 2001, On the Relation of G-Band Bright Points to the Photospheric Magnetic Field, ApJ, 553, 449–469

Berger, T. E., Schrijver, C. J., Shine, R. A., Tarbell, T. D., Title, A. M., Scharmer, G., 1995, New Observations of Subarcsecond Photospheric Bright Points, ApJ, 454, 531

Berger, T. E., Löfdahl, M. G., Shine, R. S., Title, A. M., 1998, Measurements of Solar Magnetic Element Motion from High-Resolution Filtergrams, ApJ, 495, 973

Berger, T. E., Rouppe van der Voort, L. H. M., Löfdahl, M. G., Carlsson, M., Fossum, A., Hansteen, V. H., Marthinussen, E., Title, A., Scharmer, G., 2004, Solar magnetic elements at 0.1 arcsec resolution. General appearance and magnetic structure, A&A, 428, 613–628

Berger, T. E., Rouppe van der Voort, L., Löfdahl, M., 2007, Contrast Analysis of Solar Faculae and Magnetic Bright Points, ApJ, 661, 1272–1288

Blanco Rodríguez, J., Okunev, O. V., Puschmann, K. G., Kneer, F., Sánchez-Andrade Nuño, B., 2007, On the properties of faculae at the poles of the Sun, A&A, 474, 251–259

Bonet, J. A., 1999, High Spatial Resolution Imaging in Solar Physics, in Motions in the Solar Atmosphere, (Eds.) A. Hanslmeier, M. Messerotti, vol. 239 of Astrophysics and Space Science Library, pp. 1–12

Borrero, J. M., Tomczyk, S., Kubo, M., Socas-Navarro, H., Schou, J., Couvidat, S., Bogart, R., 2009, VFISV: Very Fast Inversion of the Stokes Vector for the Helioseismic and Magnetic Imager, ArXiv e-prints, `0901.2702`

Borrero Santiago, J., 2004, The fine structure of the sunspot penumbra, Ph.D. thesis, International Max-Planck Research School on Physical Processes in the Solar System and Beyond, Universität Göttingen

Bovelet, B., Wiehr, E., 2001, A New Algorithm for Pattern Recognition and its Application to Granulation and Limb Faculae, Sol. Phys., 201, 13–26

Bovelet, B., Wiehr, E., 2003, Dynamics of the solar active region finestructure, A&A, 412, 249–255

Bovelet, B., Wiehr, E., 2007, Multiple-Scale Pattern Recognition Applied to Faint Intergranular G-band Structures, Sol. Phys., 243, 121–129

Bovelet, B., Wiehr, E., 2008, The quiet Sun's magnetic flux estimated from Ca II H bright inter-granular G-band structures, A&A, 488, 1101–1107

Bruls, J. H. M. J., Solanki, S. K., 1995, Infrared lines as probes of solar magnetic features. IX. MgI 12$\mu$m diagnostics of solar plage., A&A, 293, 240–251

Cannon, C. J., 1970, Line Transfer in Two Dimensions, ApJ, 161, 255

Carlsson, M., Stein, R. F., Nordlund, Å., Scharmer, G. B., 2004, Observational Manifestations of Solar Magnetoconvection: Center-to-Limb Variation, ApJ, 610, L137–L140, `arXiv:astro-ph/0406160`

Cavallini, F., 2006, IBIS: A New Post-Focus Instrument for Solar Imaging Spectroscopy, Sol. Phys., 236, 415–439

Chapman, G. A., Sheeley, Jr., N. R., 1968, The Photospheric Network, Sol. Phys., 5, 442–461

Cowling, T. G., 1976, Magnetohydrodynamics

Criscuoli, S., Rast, M., 2008, Photometric properties of resolved and unresolved magnetic elements, ArXiv e-prints, `arXiv:astro-ph/0812.1727`

Danilovic, S., Gandorfer, A., Lagg, A., Schüssler, M., Solanki, S. K., Vögler, A., Katsukawa, Y., Tsuneta, S., 2008, The intensity contrast of solar granulation: comparing Hinode SP results with MHD simulations, A&A, 484, L17–L20, `arXiv:astro-ph/0804.4230`

De Pontieu, B., Carlsson, M., Stein, R., Rouppe van der Voort, L., Löfdahl, M., van Noort, M., Nordlund, Å., Scharmer, G., 2006, Rapid Temporal Variability of Faculae: High-Resolution Observations and Modeling, ApJ, 646, 1405–1420

de Wijn, A. G., Rutten, R. J., Haverkamp, E. M. W. P., Sütterlin, P., 2005, DOT tomography of the solar atmosphere. IV. Magnetic patches in internetwork areas, A&A, 441, 1183–1190, `arXiv:astro-ph/0706.2008`

de Wijn, A. G., Lites, B. W., Berger, T. E., Frank, Z. A., Tarbell, T. D., Ishikawa, R., 2008, Hinode Observations of Magnetic Elements in Internetwork Areas, ApJ, 684, 1469–1476, `arXiv:astro-ph/0806.0345`

de Wijn, A. G., Stenflo, J. O., Solanki, S. K., Tsuneta, S., 2009, Small-Scale Solar Magnetic Fields, Space Science Reviews, 144, 275–315, `arXiv:astro-ph/0812.4465`

Deinzer, W., Hensler, G., Schussler, M., Weisshaar, E., 1984, Model Calculations of Magnetic Flux Tubes - Part Two - Stationary Results for Solar Magnetic Elements, A&A, 139, 435

del Toro Iniesta, J. C., 2003, Introduction to Spectropolarimetry, by Jose Carlos del Toro Iniesta, pp. 244. ISBN 0521818273. Cambridge, UK: Cambridge University Press, April 2003.

Domínguez Cerdeña, I., Kneer, F., Sánchez Almeida, J., 2003, Quiet-Sun Magnetic Fields at High Spatial Resolution, ApJ, 582, L55–L58, `arXiv:astro-ph/0211454`

Domínguez Cerdeña, I., Sánchez Almeida, J., Kneer, F., 2006, The Distribution of Quiet Sun Magnetic Field Strengths from 0 to 1800 G, ApJ, 636, 496–509, `arXiv:astro-ph/0509243`

Dunn, R. B., Zirker, J. B., 1973, The Solar Filigree, Sol. Phys., 33, 281–304

Egret, D., Heck, A., Nobelis, P., Turlot, J. C., 1984, Statistical classification of IUE low-despersion stellar spectra: Progress report, in Future of Ultraviolet Astronomy Based on Six Years of IUE Research, (Eds.) J. M. Mead, R. D. Chapman, Y. Kondo, pp. 512–515

Fabiani Bendicho, P., Kneer, F., Trujillo Bueno, J., 1992, On the photospheric temperature in small-scale magnetic flux concentrations, A&A, 264, 229–235

Faurobert-Scholl, M., Feautrier, N., Machefert, F., Petrovay, K., Spielfiedel, A., 1995, Turbulent magnetic fields in the solar photosphere: diagnostics and interpretation., A&A, 298, 289

Fischer, R. A., 1936, The Use of Multiple Measurements in Taxonomic Problems, Annals of Eugenics, 7, 179–188

Fligge, M., Solanki, S. K., Unruh, Y. C., Fröhlich, C., Wehrli, C., 1998, A model of solar total and spectral irradiance variations, A&A, 335, 709–718

Fracassini, M., Pasinetti, L. E., Raffaelli, G., 1984, Discriminant analysis of pulsar groups in the diagram P versus P, in Plasma Astrophysics, (Eds.) T. D. Guyenne, J. J. Hunt, vol. 207 of ESA Special Publication, p. 315

Frazier, E. N., 1971, Multi-Channel Magnetograph Observations. III: Faculae, Sol. Phys., 21, 42–53

Frazier, E. N., Stenflo, J. O., 1972, On the Small-Scale Structure of Solar Magnetic Fields, Sol. Phys., 27, 330–346

Fröhlich, C., 2000, Observations of Irradiance Variations, Space Science Reviews, 94, 15–24

Gabriel, A. H., 1976, A magnetic model of the solar transition region, Royal Society of London Philosophical Transactions Series A, 281, 339–352

Gandorfer, A., 2001, High Precision Polarimetry of the Sun, Ph.D. thesis, ETHZ Zürich

Gandorfer, A. M., Solanki, S. K., Barthol, P., Martínez Pillet, V., Schmidt, W., Title, A. M., Knölker, M., the SUNRISE team, 2007, SUNRISE: High resolution UV/VIS observations of the Sun from the stratosphere, in Modern Solar Facilities - Advanced Solar Science, (Eds.) F. Kneer, K. G. Puschmann, A. D. Wittmann, p. 69, Universitätsverlag Göttingen

Grossmann-Doerth, U., Schüssler, M., Steiner, O., 1998, Convective intensification of solar surface magnetic fields: results of numerical experiments, A&A, 337, 928–939

Hand, D., 1981, Discrimination and Classification, Wiley, New York

Hasan, S. S., 1985, Convective instability in a solar flux tube. II - Nonlinear calculations with horizontal radiative heat transport and finite viscosity, A&A, 143, 39–45

Heck, A., 1976, An Application of Multivariate Statistical Analysis to a Photometric Catalogue, A&A, 47, 129

Heck, A., Murtagh, F. (Eds.), 1989, Knowledge-Based Systems in Astronomy, vol. 329 of Lecture Notes in Physics, Berlin Springer Verlag

Heck, A., Egret, D., Nobelis, P., Turlot, J. C., 1984, Statistical classification of IUE stellar spectra by the Variable Procrustean Bed (VPB) approach, in Fourth European IUE Conference, (Ed.) E. Rolfe, vol. 218 of ESA Special Publication, pp. 257–261

Hirzberger, J., 2003, Imaging spectroscopy of solar pores, A&A, 405, 331–340

Hirzberger, J., Wiehr, E., 2005, Solar limb faculae, A&A, 438, 1059–1065

Huertas-Company, M., Rouan, D., Tasca, L., Soucail, G., Le Fèvre, O., 2008, A robust morphological classification of high-redshift galaxies using support vector machines on seeing limited images. I. Method description, A&A, 478, 971–980, `arXiv:0709.1359`

Ishikawa, R., Tsuneta, S., Ichimoto, K., Isobe, H., Katsukawa, Y., Lites, B. W., Nagata, S., Shimizu, T., Shine, R. A., Suematsu, Y., Tarbell, T. D., Title, A. M., 2008, Transient horizontal magnetic fields in solar plage regions, A&A, 481, L25–L28, `arXiv:0802.1769`

Isik, E., Holzwarth, V., Schüssler, M., 2008, Storage of Magnetic Flux in the Solar Convective Overshoot Region, 12th European Solar Physics Meeting, Freiburg, Germany, held September, 8-12, 2008. Online at http://espm.kis.uni-freiburg.de/, p.3.3, 12, 3

Jarvis, J. F., Tyson, J. A., 1981, FOCAS - Faint Object Classification and Analysis System, AJ, 86, 476–495

Keller, C. U., Schüssler, M., Vögler, A., Zakharov, V., 2004, On the Origin of Solar Faculae, ApJ, 607, L59–L62

Kenney, J. F., Keeping, E. S., 1962, Mathematics of Statistics, Pt. 1, 3rd ed., Princeton, NJ: Van Nostrand

Knölker, M., Schüssler, M., 1988, Model calculations of magnetic flux tubes. IV - Convective energy transport and the nature of intermediate size flux concentrations, A&A, 202, 275–283

Knölker, M., Schüssler, M., Weisshaar, E., 1988, Model calculations of magnetic flux tubes. III - Properties of solar magnetic elements, A&A, 194, 257–267

Knölker, M., Grossmann-Doerth, U., Schüssler, M., Weisshaar, E., 1991, Some developments in the theory of magnetic flux concentrations in the solar atmosphere, Adv. Space Res., 11, 285–295

Kosugi, T., Matsuzaki, K., Sakao, T., Shimizu, T., Sone, Y., Tachikawa, S., Hashimoto, T., Minesugi, K., Ohnishi, A., Yamada, T., Tsuneta, S., Hara, H., Ichimoto, K., Suematsu, Y., Shimojo, M., Watanabe, T., Shimada, S., Davis, J. M., Hill, L. D., Owens, J. K., Title, A. M., Culhane, J. L., Harra, L. K., Doschek, G. A., Golub, L., 2007, The Hinode (Solar-B) Mission: An Overview, Sol. Phys., 243, 3–17

Krivova, N. A., Solanki, S. K., Fligge, M., Unruh, Y. C., 2003, Reconstruction of solar irradiance variations in cycle 23: Is solar surface magnetism the cause?, A&A, 399, L1–L4

Kurtz, M. J., 1983, Classification methods: an introductory survey, in Statistical Methods in Astronomy, (Ed.) E. J. Rolfe, vol. 201 of ESA Special Publication, pp. 47–58

Kurtz, M. J., 1984, Progress in Automation Techniques for Spectral Classification, in The MK Process and Stellar Classification, (Ed.) P. A. Wayman, pp. 136–152

Langhans, K., Schmidt, W., Tritschler, A., 2002, 2D-spectroscopic observations of G-band bright structures in the solar photosphere, A&A, 394, 1069–1076

Lawrence, J. K., 1988, Multi-color photometric observations of facular contrasts, Sol. Phys., 116, 17–32

Lawrence, J. K., Chapman, G. A., Herzog, A. D., 1988, Photometric determination of facular contrasts near the solar disk center, ApJ, 324, 1184–1193

Lawrence, J. K., Topka, K. P., Jones, H. P., 1993, Contrast of faculae near the disk center and solar variability, J. Geophys. Res., 98, 18 911

Lean, J., Foukal, P., 1988, A Model of Solar Luminosity Modulation by Magnetic Activity Between 1954 and 1984, Science, 240, 906

Leka, K. D., Barnes, G., 2003, Photospheric Magnetic Field Properties of Flaring versus Flare-quiet Active Regions. II. Discriminant Analysis, ApJ, 595, 1296–1306

Limpert, E., Stahel, W., Abbt, M., 2001, Log-normal Distributions across the Sciences: Keys and Clues, BioSc., 427, 341–352

Lites, B., Socas-Navarro, H., Kubo, M., Berger, T. E., Frank, Z., Shine, R. A., Tarbell, T. D., Title, A. M., Ichimoto, K., Katsukawa, Y., Tsuneta, S., Suematsu, Y., Shimizu, T., Nagata, S., 2007, Hinode Observations of Horizontal Quiet Sun Magnetic Flux and the "Hidden Turbulent Magnetic Flux", PASJ, 59, 571

Lites, B. W., 2002, Characterization of Magnetic Flux in the Quiet Sun, ApJ, 573, 431–444

Lites, B. W., Rutten, R. J., Berger, T. E., 1999, Dynamics of the Solar Chromosphere. II. Ca II H_2V and K_2V Grains versus Internetwork Fields, ApJ, 517, 1013–1033

Lites, B. W., Scharmer, G. B., Berger, T. E., Title, A. M., 2004, Three-Dimensional Structure of the Active Region Photosphere as Revealed by High Angular Resolution, Sol. Phys., 221, 65–84

Lites, B. W., Kubo, M., Socas-Navarro, H., Berger, T., Frank, Z., Shine, R., Tarbell, T., Title, A., Ichimoto, K., Katsukawa, Y., Tsuneta, S., Suematsu, Y., Shimizu, T., Nagata, S., 2008, The Horizontal Magnetic Flux of the Quiet-Sun Internetwork as Observed with the Hinode Spectro-Polarimeter, ApJ, 672, 1237–1253

Livi, S. H. B., Wang, J., Martin, S. F., 1985, The cancellation of magnetic flux. I - On the quiet sun, Australian Journal of Physics, 38, 855–873

Mahalanobis, P. C., 1936, On the generalized distance in statistics, Proc. National Inst. Sci. India, 12

Malagnini, M. L., Pasian, F., Pucillo, M., Santin, P., 1985, FODS - A system for faint object detection and classification in astronomy, A&A, 144, 49–56

Martin, S. F., 1988, The identification and interaction of network, intranetwork, and ephemeral-region magnetic fields, Sol. Phys., 117, 243–259

Martin, S. F., Livi, S. H. B., Wang, J., 1985, The cancellation of magnetic flux. II - In a decaying active region, Australian Journal of Physics, 38, 929–959

Martínez González, M. J., Collados, M., Ruiz Cobo, B., 2007, Internetwork magnetic fields, in Modern solar facilities - advanced solar science, (Eds.) F. Kneer, K. G. Puschmann, A. D. Wittmann, p. 157

Martínez González, M. J., Asensio Ramos, A., López Ariste, A., Manso Sainz, R., 2008, Near-IR internetwork spectro-polarimetry at different heliocentric angles, A&A, 479, 229–234, `0710.5219`

Martínez Pillet, V., Lites, B. W., Skumanich, A., 1997, Active Region Magnetic Fields. I. Plage Fields, ApJ, 474, 810

Mehltretter, J. P., 1974, Observations of photospheric faculae at the center of the solar disk, Sol. Phys., 38, 43–57

Mukherjee, S., Feigelson, E. D., Jogesh Babu, G., Murtagh, F., Fraley, C., Raftery, A., 1998, Three Types of Gamma-Ray Bursts, ApJ, 508, 314–327, `arXiv:astro-ph/9802085`

Muller, R., 1975, A model of photospheric faculae deduced from white light high resolution pictures, Sol. Phys., 45, 105–114

Muller, R., 1983, The dynamical behavior of facular points in the quiet photosphere, Sol. Phys., 85, 113–121

Muller, R., 1985, The fine structure of the quiet sun, Sol. Phys., 100, 237–255

Muller, R., Roudier, T., 1984, Variability of the quiet photospheric network, Sol. Phys., 94, 33–47

Muller, R., Roudier, T., Vigneau, J., Auffret, H., 1994, The proper motion of network bright points and the heating of the solar corona, A&A, 283, 232–240

Murtagh, F., 1994, Classification: Astronomical and Mathematical Overview, in Astronomy from Wide-Field Imaging, (Ed.) H. T. MacGillivray, vol. 161 of IAU Symposium, pp. 227–233

Murtagh, F., Heck, A., 1987, Multivariate Data Analysis, Kluwer Academic Publishers, Dordrecht

Murtagh, F. D., Adorf, H.-M., 1992, Detecting cosmic ray hits on HST WF/PC images using neural networks and other discriminant analysis approaches., in 4. International Workshop on Data Analysis in Astronomy, (Eds.) V. di Gesu, L. Scarsi, R. Buccheri, P. Crane, pp. 103–111

Nagata, S., Tsuneta, S., Suematsu, Y., Ichimoto, K., Katsukawa, Y., Shimizu, T., Yokoyama, T., Tarbell, T. D., Lites, B. W., Shine, R. A., Berger, T. E., Title, A. M., Bellot Rubio, L. R., Orozco Suárez, D., 2008, Formation of Solar Magnetic Flux Tubes with Kilogauss Field Strength Induced by Convective Instability, ApJ, 677, L145–L147

Neckel, H., Labs, D., 1994, Solar limb darkening 1986-1990 (lambda lambda 303 to 1099nm), Sol. Phys., 153, 91–114

Okunev, O. V., Kneer, F., 2004, On the structure of polar faculae on the Sun, A&A, 425, 321–331

Orozco Suárez, D., Bellot Rubio, L. R., del Toro Iniesta, J. C., 2007a, Quiet-Sun Magnetic Fields from Space-borne Observations: Simulating Hinode's Case, ApJ, 662, L31–L34, `arXiv:astro-ph/0705.0096`

Orozco Suárez, D., Bellot Rubio, L. R., Del Toro Iniesta, J. C., Tsuneta, S., Lites, B., Ichimoto, K., Katsukawa, Y., Nagata, S., Shimizu, T., Shine, R. A., Suematsu, Y., Tarbell, T. D., Title, A. M., 2007b, Strategy for the Inversion of Hinode Spectropolarimetric Measurements in the Quiet Sun, PASJ, 59, 837, `arXiv:astro-ph/0709.2033`

Orozco Suárez, D., Bellot Rubio, L. R., del Toro Iniesta, J. C., Tsuneta, S., Lites, B. W., Ichimoto, K., Katsukawa, Y., Nagata, S., Shimizu, T., Shine, R. A., Suematsu, Y., Tarbell, T. D., Title, A. M., 2007c, Quiet-Sun Internetwork Magnetic Fields from the Inversion of Hinode Measurements, ApJ, 670, L61–L64, `arXiv:astro-ph/0710.1405`

Ortiz, A., Solanki, S. K., Domingo, V., Fligge, M., Sanahuja, B., 2002, On the intensity contrast of solar photospheric faculae and network elements, A&A, 388, 1036–1047, `arXiv:astro-ph/0207008`

Parker, E. N., 1978, Hydraulic concentration of magnetic fields in the solar photosphere. VI - Adiabatic cooling and concentration in downdrafts, ApJ, 221, 368–377

Pietarila, A., Solanki, S., Hirzberger, J., Zakharov, V., 2008, Fibrils in Ca II K, 12th European Solar Physics Meeting, Freiburg, Germany, held September, 8-12, 2008. Online at http://espm.kis.uni-freiburg.de/, p.2.51, 12, 2

Priest, E. R., 1982, Solar magneto-hydrodynamics

Puschmann, K. G., Wiehr, E., 2006, The flux-gap between bright and dark solar magnetic structures, A&A, 445, 337–340

Rajaguru, S. P., Hasan, S. S., 2000, Radiative Transfer Effects and the Dynamics of Small-Scale Magnetic Structures on the Sun, ApJ, 544, 522–539

Rampazzo, R., Heck, A., Murtagh, F., 1988, Classification of IUE spectra - A rule-based approach, ESA Journal, 12, 385–394

Rogerson, Jr., J. B., 1961, On Photospheric Faculae., ApJ, 134, 331

Rüedi, I., Solanki, S. K., Livingston, W., Stenflo, J. O., 1992, Infrared lines as probes of solar magnetic features. III - Strong and weak magnetic fields in plages, A&A, 263, 323–338

Rutten, R. J., 1999, Magnetic Fields and Oscillations, PASP, 111, 380–381

Rutten, R. J., Kiselman, D., Rouppe van der Voort, L., Plez, B., 2001, Proxy Magnetometry of the Photosphere: Why are G-Band Bright Points so Bright?, in Advanced Solar Polarimetry – Theory, Observation, and Instrumentation, (Ed.) M. Sigwarth, vol. 236 of Astronomical Society of the Pacific Conference Series, p. 445

Sánchez Almeida, J., 2007, A Simple Model for the Distribution of Quiet-Sun Magnetic Field Strengths, ApJ, 657, 1150–1156, arXiv:astro-ph/0611711

Sánchez Almeida, J., Asensio Ramos, A., Trujillo Bueno, J., Cernicharo, J., 2001, G-Band Spectral Synthesis in Solar Magnetic Concentrations, ApJ, 555, 978–989, arXiv:astro-ph/0103006

Sánchez Almeida, J., Domínguez Cerdeña, I., Kneer, F., 2003, Simultaneous Visible and Infrared Spectropolarimetry of a Solar Internetwork Region, ApJ, 597, L177–L180, arXiv:astro-ph/0309727

Sánchez Cuberes, M., Vázquez, M., Bonet, J. A., Sobotka, M., 2002, Infrared Photometry of Solar Photospheric Structures. II. Center-to-Limb Variation of Active Regions, ApJ, 570, 886–899

Schatten, K. H., Mayr, H. G., Omidvar, K., Maier, E., 1986, A hillock and cloud model for faculae, ApJ, 311, 460–473

Schrijver, C. J., Title, A. M., 2003, The Magnetic Connection between the Solar Photosphere and the Corona, ApJ, 597, L165–L168

Schüssler, M., 1990, Theoretical Aspects of Small-Scale Photospheric Magnetic Fields, in Solar Photosphere: Structure, Convection, and Magnetic Fields, (Ed.) J. O. Stenflo, vol. 138 of IAU Symposium, p. 161

Schüssler, M., 1992, Small-Scale Photospheric Magnetic Fields, in NATO Advanced Study Institute Series C Proc. 373: The Sun: A Laboratory for Astrophysics, (Eds.) J. T. Schmelz, J. C. Brown, p. 191

Schüssler, M., Shelyag, S., Berdyugina, S., Vögler, A., Solanki, S. K., 2003, Why Solar Magnetic Flux Concentrations Are Bright in Molecular Bands, ApJ, 597, L173–L176

Sebok, W. L., 1979, Optimal classification of images into stars or galaxies - A Bayesian approach, AJ, 84, 1526–1536

Sheeley, Jr., N. R., 1969, The Evolution of the Photospheric Network, Sol. Phys., 9, 347–357

Shelyag, S., Schüssler, M., Solanki, S. K., Berdyugina, S. V., Vögler, A., 2004, G-band spectral synthesis and diagnostics of simulated solar magneto-convection, A&A, 427, 335–343

Smith, Jr., J. B., Neidig, D. F., Wiborg, P. H., West, E. A., Hagyard, M. J., Adams, M., Seagraves, P. H., 1996, An Objective Test of Magnetic Shear as a Flare Predictor, in Solar Drivers of the Interplanetary and Terrestrial Disturbances, (Eds.) K. S. Balasubramaniam, S. L. Keil, R. N. Smartt, vol. 95 of Astronomical Society of the Pacific Conference Series, p. 55

Solanki, S. K., 1993, Smallscale Solar Magnetic Fields - an Overview, Space Science Reviews, 63, 1–2

Solanki, S. K., 2003, Sunspots: An overview, A&A Rev., 11, 153–286

Solanki, S. K., Schmidt, H. U., 1993, Are sunspot penumbrae deep or shallow?, A&A, 267, 287–291

Solanki, S. K., Steiner, O., 1990, How magnetic is the solar chromosphere?, A&A, 234, 519–529

Solanki, S. K., Keller, C., Stenflo, J. O., 1987, Properties of solar magnetic fluxtubes from only two spectral lines, A&A, 188, 183–197

Solanki, S. K., Zufferey, D., Lin, H., Rüedi, I., Kuhn, J. R., 1996, Infrared lines as probes of solar magnetic features. XII. Magnetic flux tubes: evidence of convective collapse?, A&A, 310, L33–L36

Solanki, S. K., Steiner, O., Bünte, M., Murphy, G., Ploner, S. R. O., 1998, On the reliability of Stokes diagnostics of magnetic elements away from solar disc centre, A&A, 333, 721–731

Solanki, S. K., Inhester, B., Schüssler, M., 2006, The solar magnetic field, Rep. Prog. Phys., 69, 563–668

Spruit, H. C., 1976, Pressure equilibrium and energy balance of small photospheric fluxtubes, Sol. Phys., 50, 269–295

Spruit, H. C., 1979, Convective collapse of flux tubes, Sol. Phys., 61, 363–378

Spruit, H. C., Zwaan, C., 1981, The size dependence of contrasts and numbers of small magnetic flux tubes in an active region, Sol. Phys., 70, 207–228

Spruit, H. C., Schüssler, M., Solanki, S. K., 1991, Solar interior and atmosphere, pp. 890–910, Tucson, AZ, University of Arizona Press

Stangl, S., Hirzberger, J., 2005, On small scale magnetic structures in the solar photosphere, A&A, 432, 319–329

Steiner, O., 2003, Turbulence, Waves and Instabilities in the Solar Plasma, Turbulence, Waves and Instabilities in the Solar Plasma, Eds. R. Erdélyi, K. Petrovay, B. Roberts; and M. Aschwanden, Kluwer Academic Publishers, 2003.

Steiner, O., 2005, Radiative properties of magnetic elements. II. Center to limb variation of the appearance of photospheric faculae, A&A, 430, 691–700

Steiner, O., 2007, Recent progresses in the simulation of small-scale magnetic fields, in Modern Solar Facilities - Advanced Solar Science, (Eds.) F. Kneer, K. G. Puschmann, A. D. Wittmann, p. 321, Universitätsverlag Göttingen

Steiner, O., Stenflo, J. O., 1990, Model Calculations of the Photospheric Layers of Solar Magnetic Fluxtubes, in Solar Photosphere: Structure, Convection, and Magnetic Fields, (Ed.) J. O. Stenflo, vol. 138 of IAU Symposium, p. 181

Steiner, O., Grossmann-Doerth, U., Knölker, M., Schüssler, M., 1998, Dynamical Interaction of Solar Magnetic Elements and Granular Convection: Results of a Numerical Simulation, ApJ, 495, 468

Steiner, O., Hauschildt, P. H., Bruls, J., 2001, Radiative properties of magnetic elements. I. Why are vec G-band bright points bright?, A&A, 372, L13–L16

Stenflo, J. O., 1973, Magnetic-Field Structure of the Photospheric Network, Sol. Phys., 32, 41–63

Stenflo, J. O., 1982, The Hanle effect and the diagnostics of turbulent magnetic fields in the solar atmosphere, Sol. Phys., 80, 209–226

Stenflo, J. O., 2002, Polarized radiation diagnostics of solar magnetic fields, in Astrophysical Spectropolarimetry, (Eds.) J. Trujillo-Bueno, F. Moreno-Insertis, F. Sánchez, pp. 55–100

Stenflo, J. O., 2008, Solar magnetic fields, Journal of Astrophysics and Astronomy, 29, 19–28

Stenflo, J. O., Harvey, J. W., 1985, Dependence of the properties of magnetic fluxtubes on area factor or amount of flux, Sol. Phys., 95, 99–118

Stenflo, J. O., Solanki, S. K., Harvey, J. W., 1987, Center-to-limb variation of Stokes profiles and the diagnostics of solar magnetic fluxtubes, A&A, 171, 305–316

Stenflo, J. O., Keller, C. U., Gandorfer, A., 1998, Differential Hanle effect and the spatial variation of turbulent magnetic fields on the Sun, A&A, 329, 319–328

Stix, M., 2004, The sun : an introduction, The sun : an introduction, 2nd ed., by Michael Stix. Astronomy and astrophysics library, Berlin: Springer, 2004. ISBN: 3540207414

Stoyan, D., Stoyan, H., 1994, Fractals, random shapes and point fields, Wiley, New York

Sütterlin, P., Wiehr, E., Stellmacher, G., 1999, Continuum photometry of solar white-light faculae, Sol. Phys., 189, 57–68

Title, A. M., Berger, T. E., 1996, Double-Gaussian Models of Bright Points or Why Bright Points Are Usually Dark, ApJ, 463, 797

Title, A. M., Tarbell, T. D., Topka, K. P., 1987, On the relation between magnetic field structures and granulation, ApJ, 317, 892–899

Title, A. M., Topka, K. P., Tarbell, T. D., Schmidt, W., Balke, C., Scharmer, G., 1992, On the differences between plage and quiet sun in the solar photosphere, ApJ, 393, 782–794

Topka, K. P., Tarbell, T. D., Title, A. M., 1992, Properties of the smallest solar magnetic elements. I - Facular contrast near sun center, ApJ, 396, 351–363

Topka, K. P., Tarbell, T. D., Title, A. M., 1997, Properties of the Smallest Solar Magnetic Elements. II. Observations versus Hot Wall Models of Faculae, ApJ, 484, 479

Trujillo Bueno, J., 2001, Atomic Polarization and the Hanle Effect, in Advanced Solar Polarimetry – Theory, Observation, and Instrumentation, (Ed.) M. Sigwarth, vol. 236 of Astronomical Society of the Pacific Conference Series, p. 161

Tsuneta, S., Ichimoto, K., Katsukawa, Y., Nagata, S., Otsubo, M., Shimizu, T., Suematsu, Y., Nakagiri, M., Noguchi, M., Tarbell, T., Title, A., Shine, R., Rosenberg, W., Hoffmann, C., Jurcevich, B., Kushner, G., Levay, M., Lites, B., Elmore, D., Matsushita, T., Kawaguchi, N., Saito, H., Mikami, I., Hill, L. D., Owens, J. K., 2008, The Solar Optical Telescope for the Hinode Mission: An Overview, Sol. Phys., 249, 167–196, arXiv:astro-ph/0711.1715

Tung, K., Camp, D., 2008, Solar cycle warming at the Earth's surface in NCEP and ERA-40 data: A linear discriminant analysis, J. Geophys. Res., 113

Venkatakrishnan, P., 1985, Nonlinear development of convective instability within slender flux tubes. II - The effect of radiative heat transport, Journal of Astrophysics and Astronomy, 6, 21–34

Venkatakrishnan, P., 1986, Inhibition of convective collapse of solar magnetic flux tubes by radiative diffusion, Nature, 322, 156

Vögler, A., Shelyag, S., Schüssler, M., Cattaneo, F., Emonet, T., Linde, T., 2005, Simulations of magneto-convection in the solar photosphere. Equations, methods, and results of the MURaM code, A&A, 429, 335–351

Walton, S. R., Preminger, D. G., Chapman, G. A., 2003, The Contribution of Faculae and Network to Long-Term Changes in the Total Solar Irradiance, ApJ, 590, 1088–1094

Webb, A. R., Roberts, B., 1978, Vertical motions in an intense magnetic flux tube. II - Convective instability, Sol. Phys., 59, 249–274

Wiehr, E., Bovelet, B., Hirzberger, J., 2004, Brightness and size of small-scale solar magnetic flux concentrations, A&A, 422, L63–L66

Wilson, P. R., 1981, Faculae, filigree and calcium bright points, Sol. Phys., 69, 9–14

Yelles Chaouche, L., 2008, Observational diagnostics of 3D radiation-MHD simulations of solar and stellar atmospheres, Ph.D. thesis, International Max-Planck Research School on Physical Processes in the Solar System and Beyond, Universität Göttingen

Zakharov, V., 2006, Diagnostics of the solar photosphere with high spatial resolution using CH, CN and continuum spectral bands, Ph.D. thesis, International Max-Planck Research School on Physical Processes in the Solar System and Beyond, Universität Göttingen

Zakharov, V., Gandorfer, A., Solanki, S. K., Löfdahl, M., 2007, A comparative study of the contrast of solar magnetic elements in CN and CH, A&A, 461, 695–695

Zayer, I., Solanki, S. K., Stenflo, J. O., 1989, The internal magnetic field distribution and the diameters of solar magnetic elements, A&A, 211, 463–475

Zayer, I., Stenflo, J. O., Keller, C. U., Solanki, S. K., 1990, Dependence of the properties of solar magnetic flux tubes on filling factor. II - Results of an inversion approach, A&A, 239, 356–366

Zwaan, C., 1987, Elements and patterns in the solar magnetic field, ARA&A, 25, 83–111

# Publications

**Refereed publications**

- P. Kobel, J. Hirzberger, S. K. Solanki, A. Gandorfer and V. Zakharov, *Discriminant analysis of solar bright points and faculae I. Classification method and center-to-limb distribution*, Astron. and Astrophys., 502, 303 (2009)

- P. Kobel, D. Obreschkow, A. de Bosset, N. Dorsaz and M. Farhat, *Techniques for generating centimetric drops in microgravity and application to cavitation studies*, Exp. in Fluids, 47, 39 (2009)

- J. Hirzberger, T. Riethmüller, A. Lagg, S.K. Solanki and P. Kobel, *High-resolution spectro-polarimetry of a flaring sunspot penumbra*, Astron. and Astrophys., 502, 303 (2009)

- V. Zakharov, J. Hirzberger, T. L. Riethmüller, S. K. Solanki, P. Kobel, *Evidence of convective rolls in a sunspot penumbra* Astron. and Astrophys., 488, L17-L20 (2008)

- D. Obreschkow, P. Kobel, N. Dorsaz, A. de Bosset, C. Nicollier, and M. Farhat, *Cavitation Bubble Dynamics inside Liquid Drops in Microgravity*, Phys. Rev. Lett. 97, 094502 (2006)

**Conference contributions**

- P. Kobel, J. Hirzberger, V. Zakharov, A. Gandorfer and S. K. Solanki, *Center-to-limb distribution of bright points and faculae: first results of an automated detection algorithm*, in Astronomical Society of the Pacific Conference Series, 405 (2009), ed. S. V. Berdyugina, K. N. Nagendra, & R. Ramelli, Proceeding of SPW5, Ascona, Switzerland (2007)

- P. Kobel, J. Hirzberger, A. Gandorfer, S. K. Solanki and V. Zakharov, *Discriminant Analysis of Bright Points and Faculae: Center-to-Limb Distribution, Contrast and Morphology* 12th European Solar Physics Meeting, Freiburg, Germany (2008), Online at `http://espm.kis.uni-freiburg.de/,p.2.60`

# Acknowledgements

he has been always present to discuss and clarify my doubts. A special thanks to Sami, the "solar guru", for the attention he dedicated to my work between his flights to the four corners of this world, and for the working spirit and leadership he provided to the Insitute. In terms of atmosphere (I mean "social atmosphere", in case he reads these lines;o), I am grateful to Franz Kneer, one of the great fathers of solar physics, who created such a nice working "mitarbeiter" ambience in the University...Und ich bin sehr froh un stolz ein Teil deiner "Sonnenfamilie" zu sein !!

# Curriculum Vitae

| | | |
|---|---|---|
| Name: | Philippe Kobel | |
| Geburtstag: | 09. 01. 1980 | |
| Geburtsort: | Geneva, Switzerland | |
| Staatsbürgerschaft: | swiss | |
| | | |
| Schulbildung: | 9/1995–6/1999 | College Calvin, Geneva |
| Studium: | 10/2000–07/2004 | École polytechnique Fédérale de Lausanne (EPFL) Master-Studium Physik, Titel "Ingenieur Physiker" |
| | 10/2004–02/2005 | Diplomarbeit: "FM laser locking studies for a quantum memory proposal" Group of Applied Physics, Geneva University |
| | 01/2006–02/2005 | Doktorarbeit am Max-Planck-Institut für Sonnensystemforschung, Katlenburg-Lindau. |